

**Some pages of this thesis may have been removed for copyright restrictions.**

If you have discovered material in AURA which is unlawful e.g. breaches copyright, (either yours or that of a third party) or any other law, including but not limited to those relating to patent, trademark, confidentiality, data protection, obscenity, defamation, libel, then please read our [Takedown Policy](#) and [contact the service](#) immediately

# **The Tribology of Laminated Magnetic Recording Heads**

Matthew James Keith Harrison

Doctor of Philosophy

Aston University

June 1999

This copy of the thesis has been supplied on condition that anyone who consults it is understood to recognise that its copyright rests with its author and that no quotation from the thesis and no information derived from it may be published without proper acknowledgement.

## The Tribology of Laminated Magnetic Recording Heads

Matthew James Keith Harrison

Doctor of Philosophy

1999

This thesis investigates the mechanisms that lead to pole tip recession (PTR) in laminated magnetic recording heads (also known as “sandwich heads”). These heads provide a platform for the utilisation of advanced soft magnetic thin films in practical recording heads suitable for high frequency helical scan tape recording systems. PTR results from a differential wear of the magnetic pole piece from the tape-bearing surface of the head. It results in a spacing loss of the playback or read signal of 54.6dB per recording wavelength separation of the poles from the tape. PTR depends on the material combination used in the head, on the tape type and the climate – temperature and relative humidity (r.h.). Five head materials were studied: two non-magnetic substrate materials- sintered multigranular  $\text{CaTiO}_3$  and composite  $\text{CaTiO}_3/\text{ZrTiO}_4/\text{TiO}_2$  and three soft magnetic materials- amorphous  $\text{CoNbZr}$ , and nanocrystalline  $\text{FeNbSiN}$  and  $\text{FeTaN}$ . Single material dummy heads were constructed and their wear rates measured when cycling them in a Hi-8 camcorder against commercially available metal particulate (MP) and metal evaporated (ME) tapes in three different climates:  $25^\circ\text{C}/20\%\text{r.h.}$ ,  $25^\circ\text{C}/80\%\text{r.h.}$  and  $40^\circ\text{C}/80\%\text{r.h.}$  X-ray photoelectron spectroscopy (XPS) was used to examine changes the head surface chemistry. Atomic force microscopy (AFM) was used to examine changes in head and tape surface topography. PTR versus cycling time of laminated heads of  $\text{CaTiO}_3/\text{ZrTiO}_4/\text{TiO}_2$  and  $\text{FeTaN}$  construction was measured using AFM. The principal wear mechanism observed for all head materials was microabrasion caused by the mating body – the tape surface. The variation in wear rate with climate and tape type was due to a variation in severity in this mechanism, except for tape cycling at  $40^\circ\text{C}$  in which gross damage was observed to be occurring to the head surface. Two subsidiary wear mechanisms were found: third body scratching (all materials) and grain pullout (both ceramics and  $\text{FeNbSiN}$ ). No chemical wear was observed, though tribochemical reactions were observed on the metal head surfaces. PTR was found to be caused by two mechanisms – the first differential microabrasion of the metal and substrate materials and which was characterised by a low ( $\sim 10\text{nm}$ ) equilibrium value. The second was by deep ploughing by third body debris particles, thought mainly to be grain pullout particles. This level of PTR caused by this mechanism was often more severe, and of a non-equilibrium nature. It was observed more for ME tape, especially at  $40^\circ\text{C}/80\%\text{r.h.}$  and  $25^\circ\text{C}/20\%\text{r.h.}$  Two other phenomena on the laminated head pole piece were observed and commented upon: staining and ripple texturing.

For Emma, with love

## Acknowledgements

I would like to thank Professor John Sullivan for his supervision. I would also like to thank Dr Gerard Theunissen for the excellent training provided at the Philips Research Laboratories, Eindhoven and for the discussion, ideas and technical support. I am grateful to Philips for their sponsorship. This work was funded by the EPSRC, Philips, and Aston University. Many thanks to the technical staff of the Philips Research Laboratories for their preparation of samples and provision of recorders and tapes and especially to Tijs de Jong for his technical support. At Aston University I would like to thank Dr Sayah Saied for sharing her expertise in XPS and Auger, and for much moral support and to Andrew Abbot for keeping everything working!

# Contents

Chapter 1 The Use of Laminated Inductive Recording Heads in Helical Scan Tape Recording Systems ...	13
1.1 Introduction .....	13
1.2 Basic Principles of Magnetic Recording.....	15
1.2.1 Introduction .....	15
1.2.2 Magnetic Fields .....	17
1.2.3.1 The Inductive Tape Head.....	20
1.2.3.2 Writing Signal Amplitude.....	20
1.2.3.3 Reproduced Signal Amplitude.....	21
1.2.3.4 Signal-to-Noise Ratio .....	24
1.3 Hi-8 Video Recording System.....	25
1.4 Metal Evaporated and Metal Particulate Tape.....	27
1.4.1 Introduction .....	27
1.4.2 Magnetic Recording Tape for the Hi-8 Video System.....	29
1.4.3 Metal Particulate Tape.....	30
1.4.3.1 Structure of MP Tape .....	30
1.4.3.2 Magnetic Particles .....	31
1.4.3.3 Binder System.....	32
1.4.3.4 Substrate .....	33
1.4.3.5 Back Coat .....	34
1.4.3.6 Advanced MP Media.....	34
1.4.4 Metal Evaporated Tape.....	35
1.5 Laminated (Sandwich) Heads.....	38
1.5.1 Introduction .....	38
1.5.3 Soft Metal Laminated and Ferrite Heads .....	41
1.5.4 Sandwiched Laminated Recording Heads .....	43
1.5.4.1 Sandwich Laminate Head Structure.....	43
1.5.4.2 Producing the Magnetic Thin Film.....	44
1.5.4.3 Lamination Structure and Head Performance.....	45
1.5.4.4 Magnetic Materials for Use in Sandwich Heads.....	46
1.5.4.4.1 Amorphous Materials .....	46
1.5.4.4.2 Nanocrystalline Films.....	47
1.5.5 Sandwich Heads and Materials Studied in This Work .....	48
Chapter 2 Tribology.....	51
2.1 Head-Tape Contact.....	51
2.1.1 Introduction to Intimate Head Tape Contact – Lubrication Regimes and Position on the Stribeck Curve .....	51
2.1.2 Friction .....	53
2.1.2.1 Friction and Lubrication in Flexible Magnetic Recording Systems .....	54
2.1.3 Surface Roughness and Contact .....	55
2.1.3.1 Definitions of Roughness .....	55
2.1.3.2 Contact Mechanics at the Head-Tape Interface .....	57
2.1.3.3 Measurement and Modelling of the Spacing at the Head-Tape Interface.....	61
2.1.4 The Effects Water Adsorbed at the Head-Tape Interface on Contact.....	64
2.2 Wear Mechanisms .....	68
2.2.1 Introduction .....	68
2.2.2 Adhesive Wear .....	68
2.2.3 Abrasive Wear .....	70
2.2.4 Fatigue .....	71
2.2.5 Impact Wear .....	72
2.2.5.1 Erosion.....	72
2.2.5.2 Percussion.....	73
2.2.6 Corrosive Wear.....	73
2.2.7 Electrical-Arc Induced Wear .....	74
2.2.8 Fretting and Fretting Corrosion .....	74
2.3 Tribo-elements of the Hi-8 Video Recorder .....	75
2.3.1 Tape Path.....	75
2.3.2 Tape Path Components – Pins, Guides, and Flanges.....	76

2.3.2.1 Drum.....	76
2.3.2.2 Capstan .....	76
2.4 Head Wear .....	77
2.4.1 Tribo-System Parameters.....	77
2.4.1.2 Head-Tape Conformation and the Run-in Process .....	77
2.4.1.3 Head Shape.....	79
2.4.1.4 Tape Sliding Length, Repeat Passes and Head-Tape Velocity.....	79
2.4.1.5 Tape Tension and Head Protrusion- the Effect of Pressure .....	80
2.4.2 Tape Type.....	80
2.4.2.1 Abrasivity of the Magnetic and Head Cleaning Particles .....	81
2.4.2.2 Mechanical Properties of the Tape .....	81
2.4.2.3 Lubricants .....	82
2.4.3 Environment – The Effects of Temperature and Humidity .....	82
2.4.3.1 Temperature.....	82
2.4.3.2 Humidity.....	83
2.4.4 Materials Dependence of Head Wear .....	84
2.4.4.1 Ceramic.....	85
2.4.4.2 Mechanisms of Ceramic Wear at Elevated Humidity.....	87
2.4.4.3 Stress Corrosion.....	88
2.4.4.4 Magnetic Material.....	91
2.5 Media Wear .....	92
2.5.1 Media Wear and Dropouts.....	92
2.5.2 A Comparison of ME and MP Tapes.....	93
2.5.3 Wear Mechanisms in ME Media .....	94
2.5.4 Wear Mechanisms of MP Tape .....	95
2.6 Stain.....	96
2.7 Pole Tip Recession (PTR) .....	99
2.7.1 PTR and Head Structure .....	100
2.7.2 The Relation between PTR and Magnetic Core Material.....	100
2.7.3 The Relationship between PTR and Substrate and Metal Core Combination .....	101
2.7.4 The Relationship between Tape Type and PTR .....	102
2.7.5 Modelling of PTR and the Action of Alternative Mechanisms .....	104
Chapter 3 - Experimental.....	107
3.1 Introduction .....	107
3.2 Cycling Tests .....	108
3.2.1 Heads, Tapes and Recorders.....	108
3.2.3 Climate, Head Material and Tape Combinations Selected for Cycling Tests.....	109
3.2.4 Cycling Test Procedure .....	109
3.2.5 Cycling Apparatus .....	111
3.2.6 Head Mounting and Measuring Head Protrusion, and Subsequent Optical Monitoring of the Head during Cycling .....	113
3.2.7 Measuring Wear Rates Using the Microhardness Indentation Method .....	115
3.3 Surface Analytical Techniques .....	117
3.3.1 X-ray Photoelectron Spectroscopy (XPS) .....	117
3.3.1.1 Experimental Set Up` .....	117
3.3.1.2 XPS Data analysis.....	117
3.3.1.2.1 Peak Identification and Charge Referencing .....	117
3.3.1.2.2 Background Subtraction .....	118
3.3.1.2.3 Data Smoothing .....	119
3.3.1.2.4 Quantification .....	119
3.3.1.2.5 Peak Fitting.....	120
3.3.1.3 Sputter Depth Profiling.....	120
3.3.2 Atomic Force Microscopy .....	121
Chapter 4 Results.....	123
4.1 AFM Analysis of the Tapes Used in the Cycling of Dummy and Sandwich Heads.....	123
4.1.1 Introduction .....	123
4.1.2 AFM Images.....	124
4.1.3 Roughness, Bearing Ratio and Peak-Valley Measurements of the Asperities of ME and MP Tapes .....	130
4.1.3.1 Roughness Values.....	131

4.1.3.2 Bearing Ratio Values .....	132
4.1.3.3 Peak-Valley Analysis .....	134
Tape .....	134
4.2 Cycling Tests and Wear Rates of Dummy Heads .....	135
4.2.1 Introduction .....	135
4.2.3 Wear Rate Data Tables .....	136
4.2.4 Longitudinal Wear Rate Profiles .....	140
4.2.5 Effects of Head Size and Protrusion on Wear Rate .....	143
4.2.6 Trends in Average Wear Rate .....	143
4.3 Topographical Analysis of Cycled Dummy Heads by Optical and Atomic Force Microscopy. ....	146
4.3.1 Introduction .....	146
4.3.2 The Data .....	146
4.3.2.1 AFM Data .....	146
4.3.2.2 Optical Images .....	154
4.3.3 Analysis of Topographical Data of the Cycled Dummy Heads .....	157
4.3.3.1 Grain Fracture/Pullout in S1 and S2 .....	157
4.3.3.2 AFM of Uncycled Metal Heads .....	159
4.3.3.3 The Contact Zone .....	159
4.3.3.4 Roughness Values .....	160
4.3.3.4.1 Trends in Roughness Observed in the Ceramic Heads, S1 and S2 .....	160
4.3.3.4.2 Trends in Roughness Observed in the Metal Heads, M1-3 .....	161
4.3.3.5 Microgrooving .....	161
4.3.3.5.1 Peak-Valley Analysis of Microgrooving .....	162
4.3.3.5.2 Differences in Microabrasion of Ceramic Substrates between ME and MP Tapes .....	164
4.3.3.6 Fracture Damage in Metals .....	164
4.3.3.7 Debris, Deposits and Staining Observed on the Head Surface .....	164
4.4 XPS Results .....	168
4.4.1 Introduction .....	168
4.4.2 Metals .....	168
4.4.2.1 Sample Preparation .....	168
4.4.2.2 Corrosion Tests .....	169
4.4.2.3 Quantification and Identification of XPS Spectra .....	169
4.4.2.4 CoNbZr XPS Results .....	170
4.4.2.5 FeNbSiN XPS Results .....	174
4.4.2.6 FeTaN XPS Results .....	183
4.4.2.7 Comparison of the XPS Data Collected for CoNbZr, FeNbSiN and FeTaN .....	187
4.4.3 XPS Analysis of the Ceramics S1 and S2 .....	189
4.4.4 XPS Evidence for the Transfer of PFPE Lubricant from ME Tape .....	194
4.5 Sandwich Heads Results Section .....	196
4.5.1 Introduction .....	196
4.5.2 The Heads .....	196
4.5.3 Cycling Experiments .....	197
4.5.4 Measurement of PTR .....	199
4.5.5 Wear History of Sandwich Heads .....	200
4.5.5.1 H1 and H2: Cycled Against ME Tape at 30°C/90%r.h. for 200 Hours .....	200
4.5.5.2 H3 and H4: Cycled against MP Tape for 150 Hours at 30°C/90%r.h. ....	201
4.5.5.3 H5 and H6: Cycled against ME Tape for 300 Hours at 22°C/80% r.h. ....	204
4.5.5.4 H7 and H8: cycled against MP Tape for 300 Hours at 22°C/80%r.h. ....	213
4.5.5.5 H9 and H10: Cycled against ME Tape for 200 Hours at 25°C/20%r.h. ....	215
4.5.6 Comparison between Sandwich Heads Cycled against ME Tape under 30°C/90%r.h., 22°C/80%r.h. and 25°C/20%r.h. ....	217
4.5.7 Comparison of Features between Sandwich Heads Cycled against MP Tape under 30°C/90%r.h. and 22°C/80%r.h. ....	218
4.5.8 Comparison of PTR with Time Between 30°C/90%r.h., 22°C/80%r.h. and 25°C/20%r.h. ....	218
4.5.9 AFM Hardness Measurements of Insulation Layers and MP Generated Particles .....	218
4.5.10 Staining Observed by Optical Microscopy .....	220
Chapter 5 Discussion .....	221
5.1 Introduction .....	221
5.2 Media Wear .....	221
5.3 Microabrasion Texture on the Wear Surfaces of the Dummy Heads .....	223



5.4 Relation of Measured Knoop Microhardness on the Observed Wear Rates.....	224
5.5 Wear Mechanisms Observed in the Ceramic Materials.....	224
5.6 Surface Chemistry of the Three Metallic Materials, Topographic Features and Wear Mechanisms...	228
5.7 Observed Pole Tip Recession .....	230
5.8 Staining.....	233
5.9 Ripple Texturing of the Metal laminations of the Sandwich Heads.....	235
Chapter 6 Conclusion and Suggestions for Further work.....	236

## List of Tables

1.1 Review of Magnetic Field Units	18
1.2 Specifications of the Hi-8 Video System	27
1.3 Magnetic Properties of Hi-8ME, Hi-8MP and 8mm MP Video Tapes	29
1.4 Comparison of Particle Size	34
1.5 Chemical Structure of Commercial PFPE Lubricants	37
1.6 Chemical Structure of Commercial Functional PFPE Lubricants	38
1.7 Magnetic Properties of Various Ferrites and Soft Magnetic Materials	42
4.1 Tapes Used During Cycling Experiments	123
4.2 Details of Cycled Tape Samples	124
4.3 Roughness Values of the Sample Tapes after Background Substitution	131
4.4 Peak-Valley Analysis of the Tape Samples after Background Substitution.	134
4.5 Materials Used in Dummy Heads and their Measured Knoop Microhardness ( $H_k$ )	135
4.6 Wear Rate Data for S1 (CaTiO <sub>3</sub> ) Dummy Heads	138
4.7 Wear Rate Data for S2 (Zr-CaTiO <sub>3</sub> ) Dummy Heads	138
4.8 Wear Rate Data for Metal Dummy Heads	139
4.9 S1 Dummy Heads – Summary of AFM Data	148
4.10 S2 Dummy Heads – Summary of AFM Data	148
4.11 M1 and M3 Dummy Heads – Summary of AFM and Optical Data	149
4.12 M2 Dummy Heads – Summary of AFM and Optical Data	149
4.13 CoNbZr Identification and Quantification of XPS Data	171
4.14 FeNbSiN Identification and Quantification of XPS Data	176
4.15 Peak Fit Table for Nb 3d	181
4.16 FeTaN Identification and Quantification of XPS Data	184
4.17 Peak Fit Table Ta 4f	187
4.18 Depth and Composition of the Native Oxides of the Metals by XPS	187
4.19 The Binding Energies and Chemical States of S1 and S2 Dummy Heads by XPS	190
4.20 Quantification of the Surface Components of Cycled S1 Dummy Heads	190
4.21 Quantification of the Surface Components of Cycled S2 Dummy Heads	191
4.22 Binding energies (eV) of F1s Spectra	194
4.23 Sandwich Head Cycling Experiments	196
4.24 Sandwich Head Dimensions	197
4.25 Protrusion Measurements Taken During the Cycling of Sandwich Heads	198
4.26 Average PTR Values for Cycling at 30C/90%r.h.	200
4.27 MP Generated Particles	204
4.28 Dimensions of the ME Generated Particles	205

## List of Figures

1.1 Inductive Reading and Writing Process	16
1.2 Hysteresis Loop for the Magnetisation Process	19
1.3 Design Features of Magnetic Recording Head	20
1.4 Thickness, Spacing and Gap Loss in Magnetic Recording	23
1.5 Frequency spectrum of a Hi-8 Video Signal	25
1.6 Rotary Scanner	26
1.7 Track Positions on a Tape Written by a Hi-8 Recorder	26
1.8 Cross Section of a Particulate Tape Showing Dimensions Typical of a MP Tape	30
1.9 MP++ Media in Cross section	35
1.10 Characteristic Curved Columnar Structure of a ME Thin Film	36
1.11 Cross Section of Advanced Metal Evaporated Tape	36
1.12 Outline of a Laminated Head	41
1.13 Schematic Diagram of a Metal in Gap (MIG) Recording Head	43
1.14 Schematic Diagram of a Sandwich (Laminated) Head	44
1.15 Magnetostatic Coupled Laminated Thin Film Structure	46
1.16 Sandwich Head of the Type Studied in this Thesis	49
1.17 Zoom in on the Magnetic Track of the Sandwich Head	50
2.1 Typical Stribeck Curve For the Head-tape Interface	52
2.2 Surface Profile Used to Illustrate Surface Roughness Parameters	55
2.3 Schematic Diagram of the Various Lubrication Regimes	66
2.4 Abrasive Wear Model in which a Cone Removes Material from a Surface	71
2.5 Dependence of Rate of Erosion on Impact Angle	72
2.6 Tape Path in Philips M870 Hi-8 Camcorder used in this Study	75
2.7 Schematic of Various Head-Tape Conformations along the Longitudinal Head Radius	78
2.8 Michalske and Freiman Reaction for Water Enhanced Si-O-Si Bond Rupture	89
2.9 Crack Velocity Vs. Stress Intensity for Soda-Lime-Silica Glass	90
2.10 Diagram of Head-Tape Contact used in the PTR Model of Abe, Tsuchiya and Noro	104
3.1 Flow Chart Showing the Steps Involved in Conducting Cycling Tests	110
3.2 Schematic of a Simple Environmental Chamber for High Humidity Cycling Tests	112
3.3 Diagram Showing the Placement of Heads in the Drum.	113
3.4 Mounting of the Drum on the Microscope for Optical Inspection	114
3.5 Geometry of the Knoop Microhardness Indentation	115
3.6 Microhardness Indentations Made in Dummy Head Surfaces	116
4.1 HCT AFM. Uncycled, 3-d Representation	124
4.2 (a) Uncycled ME1 AFM	125
4.2 (b) 3-d Representation of 4.2 (a)	125
4.3 (a) Cycled ME1 AFM	125
4.3 (b) 3-d Representation of 4.3 (a)	125
4.4 (a) Cycled ME2 AFM	125
4.4 (b) 3-d Representation of 4.4 (a)	125
4.5 (a) Uncycled ME3 AFM	126
4.5 (b) 3-d Representation of 4.5 (a)	126
4.6 (a) Cycled ME1 AFM	126
4.6 (b) 3-d Representation of 4.6 (a)	126
4.7 (a) Uncycled MP1 AFM	127
4.7 (b) 3-d Representation of 4.7 (a)	127
4.8 (a) Cycled MP1 AFM	127
4.8 (b) 3-d Representation of 4.8 (a)	127
4.9 (a) Cycled MP2 AFM	127
4.9 (b) 3-d Representation of 4.9 (a)	127
4.10 (a) Uncycled MP3 AFM	128
4.10 (b) 3-d Representation of 4.10 (a)	128
4.11 (a) Cycled MP3 AFM	128
4.11 (b) 3-d Representation of 4.11 (a)	128
4.12 ME1 Cycled AFM: After Background Substitution	130
4.13 Cycled MP2: After Background Substitution	131
4.14 Bearing Ratio Plots for the Sample ME Tapes After Background Substitution	133

4.15 Bearing Ratio Plots for the Sample MP Tapes After Background Substitution	133
4.16 S1C Longitudinal Wear Profile	141
4.17 S2D Longitudinal Wear Profile	141
4.18 S1F Longitudinal Wear Profile	142
4.19 S2H Longitudinal Wear Profile	142
4.20 M1D Longitudinal Wear Profile	142
4.21 Wear Rates of Dummy Heads Vs. ME Tape	145
4.22 Wear Rates of Dummy Heads Vs. MP Tape	145
4.23 S1A AFM: ME Tape, 25°C/20%r.h.	150
4.24 S1E AFM: ME Tape, 25°C/90%r.h.	150
4.25 S1J AFM: ME Tape, 40°C/80%r.h.	150
4.26 S1D AFM: MP Tape, 25°C/20%r.h.	150
4.27 S1G AFM: MP Tape, 25°C/90%r.h.	150
4.28 S1L AFM: MP Tape, 40°C/80%r.h.	150
4.29 S2B AFM: ME Tape, 25°C/20%r.h.	151
4.30 S2F AFM: ME Tape, 22°C/90%r.h.	151
4.31 S2I AFM: ME Tape, 40°C/80%r.h.	151
4.32 S2C AFM: MP Tape, 25°C/20%r.h.	151
4.33 S2K AFM: MP Tape, 22°C/90%r.h.	151
4.34 S2I AFM: MP Tape, 40°C/80%r.h.	151
4.35 M1 AFM: Uncycled	152
4.36 M1B AFM: ME Tape, 25°C/90%r.h.	152
4.37 M1C AFM: MP Tape, 25°C/90%r.h.	152
4.38 M3 AFM: Uncycled	152
4.39 M3A AFM: ME Tape, 25°C/90%r.h.	152
4.40 M3C AFM: MP Tape, 25°C/90%r.h.	152
4.41 M2 AFM: Uncycled	153
4.42 M2C AFM: MP Tape, 20°C/90%r.h.	153
4.43 M2E AFM: ME Tape, 40°C/80%r.h.	153
4.44 M2A AFM: ME Tape, 20°C/90%r.h.	153
4.45 M2C AFM: Zoom in on Figure 4.42 Showing Fracture Scar	153
4.46 M2H AFM: MP Tape, 40°C/80%r.h.	153
4.47 S1L Optical Micrograph. Absence of Stain	154
4.48 S1G Optical Micrograph. Smearing of Ceramic Head Debris	154
4.49 M3A Optical Micrograph. Contact Zone	155
4.50 M1C Optical Micrograph. Trailing edge Debris	155
4.51 AFM of ME Tape Debris on the Trailing Edge of S2F	155
4.52 M1E Optical Micrograph. Lubricant Melted on Head Surface	156
4.53 M1E Optical Micrograph. Lubricant Melted on Head Surface – Side View	156
4.54 M2H Optical Micrograph. Ribbon-Like Staining	156
4.55 M3D Optical Micrograph. Ribbon-Like staining	156
4.56 S1I, MP2 Tape, 40°C/80%r.h. Zoom on Cracks Under Particle	158
4.57 S2C (MP1 Tape, 25°C/90%r.h) Line Scan Perpendicular to Microgrooving	162
4.58 M1 (ME1 Tape, 20°C/90%r.h) Line Scan Perpendicular to Microgrooving	162
4.59 Peak Angle and Spacing Distribution Histograms. M1B, ME1 Tape, 25°C/90%r.h.	163
4.60 Peak Angle and Spacing Distribution Histograms. S2F, ME1 Tape, 22°C/90%r.h.	163
4.61 CoNbZr on CaTiO <sub>3</sub> Head Ar Ion Sputter Depth Profile	172
4.62 CoNbZr Comparison of Co 2p Spectra	172
4.63 CoNbZr Comparison of Nb 3d Spectra	173
4.64 CoNbZr Comparison of Zr 3d Spectra	174
4.65 FeNbSiN Deposited on Si(100) Ar Ion Sputter Depth Profile	177
4.66 FeNbSiN Comparison of Fe 2p Spectra	178
4.67 FeNbSiN Fitting of the Fe 2p <sub>3</sub> Metal Peak	178
4.68 FeNbSiN Fitting of the Fe 2p <sub>3</sub> Oxide Peak	179
4.69 FeNbSiN Fitting of the Fe 2p <sub>3</sub> Hydroxide Peak	179
4.70 FeNbSiN Comparison of Nb 3d Spectra	180
4.71 FeNbSiN Fitting of the Nb 3d Peak	181
4.72 FeNbSiN Comparison of Si 2p Spectra	182
4.73 FeNbSiN Comparison of N 1s Spectra	182

4.74 FeTaN deposited on CaTiO <sub>3</sub> Head Ar Ion Sputter Depth Profile	184
4.75 FeTaN Comparison of Fe 2p <sub>3/2</sub> Spectra	185
4.76 FeTaN Comparison of Ta 4f Spectra	185
4.77 FeTaN Comparison of N 1s Spectra	186
4.78 FeTaN Fitting of Ta 4f Peak	186
4.79 O 1s XPS Peak from S2I	191
4.80 Ca 2p XPS Peak from S2I	192
4.81 Ti 2p XPS Peak from S2I	193
4.82 Zr 3d XPS Peak from S2I	193
4.83 Peak Fitting to Two Synthetic Peaks of the F 1s Spectra of M1E	195
4.84 H6 After 10s HCT	198
4.85 An example of Line Scans and Points Used to Calculate Average PTR	200
4.86 H1 AFM: 200 Hours ME tape 30°C/90%r.h.	202
4.87 H3 AFM: 150 Hours MP tape 30°C/90%r.h.	202
4.88 H4 AFM: 150 Hours MP tape 30°C/90%r.h.	202
4.89(a) AFM of MP Generated Particles	203
4.89(b) 3-d Representation AFM of MP Generated Particles	203
4.89(c) Linescan Through AFM of MP Generated Particles	203
4.90 Average PTR Vs. Time for H5 and H6 Cycled Against ME Tape 22°C/80%r.h.	205
4.91(a) H5 AFM: 10 Hours ME tape 22°C/80%r.h.	206
4.91(b) 50 Hours	206
4.91(c) 100 Hours	206
4.91(d) 150 Hours	206
4.91(e) 200 Hours	206
4.91(f) 300 Hours	206
4.92(a) H6 AFM: 10 Hours ME tape 22°C/80%r.h.	207
4.92 (b) 50 Hours	207
4.92(c) 100 Hours	207
4.92(d) 150 Hours	207
4.92(e) 200 Hours	207
4.92(f) 300 Hours	207
4.93(a) AFM of ME Generated Particles: H6 50 Hours ME Tape 22°C/80%r.h.	209
4.93(b) Zoom in on 4.93(a)	209
4.93(c) Three-Dimensional Representation of 4.93 (a)	209
4.94 H5 AFM: 300 Hours ME 22°C/80%r.h. Particles in the Debris Smear over Track	210
4.95(a) AFM of Ripple Pattern Observed Running Perpendicularly to the Tape Direction	212
4.95(b) 3-d Representation of 4.95(a)	212
4.95(c) AFM Linescan Through Ripple Pattern	212
4.96 Average PTR Vs. time for H7 and H8 Cycled Against MP Tape 22°C/80%r.h.	213
4.97(a) H8 AFM: 10 Hours MP tape 22°C/80%r.h.	214
4.97 (b) 50 Hours	214
4.97(c) 100 Hours	214
4.97(d) 150 Hours	214
4.97(e) 200 Hours	214
4.97(f) 300 Hours	214
4.98 Average PTR Vs. time for H9 and H10 Cycled Against ME Tape 25°C/20%r.h.	215
4.99(a) H9 AFM: 10 Hours ME tape 25°C/20%r.h.	216
4.99 (b) 50 Hours	216
4.99(c) 100 Hours	216
4.99(d) 200 Hours	216
4.100 H7: Comparison of Topographic and Z-Modulation (Hardness/Compliance) Maps	219
4.101 H3 Optical Micrograph: "Brown Stain" on Metal Layers 150Hours MP 30°	220

# Chapter 1 The Use of Laminated Inductive Recording Heads in Helical Scan Tape Recording Systems

## 1.1 Introduction

In this work the tribology of laminated (or sandwich) recording heads in Hi-8 video recorders has been studied. Ferrites, the traditional materials of choice for video recording heads do not meet the soft magnetic criteria for high frequency magnetic recording systems such as Hi-8 or digital video recording, or for computer data storage systems that utilise the same helical scan recording system such as the DDS – digital data storage system family. Sandwich heads are so called because a thin layer of soft magnetic laminations (hence the name laminated head) forming the electro-magnetically active part of the head is sandwiched between two layers of a non-magnetic substrate. These substrate layers provide the majority of the tape-bearing surface. Thus the sandwich head provides a platform for the utilisation of advanced soft magnetic thin films in practical recording devices. Their major draw back is tribological – differential wear between the magnetic material and the substrate will result in a spacing between the magnetic pole pieces and the tape bearing surface of the head and the tape. This phenomenon is called pole tip recession or PTR. This spacing introduces a loss in the playback signal – “spacing loss” that increases exponentially with recording frequency and exponentially with the spacing. It corresponds to a 1dB loss in the signal with every 10nm of spacing at a recording wavelength of 0.1 $\mu$ m. As the recording bandwidth increases to achieve ever-higher data transfer rates spacing loss becomes more critical.

PTR has been found to vary with material combination, climate (temperature and humidity) and tape type<sup>1</sup>. Practical tape drives, especially portable video cameras must be able to operate under the various extremes of climatic condition found in the world – from the hot and humid tropical conditions to the cool and hot and arid deserts to the colder, but damp temperate zones! They must also be able to cope with the range of magnetic tapes present on the market. For high frequency recording applications this consists of a mix of metal particulate (MP) and metal evaporated (ME) media with differing surface textures, surface chemistries and mechanical properties. Philips Research Laboratories provided the

impetus behind this project. They wished to understand the mechanisms behind pole tip recession for a narrow band of promising materials under varying climatic conditions against MP and ME tapes.

The five materials were chosen included two non-magnetic substrate materials. These were both sintered multigranular ceramics: S1 –  $\text{CaTiO}_3$  and S2 – a composite consisting of  $\text{CaTiO}_3/\text{ZrTiO}_4/\text{TiO}_2$ . Three soft magnetic materials were chosen: M1 – amorphous  $\text{CoNbZr}$ , M2 – nanocrystalline  $\text{FeNbSiN}$ , and M3 – nanocrystalline  $\text{FeTaN}$ .

With a strong humidity dependence of PTR chemical wear mechanisms were suspected. To study this single material dummy heads were prepared of these five materials by Philips. These had sufficient surface area for their surface chemistry to be studied by x-ray photoelectron spectroscopy at Aston University. Room temperature and high humidity ( $25^\circ\text{C}/80\%\text{r.h.}$  – where r.h. = relative humidity) were selected as conditions likely to promote tribochemical corrosion. MP and ME tape types were chosen for study as both types are available on the market and hence it was of equal importance to study the effect of both. In addition to the chemical analysis two other major tools were employed at Aston University to help elucidate the wear mechanisms operative in this system. The rate of change of depth Knoop microhardness indentations made into the head surfaces was used to determine wear rates. And atomic force microscopy, AFM was used to study the topography of the head and tape wear surfaces on the nanoscopic scale to help identify mechanical wear mechanisms. Philips Hi-8 camcorders and commercially available Sony 8mm MP and ME tapes were provided by Philips to conduct the cycling test on the heads. The heads were mounted, the cycling tests, wear rate measurements and all the subsequent analyses were conducted at Aston University by the Author.

The wear rates and wear mechanisms of the two substrate materials were studied at two further climates – warm and wet ( $40^\circ\text{C}/80\%\text{r.h.}$ ), and room temperature and dry ( $25^\circ\text{C}/20\%\text{r.h.}$ ). Finally PTR with respect to cycling time of sandwich heads constructed from a combination of S2 and M3 was measured at all three climates, and the mechanisms responsible for PTR elucidated from data gathered from these heads and from the dummy heads.

The purpose of this chapter is to introduce the magnetic recording process and the systems studied in this work. Section 1.2 gives a brief overview of inductive magnetic recording theory, leading to a description of spacing loss and signal to noise considerations in head design. Section 1.3 then goes on to describe the Hi-8 video recording system, the platform used to evaluate the various heads studied. The magnetic recording media used is described in 1.4, and the sandwich heads and the materials used within them in Section 1.5. The literature covering the tribology of helical scan flexible magnetic recording systems is reviewed in Chapter 2, including factors influencing head wear and pole tip. The experimental techniques used are described in Chapter 3, and the results found in Chapter 4. These results are discussed in Chapter 5, and conclusions drawn in Chapter 6.

## 1.2 Basic Principles of Magnetic Recording

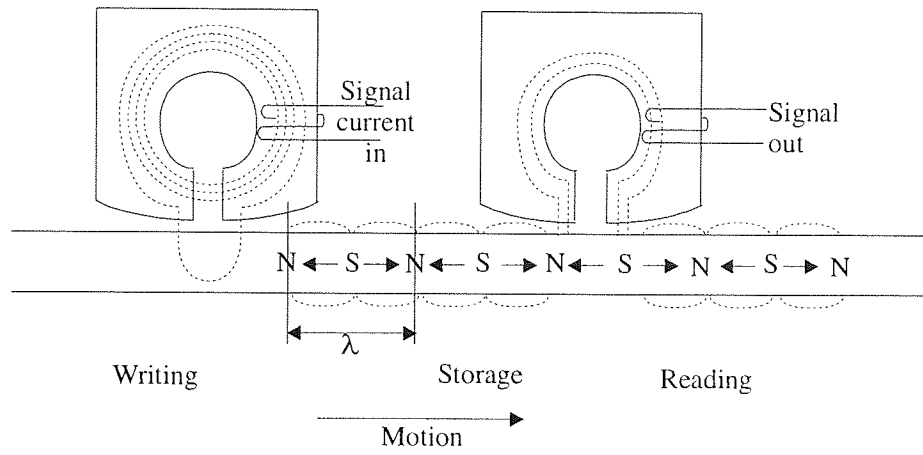
### 1.2.1 Introduction

Figure 1.1 shows the basic writing and reading processes on a magnetic tape. The inductive head is a soft magnetic gapped toroid wound about its core with a coil bearing the signal current. The tape consists of magnetically hard single domain particles or crystal grains on a flexible polymeric substrate. In the write process a signal current applied to the core windings magnetise the head. The flux patterns follow the head path and fringe the gap, magnetising the medium. The relative motion of the head against the tape allows the temporal signal to be recorded in the spatial domain of the media. If the signal is of a frequency  $f$  and the relative velocity is  $v$ , then the magnetisation pattern is recorded with a fundamental wavelength  $\lambda$ , according to Equation 1.1

$$\lambda = v/f$$

Equation 1.1





**Figure 1.1 Inductive Writing and Reading Process on Magnetic Tape using a Torroidal Head**

In the reading, or reproduction, process the dipolar magnetisation pattern of the media causes spatially varying magnetic fields that thread the core of the head (ideally of a high permeability) as the tape passes the gap. A signal of voltage,  $V$ , is induced into the core windings according to Faraday's Law of Induction, shown in Equation 1.2 where  $\phi$  is the flux,  $N$  is the number of turns,  $t$  is time,  $v$  is the head-tape velocity and  $x$  is distance.

$$V = - (d\phi/dt) = -Nv(d\phi/dx) \quad \text{Equation 1.2}$$

The voltage induced in the read coils is very small, and becomes vanishingly so at small track widths.

An alternative to inductive reading is provided by the magnetoresistive effect. In its simplest form this is the dependence of the resistivity of a conductor,  $\rho$ , upon the angle,  $\theta$ , between the direction of the current – density vector and the applied magnetic field, as given in Equation 1.3:

$$\rho = \rho_0 + \Delta\rho\cos^2\theta \quad \text{Equation 1.3}$$

Typical materials employed in magnetoresistive heads such as Ni-Fe, Ni-Co and Co-Fe show a change in base resistivity,  $\rho_0$ , in the order of 2-6%<sup>2</sup>. Magnetoresistive heads are read only, but in this function they tend to exhibit higher signal levels, especially at low velocities, than inductive heads and are currently being employed in both disc and tape applications.

### 1.2.2 Magnetic Fields

The three field vectors  $H$ ,  $M$  and  $B$  collectively form the magnetic field. This can exist anywhere in space, both inside and outside the magnetic material and arises from the motion of electronic charges. In the magnetic recording system (head and medium)  $H$  is due the current in the coil and the magnetised materials.  $M$  is the magnetisation, a specific quantity representing the average atomic moment, non-zero only in a magnetic material.  $B$  is the induction or flux density and is given (In S.I.) by Equation 1.4, where  $\mu_0 = 4\pi \times 10^{-7}$  H/m, the permeability of free space.

$$B = \mu_0(H+M) \quad \text{Equation 1.4}$$

When  $M$  results from the application of an external field,  $H$ , it is given by Equation 1.5, where  $\chi$ , the susceptibility can be a tensor representing an isotropic material:

$$M = \chi H \quad \text{Equation 1.5}$$

Combining Equations 1.4 and 1.5,  $B$  can be expressed in terms of  $H$ , where  $\mu = \mu_0(1+\chi)$ :

$$B = \mu H \quad \text{Equation 1.6}$$

Unfortunately, two different sets of units, the cgs and the S.I. are both in current usage by the magnetic recording industry to describe magnetic field properties. They are reviewed in Table 1.1. Though the two systems are not entirely analogous as demonstrated by the definition of  $B$  included in the table, they are often used interchangeably in the literature.

Units:	S.I.	cgs	conversion
	$B = \mu_0(H+M)$	$B = H+4\pi M$	
B	T	G	$1T = 10^4G$
H	A/m	Oe	$80A/m \approx 1 \text{ Oe}$
M	A/m	G	$1KA/m = 1G \text{ (emu/cc)}$
$\mu_0 = 4\pi \times 10^{-7} \text{ H/m}$			

**Table 1.1 Review of Magnetic Field Units**

The process of magnetisation is hysteretic with applied field. This is a result of irreversible changes that cause loss of energy as heat during the magnetisation process, the area enclosed by the hysteresis loop being a measure of this. A Typical M-H hysteresis loop is shown in Figure 1.2.

On the hysteresis loop the saturation magnetisation is represented by  $M_s$ . As the applied field is reduced to zero the remanent magnetisation is represented by  $M_r$ . The field required to reduce the magnetisation to zero,  $H_c$ , is called the coercivity. An analogous hysteresis

curve may be plotted for the magnetic induction,  $B$ , with corresponding  $B_r$  and  $B_s$  values representing remanent and saturation magnetic induction respectively.

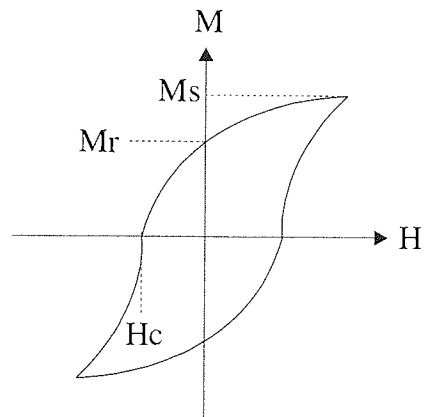


**Figure 1.2 Hysteresis Loop for the Magnetisation Process**

### 1.2.3.1 The Inductive Tape Head

Figure 1.3 shows the essential features of the head chips typically used in helical scan magnetic tape recording systems. In the following sections the physics of the magnetic recording process that affect optimisation of the design parameters of the magnetic head are discussed. The tapes studied in this work are described in Section 1.4 and the heads in Section 1.5.

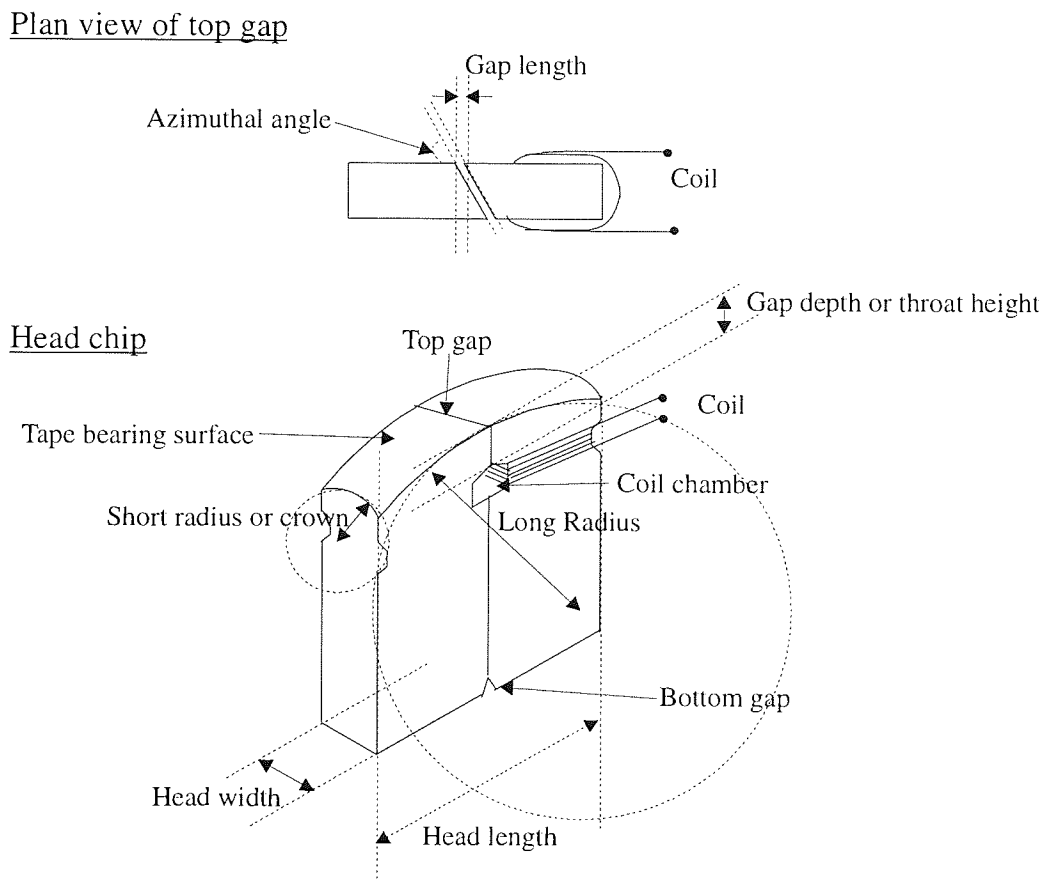


**Figure 1.3 Design Features of a Magnetic Recording Head**

### 1.2.3.2 Writing Signal Amplitude

The writing process is much less critical than the reproduction process in terms of head output, providing the head has sufficient  $B_s$  to write the coercivity of the media. This is due to the very small voltages induced in the reproduce head coils as compared to the large fields produced by a similar head in writing. The features of the head that improve the reproduced signal amplitude are discussed in the next section. Head designs to write a high coercivity tape are discussed in Section 1.5.

### 1.2.3.3 Reproduced Signal Amplitude

The play-back or reproduce signal amplitude in magnetic recording is dependent on recording wavelength, the gap length, the head-medium separation, the magnetic properties of the medium, and its thickness. Wallace<sup>3</sup> gave a general expression for playback amplitude, shown in Equation 1.7:

$$e(t) = 10^{-4} \alpha N W \{ \mu_r / (\mu_r + 1) \} M_r U (2\pi\delta/\lambda) T(\lambda) S(\lambda) G(L) \cos(2\pi x_0/\lambda)$$

Equation 1.7

Where the major factors are:

$$\begin{aligned} M_r &= \text{remnant magnetisation of the media (Wb/m}^2\text{)} \\ &= S_p \sigma_s \rho \end{aligned}$$

$$\begin{aligned} T(\lambda) &= \text{media thickness loss} \\ &= \{ 1 - \exp(-2\pi\delta/\lambda) \} / \{ 2\pi\delta/\lambda \} \end{aligned}$$

$$\begin{aligned} S(\lambda) &= \text{head-media spacing loss} \\ &= \exp(-2\pi d/\lambda) \end{aligned}$$

$$\begin{aligned} G(\lambda) &= \text{read gap length loss} \\ &= \{ \sin(\pi g/\lambda) \} / (\pi g/\lambda) \end{aligned}$$

$$\alpha = \text{head efficiency factor}$$

And where:

N = number of turns in the head

W = head width (mm)

$\mu_r$  = relative permeability of the core

U = relative velocity of the head to the media (m/s)

$x_0 = Ut$ , the longitudinal position of the head along medium relative to an arbitrary reference (mm)

t = time (s)

$\lambda$  = recorded wavelength ( $\mu\text{m}$ )

$\delta$  = thickness of medium ( $\mu\text{m}$ )

$d$  = effective spacing between the head and the surface of the medium

$g$  = gap length

$S$  = remanence squareness (reduced saturation remanence) of the medium =  $M_r/M_s$

$M_s$  = saturation magnetisation of the medium ( $\text{Wb/m}^2$ )

$p$  = packing fraction of particles in media (0-1.0)

$\sigma_s$  = specific saturation magnetisation of particles ( $\text{emu/g}$ )

$\rho$  = density of particles ( $\text{g/cm}^3$ )

The three loss functions characterised by Wallace are usually expressed in decibel (dB) form, as shown below in Equations 1.8 –1.10:

$$T(\lambda) = -20\log_{10}\{2\pi\delta/\lambda\}/\{1-\exp(2\pi\delta/\lambda)\} \quad \text{Equation 1.8}$$

The tape thickness loss shows that as recording wavelength decreases then the effective thickness of the medium decreases.

$$S(\lambda) = -54.6 d/\lambda \quad \text{Equation 1.9}$$

This is the so-called “Wallace” or spacing loss equation. Contributions to spacing loss may arise from such features as media and head surface roughness, compliance of surface asperities, magnetic dead layers in the head or media and build up of debris or staining at the interface. These are described in greater detail in the next chapter on tribology of the head-tape interface. Study of such features form the main body of this thesis.

$$G(\lambda) = -20\log_{10} \{(\pi g/\lambda)/\sin(\pi g/\lambda)\} \quad \text{Equation 1.10}$$

The gap loss gives a null in the signal at a recording wavelength equal to the gap length. In fact a more exact solution<sup>4</sup> of the magnetic field about the gap yields an “electrical” gap null 1.11 times that of the “optical” gap (that measured by microscopy).

The contributions (in dB) of the three losses are shown graphically in Figure 1.4 as a function of  $\delta$ ,  $d$  and  $g$ , each expressed as multiples of the recording wavelength. Recorded data must be either encoded so as to fall in a frequency range with little loss, or the signal

must be equalised electronically before writing, so as to extend the bandwidth output of the recording system.

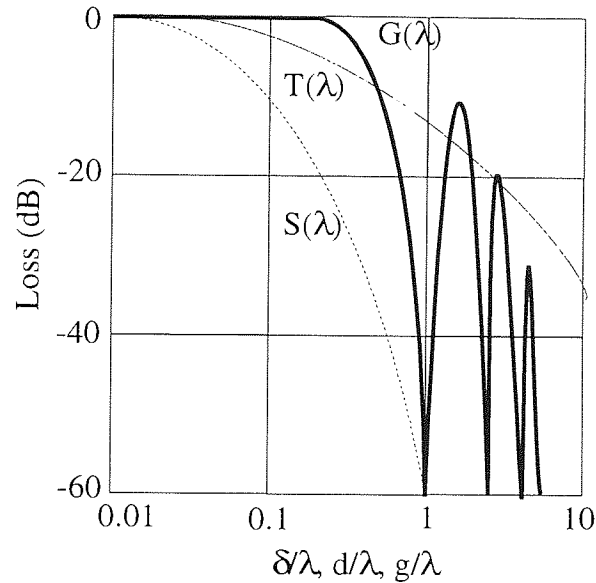


**Figure 1.4 Thickness loss,  $T(\lambda)$ ; Spacing Loss,  $S(\lambda)$ , and Gap Loss,  $G(\lambda)$  in Magnetic Recording**

Signal amplitude increases with increasing remnant magnetisation of the medium, which may be improved, by increasing the packing density of the particles in the medium, and by improving the magnetic properties of the particles themselves as witnessed in the trend from ferrite to metal iron particles and cobalt-nickel thin films. Such increases in medium output, together with increasing the number of the turns on the head, by minimising spacing loss between head and tape and thickness loss in the tape allow an increase in either track density or linear density which both act so as to decrease the signal amplitude.

The head efficiency factor takes account of the fact that the head material is of finite permeability and that not all the magnetomotive force (MMF) is transferred to the gap. It can be defined in terms of the ratio of the reluctance (magnetic resistance, analogous to electrical resistance) across the front gap ( $R_{fg}$ ) to the sum of the other reluctances ( $R_m$ ) about the magnetic circuit represented by the head (e.g. through the core + through the back gap). This is shown in Equation 1.11.

$$\eta = R_{fg} / \Sigma R_m$$

Equation 1.11

The reluctance across the front gap increases as gap depth decreases, thereby increasing the head efficiency and the reproduce signal amplitude. The requirement of low gap depth for



efficiency must be balanced, however, against the need for sufficient gap depth to be built into the head against wear of the head during its useful life.

#### 1.2.3.4 Signal-to-Noise Ratio

A high signal-to-noise ratio (SNR) in the reproduced signal is naturally desirable. This is usually expressed as a dB ratio of the output voltage of the signal to that of the noise, as shown in Equation 1.12:

$$\text{SNR} = 20\log(V_{\text{signal}}/V_{\text{noise}}) \quad \text{Equation 1.12}$$

The narrow-band frequency for a slot of flux density of width  $\Delta k$ , from Mallinson<sup>5,6</sup>, is given in Equation 1.13:

$$\text{SNR}_{\text{narrow}} = \{2\pi n w F^2 [1 - \exp(-k|\pi\delta')]\}^2 / \{k|1 - \exp(-k|\pi\delta)|\} \Delta k \quad \text{Equation 1.13}$$

Where:

$n$  = number density of magnetic particles ( $1/\text{mm}^3$ )

$w$  = track width of medium ( $\mu\text{m}$ )

$F$  = fraction of total magnetic moment of the medium

$\delta'$  = depth of recording

$k$  = number of flux reversals / distance ( $1/\text{mm}$ ) =  $2/\lambda$

$\delta$  = thickness of medium

The narrow-band SNR is independent of head-medium spacing. Non saturation (1-F) of the medium and of partial recording depth,  $\delta'$ , will lower SNR, because whilst all the magnetised particles are contributing to the noise, only a fraction of the particles are contributing to the signal.

Mallinson<sup>5,6</sup> approximated wide-band SNR for a slot of flux density width ( $k_{\text{max}} - k_{\text{min}}$ ) as Equation 1.14:

$$\text{SNR}_{\text{wide}} \sim 4\pi n m F^2 / (k_{\text{max}}^2 - k_{\text{min}}^2)$$

Equation 1.14

### 1.3 Hi-8 Video Recording System

The variety of magnetic recording systems is vast. This work concerns itself with studying head-tape interactions in 8mm helical scan home video tape recorders. These are related to, but advanced from the home VHS systems, and are representative of other higher density helical scan recording systems such as digital video, 8mm data storage systems and the 4mm DDS digital data storage system. In this section the Hi-8mm video system is introduced and in the remaining sections of this chapter the media and heads studied using this system are described.

The development of the Hi-8 (High band, 8mm) consumer video recorder is described by Tsuneki *et al*<sup>7</sup>. It operates with 8mm-width tape, of either metal particulate (MP) or metal evaporated (ME) variety. It has a bandwidth of 7.7MHz. This allows for a resolution of 424 vertical TV lines, as compared with 260 for VHS and 540 for broadcast TV (PAL) in the UK. The recorded signal is frequency modulated and the division of the bandwidth between the chrominance (colour); luminance (basic monochrome signal) and the FM audio signal are shown in Figure 1.5.

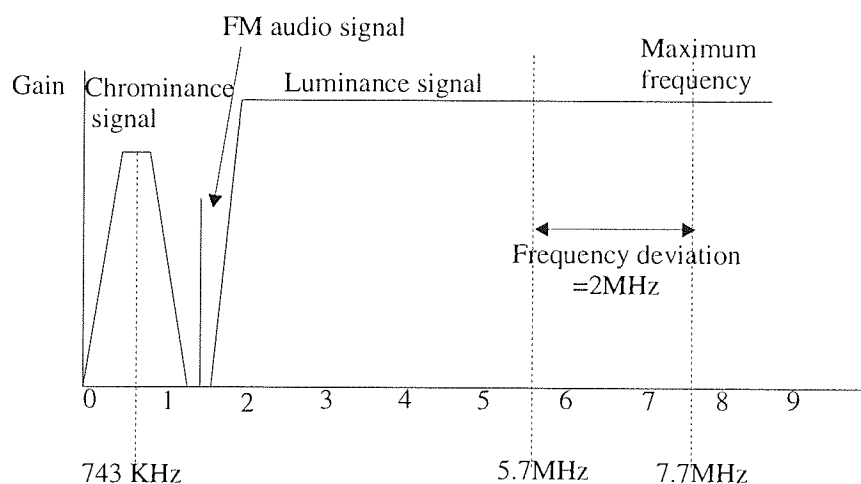


**Figure 1.5 Frequency Spectrum of a Hi-8 Video Signal**

The high head to tape speed required to produce such a high frequency is achieved using a helical scan rotary scanner. The operating principal of a rotary recorder is shown in Figure 1.6. The scanner consists of two drums, the lower of the two remains stationary. The heads

are mounted on the upper drum and this drum is rotated at high velocity, whilst the tape which is wrapped around the drums passes at much slower velocity, thus writing helical tracks on the tape, as shown in Figure 1.7. Two heads, mounted at  $180^\circ$  to each other on the drum in Hi-8, have their respective gaps cut with opposing azimuthal angle. These are used to write neighbouring tracks with their phase transitions at an angle to one another (as shown in Figure 1.7), thus reducing cross talks between the tracks, allowing them to be placed closer together and thereby increasing track density. Figure 1.7 also shows linearly written tracks at the edges of the tape, on the top edge two audio tracks, and on the bottom a control track. These are written by heads mounted independently of the scanner. The Hi-8 specifications for drum diameter, drum speed, writing speed, forward tape speed, tape wrap angle, track length, track angle and track pitch are given in Table 1.2.

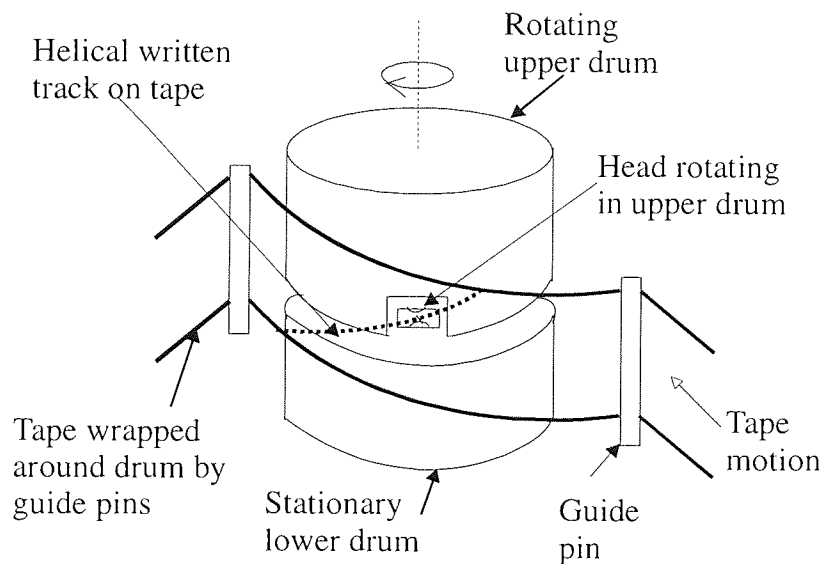


**Figure 1.6 Rotary Scanner**

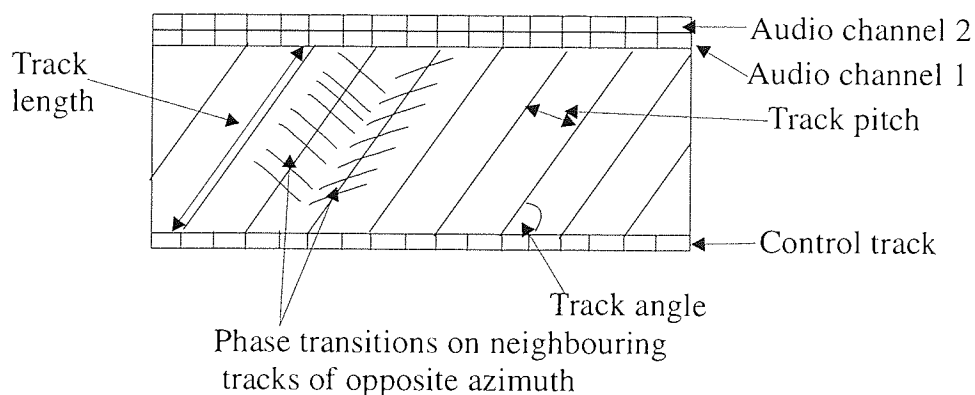


**Figure 1.7 Track Positions on a Tape Written by a Hi-8 Recorder**

Drum Diameter	40mm
Drum Speed	1800rpm
Writing Speed	3.76m/s
Forward Tape Speed	14.35mm/s
Tape Wrap Angle	180°
Track Length	63mm
Track Angle	4.9°
Video Track Pitch	20.5µm

**Table 1.2 Specifications of the Hi-8 Video System**

## 1.4 Metal Evaporated and Metal Particulate Tape

### 1.4.1 Introduction

Magnetic recording tapes have been in constant evolution since their introduction in the 1930s in order to increase their data storage density and transfer rate and to improve their data integrity, durability and longevity. Metal particulate (MP) tapes, realised in the 1980s belong to the broadest class of magnetic tapes – the particulate. The cross sectional diagram of a particulate tape in Figure 1.8 includes the main features of this type: The magnetic layer consisting of a polymeric binder containing magnetic and head cleaning particles on a continuous polymeric substrate. The magnetic layer is deposited by first dispersing the magnetic particles and the binder polymer precursors in a solvent. This dispersion is then coated onto the substrate and dried in a magnetic field to orientate the magnetic particles. The resultant polymer matrix will contain remnants of the solvent, wetting agents and plasticisers in addition to the magnetic and head cleaning particles. Metal evaporated (ME) tape, demonstrated in Figure 1.11, differs from particulate media in that the magnetic layer consists of a continuous thin film evaporated onto the surface of the substrate.

An increase in the storage density of a fixed size of cassette can be achieved by reducing the thickness of the tape. As can be seen for both MP and ME tapes the major savings in

thickness to be made are by using a thinner substrate. The ME magnetic coating also provides for some saving in tape thickness over MP.

An increase in the areal density of magnetic tape maybe made by decreasing the track width of the written information and by decreasing the bit length. Increasing the data transfer rate can be achieved by reducing the bit length at constant head-tape velocity, or by increasing the head-tape velocity, thereby reducing the storage capacity unless track width or tape thickness are reduced.

Decreasing the bit length and the track width will necessarily mean the head will “see” less magnetic flux, thus decreasing the read signal in the head and increasing the signal to noise ratio. To compensate, Equation 1.7 shows that we can increase the read signal amplitude by using a media with a higher remanent magnetisation and squareness, providing the flux from the write head is sufficient to saturate the media particles. Reducing spacing loss by using a smoother medium will also increase read signal amplitude. Equation 1.13 shows that increasing the number density of the magnetic particles increases the signal to noise output of the system. Thus MP tape in which the magnetic particles exist within the binder system is at a disadvantage to the ME film. Decreasing the size of the magnetic particles within the medium can increase the number density of particles in MP tape, as well as necessary for smaller bit lengths, and thus is a major area for research<sup>8</sup> for advancing MP tape. Equation 1.13 also shows that if the medium is not fully magnetised then signal to noise will deteriorate, and that this may be achieved by reducing the thickness of the magnetic layer.

Decreasing the particle size (or decreasing the thickness of a thin film coating) also acts to increase the coercivity of the magnetic film on the tape<sup>9</sup>. An increase in coercivity is desirable in its own right as it reduces the self-demagnetisation fields within the media. The coercivity of magnetic particles is dependent upon their shape and size, with acicular particles exhibiting high coercivity. Generally the coercivity increases with a decrease in size until below a certain critical size they switch to super-paramagnetism<sup>10</sup> and thus lose their magnetic moment. As magnetic media thus exhibit higher coercivities as their storage density increases, so must the  $B_s$  of recording heads increase to prevent saturation.

#### 1.4.2 Magnetic Recording Tape for the Hi-8 Video System

Two different tape types were designated for the introduction of the Hi-8 video system in 1989, Metal Particulate (MP) and Metal Evaporated (ME). Their magnetic properties<sup>11, 12</sup> are compared to MP tape then used in 8mm video systems of the time in Table 1.3.

	Hi-8 ME	Hi-8 MP	8mm MP
$H_c$ (KA/m)	8	12	11.6
$B_r$ (T)	0.37	0.25	0.24
$T_{mag}$ ( $\mu\text{m}$ )	0.2	4.0	4.0
Particle Length(nm)		102	148

**Table 1.3 Magnetic Properties of Hi-8ME, Hi-8MP and 8mm MP Video Tapes at the Time of Introduction of the Hi-8 System. Where  $H_c$  = coercivity,  $B_r$  = Remanence Magnetisation, and  $T_{mag}$  = Length of the Magnetic Particle in MP Tape and the Grain Size in the ME Tape**

From Table 1.3 it can be seen that the  $B_r$  of the ME tape and hence the output is 4dB higher than the 8mm MP tape. Although the coercivity of the ME tape is lower than that of the MP tape, the grain orientation itself in the ME tape helps to reduce the self-demagnetisation loss within the media. The ME media is twice as smooth as the 8mm MP reducing spacing loss, which combined with the high  $B_r$  value, and including a higher self-demagnetisation loss, contributes to a 6dB increases in output over the 8mm tape with same head. Because the ME tape has a continuous thin magnetic film rather than a magnetic layer containing a binder, head cleaning agents, curing agents etc. in addition to the magnetic particles it has an effective higher packing density of magnetic “particles”. This means that it has achieves a higher carrier-to-noise ratio of 5dB over the 8mm MP tape at a recording wavelength of  $0.5\mu\text{m}$ . A higher  $B_r$  and a smoother surface to the Hi-8 MP tape compared to the conventional 8mm MP tape contributes to a 3dB higher output with the same head. For the introduction of the Hi-8 video system, the use of ME tape offered an advantage in terms of signal performance. However ME tape is less durable and more expensive than MP tape to produce. Since the introduction of Hi-8 MP the signal output of MP tapes has been improving, and ME tape has become more durable thus MP and ME tape continue to compete in the market for high density magnetic recording media. The changes carried out in order to achieve these improvements are discussed in the

following sections on MP and ME media. The tribology of MP and MP tape at the head-tape interface are described in the next Chapter.

### 1.4.3 Metal Particulate Tape

#### 1.4.3.1 Structure of MP Tape

The general structure of particulate tapes is shown in Figure 1.8, with dimensions quoted typical of first generation MP tape, and the various components discussed below.

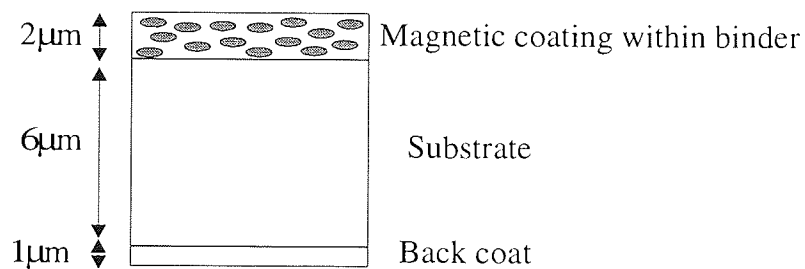


**Figure 1.8 Cross section of a Particulate Tape Showing Dimensions Typical of MP Tape**

### 1.4.3.2 Magnetic Particles

Gamma-iron oxide ( $\gamma\text{-Fe}_2\text{O}_3$ ): One of the earliest used, and most commonly applied magnetic particle types.  $\gamma\text{-Fe}_2\text{O}_3$  particles are acicular with a typical aspect ratio of 10:1, and lengths in the range of 0.15-0.5 $\mu\text{m}$ . They have a saturation magnetisation of 73-75  $\text{Am}^2/\text{Kg}$ . Typical coercivity values of 20-32  $\text{KA/m}$  are too low for higher density applications such as video

Cobalt Modified  $\gamma\text{-Fe}_2\text{O}_3$ : Substitution of Co for Fe ions in  $\text{Fe}_3\text{O}_4$  was shown to result in an increased magnetocrystalline anisotropy<sup>13</sup>. Similarly this has proved the case for cobalt doped  $\gamma\text{-Fe}_2\text{O}_3$  particles with a resulting increase in coercivity to values in the range of 30-75 $\text{KA/m}$ . These particles are widely used in VHS video recording tapes. At temperatures above 300°C the coercivity becomes temperature dependent due to the diffusion of Co into the particles.

Chrome Dioxide ( $\text{CrO}_2$ ): These particles also exhibit a higher coercivity than  $\gamma\text{-Fe}_2\text{O}_3$ , in the range of 30-58 $\text{KA/m}$ . However these particles can be chemically unstable towards the atmosphere, requiring surface passivation. They also tend to be more abrasive than  $\gamma\text{-Fe}_2\text{O}_3$  and thus may reduce head lifetimes.

Metallic Iron Particles: These offer much higher specific values of  $M_s$  and  $H_c$  values over  $\gamma\text{-Fe}_2\text{O}_3$ : 125-175 $\text{Am}^2/\text{Kg}$  and 75-144 $\text{KA/m}$  respectively. Corrosion is inhibited in these particles by surface passivation as an oxide (which can also be used to control  $M_s$  and  $H_c$ ). MP particle technology was chosen to meet the needs of Hi-8 recording, and continues to develop as outlined below.

Barium Ferrite,  $\text{BaFe}$ , ( $\text{BaFe}_{12}\text{O}_{19}$ ): These highly coercive (>100  $\text{KA/m}$ ) particles are not used commercially, but show promise due their hexagonal platelet structure, with the easy axis of magnetisation lying within the plane of the particle (therefore making them candidates for perpendicular recording media). Barium ferrite particles have low aspect ratios (4:1) and their lower achievable length -  $\text{BaFe}^{++}$  particles have half the length of that achieved for advanced  $\text{MP}^{++}$  particles<sup>14, 15</sup> (40 vs. 80nm), thus offering the opportunity for higher bit density and higher SNR media.



### 1.4.3.3 Binder System

The magnetic particles are contained within a polymer binding system. This has commonly been a polyester polyurethane copolymer. The polyester section of the copolymer gives a “soft” phase for flexibility, and the polyurethane gives a “hard” phase for rigidity and thermal stability. The ratio of hard to soft polymer will affect the properties of the final tape, with too much of the hard phase leading to high head wear. Hydrophilic functional groups are added to the binder to anchor the hydroxyl terminated magnetic particles. This is important, as the inorganic magnetic particles must be dispersed in a solvent together with the organic binder in order to be applied to the substrate. Incorporating a wetting agent with the binder minimises the number of non-magnetic components in the binder system. Vinyl chloride and vinyl acetate copolymers with polyurethane are in widespread use as wetting binders, incorporating hydroxyl and carbonyl functional groups to bind to the magnetic particles. Dispersion of high magnetisation, ultra fine particles requires a particularly effective wetting-dispersion system. AB block copolymer wetting agents, in which the A block is optimised as a wetting agent and the B block for stabilisation have shown<sup>16</sup> higher rates of dispersion of such particles than vinyl chloride – vinyl acetate wetting binders.

The binder system also incorporates a number of other non-magnetic components which may possibly include plasticisers to improve the flexibility of the binder, remnants of surfactants used to wet the magnetic particles in the solution, such as organophosphates, and remnants of the solvent used to form the dispersion. Typical examples of solvent include ketones and tetrahydrofuran (THF).

Deliberately added to the binder system are head cleaning agents (HCA) and Lubricants. HCA are abrasive particles, typically of alumina or zirconia. In size they are usually slightly larger than the magnetic particles employed. They are incorporated to remove debris from the head as the medium is run to maintain low effective head-tape separation. They aid the contouring of the head with running to achieve an intimate head-tape contact, help prevent stiction, and provide a mechanically stable bearing surface. The lubricant found in particulate tapes are fatty acid esters such as butyl stearate. The lubricant at the surface may be replenished by diffusion through the channels left in the binder system by

solvent evaporation. Lubricant is stored within the binder system for older, single layer metal particulate tapes or from the non magnetic underlayer employed in the dual layer MP tapes described in Section 1.4.3.6

#### 1.4.3.4 Substrate

The substrate upon which the magnetic layer is deposited is a thin film polymer. Imperfections in the base film can critically effect the tribological and magnetic properties of the magnetic layer. The most commonly used substrate is polyethylene terephthalate (PET). With the need to increase storage density by decreasing tape thickness alternative substrates are being used. Media for high areal density applications must show a low roughness together with a high mechanical and environmental stability. Lateral contraction of the substrate due to thermal, hygroscopic, viscoelastic and/or shrinkage effects during storage on the reel or during use will lead to off-track errors where track widths are small. To avoid stretching of thinner substrates, they should possess high modulus of elasticity, yield strength, and tensile strength in the longitudinal (machine) direction. Substrate materials should be able to withstand temperatures in excess of 100-150°C as magnetic layers are deposited (as in ME media) or heat-treated at high temperature.

Alternative substrates to PET that have been considered<sup>17</sup> and evaluated for their effect with environment on the stability of advanced magnetic recording media<sup>18</sup> include polyethelene naphthalate (PEN), an aromatic polyamide (ARAMID) a polyimide (PI) and polybenzoxazole (PBO). Weick and Bhushan<sup>19</sup> compared their tribological and dynamic behaviour to PET. PEN, ARAMID and PBO were shown to be superior to PET and PI, being less prone to deformations when manufactured, stored or used. The greater stiffness of these three over PEN is compensated for by an intended reduction in thickness, and hence a greater force will not be required to conform the tape to the head, which could be the source of greater head wear. Currently both PEN and ARAMID are being used as the substrate in advanced media.

#### 1.4.3.5 Back Coat

The back coat exists primarily to enhance tape transport and to dissipate static charges. To this aim it consists of a polymeric binder matrix containing anti-static agents (such as carbon black) and tribological additives.

#### 1.4.3.6 Advanced MP Media

MP media has undergone evolution through the MP<sup>+</sup> and MP<sup>++</sup> stages to rival ME media for surface smoothness and magnetic performance<sup>20,15,12</sup>. Table 1.4<sup>14,15</sup> shows the reduction in metal particle size in the evolution from MP through MP<sup>+</sup> to MP<sup>++</sup> tape, and the corresponding ability to match ME magnetic performance. Inaba et al<sup>12</sup> reported R<sub>a</sub> surface roughness values of advanced ME and MP media of 1.5 and 1.8nm respectively. The main technological advancements have been in the form of smaller, more highly coercive particles, thinner substrate materials and the adoption of an undercoat between the magnetic layer and the substrate. The structure of advanced dual-coat MP<sup>++</sup> tape is shown in cross section in Figure 1.9.

	MP	MP <sup>+</sup>	MP <sup>++</sup>	ME	ME <sup>++</sup>
Particle Shape	acicular	acicular	acicular		
Length (nm)	180	~130	~80		
Aspect Ratio	12	~9	~3.5		
B <sub>r</sub> (T)	0.25	0.28	0.35	0.37	0.46
H <sub>c</sub> (KA/m)	124	136	152	88	112

**Table 1.4 Comparison of Particle Size in MP Tapes and of the Magnetic Properties of MP and ME Media**

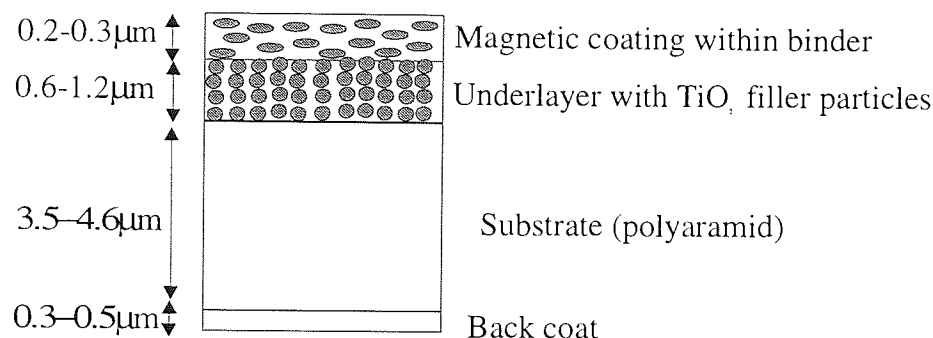


**Figure 1.9 MP++ Media in Cross Section**

It has already been stated that reducing the thickness of the magnetic layer will improve the signal to noise properties of the medium. However reducing the magnetic layer increases the occurrence of defects within the magnetic layer and the roughness of the media as this becomes dominated by the roughness of the underlying substrate surface. Such problems have been overcome<sup>21</sup> in advanced MP media by the adoption of a dual layer structure in which a layer of non-magnetic particles (~35nm diameter TiO<sub>2</sub> particles within a binder system) lies under the magnetic layer. This acts to “fill in” the roughness of the substrate, and to provide a smooth surface upon which the packing of the magnetic particles in the subsequently deposited layer is highly ordered with few defects.

#### 1.4.4 Metal Evaporated Tape

Metal Evaporated tape was introduced commercially for the Hi-8 Video system in 1989<sup>22,23</sup>. It has been introduced into other systems including the Scoopman digital recorder with a stamp size cassette<sup>24</sup>, and the DVC digital video system<sup>25</sup> with the advanced ME tape structure shown in Figure 1.11. The magnetic layer consists of a ~200nm thick coating of CoNiO or CoO. This is achieved by evaporating the metal source and directing the vapour in a stream of O<sub>2</sub> in a vacuum onto the tape substrate (11 μm thickness PET) wound about a cooling drum. Introduction of oxygen into the stream of Co-Ni in the evaporation processes enables the magnetic properties of the film to be finely tuned with H<sub>c</sub> increasing with O<sub>2</sub> content, and M<sub>s</sub> decreasing, as well as improving resistance to corrosion. The metal evaporated thin film forms a columnar structure on the tape substrate, as shown in Figure 1.10, which is anisotropic mechanically and

magnetically with respect to relative orientation of the tape passage over the head. The mechanically stronger direction is shown on the diagram.

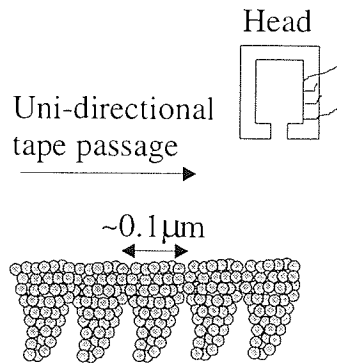


**Figure 1.10 Characteristic Curved Columnar Structure of a ME Thin Film Showing Mechanically allowed Tape Passage Direction Over a Head**

The development, introduction and magnetic and tribological properties of ME tape are summarised by Luitjens et al<sup>26</sup>. They highlight that the tribological performance with respect to both wear and corrosion is seen as a major concern with ME tape. To test for corrosion ME tape has been subjected to harsh environmental conditions. It was found that the ageing of ME tape is not fast when compared to MP tape<sup>27</sup>, that the substrate may play a part in the corrosion process<sup>18</sup>, and that protection by a diamond like carbon (DLC) is important in improving the durability and corrosion resistance of ME tape<sup>28</sup>. A DLC layer deposited over the magnetic layer has been subsequently introduced into commercial ME tape. A cross section of such advanced ME tape<sup>29</sup> is shown in Figure 1.11.

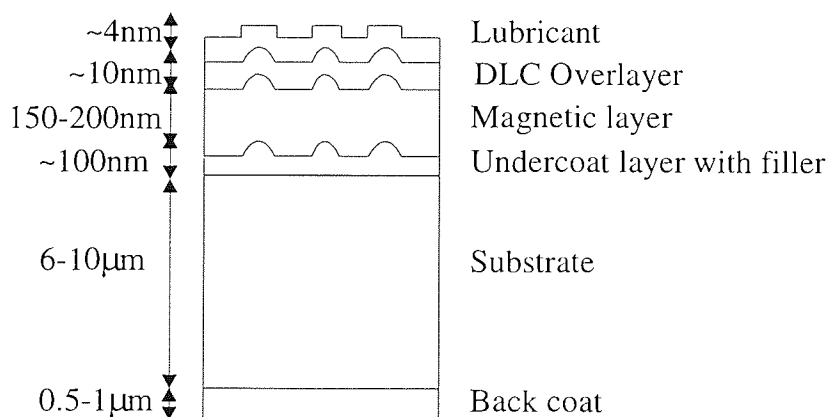


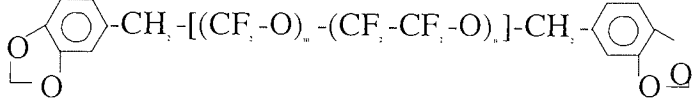
**Figure 1.11 Cross Section of Advance Metal Evaporated Tape**

The top layer is a thin (3-5nm) topically applied coating of lubricant, usually consisting of one or more members of the perfluoropolyether (PFPE) type, which are also commonly used in the rigid disk industry. The lubricant properties of PFPEs depend upon their molecular backbone, whilst their adhesive properties depend upon their functional groups. The PFPE molecular backbone should have a low surface tension, good lubricity, excellent thermal stability, low viscosity, high adhesion energy, low vapour pressure and be generally chemically inert. The structures of several commercially available PFPE lubricants are shown in Table 1.5.

Unlike particulate tapes, ME tapes can't draw from a reservoir of lubricant from the binder system. Therefore the adhesion of the lubricant to the ME tape is very important for durability of ME tape. This is achieved by the presence of bonding functional groups at the ends of the PFPE molecule. The required functionality depends upon its mating surface. A ME tape with no DLC overcoat (i.e. a metal oxide surface) requires a more polar PFPE end group than a tape with a DLC overcoat. Thus the lubricants used on a DLC coated tape are therefore more hydrophobic and corrosion resistant than those used on non-DLC coated tapes. Examples of commercially available functional PFPEs are shown in Table 1.6. Hempstock<sup>30</sup> identified that ME tapes may contain at least two components to the PFPE lubricant system, a mobile component and a static component, and that such systems show better wear properties than single component systems.

Trade name	Chemical structure
Fomblin Y	$\text{CF}_3\text{-O-}[(\text{CF}_2\text{-O})_m\text{-}(\text{CF}_2\text{-CF}_2\text{-O})_n\text{-CF}_2\text{-CF}_2]$
Fomblin Z	$\text{CF}_3\text{-O-}[(\text{CF}_2\text{-O})_m\text{-}(\text{CF}_2\text{-CF}_2\text{-O})_n\text{-CF}_2\text{-CF}_2]$
Demnum	$\text{F-}[(\text{CF}_2\text{-CF}_2\text{-CF}_2\text{-O})_n\text{-CF}_2\text{-CF}_2]$
Krytox	$\text{F-}[(\text{CF}_2\text{-CF}_2\text{-O})_n\text{-CF}_2\text{-CF}_2\text{-CF}_2]$

Table 1.5 Chemical Structure of Commercial PFPE Lubricants

Trade name	Chemical structure
Fomblin Z-Dol	$\text{HO-CH}_2\text{-}[(\text{CF}_2\text{-O})_m\text{-}(\text{CF}_2\text{-CF}_2\text{-O})_n]\text{-CH}_2\text{-OH}$
Fomblin Z-Deal	$\text{CH}_3\text{-O-C(=O)-}[(\text{CF}_2\text{-O})_m\text{-}(\text{CF}_2\text{-CF}_2\text{-O})_n]\text{-C(=O)-O-CH}_3$
Fomblin AM2001	
Krytox 157 FSM	$\text{CF}_3\text{-CF}_2\text{-O-[CF}_2\text{-CF(CF}_3\text{)-O]}_n\text{-CF}_2\text{-C(=O)-OH}$

**Table 1.6 Chemical Structure of Commercial Functional PFPE Lubricants**

Below the lubricant layer come the aforementioned DLC and magnetic layer layers. In advanced ME media there then comes in-between the magnetic layer and the base film an undercoat with a specifically textured filler to provide a controlled roughness to the tape surface that reduces stiction between the tape and the guides and the head in the tape recorder.

## 1.5 Laminated (Sandwich) Heads

### 1.5.1 Introduction

This section seeks to explain the choice of the laminated (or sandwich) head for high bandwidth helical scan recording systems.

### 1.5.2 Head Material Properties

The important material properties for the material forming the magnetic core of an inductive head are listed below<sup>2</sup>

1. Permeability,  $\mu = \mu_r \mu_0$ , where  $\mu_r$  is the relative permeability, and  $\mu_0$  the permeability of free space - the ratio of the magnetic induction,  $B$ , in the head to the applied field,  $H$ , is an important property for both read and write performance.  $\mu_r$  is sensitive to purity, thermal history, mechanical cold working and the wear environment.
2. Saturation magnetic induction,  $B_s$ , the maximum flux density at the head poles. A high  $B_s$  is necessary to writing high coercivity media, and to read and write high frequencies (see 6.).
3. Coercivity,  $H_c$  – a low coercivity is required of the head core for ease of switching of the magnetisation. Like the permeability this is sensitive to its handling history.
4. Remanent magnetic induction,  $B_r$  – it is desirable that the magnetisation falls to zero after writing has ceased.
5. Electrical resistivity,  $\rho$ , - a high resistivity helps prevent eddy currents which reduce the high frequency performance of the head<sup>2</sup>. Eddy currents decrease the penetration of applied fields to the core of the head thereby reducing effective permeability and modify the local fields about the gap. For a semi-infinite magnetic material, the maximum field amplitude follows a decaying exponential dependence with distance from the surface ( $x$ ), as shown in Equation 1.15.

$$H_{\max} \propto \exp(-x/\delta) \quad \text{Equation 1.15}$$

Where  $\delta$ , the penetration depth is related to the frequency,  $f$ , and the material properties of resistivity and permeability by Equation 1.16

$$\delta \propto \sqrt{(\rho/f\mu\mu_0)} \quad \text{Equation 1.16}$$

6. High frequency performance. The permeability of ferrites decreases towards higher frequencies. This is an intrinsic damping phenomenon associated with spin resonance characterised by a carrier frequency above which ferrite type magnetic materials cannot follow magnetic fields at high frequencies. It is in the range of 1-10MHz for common head materials, and increases with the ratio of  $B_s/\mu\mu_0$ . The limit of ferrite of about 10MHz encourages the use of higher  $B_s$  materials for magnetic head cores.
7. Thermal coefficients. It is desirable for the head core materials to have relatively high Curie temperatures to render them less sensitive to temperature rises, either in use or



during production. It is also desirable, where magnetic thin films are used in head construction for their thermal expansion coefficients to be similar to the substrate upon which they are deposited.

8. Magnetic anisotropy – when the magnetic material is in the form of a single crystal or thin film with a pronounced crystalline orientation texture then properties such as permeability, coercivity and residual magnetic induction need to be specified as a function of orientation. In thin film heads with a uniaxial magnetic anisotropy, this is characterised by the anisotropy field  $H_k$ , at which the film saturates in the hard axis direction is related to the saturation magnetic induction and the permeability in the hard axis direction by Equation 1.17. Problems associated with magnetisation orientation and related domain closure in thin films in sandwich heads, and how they may be overcome are discussed in Section 1.5.4.3

$$H_k = B_s / \mu\mu_0 \quad \text{Equation 1.17}$$

9. Magnetostriction – This is a consequence of crystalline anisotropy that causes a resultant magnetic anisotropy in a magnetic material where in the magnetisation along a particular direction causes a change in length ( $\Delta l$ ) in that direction and vice versa, a strain applied to the head causes a change in magnetisation. The magnetostriction coefficient,  $\lambda$ , is defined in Equation 1.18. A zero magnetostriction is desired of a head material as in use a head is subject to a variety of mechanical and thermal stresses that could lead to noise with non zero  $\lambda$ .

$$\lambda = \Delta l / l \quad \text{Equation 1.18}$$

10. Purely Mechanical properties such as microhardness, fracture toughness, porosity etc are useful not only in determining the manufacture of magnetic recording heads, but also in the tribology (especially wear) of the head-media interface and are discussed in greater detail in Chapter 2.

### 1.5.3 Soft Metal Laminated and Ferrite Heads

Laminated magnetic alloys have been used as head cores from the earliest days of magnetic recording<sup>31</sup>. A laminated head is shown schematically in Figure 1.12. Initially the laminations were made of thin metallic sheets and thus of low electrical resistance. Insulated laminations increased resistivity and thus lowered losses due to eddy currents.

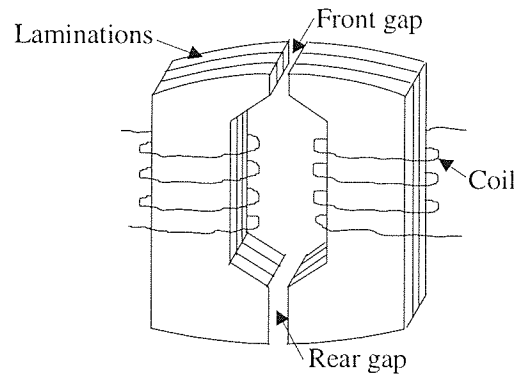


**Figure 1.12 Outline of a Laminated Head**

Three materials were commonly used to form the magnetic laminations: molybdenum Permalloy (by weight: 4% Mo, 17%Fe, 79% Ni), Alfenol (16% Al, 84% Fe) and Sendust (5.4% Al, 9.6% Si, 85% Fe). The nonmagnetic shielding laminations (or “spacer shims”) were typically of Cu-Be. They were mechanically soft (hence fast wearing) and prone to corrosion. As a consequence they were largely superseded by the development of high bandwidth (10-100MHz) ferrites from which heads could be manufactured more simply and cheaply of the required magnetic properties that were mechanically harder and thus highly durable. The magnetic properties and the Vickers hardness ( $H_v$ ) of single crystal Mn-Zn and hot pressed Ni-Zn and Mn-Zn ferrites<sup>32,33</sup> are compared to those of the magnetic alloys<sup>34</sup> Permalloy, Alfenol and Sendust in Table 1.7. The single crystal ferrite is shown to exhibit a range of hardness values dependent on the crystal orientation of the surface.

	Hot-Pressed Ni-Zn Ferrite	Hot-Pressed Mn-Zn Ferrite	Single Crystal Mn-Zn Ferrite	4% Mo Permalloy	Alfenol	Sendust
$\mu_r$	300-1500	3000-10,000	400-1,000	11,000	4,000	8,000
$H_c$ (A/m)	11.8-27.6	11.8-15.8	3.95	2.0	3.0	2.0
(Oe)	0.15-0.35	0.15-0.20	0.05	0.025	0.038	0.025
B (T)	0.4-0.46	0.4-0.6	0.4	0.8	0.8	1.0
$\rho$ ( $\Omega$ cm)	$\sim 10^5$	$\sim 5$	$>0.5$	100	150	85
$H_v$ ( $Kg/mm^2$ )	900	700	610-650	120	290	480

**Table 1.7 Magnetic Properties of Various Ferrites and Soft Magnetic Materials**

Ferrites have the spinel crystalline structure and exhibit ferrimagnetism. Ferrite itself,  $Fe_3O_4$ , is doped for use in magnetic recording heads with either Ni-Zn or Mn-Zn. Ferrites may be used in the polycrystalline phase, prepared by hot pressing, or as single crystals<sup>35</sup>. Ni-Zn ferrite is preferred<sup>33</sup> for very high frequency because its greater resistivity helps prevent eddy current losses that become important at higher frequencies. At frequencies below a few megahertz Mn-Zn is preferred because it has a lower coercivity, higher permeability, higher saturation remanence and lower magnetostriction<sup>36,37</sup>. Ni-Zn also forms a thicker magnetic dead layer (which increases spacing loss). Single crystal ferrites are preferred to polycrystalline<sup>2</sup> because magnetic dead layers formed during machining may be removed by annealing, they are less susceptible to microcracking (the damage to polycrystalline ferrite surfaces is discussed in Chapter 2 on tribology) and because they have a low porosity, which promotes chipping.

The saturation magnetic induction of ferrites (0.4) can be seen in Table 1.7 to be significantly lower than of the soft magnetic alloys (1.0T), and indeed the theoretical limit for ferrites is approximately  $0.6T^2$ . The trend towards shorter-wavelength recording attention has been focussed on high magnetisation magnetic alloys<sup>38</sup> to provide recording fields from narrow gap head designs sufficient to write the high coercivity recording media

required to support very short wavelengths. One such need is in Hi-8 video recording, and in subsequent digital video recording applications operating at even shorter recording wavelengths. The Metal in Gap (MIG) head<sup>39</sup> in which a conventional ring type ferrite head contains a high saturation metal, such as Sendust at the poles, overcomes the problem of saturation at the poles, whilst retaining a high durability tape bearing ferrite surface. Such heads are in common usage in high bandwidth video recording systems, such as Hi-8, and in other high bandwidth applications, such as Digital Audio Tape (DAT). An example of a MIG head is shown in Figure 1.13. These heads suffer from several drawbacks that hamper their operation at higher recording frequencies. These include having ferrite as the magnetic core with their high frequency switching limitations, as discussed above. They also have an ill defined track edge, and because the magnetic film must be deposited on an angled surface due to the head geometry it, the benefits occurring due to the lamination process, as described below are harder to realise in MIG heads than with the sandwiched laminate head.

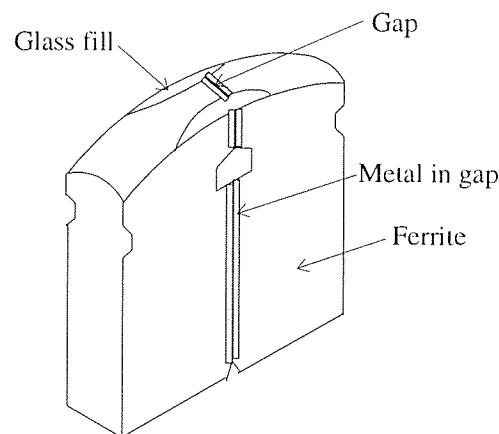


**Figure 1.13 Schematic Diagram of a Metal In Gap (MIG) Recording Head**

#### 1.5.4 Sandwiched Laminated Recording Heads

##### 1.5.4.1 Sandwich Laminate Head Structure

The laminated head design shown in Figure 1.12 forms the magnetic core of the modern laminated head in which it is miniaturised and sandwiched between two non-magnetic layers which form the bulk of the tape bearing surface, hence the alternative name of

“Sandwich Head” for such a device. A sandwich head is shown schematically in Figure 1.14. This design reconciles the tribological need for a durable, tape bearing to the head to be combined with the magnetic need of a completely soft magnetic core for a practical high  $B_s$  head.

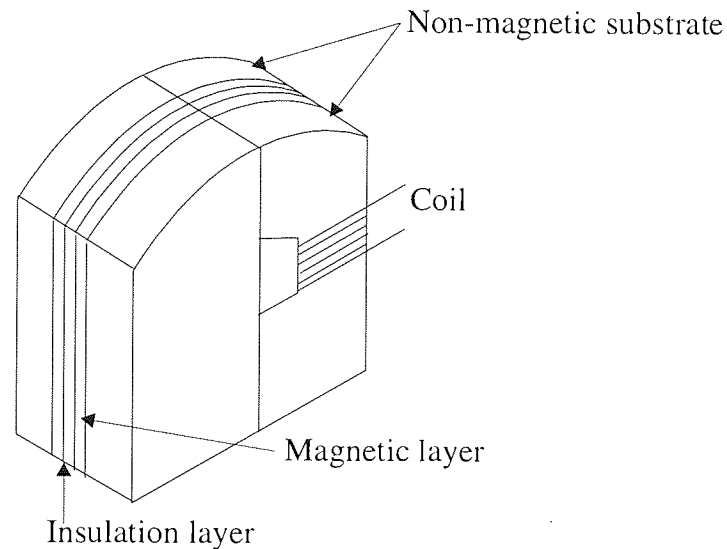


**Figure 1.14 Schematic Diagram of a Sandwich (Laminated) Head**

#### 1.5.4.2 Producing the Magnetic Thin Film

Two different methods of producing the thin soft magnetic laminations have been used. One is the liquid quench method<sup>40</sup> for forming amorphous magnetic materials in which molten magnetic material is quenched rapidly to avoid crystallisation. Ribbons of amorphous metallic glasses such as  $\text{Fe}_{4.7}\text{Co}_{70.3}\text{Si}_{15}\text{B}_{10}$ , produced by rapid quenching with a width of 10-24 $\mu\text{m}$ , sandwiched as a single laminate between two layers of glass were reported by Matsuura et al<sup>41</sup> to produce a well defined track width high saturation magnetic head. The other method is the vacuum sputter deposition method in which the magnetic material is deposited on a non-magnetic substrate<sup>42</sup>. In this method alternate layers of magnetic material and insulator can be deposited to build up the lamination. This method allows for the growth of the very thin magnetic and insulation layers necessary for high performance heads, as discussed in the next section, and is thus superior to the liquid quench method.

#### 1.5.4.3 Lamination Structure and Head Performance

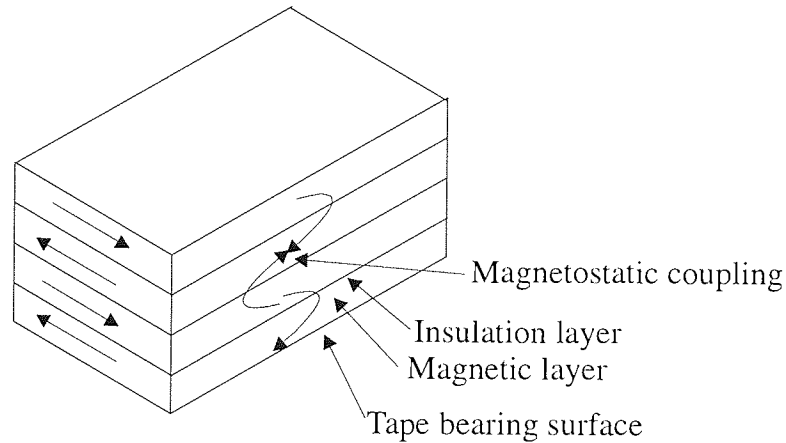
Even with relatively thick films laminated heads have been shown<sup>43</sup> to produce better performing heads at high frequencies than either bulk sendust heads or ferrite heads. At 10MHz, all other conditions being equal (tape, gap length etc), the laminated head gave a 5dB increase in output over the ferrite and sendust heads. Modelling of the impedance and efficiency of non-laminated<sup>44</sup> and laminated<sup>45</sup> thin film inductive heads of otherwise the same design and magnetic material showed the output performance of the laminated heads to be greater at high frequencies (10-200MHz) due to the suppression of eddy currents. Using a FeAlSi soft magnetic thin film, a laminated head showed a superior signal output of 2dB compared to a metal in gap head<sup>46</sup>.

Further benefit to the laminated head output can be gained from using thin magnetic films (<1 $\mu$ m thickness) separated by insulation layer of only a few nanometers. This allows neighbouring magnetic layers to be magnetostatically coupled with alternating anisotropy direction providing a flux closure path. Such head structures are known<sup>47</sup> to eliminate closure domain patterns that occur at the edges of a non-coupled film as shown in Figure 1.15.

Where the widths of the magnetic thin films are small, as within the laminations of non-coupled laminated head, switching of the edge magnetic closure domains is thought to constrain the high frequency magnetisation rotation, as has been modelled by Ohashi<sup>48</sup>, and thus reduce the high frequency operation of the head. Experimentally, domain closure structures in nanocrystalline thin film magnetic elements have been observed using MFM<sup>49</sup>. These have shown a strong influence of the edge roughness on the magnetic fine structure and thus on magnetic performance.

In practice it has been reported<sup>50</sup> that laminated heads incorporating magnetostatically-coupled FeTaN films, with the so-called double structured bias-sputtered multilayer (DSBM) structure do indeed have superior reproduction characteristics to conventional laminated heads.

Magnetostatic Coupled Laminated Structure:



Closure Domain Structure in a Non-Coupled Magnetic Thin Film:

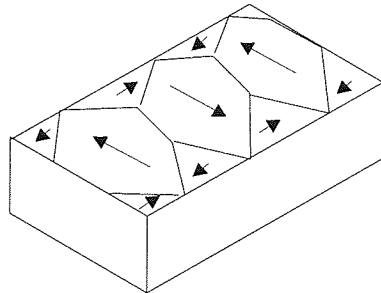


**Figure 1.15 Magnetostatic Coupled Laminated Thin Film Structure Compared to Closure Domains at Edges of a Non-Coupled Film**

#### 1.5.4.4 Magnetic Materials for Use in Sandwich Heads

##### 1.5.4.4.1 Amorphous Materials

Amorphous magnetic materials have several properties that recommends their use as magnetic thin films over microcrystalline films including zero crystalline anisotropy and therefore zero magnetostriction, and having resistivities typically 2-4 times those of the corresponding crystalline forms. They can also have the desired permeability, saturation magnetic induction, corrosion and hardness properties required. But an ideal combination of all these properties may not be associated with one composition<sup>51</sup>. The magnetostrictions of amorphous Co-Fe-Si-B or Co-Fe-B are close to zero<sup>52</sup>, but these materials have poor corrosion and wear properties. Amorphous Co-Zr alloys<sup>53</sup> show good wear characteristics, and Co-Ti<sup>54</sup> alloys good corrosion characteristics but both show positive magnetostrictions. Sakakima<sup>55</sup> produced a number of amorphous alloy films

composed mainly of Co-Nb by radio frequency sputtering that had small magnetostriction high saturation magnetisations and good wear properties. One of these alloys, CoNbZr, of the composition:  $\text{Co}_{85}\text{Nb}_{10}\text{Zr}_5$ , and  $B_s = 0.95\text{T}$  is one of the three alloys (as  $\text{Co}_{87}\text{Nb}_9\text{Zr}_4$ , with slightly improved magnetic properties) studied in comparative wear tests (against two nanocrystalline materials, as discussed below) in this thesis. The addition of Nb to ferromagnetic Co creates the amorphous alloy, and the addition of Zr raises the temperature at which the alloy crystallises. CoNbZr has been studied as a soft magnetic core material<sup>56</sup> and CoNbZr and related alloys in which niobium is replaced by tantalum and/or zirconium by hafnium are widely used as soft magnetic core materials in magnetic recording heads<sup>57,58,59</sup>.

#### 1.5.4.4.2 Nanocrystalline Films

Zero magnetostriction in a crystalline thin film magnetic material may be achieved by reducing its grain size to a nanometer size. Nanocrystalline magnetic materials have shown excellent soft magnetic properties. As the grain size of  $\alpha\text{-Fe}$  (metallic iron with a bcc structure) falls below the ferromagnetic exchange length, i.e. the width of a domain or Bloch wall, which is 35nm for iron<sup>60,61</sup> a low coercivity and a high permeability are achieved. The magnetic coupling energy between neighbouring grains reduces the effective magnetic anisotropy and therefore magnetostriction. There are two theories that explain this phenomenon – the ripple theory<sup>62,63</sup> and the random anisotropy model<sup>64,65</sup>. Nanocrystalline alloys were originally studied<sup>66</sup> in multilayer materials in which interlayers prevented the grain growth of Fe. These have been superseded by single-layer systems, in which segregation of a second phase at the grain boundaries inhibits the grain growth of Fe. Grain growth kinetics and properties maybe controlled by post sputtering annealing<sup>67</sup>. The second phase formed at the grain boundary may increase the hardness of the materials and form a barrier to corrosion giving a tribological benefit over amorphous materials. Hayashi et al<sup>68,69</sup> showed that additions of Ru and Ti into FeGaSi and FeAlSi sputtered thin magnetic films with substitution for Fe in the crystal structure led to improvements of wear performance with only a small loss in magnetic performance.

Nanocrystalline Fe alloys of the form Fe-TM-N (where TM is a group IVa-Va transition metal such as Zr, Hf, Nb or Ta) are of interest because they can be made easily by



sputtering from binary alloy targets in an Ar/N<sub>2</sub> plasma. And such films have been found to have good soft magnetic properties -  $\mu_r = 3000$ ,  $B_s = 1.7\text{T}$  can be achieved<sup>70,71,72</sup>.

Within the Fe-TM-N class of materials, FeTaN particularly has been studied as the magnetic material within a laminated head structure<sup>73,74,75</sup>. It has been identified as having favourable wear characteristics associated with having a Vickers hardness of  $>900\text{Kg/mm}^2$  and not to be susceptible to corrosion. The tribological properties of FeTaN thin films are further discussed in the next chapter. Laminated heads incorporating FeTaN have been shown constantly to have a higher performance than identical heads containing Sendust, especially at high frequencies ( $>20\text{MHz}$ ). The microstructure of RF sputtered FeTaN used as a thin film magnetic lamination consists of fine grains of  $\alpha\text{-Fe}$  with TaN grain boundaries. FeTaN has been successfully used as the magnetic material in commercially available magnetic recording drives, the first recorded<sup>76</sup> practical use of high saturation flux density ( $B_s = 1.6\text{T}$ ) and high permeability ( $\mu = 5000$  at 1 MHz) FeTaN laminated heads was in 1/2 inch component digital VCRs (D-5 Format).

Sandwich heads employing FeTaN laminations are studied in this work. Another nanocrystalline Fe-TM-N type high  $B_s$  (1.7T) soft magnetic material: FeNbSiN and the aforementioned amorphous CoNbZr were studied in comparative tribological tests.

### 1.5.5 Sandwich Heads and Materials Studied in This Work

A SEM micrograph of a sandwich head of the type studied in this thesis is shown in Figure 1.16, with a close up of the head surface in Figure 1.17. This is identical in all respects to those studied with the exception that it has fewer laminations in the track. Two different track widths – 14 and 32 $\mu\text{m}$  were studied. The exact dimensions of the heads studied are given in the results chapter. The development of these heads by Philips is described by Dirne and Ruigrock.<sup>77</sup>

The laminated track in the sandwich heads studied in this thesis contains FeTaN magnetic and Si<sub>3</sub>N<sub>4</sub> insulation laminations. The heads are made by sputtering alternate layers of the magnetic and insulating materials on a composite sintered ceramic substrate consisting of CaTiO<sub>3</sub> doped with ZrTiO<sub>4</sub> and TiO<sub>2</sub>. Two such structures are bonded together with a Mo-

Au layer (as shown in Figure 1.17) to form the sandwich. This is done in blocks from which individual head chips are sawn. The azimuthal gap and the coil chambers are sawn into the head chips.

The choice of the above ceramic non-magnetic substrate is made to satisfy several criteria: That the gross wear rate of the substrate and the metal are similar to avoid pole tip recession. The substrate and metal interface must be thermally stable over the range of temperatures, at which the magnetic film is annealed in the head. The substrate must have a similar thermal expansion coefficient to the magnetic material. It is also important that the substrate be capable of finishing (by polishing) in such a way as to improve the magnetic performance of the deposited layer<sup>78</sup>.

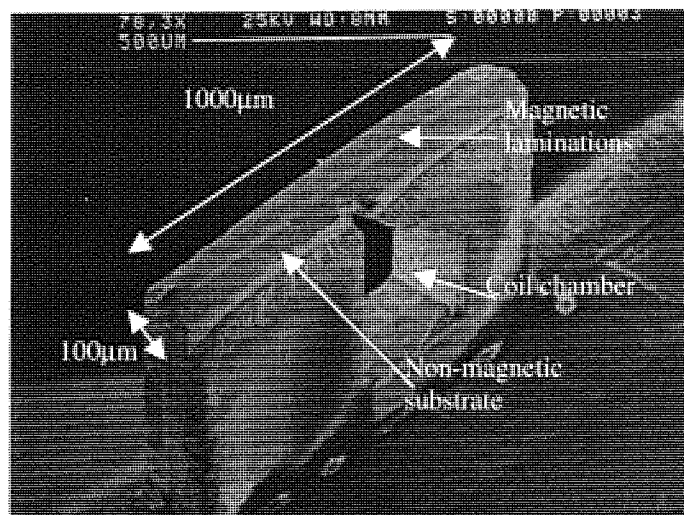


**Figure 1.16 Sandwich Head of the Type Studied in This Thesis**

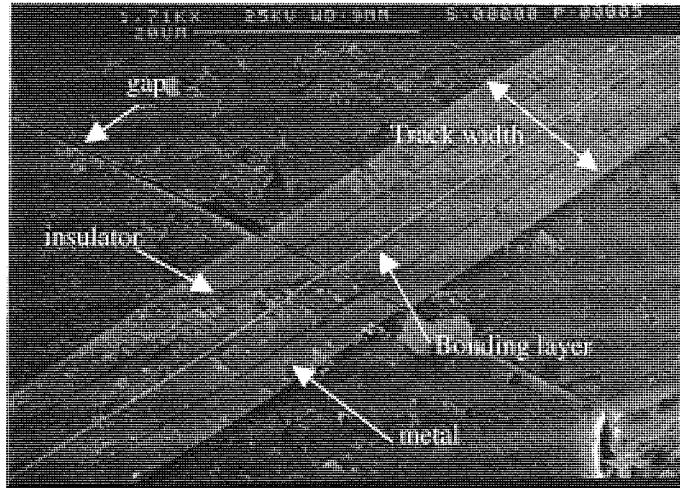


**Figure 1.17 Zoom in on the Magnetic Track of the Sandwich Head Shown in Figure 1.16. The Actual Sandwich Heads Studied Had More Laminations**

The high frequency performance of such sandwich heads will be impaired by spacing loss. The main aim of this thesis is to investigate possible contributions to spacing loss such as staining and pole tip recession formed when cycling sandwich heads against the two tape types used in Hi-8 recording at the time of the investigation: Metal Evaporated and Metal Particulate. To highlight the contribution of the individual wear mechanisms of the magnetic material and the substrate to differential wear that may lead to PTR, and because wear in general of the heads, especially accelerated wear at high humidity, acts to lower the useful life of the head, the wear properties (rates and mechanisms) of possible individual magnetic and substrate components against ME and MP media were studied. This was done for the three magnetic materials mentioned above: CoNbZr (M1), FeNbSiN (M2), and FeTaN (M3). And for two sintered ceramic substrate materials: CaTiO<sub>3</sub> (S1) and CaTiO<sub>3</sub>/ZrTiO<sub>4</sub>/TiO<sub>2</sub> (S2). It was achieved by making single material dummy heads of S1 and S2, of similar dimensions to the sandwich heads to cycle against tape in Hi-8 recorders. The magnetic materials could be studied in isolation by first depositing thin films over the entire surface of a ceramic dummy head.

The tribology of magnetic recording systems is introduced in the next chapter. That is followed in chapter 3 by a description of the experimental systems and the analytical techniques for investigating surface topography, mechanical and chemical wear mechanisms. The results are presented in chapter 4, discussed in chapter 5, and conclusions are presented in chapter 6.

## Chapter 2 Tribology

In this chapter the application of tribology to helical scan tape systems is described. In Section 2.1 the need for intimate head-tape contact in such is introduced, followed, after a brief description of friction and surface topography, by a discussion of the contact mechanics of the flexible media – head system. In section 2.2 wear mechanisms are discussed. In 2.3 the tribo-system – a Hi-8 camcorder tape path studied in this work is described, introducing the various tribo-elements within that system. This is followed in 2.4 by a more detailed discussion on the wear of the magnetic recording head within that system. In 2.5 the wear of the counter surface, the magnetic recording tape is described. Finally the two tribological phenomena of most interest in this work because of their contributions to spacing loss in high frequency magnetic recording – Stain and Pole Tip Recession are discussed in Sections 2.6 and 2.7 respectively.

### 2.1 Head-Tape Contact

#### 2.1.1 Introduction to Intimate Head Tape Contact – Lubrication Regimes and Position on the Stribeck Curve

In the Chapter 1 the requirement for intimate recording to prevent signal loss are discussed. In this section it is discussed what this requirement means for head-tape contact. This can be better understood by reference to the Stribeck<sup>79</sup> curve, an example of which is shown in Figure 2.1 for two rough surfaces, of combined roughness  $R$ , moving through a medium with viscosity  $\eta$ , at a velocity  $v$ , with a normal force  $F_n$ , and a separation  $h$ . The Stribeck curve shows the variation in friction between two surfaces at relative motion separated by a viscous medium. In the Stribeck curve the coefficient of friction for the system is plotted against the Sommerfeld number:  $\eta/(vF_n)$ . The hydrodynamic region is obtained from a solution to the Reynolds equation, of which an example is given in Equation 2.1 for a head flying over a tape, where  $T$  = tape tension, and  $k$  = dimensionless constant.

$$\mu = k (\eta v/T)^{1/3} \qquad \text{Equation 2.1}$$

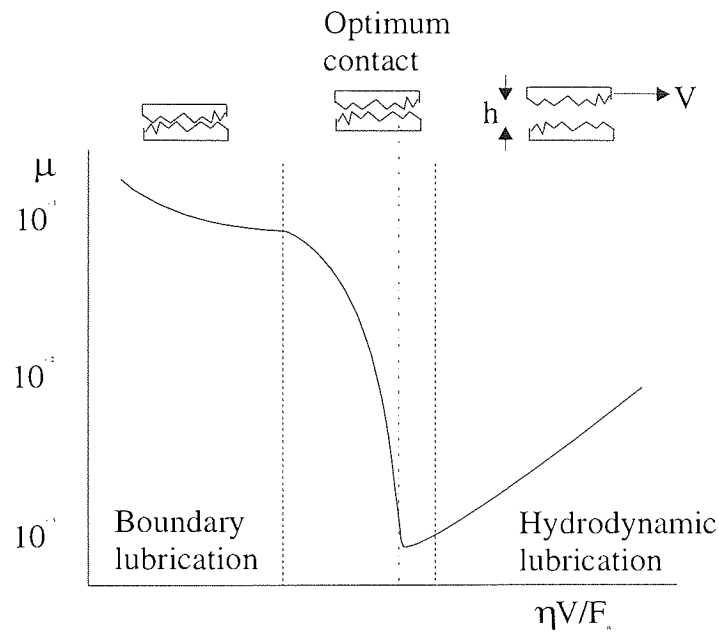


**Figure 2.1 Typical Stribeck Curve For the Head-Tape Interface**

The region to the right of the minimum in the Stribeck curve for a head tape interface corresponds to a hydrodynamic bearing of the head-tape interface by air. This is demonstrated in Figure 2.1 as a separation between the head and tape greater than the combined roughness of the tape and the head. This is created by the relative motion of the tape over the head (and especially the drum in helical scan recording) and the aerodynamics of the tape wrap, head profile and drum design. As one moves from right to left along the curve the head-tape spacing decreases. The left of the minimum corresponding to lower velocity and/or greater contact force shows a rise in friction as the head and tape come into contact, i.e.  $h \leq R$ . This is the boundary-lubricated regime. In the case of tape drives the tape will provide these lubricants. A head-media system will be optimised when the system lies just to the left of the minimum<sup>80</sup> – there is contact between the head and the tape ( $h \sim R$ ) to minimise spacing loss, but that friction is still close to its minimum.

In the rest of this section there follows a brief description of friction and lubrication, followed by a discussion on the theoretical description of contacting rough surfaces compared with the measurement of static rough surfaces encountered in magnetic recording situations by optical profilometry and AFM. A discussion of the dynamic

measurement and modelling of head-tape contact in helical scan recording will conclude the section.

### 2.1.2 Friction

Work must be done to maintain two bodies in relative motion when their surfaces are in intimate contact, i.e. to overcome *friction*. According to the first law of thermodynamics the external work done is equivalent to the energy dissipated at or near the surface in the form of heat, plastic and viscous deformation, hysteresis loss (mechanical, electrical and magnetic) and in the creation of defects such as dislocations. During this work either or both of the mating surfaces may be deformed elastically or plastically. It has long been recognised that in terms of coefficient of friction, static friction (or “stiction”) is greater than dynamic friction, and that for dynamic friction sliding is greater than rolling friction. The coefficient of friction,  $\mu$ , is defined as the ratio of the tangential force,  $F_t$ , to the Normal Force,  $F_n$ , as given in Equation 2.2. It is usually in the range of 0-1.

$$F_t = \mu F_n \qquad \text{Equation 2.2}$$

An adhesive theory of friction, advanced by Bowden and Tabor<sup>81,82</sup>, and by Rabinowicz<sup>83</sup>, formed the earliest theoretical basis for friction. It assumes that the asperities in contact are welded together and for relative motion to occur they require a tangential force to break them, thus exhibiting plastic deformation. In addition adhesion may contribute to friction in elastic contact. The force operating between asperities in the absence of plastic or irrecoverable deformation may have a physical origin, involving Van der Waals bonding<sup>84</sup>, or chemical involving ionic or covalent bonding.

For plastic contact Suh<sup>85</sup> identified that the coefficient of friction may change with sliding distance as the mode of friction changes. Initially  $\mu$  is determined by the shear stress of the asperities of the softer material as they are ploughed by the harder asperities. As the higher asperities become worn the real area of contact will increase, increasing the relative contribution of adhesive forces between the surfaces thus increasing the friction force. This contribution to friction may be negated by the presence of lubrication. If wear particles

become trapped between the two surfaces then the friction may be increased due to the ploughing action of these particles until an equilibrium concentration of these particles is achieved.

### 2.1.2.1 Friction and Lubrication in Flexible Magnetic Recording Systems

The friction regimes operating at the head-tape interface in particulate and metal evaporated media are summarised by Sullivan<sup>86</sup>. For ME tape he states that from the Greenwood and Williams plasticity index and the measured roughness of typical head and tape surfaces the deformation of the asperity contacts on the tape should be elastic-plastic. For particulate media given the viscoelastic nature of the magnetic layer, the nature of the contact and the surface topography the total deformation component to the contact between the head and the tape is negligible and the friction is due to adhesion<sup>87</sup>. Thus the frictional force can be written as Equation 2.3:

$$F_t \approx A_r \tau \quad \text{Equation 2.3}$$

Where  $A_r$  is the real area of contact, which as the tape wears, will increase, thus increasing the friction force.  $\tau$  is the interfacial shear stress, which is not constant, but will increase with pressure and fall with temperature within the operating range of the media.

Particulate media typically contains a fatty acid/fatty acid ester lubricant incorporated within the magnetic coating. This acts as a reservoir to supply a surface lubricant film of about 2-3 molecular layers thick, with coverage as low as 10%. The lubricated friction force can be written as Equation 2.4:

$$F_t = A_r \{ \tau(1-\alpha) + \tau_l \alpha \} \quad \text{Equation 2.4}$$

Where  $\tau_l$  is the shear stress in the lubricant and  $\alpha$  is the fractional area coverage. Sullivan states that the lubricant acts as both a classical boundary film and to plasticise the polymer surface. He also states that polymer surfaces in themselves have low surface energy and that this, together with the low coverage means that frictional force does not change substantially with lubrication, and that friction is largely determined by the properties of

the magnetic layer itself. A high hardness and a high complex modulus material should be used to reduce friction. However other properties are also important including a suitable glass transition temperature and toughness. An increase in surface roughness of the media will also decrease friction, but this is contrary to desire to reduce spacing loss. Sharma<sup>88</sup> reports experimental evidence for an increase in coefficient of friction with running time over the first few passes for particulate media as employed in floppy diskettes. This was shown to be accompanied by a decrease in surface roughness and a change in surface chemical composition of the binder, which may cause a change in interfacial forces between the head and the tape.

Evaporated media is coated with a boundary lubricant, which provides a low surface energy contact, which must exhibit some degree of surface mobility to replenish any loss due to excessive contact with the limited lubricant supply.

### 2.1.3 Surface Roughness and Contact

#### 2.1.3.1 Definitions of Roughness

By dragging a stylus (such as in a Talystep) or AFM tip across a surface, or by using an optical profilometer (which operate by measuring the interference of a coherent light source reflected from the surface) a surface profile (height vs. transverse distance) can be obtained. A diagram of a surface profile is shown in Figure 2.2.

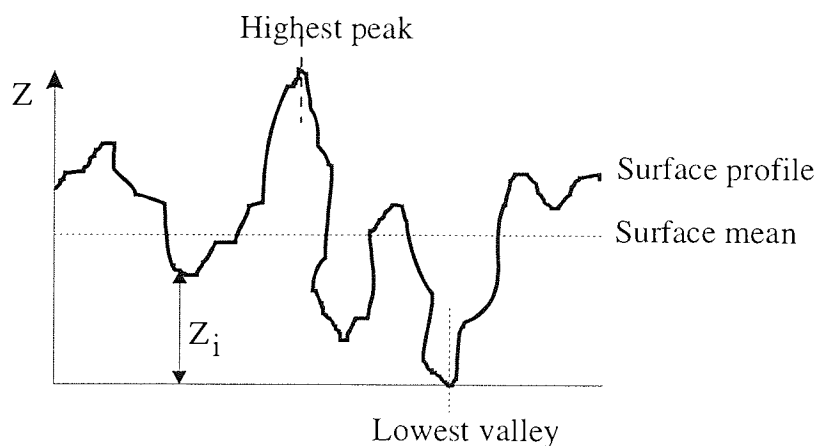


**Figure 2.2 Surface Profile Used to Illustrate Surface Roughness Parameters**



Various statistical analysis of the peak to valley heights ( $Z_i$ ) measured along the profile are used to quantify surface roughness. The surface mean,  $\bar{Z}$ , is given in Equation 2.5, where  $Z_i$  is the height relative to the lowest valley of the  $i$ th data point taken along the profile, and  $N$  is the total Number of data points. The simplest roughness value,  $r_a$  is defined as the standard deviation of the height data from this mean. This is given in Equation 2.6.

$$\bar{Z} = \frac{1}{N} \sum_{i=0}^N Z_i$$

Equation 2.5

$$R_a = \frac{1}{N} \sum_{i=0}^N |Z_i - \bar{Z}|$$

Equation 2.6

The  $r_a$  value is often quoted, however this value does not give much weight to extreme deviation from the mean - (higher asperities may bear the entire load) or to the shape of the distribution from the mean of the asperity height). The RMS (root mean squared) roughness ( $R_q$ ), given in Equation 2.7, gives a greater emphasise to the larger peak-valley heights, and deviations from a gaussian distribution of height values by the Skewness ( $R_s$ ) and Kurtosis ( $R_k$ ) roughnesses. Skewness represents an asymmetric spread and Kurtosis a peakedness of the distribution. These are given in Equations 2.8 and 2.9 respectively.

$$R_q = \sqrt{\frac{1}{N} \sum_{i=0}^N |Z_i - \bar{Z}|^2}$$

Equation 2.7

$$R_s = \frac{1}{R_q^3} \frac{1}{N} \sum_{i=0}^N |Z_i - \bar{Z}|^3$$

Equation 2.8

$$R_k = \frac{1}{R_q^4} \frac{1}{N} \sum_{i=0}^N |Z_i - \bar{Z}|^4$$

Equation 2.9

To quote a roughness value that more directly represents the highest asperities in the system, a value of the highest (or, say, mean of the highest 10%) peak-valley (P-V) or surface mean – peak ( $R_p$ ) heights are used.

### 2.1.3.2 Contact Mechanics at the Head-Tape Interface

From Equations 2.5-2.9, it can be seen that the lateral sampling resolution will affect the measured roughness values. Thus roughness values measured with different types of instrument with differing resolutions might produce differing roughness values. Asperities are likely to be observed on a rough surface at whatever the resolution of the sampling device, down to the atomic limit. Thus an asperity is not a definite “object”. A useful definition of an asperity is one that makes contact in a particular application<sup>89</sup>. As two surfaces are brought into contact, asperities on the nanoscale are the first to come into contact and deform plastically instantaneously, merging together to give asperity contact on the micro-macro scale. Under further loading, these asperity contacts may deform by elastic or elasto-plastic deformation<sup>90</sup>. The degree of plastic interaction on asperity contact strongly influences friction and wear.

The modelling of the contact between the rough surfaces is difficult as rough surfaces are random structures and may be anisotropic. Thus they require stochastic modelling. The classical statistical model combining elastic and plastic contacts between rough surfaces is due to Greenwood and Williamson<sup>91</sup>. Their model assumes that surfaces are composed of hemispherically tipped asperities of uniform radius of curvature whose heights follow a gaussian distribution about a mean plane. Whitehouse and Archard<sup>92</sup>, and Onions and Archard<sup>93</sup> modified this model. Nayak<sup>94</sup> proposed an elastic contact model that treated asperities as elliptical paraboloids with randomly oriented elliptical contact areas that has since been developed by others<sup>95,96,97</sup>. A surface with a gaussian distribution of heights can be characterised by two values: a standard deviation of the height distribution ( $R_a$  or  $R_q$ ) and the correlation length ( $\beta^*$ )<sup>98</sup>. Kotwal and Bhushan<sup>99</sup> developed a statistical model for

non-gaussian surfaces that may be described by the Skewness and Kurtosis roughnesses given above.

The elastic-plastic behaviour i.e. the contact mechanics of asperity-asperity contact are the subject of much modelling. Bhushan has reviewed the mechanics of single asperity<sup>100</sup> and multiple asperity<sup>89</sup> contact. He reviews contact mechanics modelling based on the classical Greenwood and Williamson model, as well as more sophisticated fractal analysis, and goes on to describe computerised numerical modelling contact. Briefly described below are the change from elastic to plastic deformation and the related plasticity index. There then follows a discussion of the measurement of roughnesses of engineering surfaces observed in magnetic recording systems, and the breakdown of the classical models of contact, followed by a discussion of a fractal description of asperity contact. In Section 2.1.3.3 experimental and computer modelling of contact at the head-tape interface in linear and helical scan recorders are discussed and the notion of tape asperity compliance are introduced. Of special interest is the effect of water adsorption at the mating surfaces on the contact mechanics. This is described in Section 2.1.4.

To describe the transition from elastic to plastic deformation on contact Greenwood and Williamson<sup>91</sup> defined a plasticity index -  $\psi$ , which is an indicator of the degree of plastic deformation in the contact. This is given in Equation 2.10:

$$\psi = (\sigma_p / \delta_p)^{1/2} = (E^* / H) (\sigma_p / R_p)^{1/2} \quad \text{Equation 2.10}$$

Where:

$$\sigma_p = (\sigma_{p1}^2 + \sigma_{p2}^2)^{1/2} \quad \text{Equation 2.11}$$

$\sigma_p$  is the RMS standard deviation of the standard deviation roughnesses ( $R_a$ ) of the two mating surfaces (1 and 2).  $\delta_p$  is the critical approach distance between the two surfaces at which plastic deformation occurs. Thus the plasticity index is the square root of the ratio of the critical distance moved together which causes plastic flow to the “average” roughness of the two surfaces. This is equivalent to the expression on the right hand side, where  $E^*$  is the complex elastic modulus of the two surfaces (given in Equation 2.12).  $H$  is the

hardness of the yielding material, and  $1/R_p$  (given in Equation 2.13) is the sum of the curvatures of the two mating asperities.

$$1 / E^* = [(1-\nu_1)^2 / E_1] + [(1-\nu_2)^2 / E_2] \quad \text{Equation 2.12}$$

Where  $\nu$  is the Poisson's ratio of the mating materials and  $E$  their elastic modulus.

$$1 / R_p = [1 / R_{p1}] + [1 / R_{p2}] \quad \text{Equation 2.13}$$

For a  $\psi < 0.6$  the deformation is largely elastic, and for  $\psi > 1$ , the deformation is largely plastic. From this model it can be seen that the probability of plastic flow is virtually independent of the load. It is a function of the plasticity index so long as the asperities deform independently.

For polymer contacts Bhushan defined a polymer plasticity index<sup>101</sup>, given in Equation 2.14:

$$\psi_p = (E^* / Y) (\sigma_p / R_p)^{1/2} \quad \text{Equation 2.14}$$

Where the hardness factor in Greenwood and Williamson's index is replaced by the tensile yield strength of the polymer. For  $\psi < 1.8$  elastic contact is predicted, and for  $\psi > 2.6$  plastic contact. Again this plasticity indices assume no asperity – asperity interaction, and thus the sample interval  $>$  the correlation length ( $\beta^*$ ).

Oden et al<sup>102</sup> compared the surface roughnesses of a PET magnetic tape substrate sample, a tape head and a rigid-disk slider measured first with an optical profilometer, and then with an AFM. The optical profilometer used could detect surface features at a lateral resolution of  $1\mu\text{m}$ , and a vertical resolution of 0.1-0.2nm. The AFM used had atomic lateral and vertical resolution. They found that the AFM detected sub-micron surface features characteristic of the manufacturing process not discernible by the optical profilometer. Thereby suggesting that the AFM is the superior tool for investigating surface topography in studies of magnetic tape and tape heads. They also found that statistical analysis of the roughness reveals that the RMS height, slope and curvature depended strongly on the

lateral resolution of the measuring instrument. They concluded that as classical Greenwood-Williamson models of surface contact use these parameters that the outputs of these models will also be strongly scale dependent, and inadequate for modelling asperity contacts. Poon and Bhushan<sup>103</sup> found similar results when comparing Peak-Valley roughness, Ra, Rp, and  $\beta$  values for a glass-ceramic made by a stylus profilometer, optical profilometer and an AFM.

Oden et al found that a statistical analysis of surface roughness data exhibited fractal behaviour that explained the dependence of RMS height, slope and curvature data on instrument resolution. They found that the fractal model predicts large contact spots to be in elastic contact and small contact spots to be in plastic contact in agreement with experimental observations<sup>104</sup>.

Majundar and Bhushan<sup>105</sup>, and Ganti and Bhushan<sup>106</sup> showed that engineering surfaces used in magnetic recording systems could be described by a fractal geometry that is scale independent and provides information of the roughness structure at all the length scales that exhibit the fractal behaviour. The latter model gives a structure function –  $S(\tau)$  and a power spectrum –  $P(\omega)$  for a self-affine fractal surface, which follow a power law and which can be written as Equations 2.15 and 2.16 respectively:

$$S(\tau) = C\eta^{(2D-3)\tau(4-2D)} \quad \text{Equation 2.15}$$

$$P(\omega) = c_1\eta^{(2D-3)} / \omega^{(5-2D)} \quad \text{Equation 2.16}$$

$C_1$  is given by Equation 2.17:

$$C_1 = \Gamma(5-2D)\sin[\pi(2-D)] C / 2\pi \quad \text{Equation 2.17}$$

And where  $\eta$  is the lateral resolution of the measuring instrument,  $\tau$  is the size of the distance increment and  $\omega$  is the frequency of the roughness.  $D$  and  $C$  are the two dimensionless, instrument independent fractal parameters that may be used to characterise the surface roughness.  $D$  (generally in the range 1-2) primarily relates to distributions of

different frequencies in the surface profile, and C to the amplitude of variations at all frequencies.

Following on from an asperity fractal model, Majumdar and Bhushan<sup>107</sup> and Bhushan and Majumdar<sup>108</sup>, have developed a fractal model of elastic-plastic contact. This model predicts whether contacts experience elastic or a plastic deformation on contact, the real area of contact and the statistical distribution of contact points. A critical area is determined as a function of the fractal parameters: D and C, and the hardness and elastic modulus of the mating surfaces. Plastic behaviour is predicted for contact spots smaller than the critical area and elastic for those larger. Contact is described as originating between nanoasperities that deform plastically, merging together, continuing to deform plastically and merging until contact spots become large enough to bear elastic contact.

#### 2.1.3.3 Measurement and Modelling of the Spacing at the Head-Tape Interface

Measurement and/or modelling of the spacing at the head-tape interface are done for the purpose of analysing the potential spacing losses that may occur at the interface during typical running conditions for a particular system design, and with an increased sophistication of measurement, of the head tape asperity contact. Direct measurement of the spacing at the head-tape interface may be done using interferometry. This requires the compromise of either a transparent head or tape, and thus the measured system cannot entirely replicate a real system. Lacey and Talke<sup>109</sup> considered the tape roughness to be more significant in the contact, and measured head-tape spacing between a glass head and magnetic recording tape in a linear mode by interferometry with a monochromatic light source. A good correlation between experimental and modelled data was found. Subsequent development of this method has included the development of mathematical analysis tools<sup>110</sup> that have enabled pulsed broadband light to be used<sup>111</sup>.

Initial numerical models developed for investigating head-tape spacing considered the head and tape to be perfectly smooth, with for example, Stahl et al<sup>112</sup> using finite difference models. Heinrich and Wadwa<sup>113</sup> solved the head-tape interface problem using the finite element method and Lacey and Talke<sup>114</sup> introduced tape roughness. As the tape asperities are compressed on the loaded contact with the head it is necessary to include load sharing and asperity compliance into head/tape interface modelling<sup>115</sup>. Asperity compliance refers

to the deformation of the peaks of a rough surface as a load is applied<sup>112</sup>. Head-tape spacing will decrease as a function of the contact pressure. As the individual load bearing asperities on the tape are compressed, lower asperities will be able to bear the load and the effective roughness of the tape will decrease. With an increase in the number of load bearing asperities, the effective pressure on each will decrease and thus the increase in compression with each increase in load will diminish and equilibrium spacing will be reached.

Wang et al<sup>115</sup> measured tape asperity compliance by measuring the peak-valley spacing of the tape as a function of contact pressure. This was achieved by placing the tape in a chamber in which a controlled pressure was applied to its underside by compressed air, compressing its upper surface against a glass surface. The P-V height of the tape asperities was calculated from the separation between the tape and the glass surface by interferometry at the pressure of interest. To a plot of P-V spacing vs. contact pressure they fitted a pressure–separation model due to Greenwood and Williamson<sup>91</sup> shown in Equation 2.18.

$$P_c(h) = K \int_h^\infty (s-h)^{3/2} \phi(s) ds \quad \text{Equation 2.18}$$

Where  $P_c(h)$  is the contact pressure,  $\phi(s)$  is the normalised height distribution,,  $\sigma$  is the normalised height deviation ( $R_a$ ),  $h$  is the normalised separation, ( $=d/\sigma$ ),  $s$  is the normalised height ( $=z/\sigma$ ) and  $K$  is a material property dependent on the surface properties of the two mating materials.

They found for several different tape types (ME, ferric oxide,  $\text{CrO}_2$ , MP and barium ferrite) that the starting P-V heights were less than 100nm. The  $3\sigma$  value obtained from the Greenwood-Williamson fit of spacing vs. pressure in the range 0-200kPa matched the initial P-V height of the tape. They found that  $K$  took the value in the range 0-100 kPa, and that a small value of  $k$  represented a tape in which the asperities had complied a large amount over the range of 0-200kPa. They measured the time dependence of the compression P-V spacing at a fixed pressure, and observed that spacing decreased with an exponential time constant of 37minutes – thus they concluded that the time scale of tape asperity compliance is large compared with the time scale of the head-tape contact (<1s).

Therefore the slope of the P-V spacing vs. loading curve is better guide to tape asperity compliance in head tape contact. At all contact pressures the slope of this curve is less for ME tape compared to CrO<sub>2</sub> tape from which they concluded that the surface of the ME tape is stiffer than the CrO<sub>2</sub> tape. Overall, with a contact pressure increase of 200kPa, the P-V roughness of ME tape fell from 40 to 25nm, ferric oxide from 34 to 22nm, CrO<sub>2</sub> from 100-50nm, MP from 34 to 25nm and barium ferrite from 53-40nm. Thus when comparing the spacing of two tape types, a straightforward comparison of unloaded roughness may be misleading in the absence of compliance data.

Wu and Talke<sup>116</sup> obtained head-tape spacing data by the monochromatic interference method for a linear tape system incorporating a glass head. They compared this with a finite element model of the system, incorporating tape roughness and asperity compliance. They compared data for a rough tape ( $R_a = 31.5\text{nm}$ ) and a smooth tape ( $R_a = 16\text{nm}$ ). They found good agreement between the two. They found that the spacing was limited by the roughness of the media, with the P-V roughness of the tape a more reliable indicator of the spacing value than the RMS roughness of the tape.

For a helical scan system Kwon et al<sup>117</sup> developed a finite element model for head tape spacing incorporating tape asperity compliance. They adopted a two stage zooming technique. In the first stage the air bearing between the tape and the drum was modelled to give a drum-tape spacing, and in the second the head-tape spacing was modelled using the drum-tape spacing as a boundary condition. They found that the head-tape spacing is a function of head velocity, tape tension as well as the roughness of the tape. The model gave contact pressure distributions across the head surface that could form the basis for head wear modelling. Okuwaki et al<sup>118</sup> measured head-tape spacing in a helical scan Hi-8 recorder using interferometry through a glass head mounted in the scanner. Comparing Hi-8 ME and MP tape, they found that there was good agreement between the P-V roughness of the tape and the measured head tape spacing. By isolating the spacing difference between the ME and MP media, they deduced that at equal roughness the ME tape had an output greater than the MP tape of 2dB.



#### 2.1.4 The Effects of Water Adsorbed at the Head-Tape Interface on Contact

Patton and Bhushan<sup>119</sup> have developed a model to describe how the spontaneous condensation of water menisci about wear particles and non contacting surface asperities at the head tape interface at high humidities affects the lubricity and separation of the contact. They used this model to identify four lubrication regimes which could be assigned to contact between MIG tape heads and both ME and MP media in 8mm helical scan recorders.

The model is based upon Kelvin's equation<sup>120,121</sup> for capillary condensation. This is expressed for a pure incompressible liquid in equilibrium with its vapour (assumed to be a perfect dilute gas) as Equation 2.19:

$$r_k = -\gamma V / [RT \ln (p/p_s)] \quad \text{Equation 2.19}$$

Where  $p$  is the pressure over the curved water surface of mean Kelvin radius  $r_k$ ,  $p_s$  is the saturation vapour pressure at temperature  $T$  and thus  $p/p_s$  is the relative humidity.  $\gamma$  is the surface tension of the liquid against its vapour,  $V$  is the molar volume of the liquid and  $R$  is the gas constant. The mean Kelvin radius  $r_k$  is defined as:

$$1/r_k = (1/r_1) + (1/r_2) \quad \text{Equation 20}$$

where  $r_1$  and  $r_2$  are the meniscus radii of curvature along two mutually orthogonal planes. Kelvin's equation (2.19) predicts that a liquid may be in equilibrium with its vapour at a pressure  $p$  which may be less than its saturation vapour pressure  $p_s$ , if the surface of the liquid is curved with a mean Kelvin Radius  $r_k$ . Thus capillary condensation can occur at a relative humidity less than saturated between the head and tape surface if a sufficiently curved meniscus can be formed about an entrapped wear particle or asperity. Patton and Bhushan<sup>119</sup> calculated that at 22 and 32 °C, from known<sup>122</sup> values of  $\gamma$  and  $V$  that Kelvin radii are in the order of nanometers. And that at constant temperature,  $r_k$  increases with increasing specific humidity and at constant specific humidity  $r_k$  falls with increasing temperature.

Patton and Bhushan<sup>119</sup> showed that where capillary condensation occurs between say a non-contacting tape asperity and the head surface, or about a wear particle entrapped between the two surfaces then there will be an attractive meniscus force tending to pull the surfaces together and compress the asperity or wear particle. For each contact they showed that this meniscus force  $F_m$ , given in Equation 2.21, would be equal to the sum of the Laplace force (due to the pressure difference across a curved meniscus) plus the surface tension force. The buoyancy force was negligible.

$$F_m = (\gamma/r_k) \pi (r_2^2 - a^2) + 2\pi b\gamma \sin\theta \sin(\phi+\theta) \quad \text{Equation 2.21}$$

Where  $\phi$  and  $\theta$  are the angular spread of the menisci around the particle in two mutually orthogonal planes,  $a$  is the contact radius and  $b$  is the radius of the particle.

For meniscus formation about trapped debris particles, asperity contacts and between the head and tape surfaces Patton and Bhushan<sup>119</sup> identified four lubrication regimes. These are shown in Figure 2.3. In the model the head surface is treated as rigid and flat, the tape as rough with deformable asperities and the wear debris particles as deformable. The head and tape are sliding with a relative velocity of  $v$ , and a normal load  $W$  is applied between the head and the tape. The particle is deformed as it passes through the interface depending on the topography of the rougher surface. This deformation of the debris particle can cause the formation of a capillary meniscus if the geometry of the deformation allows a Kelvin radius to be formed.

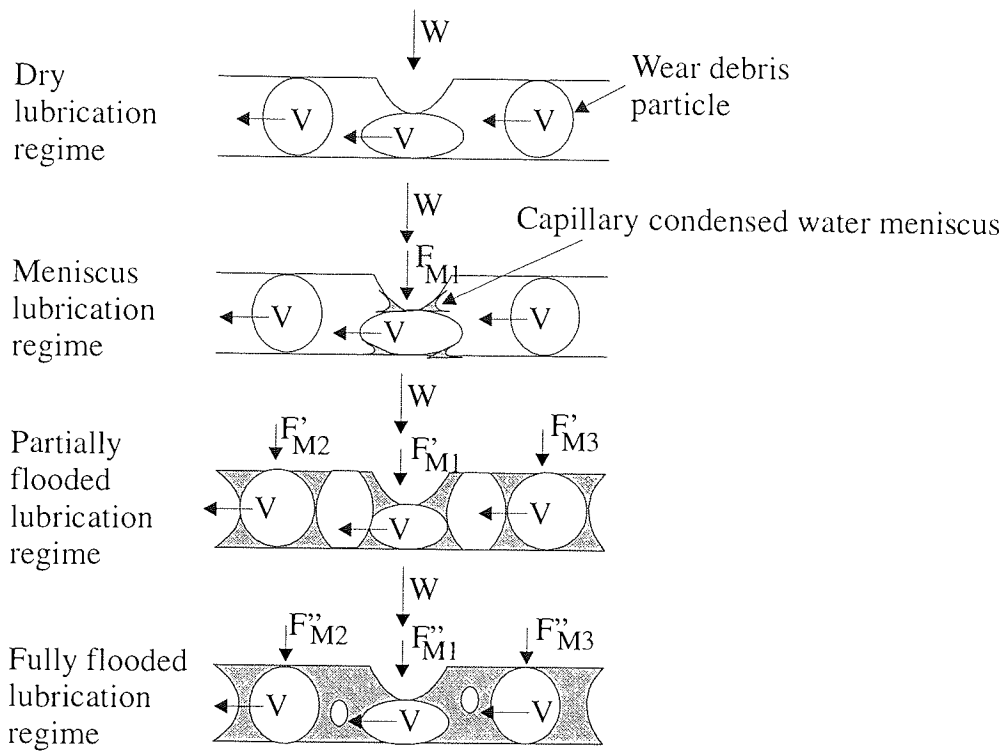


**Figure 2.3 Schematic Diagram of the Various Lubrication Regimes Identified by Patton and Bhushan<sup>119</sup> for a Deformable Wear Particle Sliding Between a Rigid Flat Surface (i.e. a head) and a Deformable Rough Surface (i.e. a Tape)**

In the dry lubrication regime deformation of wear particles produces an insufficient Kelvin radius. In the meniscus lubrication regime a meniscus is only created as the wear debris particle is deformed. Thus a meniscus force  $F_m$  is turned on and off as the particle is deformed creating tape instability. In the partially flooded regime a meniscus is formed about the wear particle independently of its state of deformation due to a sufficiently large Kelvin radius. The meniscus and the meniscus force are maintained on the particle as it slides through the interface, lubricating its passage. Finally, in the fully flooded regime a meniscus bridge is formed between the two surfaces themselves which may result in severe tape instability.

Patton and Bhushan<sup>119</sup> measured signal drop out in an 8mm camcorder system with MP and ME tape at 22 and 32.2°C and at three of four different specific humidities – 0.003, 0.009, 0.013 and 0.021 – corresponding to 20, 50 and 80%r.h. for each temperature. They classified the dropouts by depth (dB) and duration ( $\mu$ s). They used this information to estimate the frequency and size of debris entrapment events caused by the sliding of particles in the partially flooded regime. Real time monitoring of head output and friction force with change in relative humidity at both temperatures for both types was used to

deduce the change in head tape spacing (using the Wallace formula for spacing loss). And assuming Hooke's law, the spring constant for the tape surfaces and thus changes in the normal force at the tape could be deduced.

The real time monitoring of head output with changes in humidity at constant temperature showed output changing in phase with relative humidity for MP tape with output higher at higher humidity showing a decrease in spacing due to meniscus bridge formation. ME tape showed a similar increase in output as the relative humidity was raised, but unlike MP, did not decrease as the relative humidity was lowered. This suggested that water penetrated, displaced or chemically reacted with the ME topical lubricant, and was then not easily lost from the surface. Friction force showed a similar trend – increasing and decreasing in phase with changes in relative humidity for MP tape, and increasing with an increase in relative humidity for ME tape, but not following subsequent decreases in relative humidity. Thus showing meniscus bridge formation to increase friction.

The analysis of their dropout data appears convoluted, but is supported by further work<sup>123</sup>, though not yet by other authors. To summarise, they found that in general that their theory was largely supported by their experimental results. For a particular wear debris size range that lubrication regime shifted in order of meniscus to partial flooding to fully flooded with an increase in specific humidity – confirming the theory that at lubrication regimes associated with higher mean Kelvin radii should become operative at higher specific humidity. They found that as the particle size decreased at constant specific humidity that the lubrication regime shifted to one which was more flooded, as the ratio of mean Kelvin radius to the radius of the particle increases. Another important result is that ME tape showed little propensity to operate in the dry lubrication regime, and a much greater propensity than MP to operate in the fully flooded. This is thought to be due to the presence of the 5-10nm thick topical lubricant on the ME tape which is available to form meniscus bridges even at very low humidities, and can supplement water at higher humidities.

## 2.2 Wear Mechanisms

### 2.2.1 Introduction

In Section 1.1, the head-tape interface was described and the nature of the asperity-asperity contact within this system was discussed. In this section the possible mechanisms by which rubbing contact can cause wear (material removal) are described.

Bhushan<sup>124</sup> states that six distinct mechanisms for the removal of solid material from rubbing surfaces that constitute wear have been identified<sup>125,126,127,128,129,130</sup>. These are (1) adhesive; (2) abrasive; (3) fatigue; (4) impact by erosion or percussion, (5) corrosive and (6) electrical-arc-induced wear. Fretting and fretting corrosion are not distinct wear mechanisms, but rather combinations of adhesive, abrasive and corrosive wear.

### 2.2.2 Adhesive Wear

Adhesive wear is defined as that wear process occurring between two nominally flat surfaces in rubbing contact (lubricated or unlubricated) in which adhesion or bonding occurs between asperity contacts at the interface leading to fragments being pulled off one surface to adhere to the other. The wear debris may then remain bonded to the mating surface, be transferred back to the original surface or fall as loose debris<sup>131</sup>.

The Archard law<sup>132</sup> for adhesive wear, given in Equation 2.22, from an experimental investigation of unlubricated, mainly metallic contacts has been shown to describe in many cases the wear volume for plastic contacts.

$$V = kWx / H$$

Equation 2.22

The Archard law states that the wear volume is proportional to the normal load (W) and the sliding distance (x) and inversely proportional to the hardness of the material being worn away, with a proportionality or “wear” coefficient k. The coefficient k has been found to

be useful in classifying the wear properties of materials in magnetic recording applications, despite another or a combination of other wear mechanisms being active<sup>133,134,135</sup>. In these, the hardness,  $H$ , was not always seen to be relevant and can be subsumed into  $k$  in an expression of the wear law. In magnetic recording applications sliding distance,  $x$ , can be replaced by the product of the head-tape velocity,  $v$ , and the running time,  $t$ .

The Archard law suggests that  $k$  will increase with an increase in the real area of contact,  $A_r$  ( $A_r = W/H$  for plastic contacts). Bhushan<sup>33</sup> has expanded the Archard law to those situations involving largely elastic contacts, in which the real area of contact increases to bear the applied load. Such a regime is seen in contacts against polymeric systems such as magnetic tapes. The Bhushan law is given in Equation 2.23:

$$V = k' W_x / E_c (\sigma_p / R_p)^{1/2} \quad \text{Equation 2.23}$$

Where  $E_c$  is the composite modulus of elasticity,  $\sigma_p$  and  $1/R_p$  are the composite standard deviation and composite mean curvatures of the asperities of the mating surfaces. In this wear law elastic modulus and surface roughness govern the wear volume<sup>136</sup>. It must be noted that repeated stress cycling within elastic contacts may also lead to wear via fatigue, after which the wear debris may adhere to either of the mating surfaces.

Indeed the main evidence for so called adhesive wear is the observation of adhered debris of one mating surface on the other. Adhesion explains the transfer of wear debris but does not explain its generation. It is important as a classification of wear in magnetic recording, as the adhesion of wear material to the tape head will contribute to the spacing loss at the head-tape interface. Broese van Groenou<sup>137</sup> observed adhesion of Co-Cr metal onto glass dummy recording heads from ME tape in which an artificial roughness had been introduced by including particles within the tape substrate. After a number of passes microscopic investigation showed wear at the metal coating on the artificial asperity tips on the tape and corresponding metal islands, a few 100nm thick were observed on the head. Subsequent wear of the tape occurred via delamination within the metallic film of the tape, which also produced larger magnetic particles, which may also adhere to the head.

Where adhesive wear is seen, it is sometimes accompanied by phase changes to the surface to which the debris is adhered, for example re-crystallisation of the surface of a steel bearing surface below adhered wear debris thought to be due to high temperatures generated at the asperity contacts<sup>126,138</sup>.

### 2.2.3 Abrasive Wear

Abrasive wear, also known as ploughing, scratching, scoring, gouging, or cutting depending on its severity, occurs when a rough, hard surface slides on a softer surface, cutting a series of grooves in it. The surface can be ploughed, that is to say, plastically deformed without material removal. Material can then be removed in a ductile manner (in metals) - in which a “lip” of material in the ploughed material is extruded plastically by the action of the ploughing asperity front until the critical shear stress of the material is exceeded. Or a brittle manner (in ceramics) – in which a low-cycle fatigue mechanism occurs within the surface asperities of the ploughed material.

In addition to two-body abrasive wear described above, three-body abrasion occurs when particles become trapped between the rubbing surfaces. Wear debris generated by abrasion, or by any of the other mechanisms can thus become important sources of secondary wear.

Rabinowicz<sup>139</sup> derived a simple quantitative expression for abrasive wear. It assumes conical asperities cutting through a flat soft surface (as shown in Figure 2.4), and is given in Equation 2.24:

$$V = kWx \tan\theta / H \qquad \text{Equation 2.24}$$

Where  $\tan\theta$  is a weighted average of the  $\tan\theta$  values of all the individual cones and the factor  $k$  includes the geometry of the asperities and the probability that a given asperity removes material rather than just ploughing.

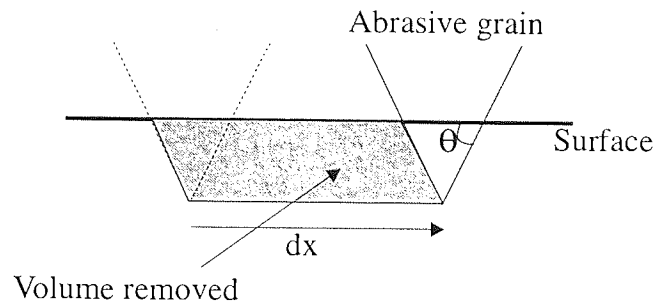


**Figure 2.4 Abrasive Wear Model in Which a Cone Removes Material from a Surface**

### 2.2.4 Fatigue

Fatigue at the surface or within the subsurface is observed during repeated stress cycling (unloading and unloading / compressive/tensile), during repeated rolling, sliding or sliding-rolling of surfaces. It is characterised by the build up of surface or subsurface cracks which propagate as a result of the stress cycling until they join and cause the loss of a fragment of material after a critical number of cycles. It differs therefore from abrasive wear in that the loss of material is not continual with time, and is better described by the number of cycles to critical failure rather than by a wear rate.

Fatigue not only depends on the cycling conditions on the component, but also on the previous history of the component: the presence of subsurface cracks, and the presence of voids, porosity, dislocations, grain boundaries and residual stresses at the surface and subsurface. Such artefacts that may be left by the processing of magnetic recording heads are discussed in a later section.

Crack propagation can also be initiated and propagated by chemical action, especially by water vapour. Such static fatigue or stress corrosion is described in more detail in the Section 2.4.4.2.

Delaminative wear, such as the mechanism exhibited in metal surfaces proposed by Suh<sup>140</sup>, is observed as the (often-catastrophic) removal of large, slender sheets (“laminations”) by wear from the worn surface. This occurs via a fatigue mechanism in which crack propagation in the subsurface proceeds parallel to the surface. It is particularly prevalent in



thin films, in which the interface between the film and the substrate is weak and susceptible to crack propagation.

### 2.2.5 Impact Wear

This can be divided into erosion and percussion. Erosion is caused by the impingement of streams of solid particles, liquid droplets or from the implosion of bubbles formed in a fluid medium. Percussion is caused by repeated solid body impacts.

#### 2.2.5.1 Erosion

Erosive wear is governed by the transfer of kinetic energy from the impinging particle to the mode of wear occurring within the material. The erosive wear rate increases with increasing kinetic energy of the incoming particle stream, and shows an angular dependence that is different between ductile and brittle materials<sup>141</sup> – this is shown in Figure 2.5.

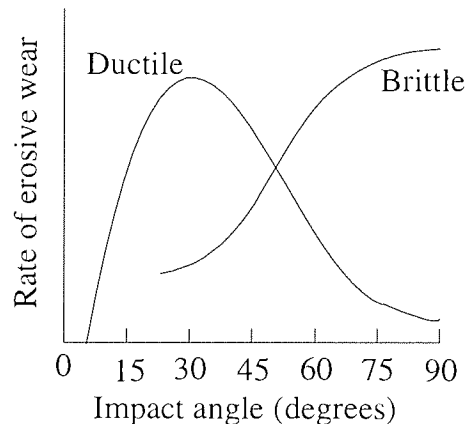


**Figure 2.5 Dependence of Rate of Erosion on Impact Angle**

Figure 2.5 suggests different erosive wear mechanisms operating for ductile and brittle materials. Ductile materials via plastic deformation with material removal by the displacement or cutting action of the incoming particles, and in brittle materials by the intersection of cracks that radiate from the points of impact<sup>142</sup>.

In the erosion of ductile materials two mechanisms have been observed<sup>143,144</sup> – cutting, and deformation erosion. In the former the incoming particle acts as an abrasive particle, and in

the latter plastic deformed material forming thin “lips” at impact crater edges is removed by subsequent impacts. Cutting erosion dominates at grazing angles and deformation at normal angles of incidence<sup>145,146</sup>.

#### 2.2.5.2 Percussion

This is defined as repetitive solid body impact, such as is experienced between the high asperities separated by an air bearing, such as may be seen in the head tape interface. The impact may be associated with sliding, as the relative approach of the two surfaces may contain both normal and tangential components – called compound impact<sup>147</sup>. The normal contact may be sufficient to fracture one or both of the contacting surfaces, if they are of low fracture toughness. Otherwise subsurface fatigue may occur, increasing with fraction of the contact time spent in relative sliding motion.

#### 2.2.6 Corrosive Wear

Corrosive wear results from chemical interaction at the contact interface –tribochemistry or corrosion and the subsequent wear of the reaction products. In the first step the contacting surfaces must react with the environment or some component in the surface e.g. lubricant, and reaction products (oxide and hydroxides) are formed on the surfaces. In the second step wear of the reaction products occurs as a result of the contact interaction between the materials, by crack formation or abrasion. If the rate of the second stage is less than the wear rate between the materials in the absence of corrosion then the tribological formation of an oxide layer may be seen as a beneficial effect.

Quinn<sup>148</sup> proposed a mechanism for the wear of steels in which tribochemically formed surface asperity layers are detached at a certain critical thickness, with a model based on the chemical kinetics of the corrosion process and of mechanics of the contact (such as asperity radius and sliding velocity). Sullivan and Saied<sup>149</sup> showed that there were two major mechanisms for the oxide film formation: a homogenous diffusion controlled mechanism and one due to agglomeration and compaction of smaller oxide particles.

Oxidation is not the only form of corrosive wear. For example it has been proposed<sup>150</sup> that phosphate containing wetting agents in the tape could react with head surfaces to produce easily sheared phosphate layers leading to accelerated head wear.

In any corrosive wear regime the exact mechanism is going to be governed by the relative rates of the tribochemical process that result in oxide film formation and mechanical processes leading to the wear of all components of the system. Thus several limiting conditions can be envisaged as a result of tribochemical wear, including: (1) the formation of a protective hard coating, well adhered to the “substrate”; (2) the cyclic delamination of the oxide film (As proposed by Quinn), to leave a fresh surface susceptible to re-oxidation; (3) removal of the oxide as it is formed to leave a fresh surface; (4) abrasion occurs only within the oxide layer, leaving no fresh surface.

The interactions (mechanical and chemical) with moisture in the environment that may lead to accelerated head wear are discussed later in Section 2.4.4.2.

#### 2.2.7 Electrical-Arc Induced Wear

This occurs due to a dielectric breakdown of an air film between two sliding surfaces leading to arcing due to a high electrical potential between the sliding surfaces. A large power density in the order of  $1\text{KW}/\text{mm}^2$  acting over a small area in a short period of time (in the order of  $1\mu\text{s}$ ) resulting in a high temperature albeit at a relatively low depth ( $50\mu\text{m}$ ). This heating, in addition to sputtering by the plasma created above the surface results in melting hardness changes and corrosion at the surface and is observed as a cratering of the surface. Subsequent sliding of the surface may lead to further wear at the arc-damaged areas. This mode of wear is seen particularly in electrical machinery<sup>151</sup>.

#### 2.2.8 Fretting and Fretting Corrosion

Fretting occurs when two metal surfaces loaded together are subject to low amplitude, high frequency oscillation<sup>152,153</sup>. It is initiated by adhesion, with wear debris created on rupture of the contact. The debris tends to be come trapped in the interface by the oscillation and

becomes a third body abrasive. The creation of fresh surfaces in metals become susceptible to corrosion, with subsequent harder oxide debris even more effective as an abrasive.

## 2.3 Tribo-elements of the Hi-8 Video Recorder

### 2.3.1 Tape Path

Figure 2.6 shows the tape path and the consequent rubbing surfaces in the Philips M-870 Hi-8 camcorder used in this study. It is typical of Hi-8 systems in particular, and of helical scan recording systems in general, which will differ in the number, geometry and placement of the guide pins, and may have additional features such as erase, control and audio heads in the tape path.

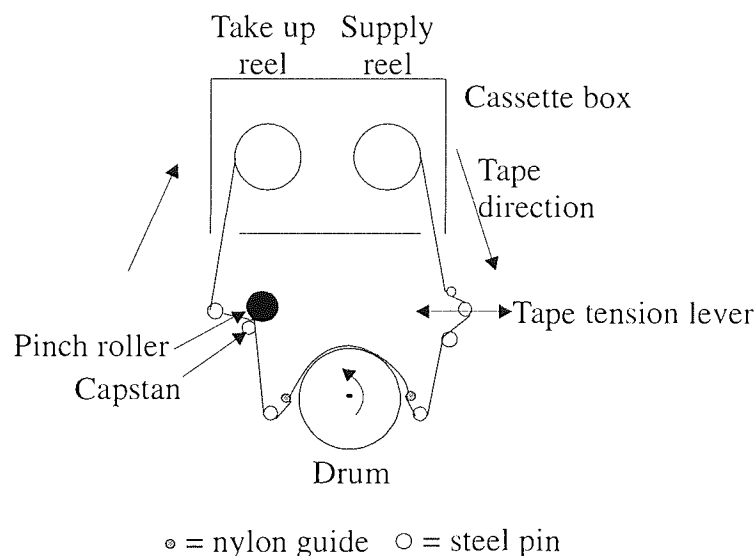


**Figure 2.6 Tape Path in Philips M870 Hi-8 Camcorder Used in this Study**

On loading of the cassette into the recorder the tape is threaded by the mechanism, consisting of steel pins and nylon guides against which either the front or the rear of the tape is in sliding or sliding/rotating contact. The tape is wound round the drum with a wrap angle of 180°, whilst the drum is rotated to maintain an air bearing between the two. The tape tension lever can move to increase the tension of the tape whilst a signal is being written or read, and to decrease the tension, and thus remove the head-tape intimate contact during load/unload and whilst tape is being wound by the reel motors. For reading and writing the tape is moved forward at 14.35mm/s by the action of the capstan and pinch

roller, and the drum is rotated at 1800rpm, giving a head-tape speed of 3.76m/s. The tape is tensioned at 0.1N, giving a head-tape contact pressure in the region of 100KPa.

A review of the tribo-elements in helical scan VCRs is given by Mizoh<sup>154</sup>. The wear of the head and the tape at the head-tape interface are described in detail in subsequent sections. Below the other triboelements in the tape path are briefly described.

### 2.3.2 Tape Path Components – Pins, Guides, and Flanges

The tape will be stressed as it is bent about the various pins, guides and flanges in the tape path. This stress may lead to a possible loss of signal from a process called reptation<sup>155</sup>, due to creep of the remanence proportional to the logarithm of the number of passes. The number of guides and the wrapping angle is limited by the friction between the pins and the tape. A wrap of  $\alpha$  radians about a pin with coefficient of friction  $f$  will cause an increase in the tension by a factor<sup>137</sup>  $\exp(f\alpha)$ . The cumulative tension increase about all the pins must be within the capacity of the capstan motor to pull the tape. The long-term wear behaviour of the guides and pins is important as debris that finds its way via the tape path to the head may cause catastrophic third body wear.

#### 2.3.2.1 Drum

The long-term operation of the rotating drum has been improved by replacing the ball bearing in the direct drive rotating drum motor<sup>156</sup> with a dynamic-pressure groove bearing<sup>157</sup> which reduces the number of metal-metal contact within the rotating drum during operation. To minimise wear at the drum-tape interface grooves are cut into the rotating drum to create an air bearing<sup>158</sup>. To further minimise friction and wear at this interface diamond-like-carbon (DLC) coating of the stationary and rotating drums has been proposed<sup>159</sup>.

#### 2.3.2.2 Capstan

Wear of the capstan surface is potentially a source of third body debris for the head-tape interface. Like the drum a DLC coating has been devised for the capstan<sup>160</sup>. The wear of

the bearing for the capstan can also be a problem, and the configuration of the bearing and lubrication system must be optimised<sup>161</sup>.

## 2.4 Head Wear

### 2.4.1 Tribo-System Parameters

The Archard wear law states that those factors that affect the normal contact force, relative sliding distance and the relative head-tape velocity will have some bearing on the wear rate of the head. These are governed by the tribo-system that was briefly described in Section 2.3. In this section, the set-up of the various parameters within this system that affect the head-tape interface are discussed in more detail. These include: the head-tape conformation, the head structure, the contact area, the tension, the head-tape velocity, the head protrusion, contact pressure, running time and multiple tape passes.

#### 2.4.1.2 Head-Tape Conformation and the Run-in Process

In Section 2.1 the microscopic nature of the contact between the head and the tape was discussed. For intimate contact to occur then the tape must conform transversely and longitudinally (along the length of the tape – also called the “machine” direction) to the short and large radii ( $r$  and  $R$ ) across the head width and length respectively. These radii are shown in Figure 1.3. If the conformation of the tape does not match the head profile at a particular tension loading, then a spacing loss in the signal will occur and the head will wear only at the contact points. This wear will lead to a re-profiling of the head to one that is stable under the applied tape and tension parameters. The conformation of the tape to the head curvature depends upon: the initial curvature of the heads; the protrusion of the head above the drum (the initial curvature of the tape is dependent upon its wrap about the drum); the bending properties of the tape -including the stiffness in both directions, tape thickness and width; and the applied tension<sup>162,163,164</sup>.

Figure 2.7 shows the possible effects of profile mismatch schematically across the longitudinal radius ( $r$ ) of a head with the gap at the highest point of the radius. In Figure 2.7(a) an “ideal contact” is shown. In Figure 2.7(b) contact is shown between a thick (or

stiff) tape that is under insufficient tension to conform to a head that has been profiled by a thinner (or less stiff) tape. In this case there is less contact, but a spacing loss doesn't exist at the gap whilst the head is in the centre of the tape. But as the head scans helically towards the tape edge, where the stiffness is half that at the centre of the tape, contact may be lost resulting in a spacing loss at the track ends. In Figure 2.7(c) contact is shown between a thin (or low stiffness) tape that is too highly tensioned to conform to a head that has been profiled by a thicker (or stiffer) tape. This results in a spacing loss at the gap.

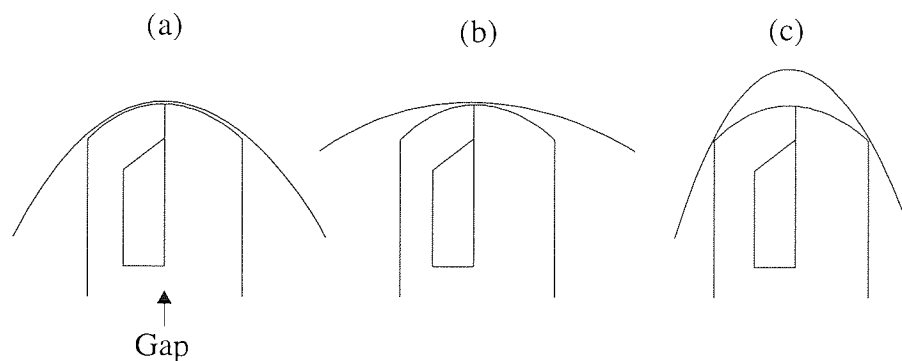


**Figure 2.7 Schematic of Various Head-Tape Conformations Along the Longitudinal Head Radius: (a) Tape Conformation Match to Head Profile, (b) Tape Tension too Low, (c) Tape Tension too Great**

The period of wear leading to head re-profiling is called the “run-in”. Broese van Groenou and Meulenbroeks<sup>165</sup> showed that after a sufficient run-in procedure subsequent wear occurs at constant profile and contact patch area. In this equilibrium wear condition other factors in the wear, such as tape type, material and environmental condition to be compared. Wear rates were gathered in the majority of experiments in this work from this condition. The run-in process is usually a two-stage process. An initial coarse profiling can be given in a short period of time using a highly abrasive lapping tape of similar substrate bending properties to the target medium. This is followed by running against the desired medium to “fine tune” the head profile and to polish the asperities left by the coarse lapping tape.

In operation, the major effects of this conformation effect result from the spacing loss that is incurred by tape type interchange during the run-in of the new media. As spacing loss becomes more critical at higher frequencies this effect is more critical for higher frequency applications, i.e. digital VCR over VHS, for example. The greater the difference between the tape bending properties of the interchanged tapes, the greater this effect is likely to be.

In Hi-8 recording this effect can be seen with the interchange between ME and MP tape types, and with interchange between old tape types the emergence of advanced ME and MP tape types that will have different bending properties due their decrease in thinness and different substrate materials.

#### 2.4.1.3 Head Shape

Hahn<sup>166</sup> reported that head wear may be reduced by effectively increasing the contact area by increasing the longitudinal radius. Increasing the head width will also increase the contact area, but Mizoh<sup>154</sup> suggested that this might lead to deterioration of the electromagnetic operation of the head. Maegawa<sup>167</sup> et al found through interferometric investigations of the head tape interface that the ratio of  $r/R$  is an important factor in head wear. They found minimising the  $r/R$  ratio and the head area at the trailing edge to be highly effective in achieving good head tape contact and a good head life. However head wear is not always uniform across the head, and the wear scar centre on the head has been found to move to either the leading or the trailing edge of the gap<sup>168,169,170</sup>.

#### 2.4.1.4 Tape Sliding Length, Repeat Passes and Head-Tape Velocity.

The wear volume has been found to be proportional to the sliding distance<sup>171,172,173,174</sup>. Care must be taken in extending this to running time as the abrasivity of tape has been shown to decrease with repeat passes as it becomes burnished by the action of the tape<sup>175,165,176,177,178</sup>. In the helical scan system the track width is fixed by the amount by which the trailing head (of the opposite azimuth) overwrites the track written by the leading head (governed by the velocity of the tape and the relative positions of the heads from the drum). Thus the trailing head sees media that is burnished by the leading head and has been observed to wear less than the leading head<sup>179</sup>. In general the track width is much less than the head width, e.g. in Hi-8 the track width = 20.5 $\mu\text{m}$ , and the head width is in the range 80-120 $\mu\text{m}$ . Thus in each pass both leading and trailing heads see a large proportion of media that has been burnished by previous tape passes. Tanaka et al reported that wear rate is proportional to the (repeat pass number)<sup>-0.86</sup>, but this may vary with tape type - Broese van Groenou and Meulenbroeks<sup>165</sup> found different rates of tape degradation between CrO<sub>2</sub> and MP tapes with number of passes.



Virgin tapes therefore are more abrasive than used tapes. Thus a practical wear test must use all virgin tape, or one in which the use of virgin tapes is minimised, whilst avoiding damage through overuse of used media. Mizoh<sup>154</sup> recommends changing tapes at intervals of 200-500 hours. In devising wear tests to estimate the life of a head in use, a usage model must be developed from conducting market research into likely customer use of the product.

Head-Tape velocity potentially has a more complex relation to head wear than suggested by the Archard wear law due to the potential change in the air bearing set up by the rotation of the drum by any change in velocity. A change in head-tape velocity will also cause changes in asperity temperature that may effect wear rate.

#### 2.4.1.5 Tape Tension and Head Protrusion- the Effect of Pressure

These are likely to act on the wear rate by changing the normal force of the tape on the head. The head-tape contact force is proportional to the protrusion, and increasing the force either by increasing the protrusion or tape tension have been found to increase head wear<sup>180,181</sup>. The rate of head wear has been found to decrease with decreasing protrusion experimentally and in modelling<sup>174,182</sup>. A reduction in protrusion has been found to be accompanied by a change in lateral head curvature<sup>168</sup>, which is an additional feedback factor into the wear equation that needs to be considered. Kojima et al<sup>183</sup> reported that head wear is proportional to the cube of contact pressure by changing tape tension. In section 2.1, various models were shown that modelled the pressure distribution at the head-tape interface. These pressure distribution models show promise as the basis for modelling head wear.

#### 2.4.2 Tape Type

Head wear is strongly dependent upon the type of tape used. For a particular tape head wear depends upon: (1) the abrasivity of the magnetic and head cleaning particles at the tape surface; (2) the mechanical properties of the tape; and (3) the lubricants employed.

#### 2.4.2.1 Abrasivity of the Magnetic and Head Cleaning Particles

Bhushan and Lowry<sup>184,185</sup> order the abrasivity of magnetic particles thus:  $\text{CrO}_2 > \text{Co-Fe}_2\text{O}_3 > \text{MP} > \text{ME}$ . It has been widely reported that  $\text{CrO}_2$  particles are more abrasive than  $\text{Co-Fe}_2\text{O}_3$ <sup>186,187</sup>, or metal powders<sup>165</sup>. However Mayer<sup>188</sup> reports that the head wear difference between  $\text{F}_2\text{O}_3$  and  $\text{CrO}_2$  depends upon the hardness of the head materials and the relative velocity. In the case of ME tape, head wear has found to be reduced by a diamond like carbon overlayer on the tape<sup>189</sup>. Morphology, hardness and the chemical properties of the pigments may all contribute to the differences shown between the abrasivity of the various magnetic particles<sup>190</sup>.

Most particulate magnetic recording tapes contain 1-4% by weight of abrasive head cleaning agents (HCA) within the magnetic layer. These are of a harder material, usually  $\text{ZrO}_2$  or  $\text{Al}_2\text{O}_3$ , and are of a slight larger particle size than the magnetic particles. The purpose of these are to maintain wear at such a level at the head tape interface as to prevent debris build up and remove stain. These particles also act to lower friction by providing high points of contact at the head tape interface, thus reducing over all contact area and friction, especially stiction in static head-tape contact. It has been found that the wear rates of bulk ferrite heads are proportional to the abrasive particle size within the tape<sup>191,192,193</sup> and the weight percentage of the abrasive particles to the magnetic powder<sup>194,195,181</sup>. Poor dispersion of the HCA on the surface accelerates head wear<sup>196</sup>.

#### 2.4.2.2 Mechanical Properties of the Tape

Head wear increases with the surface roughness of the tape<sup>196,181</sup>, and is roughly proportional to the number of asperities per unit area<sup>197</sup>. Burnishing of the media<sup>198</sup>, a finishing of the tape surface by either a sharp blade or an abrasive tape reduces head wear<sup>199,181</sup>. Similarly, it has already been noted that burnishing of virgin media on the first few passes reduces head wear.

Head wear is directly proportional to tape stiffness<sup>200</sup>. Tape stiffness is proportional to the cube of the tape thickness and the Young's modulus<sup>168</sup>. Thus head wear can be reduced by reducing both these factors. In Section 2.4.1.2 tape stiffness was shown to be important in

determining the pressure distribution of the head-tape contact and thus the wear profile, as well as the wear rate.

#### 2.4.2.3 Lubricants

The effects of added lubricant on head wear have been reported, but no details on the lubricant were given. Mizoh<sup>154</sup> reports that in general silicone oil at the head tape interface reduces both friction and wear of a bulk ferrite head. Where as fatty acids, which also reduce the friction coefficient, cause the coated film on the media to become fragile, thus accelerating head wear.

#### 2.4.3 Environment – The Effects of Temperature and Humidity

Magnetic recording equipment, especially portable video recorders will be required to operate at a variety of climatic conditions. These include the extremes of: 3°C & 5%r.h. – based on conditions in Alaska; 3°C & 80% r.h. – on a skiing ground; 40°C & 5% r.h. – in a desert; and 40°C & 80% r.h. – tropical.

##### 2.4.3.1 Temperature

Mizoh<sup>154</sup> found, for a ferrite head running against Co-modified  $\gamma$ -Fe<sub>2</sub>O<sub>3</sub> tape in a helical scan system that head wear was inversely proportional to the ambient temperature in the range 5 - 25°C as measured by an IR thermometer. He attributed this to an increase in the complex modulus of the tape with decreasing temperature. Conversely<sup>195</sup>, it has been found that the wear rate in linear systems rises in proportion to the temperature. On the whole it is to be expected that the dependence of wear rate on ambient temperature be a complex one, due to the changes in tape properties with temperature<sup>201</sup>. These include the bulk properties of the tape substrate such as Young's modulus mentioned above, and the properties of the tape lubricant. Long chain fatty acids such as myristic acid (C<sub>14</sub>) are commonly used as the lubricant in particulate tapes. It has a melting point of around 50°C (depending on pressure) and a breakdown temperature of 120°C<sup>202</sup>. Thus the operation of the lubricant will be affected by temperatures rises above the ambient at the head-tape interface. Temperature will also affect the diffusion of the lubricant to the surface of particulate media. Temperature rises, even of a few hundred degrees should not affect the bulk

mechanical properties of refractory ceramics that form the head. However, they may affect the tribochemistry at the head surface, especially of the magnetic layers, and may cause a change in the magnetic properties due to a raise in temperature above the Curie point, or by the re-crystallisation of an amorphous magnetic thin film.

The measurement and prediction of head-tape interface temperature is complex problem. Measurement of the interface by IR thermometry requires a change in the system to either a transparent tape or a transparent head. IR thermometry measures the radiated heat and thus excludes that absorbed by specific physical or chemical processes at the interface. In measuring black body radiation intensity at a few fixed wavelengths, they may miss higher energy states at the higher asperities. Modelling temperature rises requires an accurate model of the two mating surfaces and an understanding of the energy transferred in the asperity contacts. Average temperature rises at the interface may then be calculated. Even then localised temperature rises where the load is supported by a lower proportion of higher asperities or by third bodies which may be of greater tribological significance.

Bhushan<sup>203,201,204</sup> predicted temperature rises for typical head-tape contacts of 7-10°C, and where magnetic particles are exposed then the contact temperature may rise in the range of 600-900°C. There was some agreement with IR thermometry results<sup>205</sup>. Mekala<sup>206,86</sup> developed a more sophisticated model based on the heat transfer between asperity contacts of real head and tape surfaces mapped by AFM. Using this the normal contact temperature predicted for a particular linear system was found to be in the order of 100°C, as opposed to the 7-10°C that was predicted by Bhushan.

#### 2.4.3.2 Humidity

Head Wear has been shown to increase<sup>207,208,209,210</sup> often severely with an increase in relative humidity. An acceleration of wear rate occurs<sup>211</sup> above 45%r.h. A tape may store moisture at high humidity up to its equilibrium water level<sup>212</sup>, and consequently such “stored” humidity can cause accelerated wear on subsequent running<sup>195</sup>.

In the case of the magnetic metal thin films employed in magnetic recording heads corrosion may easily be envisaged as the cause of accelerated wear at high relative

humidity. However the mechanisms of accelerated wear in ceramics at high humidity are less easy to explain as they are already in the stable oxide state, and indeed the wear rate of ferrite has been shown to increase more with relative humidity than metallic permalloy<sup>191</sup>. Potential mechanical and chemical wear mechanisms for ceramics (which may also be applicable to the metallic layers of the sandwich head) at elevated humidity are discussed in the following sections on material dependent wear.

The work of Patton and Bhushan<sup>119</sup>, as discussed in Section 2.1.4 shows that below saturation, with increasing relative humidity, capillary meniscus condensation causes a decrease in head-tape spacing and an increase in the normal force at the surface. This may lead to an increase in abrasive wear as the tape asperities may plough deeper into the head with a greater force. The flooded and partially flooded interface lubrication regimes may accelerate the removal of the wear debris, thus accelerating the wear rate.

#### 2.4.4 Materials Dependence of Head Wear

Head wear rate will be material dependent. Of the various constituent materials of magnetic heads discussed in Chapter 1, Mizoh<sup>154</sup> found the general order of wear resistance to be in the order AlTiC > ferrite > various non magnetic ceramics > permalloy&sendust > glass. In the sandwich laminate heads studied in this work (those with 32 $\mu$ m track width – see Section 4.5.2), approximately 83% of the tape (load) bearing surface is formed from sintered CaTiO<sub>3</sub> or Zr-doped CaTiO<sub>3</sub>. Of the remainder of the tape bearing surface the majority (16% of total) consists of thin film magnetic metal laminations (in ~1.75 $\mu$ m widths), with thin film ceramic (Si<sub>3</sub>N<sub>4</sub>) spacer laminations (<1%total, in ~0.25 $\mu$ m widths) and a single metallic (Mo-Au) bonding layer (of width ~0.25 $\mu$ m). Thus the wear rate will be largely determined by the CaTiO<sub>3</sub> ceramic wear rate - this is discussed in the next section. The tribological properties of the magnetic materials are discussed in the following section. The problem of differential wear is discussed later in Section 2.7.

#### 2.4.4.1 Ceramic

Sintered  $\text{CaTiO}_3$  based ceramics, of the perovskite type crystal structure, are one of several types of ceramic investigated as a possible substrate for magnetic films in recording heads for disk sliders, linear and helical tape systems<sup>213,214,215,216,217,218,1</sup>. These include SiC, non-magnetic ferrites, alumina and various alumina composites. Of the latter variety,  $\text{Al}_2\text{O}_3$ -TiC or “AlTiC”, has found to be very hard and wear resistant and is often used in hard disk sliders and linear tape drive heads. For helical scan heads the material need is different in that some head wear is required for head-tape conformation about the long and short radii of the head. In sandwich heads it is also necessary to match the wear rate of the magnetic material to avoid pole tip recession which condition has been found to be satisfied by  $\text{CaTiO}_3$  based ceramics<sup>1</sup>. Sony use sintered  $\text{CaTiO}_3$ , with  $\text{TiO}_2$  and NiO dopants as the substrate in their wear resistant laminated head structures<sup>219</sup>. The dopants tune the wear rate and the compatibility between the substrate and the magnetic laminations.

The wear mechanisms of  $\text{CaTiO}_3$  based sintered ceramics in magnetic recording heads (under conditions that include low contact pressures, but with a higher number of repeat passes) have not been discussed specifically in the open literature, but their behaviour is likely to be similar to other sintered metal oxide ceramics, such as hot-pressed ferrites.

The wear rate of ceramics in magnetic recording heads does not necessarily follow trends in bulk properties such as microhardness or fracture toughness. Broese van Groenou et al<sup>134,220</sup> found no correlation between microhardness or fracture toughness and wear coefficient. However Tanaka and Miyazaki<sup>173</sup> found that wear is inversely proportional to hardness, as to be expected from purely abrasive wear. The scale on which such material properties are collected is important, for example by using a nanoindentation technique, Bhushan and Lowry<sup>218</sup> demonstrated a correlation between nanohardness and wear rate for several materials used as head surfaces. When other wear mechanisms occur alongside abrasion then hardness, even when obtained under loading conditions observed in magnetic recording, will be insufficient to describe resistance to wear.

Wang and Hsu<sup>221</sup> investigated the transition of wear mechanisms that occur in sintered ceramics (in their case  $\text{Al}_2\text{O}_3$ ) in proceeding from low contact through to high contact stress, by indentation, scratching and ball-on-flat wear tester. They identified four distinct

wear zones with increasing contact stress. (1) Below the elastic limit no wear occurs. (2) With moderate contact forces, below the plasticity limit, wear is controlled by plastic deformation, i.e. by abrasion. (3) As the critical fracture stress is approached, radial and cone cracking are observed, and the wear becomes controlled by microcracking or grain pull out. (4) Above a critical stress, fracture occurs. The critical microcrack stress to fracture fell with the number of loading cycles, e.g. for  $\text{Si}_3\text{N}_4$  it fell from 11GPa for one loading to 2GPa for 100 loading cycles. The contact pressures at the head-tape interface are very low in comparison (in the order of 100kPa), but the number of repeat passes are very high thus allowing for microcrack controlled wear. They also found that for sintered ceramics, at high humidity and the presence of lubricating films, tribochemical reactions may occur which accelerate wear. It is part of the aim of this work to identify which mechanisms are occurring and which are controlling the wear rate for the two  $\text{CaTiO}_3$  ceramics studied with cycling against magnetic tapes under typical loads.

Ozawa et al<sup>222</sup> investigated the wear mechanisms of ferrite heads against  $\gamma\text{-Fe}_2\text{O}_3$ , MP and ME tape by scanning electron microscopy. They found that against  $\gamma\text{-Fe}_2\text{O}_3$  tape the principal wear mechanism was due to the abrasive action of the magnetic particles of the tape. For MP tape a mixture of abrasive and adhesive wear was observed, and for low abrasivity ME tape they found wear to occur primarily due to adhesion.

Bhushan<sup>223</sup> observed that the first sign of ferrite wear against a  $\text{CrO}_2$  or  $\gamma\text{-Fe}_2\text{O}_3$  tape are very fine scratches parallel to the direction of tape passage as small as 25nm. These scratches maybe caused by hard particles from the environment or from the tape, but appear to be of similar frequency, whether or not the tape recorder is isolated from the environment suggesting that the frequency be controlled by the abrasivity of the tape. He also observed that microfragmentation of the oxide crystal structure can occur leading to pullouts from the surface that may cause additional localised plastic deformation and grooving (by three-body abrasion). Large thermal stresses may accompany the third body plastic deformation<sup>224</sup> that may cause damage to the magnetic properties of the tape or the head. In ferrites work hardening is observed which suggests that there is a shift from a transgranular fracture mechanism – to one dominated by intergranular fracture<sup>225</sup>. Finally Bhushan observed chipping to occur in ferrites where contact stresses are particularly high – at the gap, and at the interface between ferrite and the glass.

#### 2.4.4.2 Mechanisms of Ceramic Wear at Elevated Humidity

Water adsorbed at the ceramic surface may cause accelerated wear via the mechanical action of physical ingress by that water into microcracks and pores in the ceramic surface. This is a mechanical effect due to the non-compressibility of water and is well known in the pitting of metals<sup>226</sup>. Sintered ceramics are always porous to a certain extent. An increase in porosity,  $p$ , also leads to lower critical bending stresses. These are proportional to the elastic modulus, which is in turn proportional to  $\{\exp(-p)\}$ . Thus a more porous ceramic is more susceptible to microabrasive wear, and an increase in porosity due to water molecule ingress will increase the abrasive wear rate.

Alternatively water adsorbed at the ceramic surface may cause accelerated wear via a chemical mechanism. Hsu and Shen<sup>227</sup> plotted ceramic wear maps (in which wear rate is plotted both as a function of sliding speed and pressure) for a wide range of ceramics ( $\text{Al}_2\text{O}_3$ , yttria-doped zirconia ( $\text{ZrO}_2$ ), SiC and  $\text{Si}_3\text{N}_4$ ). These showed transitions to severe wear mechanisms when sliding in the wet that are due to the chemical action of water. Non oxide ceramics, such as SiC and  $\text{Si}_3\text{N}_4$  are susceptible to tribo-oxidation to the more thermodynamically stable oxides<sup>228,229</sup>. The reaction of water with oxides such as alumina<sup>230</sup> and zirconia<sup>231</sup> is explained by applying the Lewis acid-base theory<sup>232,233</sup>. Partial charge transfer between the water molecule and the oxide surface contribute to the attractive forces that cause adsorption of the water. Complete charge transfer is required for the dissociation of the adsorbed water molecule and reaction with the surface. This is dependent upon the relationship between the position of the Fermi level in the band gap of the ceramic and the point of zero charge (pzc) in the water. Thus the surface chemistry of water adsorbed at the oxide surface can be altered by impurities – dissolved ions etc in the water and by altering the Fermi level of the oxide surface. The Fermi level of an oxide surface can be changed by the presence of chemical impurities and by structural defects. For example the presence of Y impurities in  $\text{ZrO}_2$  is thought<sup>234</sup> to be involved in the tribochemical reaction of water and point defects in  $\text{ZrO}_2$ . Structural defects may be introduced at a ceramic surface by the action of surface deformation by wear, and may thus promote oxide-water reactions that do not occur at the unstressed surface.



#### 2.4.4.3 Stress Corrosion

Tribochemical reactions at the ceramic surface may lead to removal of material as described in section 2.2.6 on corrosive wear mechanisms. An additional mode of wear due to corrosion is stress corrosion or static fatigue in which crack propagation occurs due to chemical action at the crack tip. One of the most widely studied<sup>235,236,237</sup> examples of this are the stress corrosion of silicates, such as silica glasses. It is well known that water makes silica glass fracture more easily, and glaziers wet the scribe lines about which plate glass is broken to size. The reaction according to the Freiman and Michalske<sup>238</sup> model is shown in Figure 2.8. In the first step a water molecule is adsorbed at a strained Si-O-Si bond at the crack tip. An electron lone pair on the oxygen of the water molecule interacts with a silicon atom and a proton forms a hydrogen bond between the water molecule and the bridging oxygen. In the second step the Si-O bond and the O-H bond in the adsorbed water molecule cleave to leave two hydrogen bonded silanol groups. The final step involves a breaking of the remaining hydrogen bond.

The attacking molecule satisfies three criteria: (1) It acts as a Lewis base i.e. has at least one lone non-bonding pair of electrons; (2) It is a Bronsted acid i.e. contains a labile proton and the distance between the acid and base sites conforms with the Si-O distance (0.163). Michalske and Bunker<sup>239</sup> found other small molecules that adsorb on to silica such as ammonia and methanol which also satisfy these criteria also accelerate fracture in silica.

The experimental observation of such crack tip reactions is very hard to achieve using the normal range of surface chemical analytical techniques such as XPS, Auger, SIMS or FT-IR for example due the nature of the geometry and low areal coverage of such cracks. The greatest evidence for such reactions are provided by molecular orbital calculations for strained bonds. Michalske and Bunker<sup>239</sup> used molecular orbital calculations to show that changes in either the O-Si-O or the Si-O-Si greatly increase reactivity by creating Lewis acid sites on the silicon and Lewis base sites on the oxygen. They showed that crack velocity grows in proportion to the stress intensity with the constant of proportionality dependent on the reagent used to promote the cracking. Furthermore reaction products have been observed on the surface of silica glass by IR spectroscopy between silica and

such compounds as  $\text{H}_2\text{O}$ ,  $\text{NH}_3$  and  $\text{BF}_3$  when the silica was strained, but which were absent in the absence of stress<sup>240,241,242</sup>.

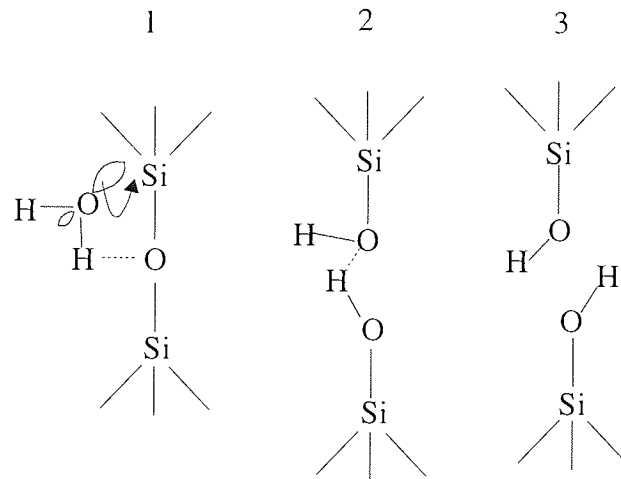


**Figure 2.84 Michalske and Freiman Reaction for Water Enhanced Si-O-Si Bond Rupture. The Strained Crack Tip Bond 1. Absorbs a Water Molecule 2. Is Cleaved via a Dissociative Reaction and 3. Results in Two Surface Silanol Groups.**

Alumina<sup>243</sup> shows similar activity towards compounds such as water, ammonia and hydrazine, but unlike silica crack velocity vs. stress intensity curves are not linear, showing stress independent corrosion of alumina, consistent with its known surface chemistry<sup>244</sup>. In general oxide ceramics will be susceptible to chemical interactions with water if the applied stresses are such as to distort the metal-oxide bonds so as to enable them to undergo a Lewis acid-base type reaction with a water molecule as shown in Figure 2.8. This will be inhibited the greater the degree of ionic bonding existing in the metal-oxide bonds of the ceramic.

Wiederhorn<sup>245</sup> et al investigated the effects of water and other dielectrics on crack growth, again in the case of soda-lime-silica glass. They found that when water is present in organic liquids that it is the principal agent that promotes crack growth. They found that the curve of crack velocity vs. stress-intensity factor contains three distinct regions, as shown in Figure 2.9. In region 1 the curve is linear with crack velocity proportional to stress, followed by a levelling off in Region 2 in which crack velocity remains constant with an increase in stress followed in Region 3 by a steep rise in velocity with stress.

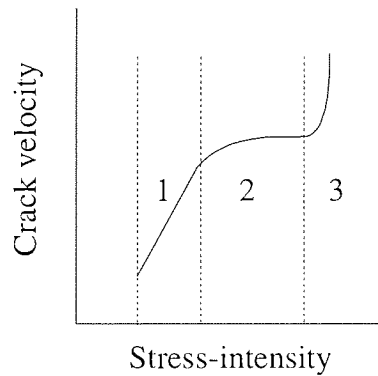


**Figure 2.9 Crack Velocity Vs. Stress Intensity (Arbitrary Units) for Soda-Lime-Silica Glass Showing Three Regions**

In Region 1 crack growth shows a strong dependence on both the stress intensity, as shown in Figure 2.9, and on the activity of the water in the system. If the water vapour above the stress contact is assumed to behave as ideal gas, then the activity,  $a_s$ , of the water in an organic solvent (such as in a lubricant layer at the head-tape interface) is given by the ratio of the partial pressure,  $p_s$ , of the water over the solution to that over pure water,  $p_{s0}$  – Equation 2.25.

$$a_s = p_s / p_{s0}$$

Equation 2.25

As Equation 2.25 is defined as the relative humidity, then crack velocity should increase with increasing relative humidity, and this was found to be the case. Wiederhorn et al considered that Region 1 would control the lifetime of the ceramic with respect to crack formation and fatigue, and therefore the chemical potential or activity of water at the ceramic surface is an important factor in the life of the ceramic. In Region 2 the crack velocity is such that water is being consumed faster than it can be supplied at the crack tip and thus the velocity becomes limited by the diffusion of water to the crack tip. In region three the crack is now being propagated by reaction with the solvent, and the slope of the curve is dependent on the dielectric constant of the solvent.

Bhushan and Khatavkar<sup>246</sup> investigated the wear of multigranular ceramic Mn-Zn ferrite and metallic mu-metal (Ni-Fe-Mo alloy) at elevated humidities against CrO<sub>2</sub> tape. Both

materials exhibited extremely high wear above 65% r.h. For mu-metal they found that this was due to high meniscus forces and three-body abrasive wear due to build up of debris at the interface. Above 65% r.h. the ferrite showed both accelerated abrasion and showed evidence of static fatigue at the grain boundaries during static fatigue tests (maintaining a bar of the material under tensile stress) at high humidity. They speculated that debris generated via a static fatigue mechanism became attached to the tape and caused the observed increasing in abrasive scratching on the ferrite, though no such particles themselves were observed. These two mechanisms together were thought to account for the increase in wear at high humidity.

#### 2.4.4.4 Magnetic Material

Ozawa et al<sup>222</sup> found the wear mechanisms of heads of Sendust and a Fe-Co-B amorphous alloys to show similar wear mechanisms against  $\gamma$ -Fe<sub>2</sub>O<sub>3</sub>, MP and ME tapes to heads composed of ferrite. They postulated that surface crystallisation or oxidation might occur during rubbing of magnetic tapes against amorphous magnetic alloys that may act to decrease or increase the wear rate. The wear of magnetic thin films has been found<sup>247</sup> not always to be inversely proportional to hardness, with amorphous alloys of 75-8% transition elements (Fe, Ni, Co) with a glass forming metalloid (B, C, Si, P or Al) exhibiting a higher hardness than Sendust, but also a higher wear rate. This was thought to be due to corrosion. Katori et al<sup>248</sup> compared the wear rates, as the surface coating on dummy heads in 8mm helical scan video recorders of various magnetic thin films against ME and MP tapes. These included Fe-N based (FeTaN, FeAlN, FeAlVNbON) and other magnetic thin films (FeAlSi, FeRuGaSi and CoTaZr). They found that the ordering of the wear resistance of these materials did not follow the ordering of their microhardness, and concluded that the wear mechanism was more complex than abrasion, but found no decisive evidence for the nature of the wear mechanisms in operation. Nanocrystalline alloys of Fe with Nb-N or Nb-B amorphous grain boundaries suffer from both brittle fracture and corrosion<sup>249</sup>. Such grain boundaries maybe suspect towards stress corrosion, as described above leading to grain pullout. Corrosion resistance is an important prerequisite for a magnetic material to be chosen as a potential head material. All three of the magnetic materials studied in this work: CoNbZr, FeNbSiN, and FeTaN were found not to corrode with immersion in water

at 60° for 48 hours<sup>250</sup>. In the course of this work these three materials were worn against MP and ME tapes at high humidity and their surface chemistry studied by XPS.

Deng et al<sup>251</sup> studied the mechanical properties (hardness and elastic modulus) by nanoindentation and the wear properties against MP tape (by sphere-on-flat) of FeTaN. They found that on increasing the N content of the film from zero to a very small amount, the hardness, elastic modulus and wear resistance until a maxima was reached, after which further incorporation of N caused the hardness and elastic modulus to decrease and the wear rate to rise. They also observed pitting within the worn area of the FeTaN film, and two distinct wear/friction regimes: a linear regime in which wear rate was constant with time and a non-linear region in which wear rate declined as the surface was protected by the build up of tape debris. In further work Deng et al<sup>252</sup> further optimised the mechanical properties by compositional change. The maximum in the hardness was at around 17GPa, and the elastic modulus was around 210GPa. Deng et al also showed<sup>253</sup> the superiority of the mechanical properties of FeTaN over Permalloy, however, in this case sub-micron pitting was again observed on the FeTaN surface in the low load abrasive wear regime. This may suggest either pullout or corrosion is occurring at a low rate, and which therefore becomes unmasked when the abrasive wear rate is correspondingly low.

## 2.5 Media Wear

The wear of the magnetic media is intimately connected to the wear mechanisms occurring at the head. Media wear is of concern, not only because of the concern over media life, but also because it affects short and long term signal output (in the form of “dropouts” in the reproduced signal). In terms of head wear, media wear is a generator of third bodies available to wear the heads, and is an indicator of the forces occurring between the head and the tape.

### 2.5.1 Media Wear and Dropouts

In a helical scan recording system with continual monitoring of the heads after they have scanned by MP tape using a stroboscope and TV camera, Osaki et al<sup>254</sup> observed the build up of media debris at the trailing edge of the contact patch on the leading head. This

agglomerated to a size at which it could be contacted by the tape by which it was picked up and transferred to the rubbing surface of the following head, causing a “clog” with an associated spacing loss with consequential decrease in reproduced voltage, known as a dropout. Dropouts may also result from the removal of magnetic material in the tape, causing a permanent loss of signal at that point. They found that an initial large volume of wear from virgin tapes occurred due to defects (aggregations of filler) in the base film of the tape which resulted in more loosely adhered patches - “swellings” of the magnetic coat which could easily be removed via scratching or shear-fracture either by rubbing on the tape guides or at the head. Mature wear of the tape occurred at both the defect sites and the “normal” areas of the tape.

### 2.5.2 A Comparison of ME and MP Tapes

It has been widely reported for linear and helical scan recording applications that ME tapes are far less durable than MP tapes<sup>255,256,257,258,259</sup>. For example Hempstock and Sullivan<sup>259</sup> showed that under the same running conditions, in a Hi-8 recorder, that commercially available ME Hi-8 tape showed catastrophic failure as indicated by a sudden rise in the drop out rate at just over 300 cycles, whereas commercially available MP tape showed severe drop out growth after 2500 cycles.

Bhushan and Koinkar<sup>256</sup> used nanoindentation and microscratching to compare ME and MP tapes. They found that with normal loads of less than 50 $\mu$ N ME tape exhibited a higher scratch resistance and showed a greater microhardness than MP tape. With normal loads of greater than 50 $\mu$ N ME tape exhibited a catastrophic brittle failure mode, whereas the particulate media showed a continuous increase in wear rate with load beyond this value. They also found the scratch resistance of the ME media to be anisotropic, which may be related to the anisotropic nature of the columnar crystal structure of the ME media. The scratch resistance of the MP tape was isotropic. Hibst<sup>260</sup> also observed a directional effect in the wear of ME tapes in head-tape wear studies, with the wear rate being lower when the head ran in the direction corresponding to the columnar orientation as compared with the opposite direction. Comparing the microfriction properties (by friction force microscopy) of MP and ME tapes, Bhushan and Koinkar found them to be similar, with localised

friction values for both tapes correlating to the slope of the local surface roughness profiles.

Bhushan and Patton<sup>257</sup> related the greater durability of particulate over evaporated media to the bearing of the head-tape interface by the HCA. They observed a head clogging mechanism similar to that observed by Osaki et al., which was more prevalent for ME media. This was also observed by Bhushan and Monahan<sup>258</sup>, and attributed to the nature of the topical lubricant being used in the ME tape, purported to better bind and cement the wear debris to the head. However, the greater build up of debris in the case of ME tape maybe due to the lower material removal rate that is observed for this tape type as compared with MP. Interestingly they observed that ME tape shows a lower friction and greater durability than particulate tapes against softer mating materials seen in the tape path, such as acetal plastic (used in some guiding pins) or aluminium (used in the drum in helical scan recording). But that against harder materials such as steel (guiding pins) or ferrite (head) the opposite trend is observed, and that greatest damage is seen at the ferrite surface with sliding against ME rather than particulate tapes.

Work has been done to elucidate the wear mechanisms operative in ME and MP media in the helical scan recording mode, and these are summarised below.

### 2.5.3 Wear Mechanisms in ME Media

Hempstock and Sullivan<sup>30</sup> investigated the lubrication of ME tapes by SIMS and XPS surface chemical analysis. They compared two different tapes with two different types of PFPE lubricants. They found that one tape had a more mobile lubricant coverage, and this tape showed a durability of 350 passes, as compared to less than 50 cycles for the other tape. They accelerated tape wear by operating in pause mode in which the drum spins against a stationary tape. Wear scars generated in this manner showed a depletion of lubricant. Thus it was deduced that wear in ME tape is preceded by local lubricant depletion and that this can be lessened by employing a lubricant which exhibits a greater mobility over the tape surface. The actual failure mode of the tape was observed to consist of removal of lamellar particles of the magnetic coating along the written track. This was thought to occur by classical Suh delamination, due to repeated loading and unloading cycles of the head tape contact causing growth of subsurface cracks at the interface

between the magnetic layer and the tape substrate. A similar failure mode was observed by Osaki et al<sup>261</sup>. They attributed the catastrophic delamination to an increase of the friction force between the head and tape beyond the adhesive force between the magnetic layer and the substrate, rather than a fatigue mechanism. Osaki et al<sup>262</sup> found that an increase in friction force can be caused by the removal of lubricant and absorbed contamination and by an increase in real area of contact caused by the smoothing of the tape surface by wear.

The durability and friction properties of ME tape has been improved by the application of a diamond like carbon coating on the magnetic layer<sup>263,264,265</sup> – the structure of such tape is shown in Figure 1.11. The evaporation of such elastic asperities on to the tape surface are thought to reduce the real area of contact and reduce friction<sup>266,267</sup>. Xu et al<sup>268</sup> reported that a major tribological concern with carbon coated ME tape is the action of temperature and humidity. They noted that changes in the physical properties of the PFPE lubricant controlled the friction properties with temperature. They found that below 5°C that the friction coefficient is low at low humidities and rises with r.h. to a maximum between 50-80% r.h., before decreasing with further increase in r.h. Above 10°C the opposite trend was observed - friction decreased with an increase in r.h. to minimum in the range 50-80% r.h., before increasing with further increase in r.h. Most practical recording applications are likely to be running in the second temperature regime. Below 5°C they observed a greater propensity for cracking in the media, and above 80% r.h. an increased tendency for agglomeration of wear debris.

#### 2.5.4 Wear Mechanisms of MP Tape

Hempstock and Sullivan observed similar patterns of dropout growth upon repeat cycling with MP tape as they had observed for ME tape<sup>259</sup>, that is to say dropouts remain constant and low throughout the life of the tape, before growing catastrophically at the end of life (3500cycles). This they attributed to a similar fatigue mechanism leading to loss of magnetic particles in conglomerations large enough to affect signal loss. In addition, material removal must be continually effected as observed in the generation of head clogging material at the trailing edge of the contact patch, which does not affect signal out from the tape. Support for a fatigue mode of particulate media wear is given by Osaki et



al<sup>269</sup> who observed many small shear fractures in the tape surface prior to debris generation, which act as third body agents which in turn cause catastrophic wear.

## 2.6 Stain

Magnetic recording head stain is defined as a build up of material on a recording head that is not easily removed by, for example, wiping with a common solvent. The first published observation of stain was by Lemke<sup>270</sup> of a thin (<10nm thick) brown stain found on ferrite heads in use against an iron oxide tape. At the time this stain was too thin to cause spacing loss at the read heads at the wavelengths then employed. In the absence of spacing loss, stain build may be regarded as favourable as it can reduce head wear<sup>271</sup>. As recording wavelengths become ever smaller, spacing loss caused by stain is a major problem. Bhushan and Hahn<sup>272</sup> have reviewed the history of stain. It is common to most types of head materials including ferrite, glass and various soft magnetic alloys (such as Permalloy, sendust and CoNbZr), and to most particulate tape types including  $\gamma$ -Fe<sub>2</sub>O<sub>3</sub>, Co- $\gamma$ Fe<sub>2</sub>O<sub>3</sub>, MP and barium ferrite. It is usually brown (characteristic “brown stain”), but may also be observed to be black, blue or even transparent in colour. It is typically inorganic in composition (usually the oxide of the magnetic pigment in the tape), but usually with some degree of polymeric component. Stain normally only forms at low humidity – below 30-45%r.h. This is generally thought to be due to stain being in dynamic equilibrium, with the greater abrasivity observed in tapes as humidity increases causing the rate of abrasive removal of stain to be greater than its rate of formation.

Staining has been described as a friction polymer<sup>273</sup> – but most chemical analysis of stain (summarised below) now show the primary constituents to be inorganic, with some, but very little organic material from the tape – dispersing agents and binder.

Sullivan's<sup>86</sup> theory of stain formation arising from extensive surface chemical analysis of stained heads states that an adhesive transfer of tape material occurs at the head-tape interface. Polymers such as those used in binder systems in magnetic tapes which are non linear and of relatively low crystallinity are known<sup>274</sup> to transfer as a discontinuous lumpy film with the lumps of material ranging from the sub-micron to a few microns in diameter. The inorganic particles filling these polymer transfer films form ion-dipole bonds with the

inorganic materials on the head surface yielding a strongly bonded stain. The ion dipole bonds may not be formed if the head surface bonds are saturated with water (occurring at around 45%r.h.), thus presenting an alternative theory for the humidity dependence of stain formation.

Sullivan's theory is backed up by surface chemical analysis of stain by a number of workers working on systems similar to those studied in this thesis. Arudi and McCracken<sup>275</sup> found stain build up on the metal part only of MIG heads in an 8mm helical scan system against MP and barium ferrite media. They found stain build up to be independent of the nature of the tape binder or lubricant. Secondary ion mass spectrometry (SIMS) and Auger electron spectroscopy were used to show that the stain consisted mainly of iron and oxygen. Reichlmaier<sup>276</sup> analysed the stain found on ferrite heads running against MP tape by TOF-SIMS and found it to consist of a smearing of iron from the tape. Stahle and Lee<sup>277</sup> investigated staining on MIG recording and ferrite playback heads in helical scan video recording systems against MP tape. They found that at a humidity of less than 30%r.h. staining was formed that resulted in a considerable reduction in head output, data reliability and head wear. The stain on the ferrite was of a spotty nature and contained both inorganic head and tape material, where as the stain formed on the MIG contained mostly inorganic material from the tape, with little organic component in either case.

Ota, Namaura and Ohmae<sup>278</sup> investigated brown stain on sendust VCR heads cycled against  $\gamma\text{-Fe}_2\text{O}_3$  tape. They found that it did not form above 45%r.h. and that the stain increases with a decrease in tape tension. TEM showed the stain to be formed from small agglomerations of small grains of  $\gamma\text{-Fe}_2\text{O}_3$  and some tape binder. Dynamic recrystallisation of copper, but not iron dummy heads, showed that the head-tape interface asperity contacts reached the temperature required to recrystallise copper: 200-500°C, and that these temperatures were responsible for the adhesive wear of the tape onto the head.

Liew et al<sup>279</sup> analysed head stain from the sliding of  $\gamma\text{-Fe}_2\text{O}_3$  tape against composite heads (ferrite with copper and nickel inserts) using FTIR spectroscopy. They saw that the stain on the metal inserts consisted of  $\text{Fe}_3\text{O}_4$ , in contrast to the  $\gamma\text{-Fe}_2\text{O}_3$  in the tape, showing a tribochemical reaction of the tape particles. They found that Ni inhibited stain formation whilst copper promoted it.

Tsuchiya and Bhushan<sup>280</sup> investigated stain build up on MIG heads with CoNbZr cores and a ferrite substrate in sliding mode in a linear tape drive against MP and Co- $\gamma$ Fe<sub>2</sub>O<sub>3</sub> tape types. The resulting stains were analysed<sup>281</sup> by EDAX, AES, FTIR, Raman, and TOF-SIMS. The stains produced by the iron oxide tape consisted of organic material, iron and oxygen – possibly Fe<sub>3</sub>O<sub>4</sub>. Those produced by the MP tape consisted mainly of Fe and O, with a small amount of organic material that was different to the tape binder. They speculated that the greater chemical activity of metal particles might be responsible for the greater relative concentration of inorganic components. They found that the thickness of the stain formed by the Co- $\gamma$ Fe<sub>2</sub>O<sub>3</sub> and the MP tape were 90 and 20nm respectively – of a similar magnitude to the particle size. They speculated that crushing of the particles during interfacial sliding may be responsible for thin stains. The greater ductility of metal particles over metal oxide particles might also contribute to the thinner films observed with MP tapes. Tsuchiya and Bhushan<sup>282</sup> also studied staining of CoNbZr MIG heads against barium ferrite, MP and ME tape in 8mm helical scan camcorders in sliding mode and Patton and Bhushan<sup>261</sup> in pause mode. The barium ferrite and MP tape produced brown stain, mainly on the MIG and the glass, but with some on the ferrite consisting mainly of tape particles. The barium ferrite produced a thicker stain layer. Micrographs of the metal surface in the MIG region of the heads generally showed a texture of scratches in the direction of the tape passage. However the micrograph for the MIG surface in a head that had been run in sliding mode against barium ferrite tape showed a texture perpendicular to the tape transport mechanism. This was not explained. The change in topography of soft metal surfaces in composite heads and its relation to stain formation is as yet an under reported, and unexplained phenomena. With the trend towards shorter recording wavelengths small dynamic changes in head-tape contact will become critical.

The ME tape produced a spotty deposit that appeared in a uniform manner over the head surface. It was found to contain PFPE molecules from the tape lubricant and cobalt and nickel from the magnetic layer. This deposit was easily removed by swabbing with solvent and was thus not considered a stain.

Patton and Bhushan<sup>283</sup> reported that stain build up on MIG heads in helical scan recorders was accelerated by lower tape tensions and head-tape contact pressures, attributed to lower abrasive wear rates by the tape allowing the build up stain.

In a private communication to Bhushan and Hahn<sup>272</sup>, Biskeborn reported that stain formed on the sendust MIG of ferrite MIG heads cycled against MP tape consisted of 90% iron oxide by AES, with no organic component by TOF-SIMS. Sputter depth Auger depth profiling showed the stain to penetrate into the sendust by up to 10nm. This was attributed to an oxidation of the iron in Sendust. However it could also be indicative of an embedding of the iron oxide particle into the Sendust layer.

The main way in which stain may be controlled with particulate media is to include a head cleaning agent (HCA) – hard particles such as Al<sub>2</sub>O<sub>3</sub> included in the binder system alongside the magnetic pigment which act to increase tape abrasivity thus preventing initial stain formation or replenishment<sup>284</sup>.

## 2.7 Pole Tip Recession (PTR)

Composite tape recording heads such as sandwich, MIG or thin film heads are liable, like all composite structures to suffer from differential wear of the materials at the contacting surface. A recession of the magnetic pole tips of a recording head relative to the tape bearing surface is undesirable as it introduces a spacing loss, and a collection point for mobile debris causing dropouts in the reproduced signal. A spacing of 10nm will cause a drop in output of 1dB at a recording wavelength of 1µm.

Possible mechanisms for differential wear include abrasive wear by the tape bending into or the highest tape asperities impinging into the softer magnetic material, abrasive or erosive wear by third bodies such as head or tape wear debris, pitting corrosion/oxidation and galvanic corrosion. PTR has been shown experimentally to vary with head material combination, tape type and abrasivity and climatic condition<sup>1,285,217</sup>.

### 2.7.1 PTR and Head Structure

Although sandwich, MIG and thin film tape heads all have slightly different structures at the tape-bearing surface, they share a number of features that suggest that mechanisms identified in one may be operative in another. In all three types the majority (typically greater than 90% by area) of the tape bearing surface is formed by a mechanically hard ceramic. The magnetic pole pieces are different in structure but share a common material set including similar magnetic thin films and spacers such as  $\text{Al}_2\text{O}_3$  and  $\text{SiO}_2$ . Broese Van Groenou and co-workers<sup>1</sup> found that with similar materials that less PTR was found with MIG heads as compared to sandwich heads, and for sandwich heads that metal core thickness and length effected PTR. However Abe, Tsuchiya, and Noro<sup>285</sup> found that for a similar material set that PTR did not vary significantly with shape.

### 2.7.2 The Relation between PTR and Magnetic Core Material

Historically Permalloy ( $\text{Ni}_{0.8}\text{Fe}_{0.2}$ ) pole pieces have been shown to be subject to pitting corrosion at high humidity or in corrosive atmospheres (e.g. 10ppb  $\text{Cl}_2$ , 10ppb  $\text{H}_2\text{S}$ , 100ppb  $\text{SO}_2$  and 200ppb  $\text{NO}_2$ ) where preferential oxidation of the Fe to antiferromagnetic  $\alpha\text{-Fe}_2\text{O}_3$  has been shown to occur<sup>286,287,288</sup>.

Broese Van Groenou et al<sup>1</sup> found that sandwiches of easily corroding magnetic metals such as  $\text{CoFeSiB}$  produced oscillating PTR values with time that they attributed to a cyclic build up and subsequent delamination of corroded metal. The time period of this oscillation was found to shorten with an increase of humidity from 60 to 80%r.h. Other sputtered soft magnetic films such as  $\text{CoNbZr}$  and  $\text{FeAlSi}$  (Sendust) when used as sandwiches showed this effect but to a lesser extent and with poorer humidity dependence. Thus other mechanisms may be contributing to the PTR. They found that for thicker ( $>35\mu\text{m}$ ) sandwiched soft metals such as  $\text{NiFe}$ ,  $\text{CuZn}$  or  $\text{Zn}$ , third bodies, identified by EDAX as emanating from the tape, could be seen embedded in the metal. Thus identifying three body erosion or abrasion by the tape debris as a possible mechanism for PTR.

Tsuchiya and Bhushan<sup>280</sup> compared three different sputtered soft magnetic films as the core in single crystal Mn-Zn ferrite heads. These were  $\text{CoNbZr}$ ,  $\text{CoTaZr}$  and  $\text{FeTaC}$ . They

all behaved in a similar fashion reaching equilibrium PTR values that showed a greater dependence on the tape type – iron oxide or MP rather than on the metal. For all three metals stain build up was observed and the equilibrium PTR will be connected to the build up of this stain.

### 2.7.3 The Relationship between PTR and Substrate and Metal Core Combination

Broese Van Groenou et al plotted PTR vs. substrate wear rate for a number of substrate and core metal combinations for both MIG and sandwich heads and found that PTR tends to zero as the wear rate of the substrate increases. Thus for a particular magnetic material a substrate can be chosen to minimise PTR. Matsuura and Uchizawa<sup>289</sup> investigated a number of possible ceramic substrate and thin film core materials for thin film heads in sliding against ME tape. They again concluded that the wear rate of the metal in the sandwich, the wear rate of the ceramic and any other component, such as insulating layers should be closely matched to ensure a low equilibrium PTR and a short time to that value. They identified that the magnetic material CoNbZr was closely matched to CaTiO<sub>3</sub>, with Al<sub>2</sub>O<sub>3</sub> as a closely matched insulating material.

Patton and Bhushan<sup>290</sup> investigated the wear of thin film heads for linear tape systems against MP tape. These heads employed an Al<sub>2</sub>O<sub>3</sub>-TiC substrate, Al<sub>2</sub>O<sub>3</sub> spacer elements and a choice of NiFe, CoTaZr or FeAlSi magnetic thin films. All these materials were characterised for hardness and scratch resistance by nanoindentation. The Al<sub>2</sub>O<sub>3</sub>-TiC had superior hardness and scratch resistance, and all measured wear was relative to this. NiFe and CoTaZr, although they were of roughly equal hardness to the Al<sub>2</sub>O<sub>3</sub> spacer elements, had a lower scratch resistance and wore relative to the Al<sub>2</sub>O<sub>3</sub>. The scratch resistance of FeAlN was roughly equal to the Al<sub>2</sub>O<sub>3</sub> spacer elements, but it had a higher hardness and the Al<sub>2</sub>O<sub>3</sub> spacer elements were found to wear more than the FeAlN thin film. In both cases the preferentially wearing material reached an equilibrium wear depth as compared to the substrate, and the lower wearing material then wore at a faster rate until it too had reached an equilibrium wear depth relative to the substrate. This wear sequence was found to repeat itself cyclically as the substrate wore. The superior wear resistance of one material over another when either one of scratch resistance or hardness of both materials were equal and the other property was superior shows the equal contribution of abrasion and deeper ploughing to the wear of these materials. The cyclic nature of the wear within

the low overall wear depth relative to the substrate (<30nm) suggests that tape asperity contact was dominating both the abrasion and ploughing – third body ploughing would tend to wear both the Al<sub>2</sub>O<sub>3</sub> spacer and magnetic layer concurrently.

#### 2.7.4 The Relationship between Tape Type and PTR

The ordering of the amount of PTR caused by different tape types in streaming mode is generally found to fall in the opposite order to their abrasivity.

Broese Van Groenou et al compared PTR caused by streaming rough, thick lapping tapes (Al<sub>2</sub>O<sub>3</sub>: R<sub>a</sub> = 130nm, thickness = 22μm and CrO<sub>2</sub>: R<sub>a</sub> = 7nm, thickness = 18μm) to thin, smooth MP and ME tapes (R<sub>a</sub> ~5nm, thickness = 12-13μm). They used sandwich heads composed of a glass ceramic substrate with a thin (<10nm) NiFe, FeSiAl or FeSiAlN magnetic core into which they calculated that the tapes could not bend into. They found that with the highly abrasive lapping tapes PTR was small (<10nm), but in the order of tens of nm (35-85nm) with magnetic tape. When they employed a wider magnetic core (35-100μm) they observed particles to be embedded in the core that were identified by EDAX as originating from the tape.

Tsuchiya, Abe, Noro and Inada<sup>217</sup> in comparing PTR in MIG heads employed in 8mm helical scan video recorders found that Hi-8ME produced the greatest PTR, followed by Hi-8MP, with lapping tape producing the least amount of PTR. A loss in playback signal amplitude was observed with the increase in PTR, indicating that the tape doesn't conform to the recessed poles. Patton and Bhushan<sup>283</sup> found similar results for the relationship between output drop and PTR. In comparing PTR produced in CoNbZr MIG heads streaming in an 8mm helical scan recorder by ME and MP, barium ferrite and lapping particulate tapes they found that the ME tape produced twice the PTR as the other tapes which all produced roughly the same equilibrium PTR. Interestingly, in performing similar experiments, but operating the recorder in pause mode in which the drum is rotating, but the tape is stationary, they<sup>261</sup> found that PTR did not change from its initial value. This was thought to be due either to the fact that tape was stationary and that absolute rather than relative tape motion is necessary for PTR propagation, or that pause mode generates

greater amounts of debris, or that the large amounts of media reuse lowers the tape abrasivity.

Tsuchiya and Bhushan<sup>282</sup> compared PTR in MIG heads of single crystal Mn-Zn ferrite with CoNbZr core with streaming against MP, barium ferrite (Ba-Fe) and ME tapes in a helical scan 8mm camcorder. They found that for each tape type core recession was matched by a decrease in the playback signal amplitude, again indicating that the tape is not conforming to the recessed pole pieces. The recession was seen to grow more rapidly over the first ten hours of streaming before slowing down to an approximately constant level over the next 20 hours. The recession was greatest (about 60nm), and still growing after 30 hours in the case of the ME tape. The MP and the Ba-Fe tape types produced similar PTR values (30nm) that were roughly half those produced by ME. All three tapes exhibited similar surface RMS roughnesses before and after cycling (8-11nm).

Tsuchiya and Bhushan<sup>280</sup> went on to compare Co- $\gamma$ -Fe<sub>2</sub>O<sub>3</sub> and MP tapes. Three different pole materials were used in the magnetic core of the single crystal Mn-Zn MIG heads. All three materials behaved identically towards the two different tape types as discussed in Section 2.6.x. Again the PTR was shown to develop towards an equilibrium value with an increasing number of passes. Where the initial PTR was greater than the equilibrium level the PTR was observed to fall to this level. The equilibrium PTR values for the oxide tapes were typically 5-10nm lower than those values observed for the MP tapes (where PTR was in the order of 40nm). Both tape types contained Al<sub>2</sub>O<sub>3</sub> head cleaning agents. The substrate and total thickness of the oxide tape (15 $\mu$ m and 18 $\mu$ m respectively) were greater than those of the MP tape (10 $\mu$ m and 13 $\mu$ m). The RMS roughness was greater for the oxide tape (10nm vs. 6nm). The real area of contact of these tapes was measured by pressing them pneumatically against a glass slide containing a recessed grid of similar dimensions to those observed in the MIG heads under typical head-tape contact pressures. The density of contact spots of the tape on the glass slides was measured. They found that the real area of contact of the tape was less, but not zero in the recessed areas, and that the contact in the recessed areas was greater for the oxide tape. As greater PTR was found however for the less intrusive and smoother MP tape they concluded that the mechanism for PTR development was not based neither upon the tape bending into the recess, nor on the penetration of the highest tape asperities. They speculated that the main cause of the PTR



is abrasion by third bodies, head and tape debris, caught between the relative motion of the head and the tape. That the debris produced by ME tape at the MIG head-tape interface in their earlier work was loose rather than adhesive, as opposed to the stain generated by the particulate tapes was seen as a reason for the greater PTR created by ME tape.

### 2.7.5 Modelling of PTR and the Action of Alternative Mechanisms

Abe, Tsuchiya and Noro<sup>285</sup>, and Tsuchiya, Abe, Noro and Inada<sup>217</sup> measured differential wear (PTR) in dual material dummy heads, MIG heads and sandwich heads. They found that in general PTR was independent of head structure and head-tape pressure, but was related to the tape and the relative wear rates of the two materials. Experimentally they found the value of PTR increased with running distance against tape until an equilibrium value (as described by a number of authors – see above),  $\Delta d$ , was reached.  $\Delta d$  was found to be proportional to the natural log of the ratio of the isolated wear rate of the recessed component ( $k_2$ ) to the isolated wear rate of the proud component ( $k_1$ ). The constant of proportionality,  $C$ , is dependent upon the tape – a diagram of the system is shown in Figure 2.10. and the equation is given in Equation 2.26:

$$\text{PTR} = C \ln (k_2/k_1)$$

Equation 2.26

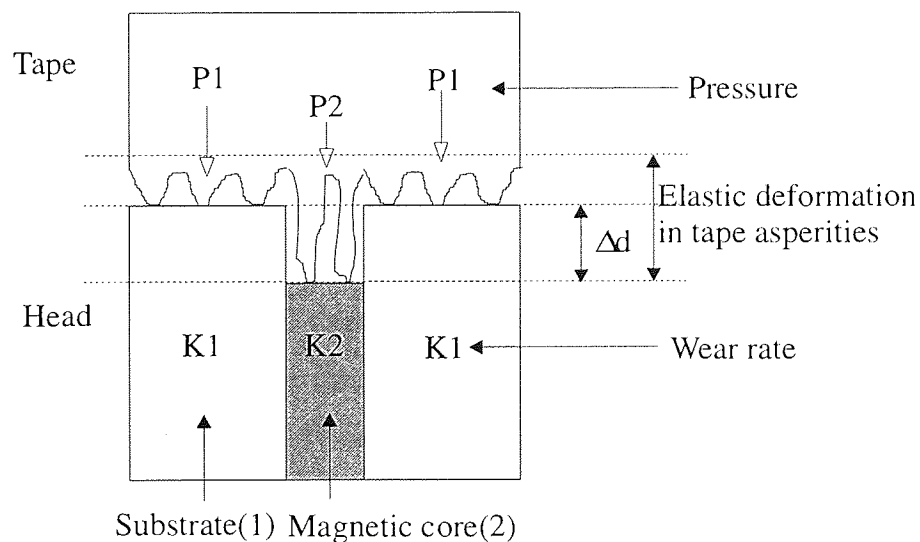


**Figure 2.10 Diagram of Head-Tape Contact used in the PTR Model of Abe, Tsuchiya and Noro**

They assumed that with a linear, Archard type relation between pressure and wear rate as the recession grew the contact pressure of the tape on the recessed area would fall until the

wear of the two materials and hence PTR would reach an equilibrium. If  $p_1$  and  $p_2$  are the head-tape contact pressures on the proud and recessed components respectively, then the condition for this equilibrium is given in Equation 2.27:

$$k_1 p_1 = k_2 p_2 \quad \text{Equation 2.27}$$

From Equation 2.26, and defining  $\Delta p = p_1 - p_2$ :

$$p_2/p_1 = \exp(-\Delta d/C) \quad \text{Equation 2.28}$$

$$\Delta p/p = \exp(\Delta d/C) - 1 \quad \text{Equation 2.29}$$

If  $\Delta d$  represents some elastic compression of the tape asperities  $x$ , then following from Equation 2.29, the head tape contact pressure  $p$  is shown by Equation 2.30:

$$P \propto \exp(x/C) \quad (x/C \gg 1) \quad \text{Equation 2.30}$$

This shows the elastic nature of the tape surface to follow an exponential rather than a simple linear Hooke's law behaviour. Thus the coefficient  $C$  is representative of the micro-elastic behaviour of the asperities of the tape in question.

Abe, Tsuchiya and Noro explain the non-linearity of the elastic compression as due to a change in the real area of contact of the head and tape asperities as they are brought together. This model is supported by the model, supported by experimental evidence, of tape asperity compliance given by Wang et al as discussed in Section 2.1.3.3. This shows the pressure dependence of tape asperity compliance to be non-linear, as shown in Equation 2.18. Thus Wang et al's result that the asperities of ME media are stiffer than those in particulate media may be used to explain, via a tape asperity intrusion mechanism, the greater value of equilibrium PTR observed in ME over particulate tapes, despite the lower static roughnesses observed for ME media.

Van Groenou et al also used the Archard equality given in Equation 2.27 to derive similar expressions for equilibrium PTR based on the ratio of wear coefficients of the two materials. They assumed however that the contact pressure would fall linearly with  $\Delta d$ , and

did not take into account tape asperity compliance. This was because they were observing PTR values that were larger than could be accounted for by tape asperity height distributions, without a gross bending in of the tape into the recess, which they calculated as impossible. And on occasions they were also seeing non-equilibrium PTR propagation. These observations however do not necessarily confound the tape asperity impingement model, but point the finger at additional mechanisms, summarised in the preceding sections that have been shown to contribute to PTR propagation. Mechanisms such as corrosion, third body wear and the competing process of stain build up, which has been shown to occur preferentially on the magnetic pole pieces. It was the potential operation of chemical and third-body wear mechanisms on the ceramic and magnetic materials used in sandwich heads identified by the work of Broese van Groenou and co-workers that prompted this investigation.

## Chapter 3 - Experimental

### 3.1 Introduction

The experimental work falls into two categories –

*The Cycling Tests* in which video heads are cycled in recorders against Metal Evaporated (ME) and Metal Particulate (MP) tapes under controlled climatic conditions. Two classes of head were studied – Dummy Heads, the tape-bearing surface of which consisted of a single material and Sandwich Heads, which were functional read-write heads (though not used to read or write a signal in this work). During the course of the cycling experiments, the wear rate of the head was measured by the Indentation Method and Pole Tip Recession (PTR) was measured in the Sandwich heads by AFM. The procedure and apparatus used in the cycling tests are described in Section 3.2.

*Surface Analysis by XPS and AFM.* XPS was used to investigate surface chemical changes of the single material dummy heads as a result of the cycling. The smallest spot size available for XPS analysis was 150 $\mu\text{m}$  in diameter. It thus could not be used to investigate the surface chemistry of the individual materials within the Sandwich Head in which the magnetic track was 32  $\mu\text{m}$  or less in width, itself being composed of 1-2 $\mu\text{m}$  width laminations. AFM was used to investigate the topography of both Dummy and Sandwich Heads, and to measure PTR in the case of Sandwich Heads. These techniques are described in Section 3.3 with particular emphasise on the data processing techniques employed to obtain the results presented in Chapter 4.

## 3.2 Cycling Tests

### 3.2.1 Heads, Tapes and Recorders

The Dummy and Sandwich Heads were manufactured by Philips. Five materials were studied as single material dummy heads. There were two sintered ceramic substrates:  $\text{CaTiO}_3$  and a composite consisting of  $\text{CaTiO}_3$ ,  $\text{ZrTiO}_4$  and  $\text{TiO}_2$ . They are denominated in this thesis as S1 and S2 respectively. And three soft magnetic metals: Amorphous CoNbZr and nanocrystalline FeNbSiN and FeTaN, denominated as M1, M2 and M3 respectively. The metals dummy heads were prepared by sputter depositing a thin ( $3\mu\text{m}$ ) film of the metal on a profiled ceramic dummy head. The sandwich heads studied contained an S2 substrate with M3 magnetic layers,  $\text{Si}_3\text{N}_4$  insulation layers, and a Mo-Au bonding layer.

These heads were cycled against commercially available ME and MP tapes in commercially available Philips M870 Hi-8 recorders to reproduce and measure the tribology encountered during actual operation of these devices. Three different ME and three different types of MP tape were used (ME1, ME2, ME3, MP1, MP2 and MP3) they are listed in Table 4.1 of Section 4.1 together with an AFM analysis of their topography and roughnesses before and after cycling.

### 3.2.2 Running In

In Section 2.4.1.2 the running-in process was described. The purpose of the run in is to establish an equilibrium head-tape profile for the tape type and climate (temperature and humidity) of interest. A rough head profile was achieved by passing a highly abrasive lapping tape over the head. The equilibrium profile was then established by cycling with the desired tape/climate/recorder combination. The running in procedures for the climate and tape types used are described in section 4.2.2. Ceramic and Sandwich Heads were ran in at Philips prior to delivery. Further running in prior to cycling at low humidity (see below) was conducted at Aston University. The metal-coated heads were not run in after deposition due to the limited amount of metal on the surface.

### 3.2.3 Climate, Head Material and Tape Combinations Selected for Cycling Tests

For each climate and material selected two heads of that material selected were cycled against ME and two against MP Tape. High humidity ( $\geq 80\%$ ) was of interest because of the possibility of corrosion. All 5 Dummy Head materials and the Sandwich Heads were cycled at high humidity and ambient laboratory temperature ( $20^{\circ}$ - $25^{\circ}$ C). For comparison heads were also cycled at high humidity at an elevated temperature:  $60^{\circ}$ C-M1,  $40^{\circ}$ C-S1 and S2, and  $30^{\circ}$ C-Sandwich Heads; and some at low humidity (20%) and  $25^{\circ}$ C: S1, S2 and Sandwich (Sandwich ME tape only). The full list of cycling experiments done (conditions and results) is presented in Section 4.2 for the Dummy Heads and Section 4.5 for the Sandwich Heads.

### 3.2.4 Cycling Test Procedure

Figure 3.1 contains a flow diagram showing the stages taken during the cycling tests. In the following sections the apparatus and procedures followed in the individual stages are described. The heads were usually examined at 10, 50 and 100 hours and at intervals of 50 or 100 hours thereafter. Exceptions include where the cycling stops due to a temporary fault (see Section 3.5 for fault reporting and recovery) or where experience led to the expected wear rate to be very small (longer time between examinations) or very large (shorter time between examinations). The cycling experiments were stopped in the case of the Dummy Heads when the indentations made to measure the wear rate were almost worn away and where PTR was found to reach an equilibrium level in the case of Sandwich Heads.

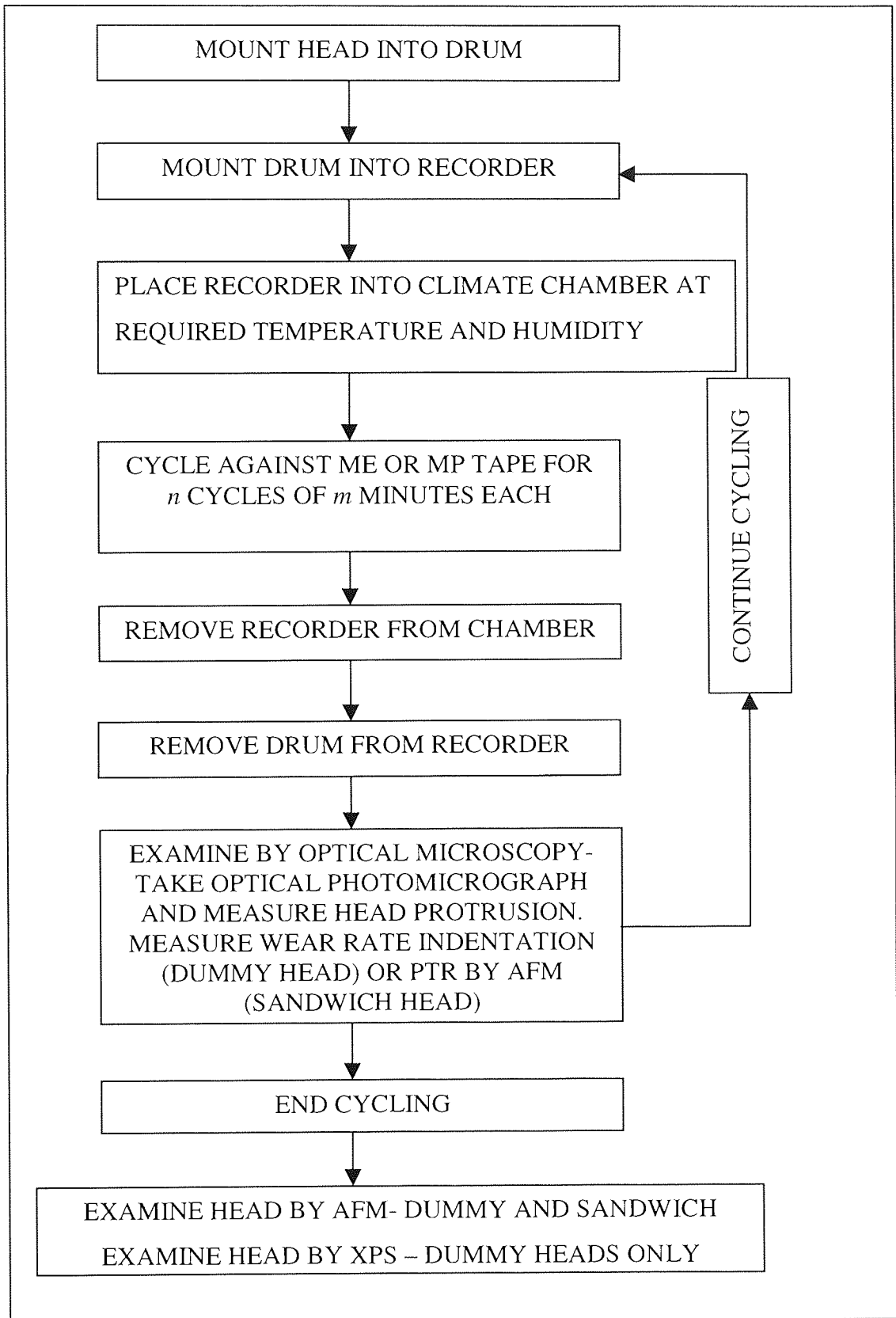


Figure 3.1 Flow Chart Showing the Steps Involved in Conducting Cycling Tests of Sandwich and dummy Heads

### 3.2.5 Cycling Apparatus

The equipment for cycling of the heads was provided by Philips. It consisted of modified drums and recorders and a computer control system. The external air-bearing surface of the drums were identical to those used in commercial systems, however internally the drums were designed so that heads may easily be replaced with user control of the setting of the head protrusion from the drum surface. The equipment and procedure for mounting a head in the drum are described in Section 3.2.6. The cycling tests were conducted in Philips M870 Hi-8 Camcorders modified to allow computer control of the play and rewind functions allowing automated cycling of the tape. The computer control was provided via an A/D board by an Apple II computer for up to 4 recorders simultaneously. This ran a simple Fortran programme that allowed for the length (in minutes) and number of cycles to be set for each recorder. It operated a simple fault detection system that sampled each recorder in play mode every 30 seconds. If the recorder was found to be no longer playing a fault was registered and the cycling countdown stopped. After rectification of the problem the countdown could be continued.

Two different types of events were found to lead to the recorder stopping during play – the potential for water condensation within the recorder and tape damage. The former was detected by a conductance humidity meter standard on most rotary tape recorder systems that acts to return the tape from the recorder mechanism to cassette. Water condensation can cause stiction between the tape and the head or tape transfer mechanism causing severe wear to either or both. Condensation was an occasional hazard running cycling tests at 90%r.h. After such shut down the recorder could be restarted by resetting the power supply to the recorder and providing that the humidity detector was no longer saturated and that the tape was not damaged. Tape damage that led to an increase friction between the tape and the tape transfer mechanism or to the tape becoming entrapped within the mechanism or to increased tape tension resulted in an increased load to the drive motor which was detected and caused the recorder to be halted and the tape to be returned to its cassette. This was an occasional occurrence after long extended cycling and after which the cycling must be abandoned at that point. Thus accounting for the variation in cycling times observed in the results.



Two different methods of climate control were used. For the early experiments a simple Environmental Chamber constructed at Aston University was used and which is shown schematically in Figure 3.2. This consisted of a ventilated Perspex box into which the recorders were placed. It operated at ambient laboratory temperature (20-25°C) with high humidity produced in the box by a supply of air provided by a compressor that was saturated with water by passing through a column of water before being introduced into the box. A humidity of 90±5%r.h. was produced within the box. Temperature and humidity were monitored with an electronic combined thermometer and hygrometer.

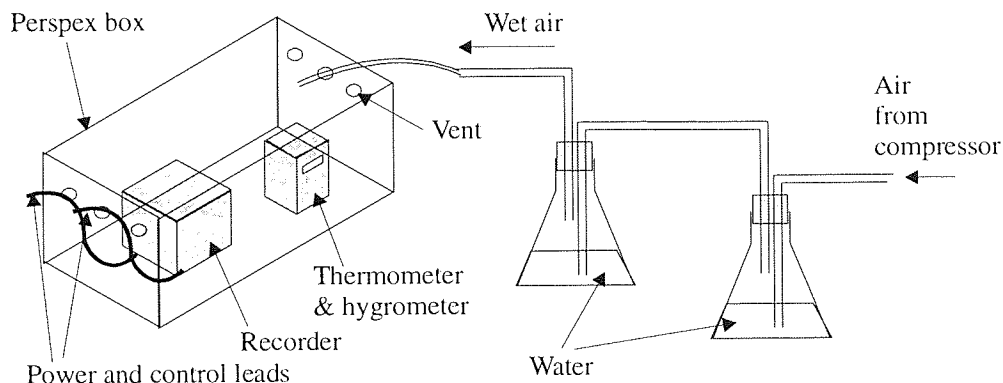


**Figure 3.2 Schematic of Simple Environmental Chamber for High Humidity Cycling Tests at Room Temperature**

The apparatus used for generating humid air shown in Figure 3.2 was superseded by a pair of commercial Heraeus Votsch VLK 04/300 Environmental Chambers for use in later experiments. These allowed independent temperature and humidity control, with ranges of -40 to 180°C ( $\pm 1^\circ\text{C}$ ) and (between 10 and 90°C) 10-95 %r.h. respectively. The commercial chambers were used for all the experiments conducted at room temperature and low humidity (25°C/20%r.h.), and all those at 40°C/60°C and 80%r.h. Of the remaining experiments conducted at room temperature and high humidity those quoted as being conducted at 80%r.h. were done so in the commercial chamber and those at 90%r.h. in the “home made”.

### 3.2.6 Head Mounting and Measuring Head Protrusion, and Subsequent Optical Monitoring of the Head during Cycling

Two heads of the same material type were mounted per drum except in the case of S1 and S2 heads cycled at 40°C/80%r.h. and at 25°C/20%r.h. in which case two S1 and two S2 heads were mounted per drum. The heads were placed in their respective sockets in the drum. If two heads were to be mounted in the drum then they were placed opposite each other so as to maintain balance as the drum was rotated in the recorder. The tip of the head was levelled by eye with the edge of the drum and the holding screw loosely tightened. A diagram of two heads thus mounted into a drum is shown in Figure 3.3. The axis of rotation of the drum in the recorder is shown. An axle could be attached as shown in Figure 3 which enabled the drum to be mounted upon the microscope stage or the AFM/Indentation mount (see later) with free rotation of the drum about this axis.

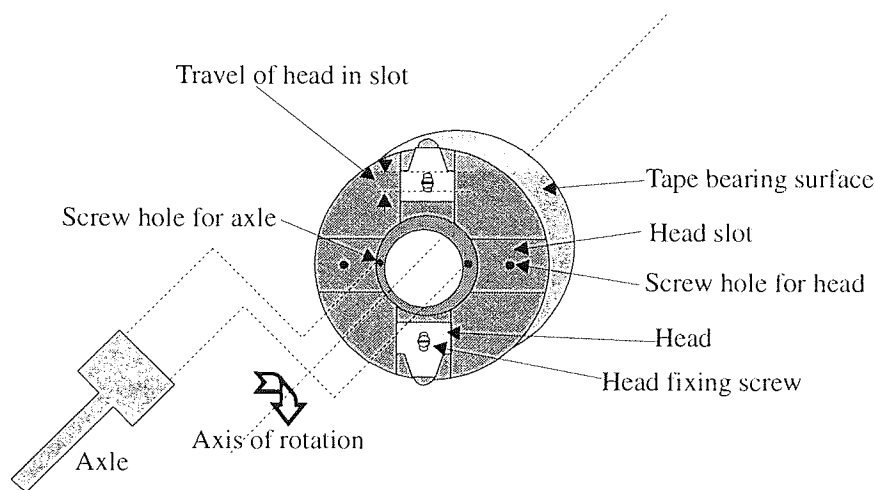


**Figure 3.3 Diagram Showing Placement of Heads in Drum. Drum Diameter 40mm.**

The attachment of the drum to the microscope stage is shown schematically in Figure 3.4. The microscope used was an Olympus Model BHC. The drum was free to rotate in a slot in the stage and the axle could be stopped if necessary. The vertical displacement of the microscope stage was measured by means of a Solatron Metrology DG 2.5 LVDT (Linear Variable Differential Transformer). This produced an output voltage that was proportional to displacement giving a reading on a digital voltmeter to 0.1µm. Thus mounted the head protrusion could be fixed and measured. During the subsequent cycling experiments, the drum was again mounted like this to examine the head surface optically, using the 35mm

camera to make photomicrographs where necessary, and to measure protrusion and the width of the microhardness indentations used to measure the wear rate (see Section 3.2.7).

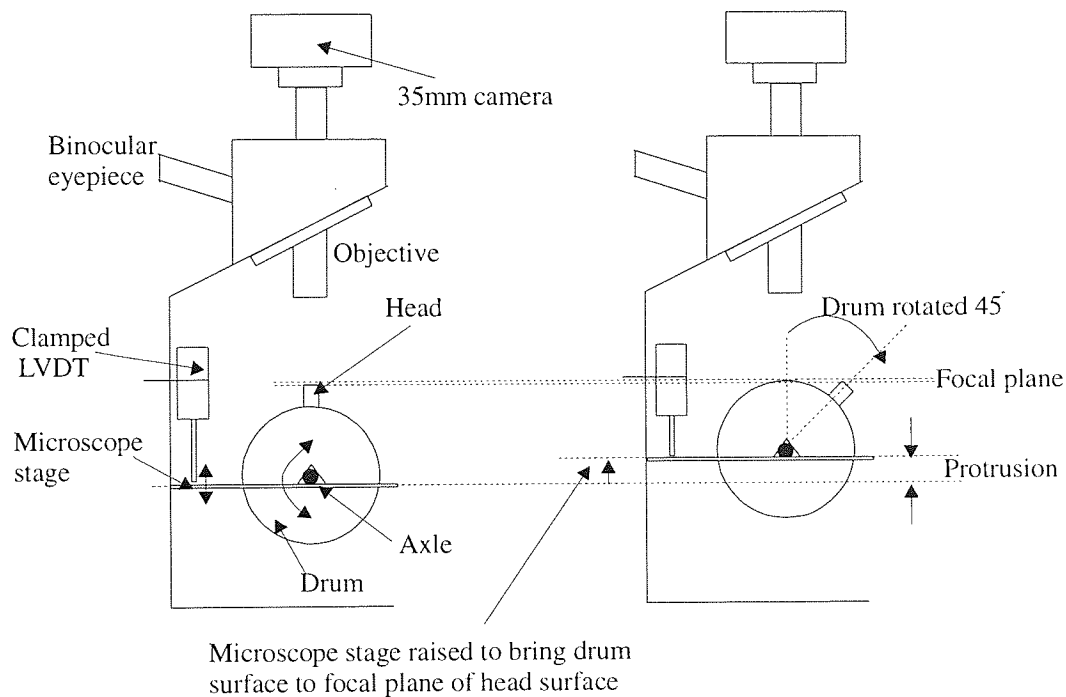


**Figure 3.4 Mounting of the Drum on the Microscope for Optical Inspection and to Measure and Fix Head Protrusion from the Drum Surface**

The protrusion of the head could be found by measuring the difference in height between the focal plane of the head surface and the drum surface, as shown in Figure 3.4. The head surface was brought into focus and the height of the microscope stage noted. The drum was then rotated  $45^\circ$ , and the highest point of the drum surface brought into focus by raising the stage and its new height was noted. The change in height of the stage was thus the protrusion of the head above the drum. All protrusion measurements quoted are from the average of three such measurements.

To fix the protrusion of the head on first mounting the height of the drum was found as above and the drum rotated back  $45^\circ$  to bring the head under the microscope objective. The height of the stage was then set so that the head surface would be in focus 25-30 $\mu\text{m}$  above the level of the drum. The head was then moved upwards in its slot until the head surface came into focus at the desired level, and thus had a protrusion of 25-30 $\mu\text{m}$  above the drum surface. In case of overshoot the head was lowered a little into the drum and the process repeated until the desired protrusion had been achieved. The head fixing screw was then

tightened and the protrusion re-measured as above to give the starting protrusion. The tightening process occasionally caused a slight change in the protrusion this was accepted if protrusion remained within the range of 20-35 $\mu\text{m}$ .

The main error in the protrusion measurement came from the finite focal depth of the lens combination employed. This consisted of X15 binocular eyepieces (Olympus BiWF15) and a Planer Achromatic X40 objective - Numerical Aperture (N.A.) 0.65, Focal Length 4.38mm. The stated<sup>291</sup> focal depth with the Aperture Iris Diaphragm open to the full N.A. (0.65) was 2.37 $\mu\text{m}$ . With this aperture fully open (1) a focal depth of about 1 $\mu\text{m}$  was measured using the LVDT (with an error of  $\pm 0.1\mu\text{m}$ ). Thus the error in each protrusion reading was  $\pm 2\mu\text{m}$  due to finite depth of focus. Further errors may have been due to mechanical relaxation in the microscope and mount during measurement.

### 3.2.7 Measuring Wear Rates Using the Microhardness Indentation Method

The geometry of the Knoop microhardness indentation is shown in Figure 3.5. The depth of the indentation is 1/30.5 the length of the long diagonal of the indentation. Thus the depth of the indentation may be measured by measuring the length of the long diagonal. The depth of a Knoop microhardness indentation made in the surface of a head will decrease as the head surface is worn, thus a measurement of indentation diagonal length with time will yield a wear rate in terms of depth of surface removed per unit time.

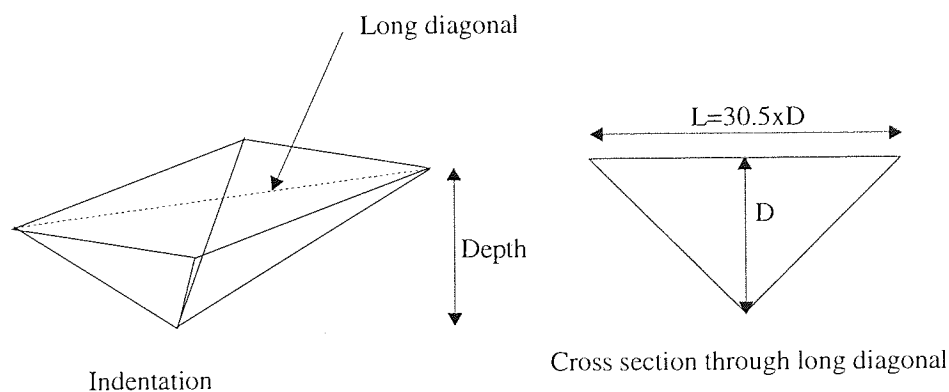


**Figure 3.5 Geometry of the Knoop Microhardness Indentation**

The Knoop microhardness indentations were made using a Buehler Micromet4 Indentor. The indentations were placed in the Dummy Heads as shown in Figure 3.6 after running in. The long diagonal of the indentation was placed perpendicular to the direction of tape travel so as to avoid scratching in the surface parallel to the direction of tape travel extending the length of the indentation<sup>284</sup>. They were made along the centre line of the head from the leading to the trailing edge at 50 $\mu\text{m}$  intervals. At less than 50 $\mu\text{m}$  intervals it was found that the cracking of the surface could occur. An indenter force of 50g was applied with a dwell time of 15s. This gave indentations in both the metals and the ceramics that were about 30 $\mu\text{m}$  in length and 1 $\mu\text{m}$  in depth, equivalent to a Knoop Microhardness of 1000Kgmm<sup>-2</sup>. The size of the indentations were constrained by the curvature of the heads. The long diagonals of the indentations were measured with the drum mounted in the microscope as shown in Section 3.2.6. using an eyepiece graticule giving a depth resolution of  $\pm 0.1\mu\text{m}$ . The resultant error in the wear rate data is discussed in Section 4.2.3.

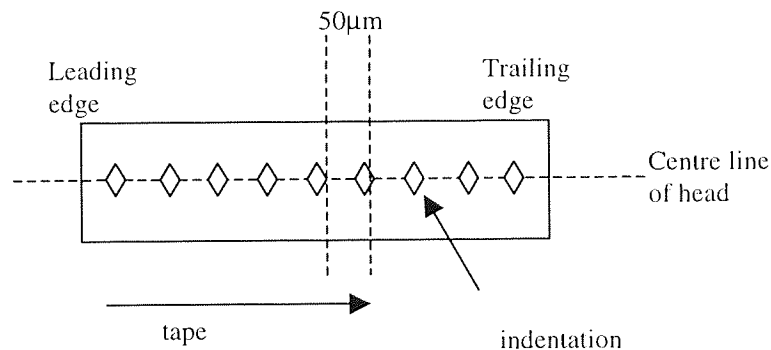


**Figure 3.6 Microhardness Indentations Made in Dummy Head Surfaces**

The microhardness indentation technique has been used by a number of workers<sup>284,68,292,248</sup> to measure head wear rate. However, ultimate depth resolution has been identified as a major drawback of the technique- it is in the order of  $\pm 30\text{-}50\text{nm}$ . They employed nano-scratches instead, with depth changes measured by AFM. This is less obtrusive upon the head-tape interface and allows a much greater depth resolution ( $\pm 2\text{nm}$ ). The implication of low depth resolution for the microindentations is fairly long experiment times for the

cycling tests. This may be troublesome, when, in the cases of the lightest wear regimes, no measurable wear may be observed over the cycling lifetime of the tape.

### 3.3 Surface Analytical Techniques

#### 3.3.1 X-ray Photoelectron Spectroscopy (XPS)

##### 3.3.1.1 Experimental Set Up

XPS is a well established<sup>293,294</sup> ultra high vacuum (UHV) technique for the chemical analysis of the top few atomic layers of a surface. The instrument used to analyse the chemical state of dummy head and reference samples was a VG ESCALAB 200D spectrometer. The instrument was controlled via a PC operating the ECLIPSE software. A Mg K $\alpha$  x-ray source at 1253.6eV was employed. The smallest available (150 $\mu$ m diameter) slit was placed in front of the analyser entry to restrict the photoelectron collection area to the head surface only. Secondary electrons were detected by a concentric hemispherical analyser operating in fixed analyser transmission (FAT) mode, with a pass energy of 50eV for survey scans and 20eV for single element scans. A lower pass energy gives a lower signal intensity, but a greater resolution. Multiple scans were used to increase the signal to noise ratio of the collected spectrum. An ion gun attached to the vacuum chamber could be used to focus and raster an argon ion beam of up to 5KeV onto the surface sample and was used to clean samples with excessive carbonaceous surface contamination, and for sputter depth profiling.

##### 3.3.1.2 XPS Data analysis

###### 3.3.1.2.1 Peak Identification and Charge Referencing

Chemical states were determined from measured binding energy levels by comparing experimental values of chemical shift with those existing on standard databases: the NIST databases versions 1.0<sup>295</sup> and 2.0<sup>296</sup> and the Handbook of Photoelectron Spectroscopy<sup>297</sup>. Initial evaluation would be made from a wide scan survey spectra (covering 1000-0eV binding energy scale). From this contaminant peaks could be identified, and peaks of

elements of interest selected for closer analysis. This further data was collected as a series of narrow elemental scan regions. The photoelectron peaks, of each particular element, chosen for further analysis, were those for which most information existed in the databases used, unless they conflicted, and were obscured by the spectra of other elements present, in which case another prominent peak was selected.

Before a peak binding energy could be assigned to a particular chemical state the spectra was be corrected for peak shifting due to a build up of charge on the sample surface as a result of photoionisation. Photoionisation may cause a build up of (positive) charge of up to 1KeV on the surface of insulators. However, the emission of low energy electrons from the Al window of the X-ray source gives at least partial charge neutralisation, and even for insulators the resultant charge shift is observed only to be of the order of a few eV. As chemical shift is also usually of the order of a few eV peak shift due to sample charging needs to be addressed. Siegbahn et al<sup>298</sup> suggested using the C 1s peak as a reference peak, the position of which can be used to determine the amount of charge shifting as atmospheric hydrocarbon contamination of sample surfaces is almost universal and unavoidable. This consists mainly of aliphatic hydrocarbons, in which the carbon atoms predominantly exist as CH<sub>2</sub> (methylene) groups bonded to each other and hence of common chemical shift. However Swift<sup>299</sup> found a range of values (284.6-285.2eV) for C 1s peaks in contamination layers compared to an Au 4f<sub>7/2</sub> standard. Even so the C 1s standard has gained widespread acceptance, and is used in the main XPS data base used in this research (NIST 1.0<sup>295</sup>) with the value of 284.6eV and was used with caution. Care was taken to ensure that the correct component of the C 1s spectra was used for charge referencing, where more than one chemical state of C was observed, that differential charging effects were not occurring, and that spectra are referenced to the same binding energy value of C 1s.

#### 3.3.1.2.2 Background Subtraction

The photoelectron spectrum is subject to a rising background with increasing binding energy due to an increase in low energy electrons resulting from inelastic loss processes. Shake-up, shake-off, and multiplet splitting of that peak may further complicate its background. The background must be removed to enable quantification, or for curve fitting. The simplest method is a straight line, drawn between the starting and finishing

points of the peak. More sophisticated is the Shirley<sup>300</sup> background subtraction, in which the background intensity of a point is determined by an iterative analysis to be proportional to the intensity of the total peak area above the background, and to higher energy. It assumes that each unscattered electron is associated with a flat background of losses. The Eclipse software allows either method to be employed and Shirley was usually chosen as it is generally the more accurate<sup>301</sup>. Tougaard<sup>302</sup> has provided an improved algorithm for the fitting of background to XPS peaks. But it can be used only when the background to the low binding energy side of the peak can be determined in the absence of any other peaks, and is thus not generally applicable.

#### 3.3.1.2.3 Data Smoothing

XPS spectra displayed in this thesis are almost all smoothed. This is mainly for cosmetic reasons, though it may make identification of the peak centre energy easier, and enhance features, such as shoulders. In general, however, the minimal amount of smoothing was carried out, so as to avoid possible peak distortion. The method used for curve smoothing is based on that of Savitsky and Golay<sup>303</sup>, who developed a convolution algorithm for smoothing data. Their method leads to loss of data points and allows only one pass. So that due to Proctor and Sherwood<sup>304</sup> with a quadratic/quintic polynomial is used on the Eclipse software.

#### 3.3.1.2.4 Quantification

After a peak of element A had been defined and the background subtracted, its area could be found by integration. This was normalised by dividing by the relevant transmission function (TF) and atomic sensitivity factor (ASF):

$$\text{Normalised area} = \text{peak area} / (\text{TF} \times \text{ASF}) \quad \text{Equation 3.1}$$

The atomic percentage of the element represented by this peak is given by the ratio of its normalised area to the sum of the normalised areas.

Tabulated Schofield<sup>305</sup> ASF values were used as these were found to be more representative of the measured asf values on the instrument used, than those of Wagner<sup>297</sup>,



which were measured on a different make of instrument (Phi). Where Schofield values have been found to be inadequate, they have been replaced by those measured on this instrument<sup>306</sup>. The transmission function is representative of the sensitivity of the instrument to electrons of that energy in that analyser mode, and is set by a manufacturer's calibration.

#### 3.3.1.2.5 Peak Fitting

An XPS peak may consist of several components corresponding to different chemical states of the same element, or two or more elements of similar binding energy. In such cases several curves can be fitted to the peak, simulating the individual components. An infinite number of curves may be fitted to a peak, but knowledge of the chemical shifts of the components, of the shape of photoelectron peaks, and clues such as shoulders apparent on the peak allow fitting with some confidence.

For each curve to be fitted four parameters were required: (1) centre energy, (2) height, (3) FWHM, and (4) Gaussian/Lorentzian mix. These were changed by the fitting algorithm, as described below, to achieve the fit. Initial values were set to roughly agree to the peak to be fitted. (4) Describes the shape of the photoelectron peak. The basic shape is mainly Lorentzian, due to the photoionisation process, with a Gaussian component due to instrumental broadening. The Gaussian/Lorentzian mix was fixed to 30%, as this was found to give the best fit for the instrument used<sup>307</sup>.

The fitting method used was the Nelder and Mead Simplex<sup>308</sup>. It works iteratively to minimise the  $\chi^2$  deviation of the simulated curve from the original datapoints. The routine was ended after a preset number of iterations, or after the convergence of  $\chi^2$  between successive iterations had reached a preset level.

#### 3.3.1.3 Sputter Depth Profiling

A depth profile could be built up by analysis after removing successive surface layers by sputtering (etching) with argon ions. This supplied data of the change in relative atomic concentrations of the various constituent elements with etch time. The depth profile was

simulated from the etch time profile using the SUSPRE<sup>309</sup> computer code to determine the etch rate. This required knowledge of the incident ion mass, energy, and current density (from ion current at the target and the etched area), and of the target composition and density. The mass of Ar is known, an ion energy of 0-5KeV could be produced by the ion gun and the ion current measured using a DVM attached to the sample. Etch areas had been calibrated for this instruments at a number of energies, magnifications and sample geometries previously<sup>310</sup>. Target composition was known from qualitative analysis of the XPS or Auger spectrum, and density from tables of material density<sup>311</sup>.

### 3.3.2 Atomic Force Microscopy

Atomic force microscopy was carried out using a Topometrix Explorer scanning probe microscope operating in contact and non-contact AFM modes. The Topometrix SPMLab V.3.06.06 software was used to control the instrument and for data processing. It was used in a standard manner according to the instrument handbook. The drum containing the magnetic recording heads was easily detachable from the camcorder. A small jig was constructed to hold the drum to allow in-situ examination of the heads during the course of a cycling test.

The AFM was also operated in one non-topographical mode called phase modulation. In this mode the tip is pressed into the sample at each data point and the elastic response of the sample surface measured, enabling a map of the surface compliance – or hardness to be built up. In general it was found that the signal to noise ratio of this technique was poor, and was not used extensively.

In the course of the analysis of the data an important step is the removal of experimental tilt from the height data for the image in question. The analysis software provided a number of proprietary routines for removal of tilt and curvature line by line or plane fit basis. Due to the flexible nature of the tape, it was assumed that it conformed to the head surface. Hence it was assumed that the head contact surface could be represented by a flattened image. This was achieved by applying at first a first order plane fit to the head data followed by a third order polynomial line fit along the microprobe fast scan direction. This was also applied to the tape AFM images. All the data analysis on the head AFM images quoted in the Results Chapter, such as roughness measurements were made after

this data manipulation routine. For the tape samples further fine structure was subtracted from the AFM images to leave the contacting asperity structure, before calculating roughness values etc. The validity of this data manipulation routine is discussed in Chapter 5. Before presentation in this thesis, AFM micrographs were subject to standard image processing techniques for presentation purposes.

## Chapter 4 Results

### 4.1 AFM Analysis of the Tapes Used in the Cycling of Dummy and Sandwich Heads

#### 4.1.1 Introduction

Three different types of ME and three different types of MP Tape were used in the cycling experiments, together with one type of Head Cleaning Tape (HCT). They are listed in Table 4.1. Samples of these tapes were analysed by AFM. From the resultant topographical images, surface roughness, bearing ratio and peak-valley data was obtained. For each tape type an uncycled (except for ME2 and MP2) and a cycled sample was analysed. An area typical of the head-tape contact area was measured. This was 50x50 $\mu$ m except for ME1 Uncycled, 20x20 $\mu$ m and MP1 Cycled, 30x30 $\mu$ m. In the case of the HCT only data for uncycled tape is presented as only one pass was made with this tape. The details of the cycling undergone by the cycled samples are shown in Table 4.2. This lists the mating head material(s), the number of cycles (head passes), the temperature and the humidity seen by the tape. A wide selection of head materials - of the dummy heads both substrates ceramics – CaTiO<sub>3</sub> and CaTiO<sub>3</sub>/ZrTiO<sub>4</sub>/TiO<sub>2</sub>, M2 – FeNbSiN, and FeTaN-CaTiO<sub>3</sub>/ZrTiO<sub>4</sub>/TiO<sub>2</sub> sandwich heads, together with the full range of climates have been experienced by the sample tapes.

Tape	Length (minutes)	Make
HCT	5	SONY V8-25CLH Head Cleaning
ME1	60	SONY Hi-8 ME60
ME2	60	SONY Hi-8 PROME60
ME3	90	SONY Hi-8 ME90 “SUPERME”
MP1	60	SONY Hi-8 MP60
MP2	90	SONY Video8 MP90
MP3	90	SONY Video8 SR90

**Table 4.1 Tapes Used During Cycling Experiments**

Tape	Head Material	No. of Cycles	T(°C)	%r.h.
ME1	M2	132	20	90
ME2	Sandwich	300	30	90
ME3	S1 and S2	240	25	20
MP1	S2	45	22	90
MP2	S1 and S2	4	40	80
MP3	Sandwich	225	30	90

**Table 4.2 Details of Cycled Tape Samples. For Information on Head Materials see Table 4.5**

#### 4.1.2 AFM Images

In Figure 4.1 a three-dimensional AFM image of uncycled HCT is shown. This has been levelled as described in Section 3.3.2. Figures 4.2-11 show AFM images of the ME and MP tape types used. They were similarly levelled. A two-dimensional view (a) and a three-dimensional view (b) of each image are shown. The former to show the distribution of features such as voids, ridges in the tape and scratches and the latter to show the height of the individual asperities.

The areas were chosen at random, but away from the edges of the sample tapes. Several areas were usually scanned, and an image recorded when a stable region found. The orientation of the images of the cycled tapes relative to the direction of head passage was not known.

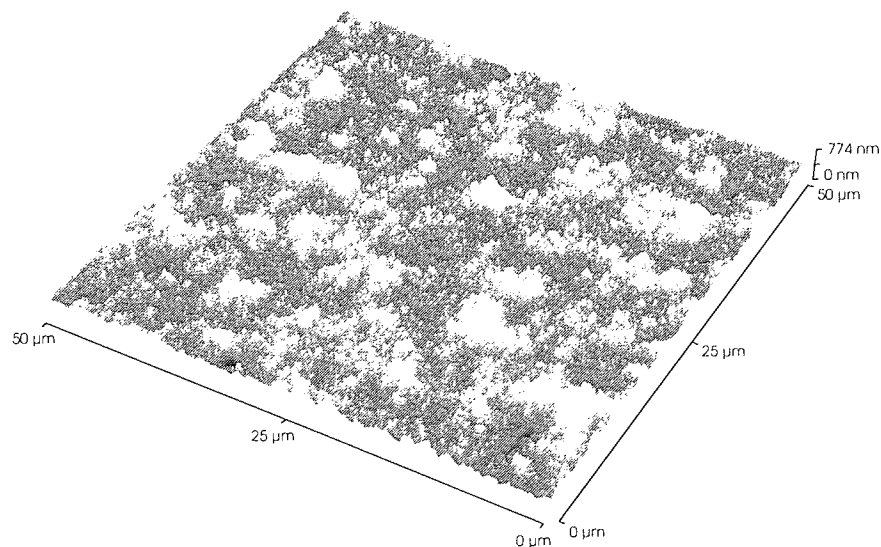


**Figure 4.1 HCT AFM. Uncycled, 3-d Representation**

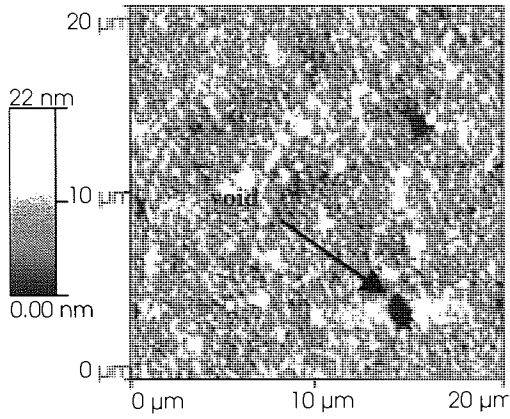


**Figure 4.2(a) Uncycled ME1 AFM, Note Different Scale**

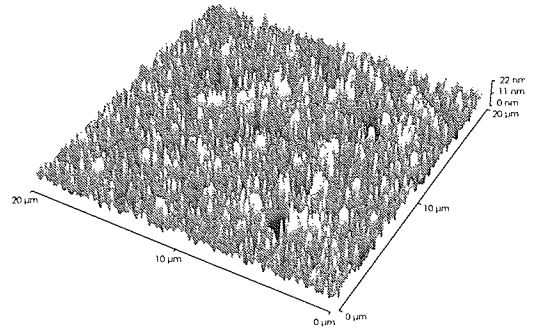


**Figure 4.2(b) 3-d Representation of 4.2(a)**

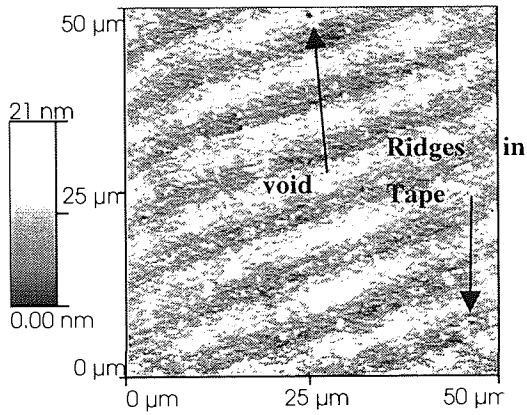


**Figure 4.3(a) Cycled ME1 AFM**

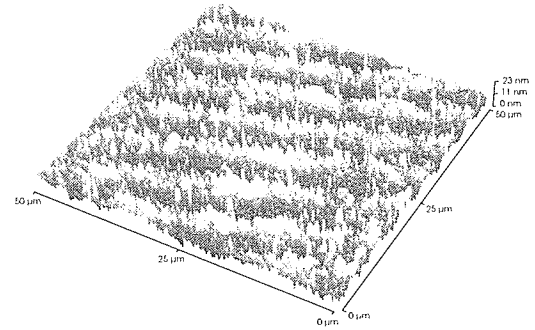


**Figure 4.3(b) 3d Representation of 4.3(a)**

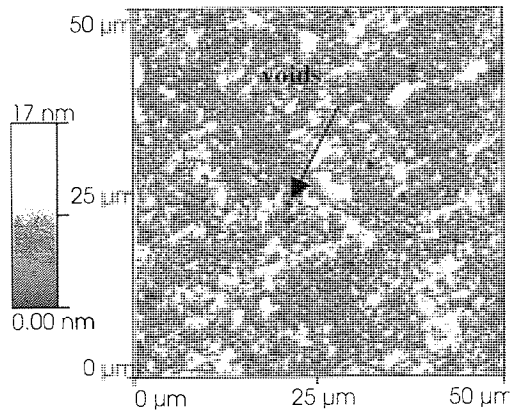


**Figure 4.4(a) Cycled ME2 AFM**

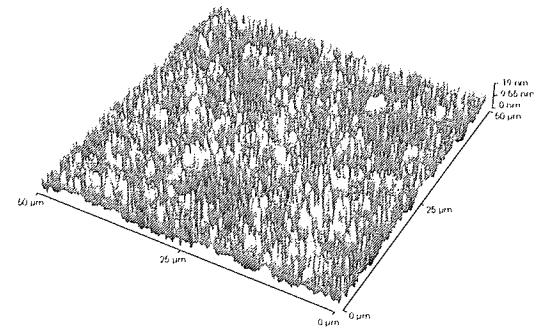


**Figure 4.4(b) 3-d Representation of 4.4(a)**

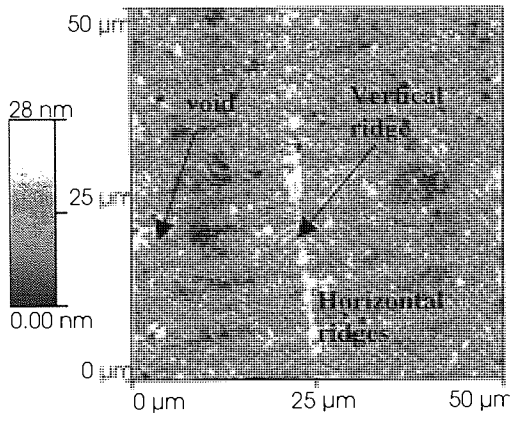


Figure 4.5(a) Uncycled ME 3 AFM

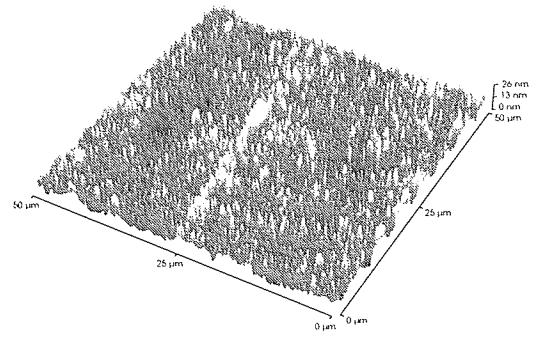


Figure 4.5(b) 3-d Representation of 4.5(a)

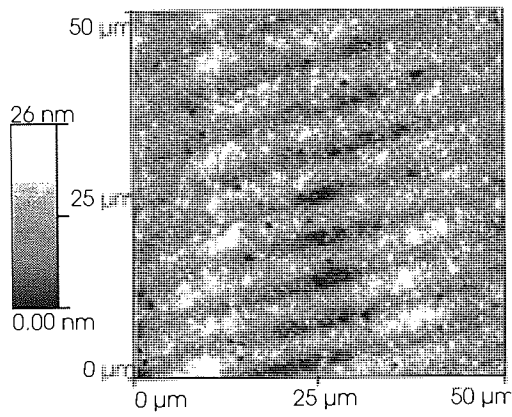


Figure 4.6(a) Cycled ME3 AFM

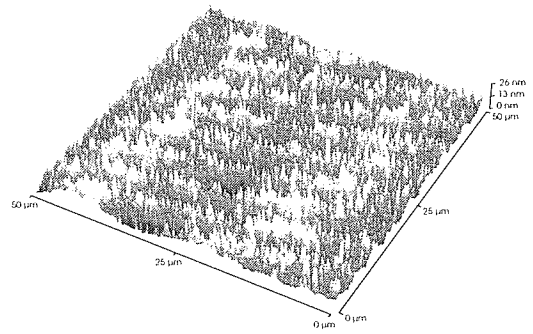


Figure 4.6(b) 3-d Representation of 4.6(a)

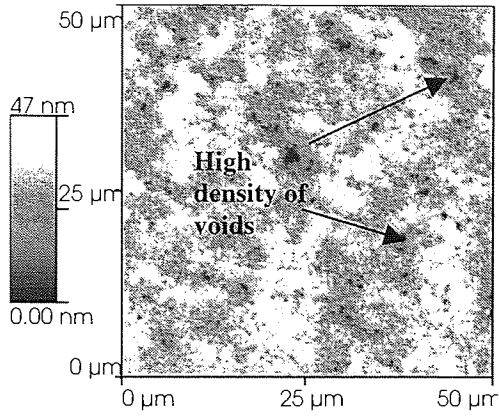


Figure 4.7(a) Uncycled MP1 AFM

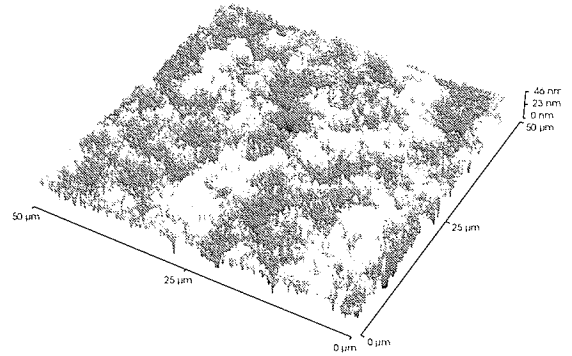


Figure 4.7(b) 3-d Representation of 4.7(a)

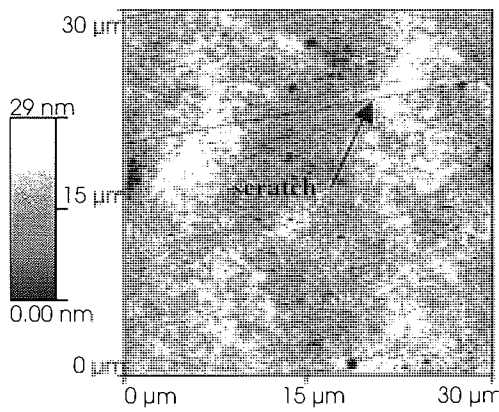


Figure 4.8(a) Cycled MP1 AFM, Note Different Scale

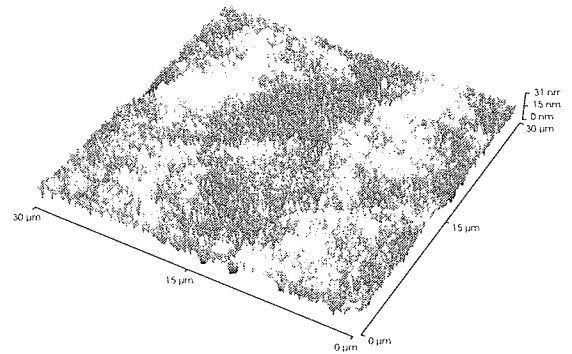


Figure 4.8(b) 3-d Representation of 4.8(a)

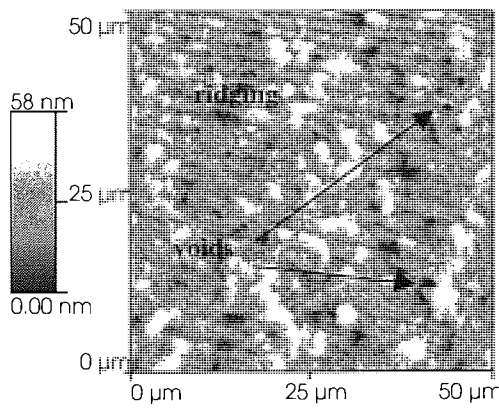


Figure 4.9(a) Cycled MP2 AFM

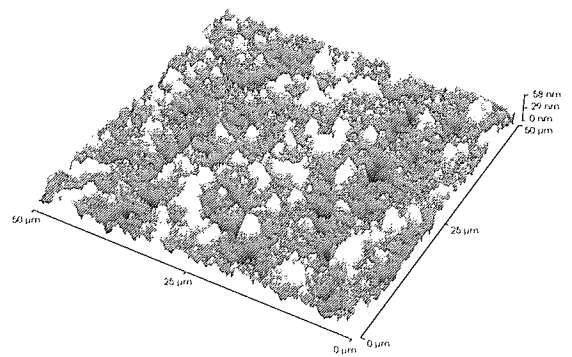


Figure 4.9(b) 3-d Representation of 4.9(a)



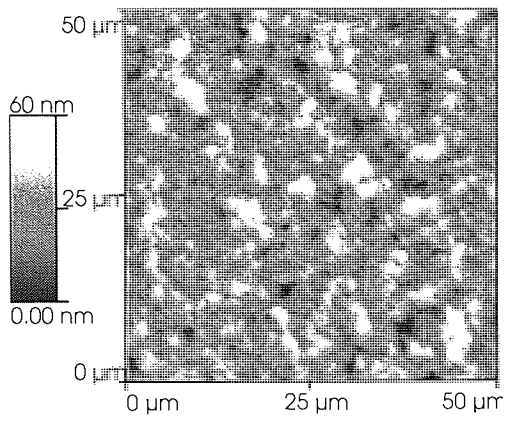


Figure 4.10(a) Uncycled MP3 AFM

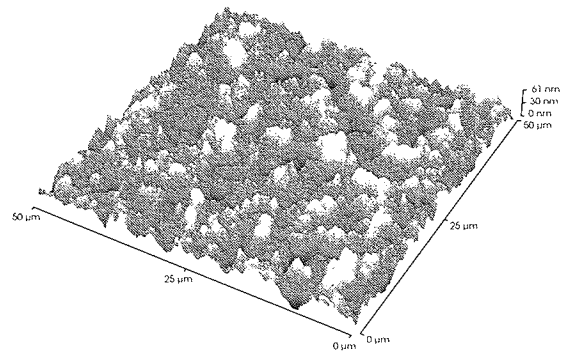


Figure 4.10(b) 3-d Representation of 4.10(a)

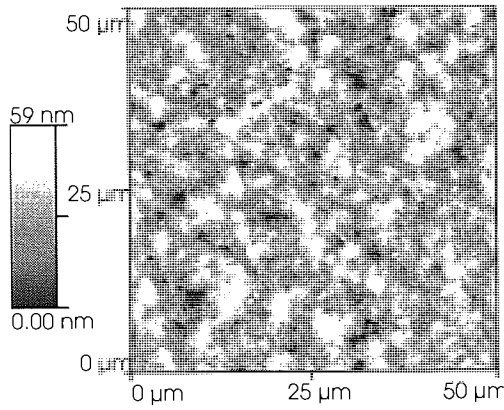


Figure 4.11(a) Cycled MP3 AFM

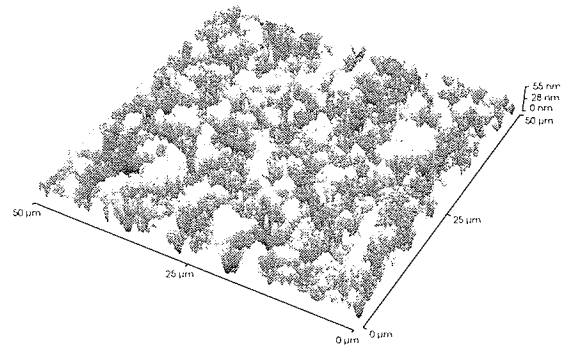


Figure 4.11(b) 3-d Representation of 4.11(a)

The ridges and scratching observed were localised and were not seen with the same distribution on other areas of the same tape. The scratch seen on cycled MP1, Figure 4.8(a), was very straight, over 30 $\mu\text{m}$  in length, 0.5 $\mu\text{m}$  wide and 12nm deep. The ridging in the tape was observed mainly on the ME tape: On the sample cycled ME1 area (Figure 4.4) with a peak-peak separation of 7 $\mu\text{m}$  and a peak-valley height of 20nm, but not on the uncycled tape (Figure 4.2). On the sample areas for uncycled and cycled ME3 (Figures 4.5 and 4.6 respectively) ridges of similar depth, 20nm, were observed but with different peak-peak separations – 1.2 $\mu\text{m}$  and 0.6 $\mu\text{m}$  respectively. In addition there is a single ridge at right angles to the others on the uncycled ME3 tape. The only observed example of such ridging on MP tape was on cycled MP2 in Figure 4.9(a) with a peak-peak separation of 1 $\mu\text{m}$  and a peak-valley height of 15nm. The origin on these ridges maybe in creases in the underlying tape substrate, possibly due to the way the tape was mounted for the AFM measurements.

The voids were visible on both ME and MP tapes, occupied less than 1% of the total area in any one 50x50 $\mu\text{m}$  image. They were generally at least 10nm deeper than the base of the surrounding asperities, and thus probably did not contribute to head-tape contact.

The asperity peaks on the ME tapes were uniformly distributed over the tape surface, where as those on the MP tape are clumped together mirroring the continuous ME film as compared to the particulate nature of the MP Tape. Numerical analysis (roughness, bearing ratio and peak-valley) of the tape asperities is presented in Section 4.1.3

The AFM image of the HCT in Figure 1 resembles qualitatively those for the MP tapes, as it was also a particulate tape. However the peak-valley height of the asperities on the HCT was at 770nm, over ten times the values seen on the MP tapes.

Over all the both MP and the ME tape types can be seen to be distinct types. But whereas the different makes of ME tape within that type were very similar, there was a bigger difference between the different makes of MP tape. For both tape types there was no regular difference between cycled and uncycled tapes.

### 4.1.3 Roughness, Bearing Ratio and Peak-Valley Measurements of the Asperities of ME and MP Tapes

These analyses were carried out using the Topometrix SPMLab software, as described in section 3.3.2, using the lateral and vertical spacing data in the gathered AFM data shown in Figures 4.2-11. In order to generate comparable peak-valley height values of the asperities for each tape sample it was necessary to remove the localised features: voids, ridges and scratches observed on these images. This was done using the “Background Subtraction” facility. A 3-dimensional image of cycled ME1 generated by such treatment is shown in Figure 4.14. By comparing with Figure 4.3(b) it can be seen that the ridges in the tape have been removed, leaving the asperities on a planar background. Thus the roughness, bearing ratios and peak-peak separations presented in this section are for these asperity features only and the head may also experience additional “roughness” due to raised ridges.

Roughness data is quoted for the whole area of the images Figs. 4.2-11. As a check to see if the quoted roughness values are representative of the tapes from which they are extracted roughness analysis were applied to sub areas within these images and compared with each other and the whole sampled area. All the values quoted below show consistency between whole and sub regions with RMS and  $r_a$  values differing by 0.3nm or less. Thus giving confidence that the sampled area is itself consistent with a larger area. Of course maximum peak-valley heights quoted relate to a single asperity comparison within each sampled region, and thus these values may only be taken as rough guide. The data pixel size is 0.1nm or less.

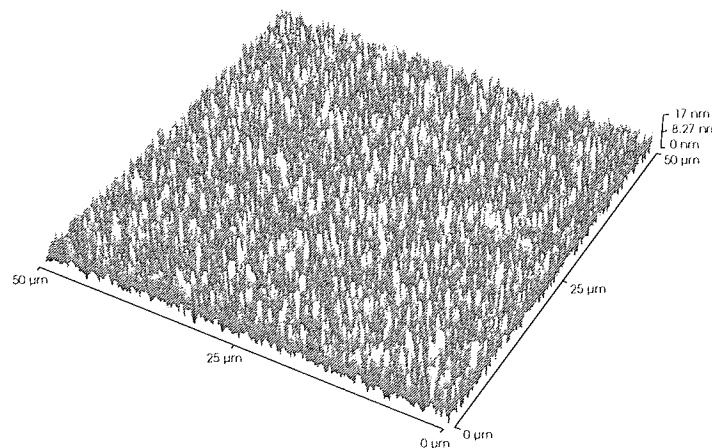


**Figure 4.12 ME1 Cycled AFM: After Background Substitution**

The sample AFM image of cycled MP2 tape after background substitution is shown in Figure 4.15. Compared with the corresponding image before background substitution in Figure 4.9(a) the ridging and the voids can no longer be observed, whilst the integrity of the particulate nature of the surface is retained.

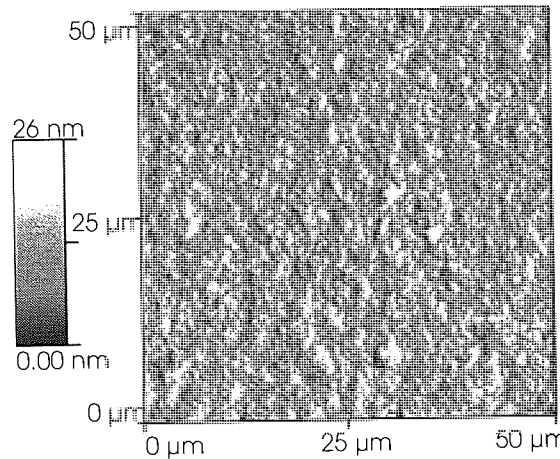


**Figure 4.13 Cycled MP2: After Background Substitution**

#### 4.1.3.1 Roughness Values

The peak-valley roughness of the asperities of HCT, as shown in Figure 4.1, was over 770nm, which is over ten times the values observed for ME and MP tapes, as shown in Figures 4.2-11. Its RMS roughness is again, at 55nm, an order of magnitude greater than the values found for ME and MP recording tape below. HCT is deliberately manufactured with a high roughness for its use in head cleaning, and thus is not included in the more detailed roughness analysis.

Tape	$r_a$ (nm)	RMS (nm)	Average Height (nm)	Max P-V Height (nm)
ME1 Uncycled	3.2	4.6	5.2	62.7
ME1 Cycled	3.4	4.6	7.8	106.0
ME2 Cycled	3.0	4.6	7.6	82.1
ME3 Uncycled	3.0	4.5	5.4	63.3
ME3 Cycled	2.8	4.4	7.9	70.5
MP1 Uncycled	9.3	11.5	20.3	233.7
MP1 Cycled	3.4	4.7	6.4	82.7
MP2 Cycled	5.0	6.3	13.3	68.3
MP3 Uncycled	5.1	6.7	13.2	232.0
MP3 Cycled	3.7	4.6	7.3	45.0

**Table 4.3 Roughness Values of the Sample Tapes after Background Substitution**

Table 4.3 contains the roughness values from the sample tape images after background substitution. The ME Tapes showed very similar  $r_a$  and RMS roughness values (~3.2 and ~4.6nm respectively), both between different makes and between cycled and uncycled tape. The maximum peak-valley (P-V) height of the ME tapes ranged from 62.7 to 106.0nm. Comparing the average asperity height for the ME tapes, the cycled tapes showed values of 7.6-7.8nm, where as the uncycled heads showed average asperity heights of 5.2-5.4nm. The cycled ME media showed an increase in both average asperity height and maximum asperity height.

The uncycled MP tapes showed roughness values (RMS,  $r_a$ ) that were slightly higher than for the uncycled ME media. On cycling the roughness values of the MP tapes decreased to values similar to ME tape.

#### 4.1.3.2 Bearing Ratio Values

Bearing Ratio Plots are given for ME and MP tapes after background substitution in Figures 4.16 and 4.17 respectively. These show the percentage (bearing ratio) of the surface area that remains at 5nm intervals in height from the base of the image, and thus give an idea of the asperity height distribution.

For the ME tape a definite trend was observed between the cycled and the uncycled tape. The cycled tape showed many more asperities at or above 5nm and a higher fraction of the mid height-range (10-15nm) asperities. The distribution of asperities of 20nm height or above was similar for both uncycled and cycled tapes. The MP tapes showed no trend in asperity height distribution.

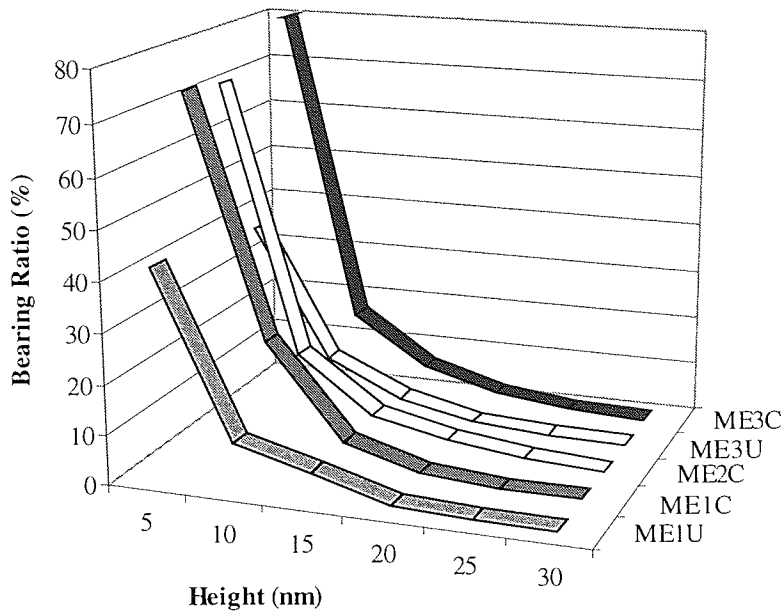


Figure 14 Bearing Ratio Plots for the Sample ME Tapes after Background Substitution. U – Uncycled, C- Cycled Tape

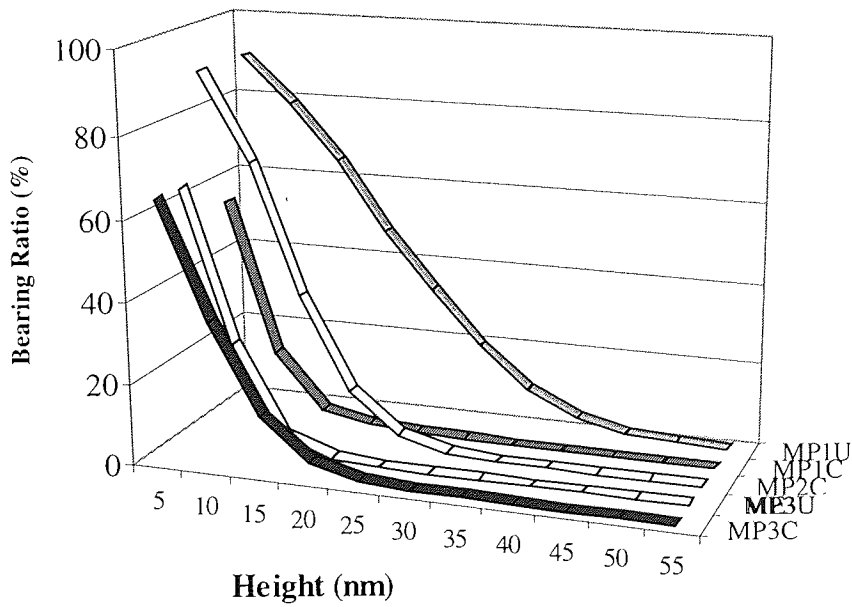


Figure 15 Bearing Ratio Plots for the Sample MP Tapes after Background Substitution. U – Uncycled, C- Cycled Tape. Note Reverse Order of Tape Types

#### 4.1.3.3 Peak-Valley Analysis

This was carried out on the tape sample images after background subtraction to give an indication of the average separation of the asperity peaks and of the asperity peak-valley angle. This data is presented in Table 4.4.

Tape	Average Peak-Peak Separation ( $\mu\text{m}$ )	Average Peak-Valley Angle ( $^{\circ}$ )
ME1 Uncycled	0.3	2.2
ME1 Cycled	0.6	1.3
ME2 Cycled	0.4	1.7
ME3 Uncycled	0.6	1.1
ME3 Cycled	0.6	1.2
MP1 Uncycled	0.4	3.3
MP1 Cycled	0.4	1.5
MP2 Cycled	0.5	1.6
MP3 Uncycled	0.6	0.9
MP3 Cycled	0.5	1.9

**Table 4.4 Peak-Valley Analysis of the Tape Samples after Background Substitution. Shows the Average Separation of Neighbouring Asperity Peaks and the Mean Peak-Valley Angle of the Asperities**

The average peak-peak separation showed a range of 0.3-0.6 $\mu\text{m}$  between all of the tape samples, with no trend discernible between ME and MP tape types or between cycled and uncycled tapes.

## 4.2 Cycling Tests and Wear Rates of Dummy Heads

### 4.2.1 Introduction

In the following sections wear rate data is presented from the cycling of single material dummy heads. The materials used are listed in Table 4.5 along with their Knoop microhardness ( $H_k$ ) values as measured during the process of making indentations for wear rate monitoring. These heads were cycled against both Metal Evaporated and Metal Particulate tapes, which are listed in Section 4.1 together with AFM analyses of these tapes. These cycling tests are described in Section 3.2, with the wear rates being calculated from the change in depth of Knoop microhardness indentations made along the length of the head (see Section 3.2.7). Three different gross environmental conditions were studied: Room temperature (20-25°C) with high humidity (80-90%); high temperature (40-60°C) with high humidity (80%r.h.); and room temperature (25°C) with low humidity (20%r.h.). The slight variations quoted for each condition are due to the two different environmental chambers used. The more primitive environmental chamber, used for initial experiments provided high humidity only (90%r.h.) at ambient room temperature which varied between 20 and 25°C. The commercial environmental chamber allowed much greater control of both temperature and humidity. So 80% r.h. was selected as the high humidity condition as opposed to 90%r.h. as the latter sometimes caused condensation within the recorder which caused it to trip off. The high temperature condition was lowered from 60 to 40°C after cycling CoNbZr heads, as melting of the lubricant onto the head surface was observed at the higher temperature, together with higher recorder malfunction.

	Design- ation	Material	$H_k$ (Kg/mm <sup>2</sup> )	Standard deviation
Ceramic Substrate	S1	CaTiO <sub>3</sub>	1082	31
	S2	CaTiO <sub>3</sub> /ZrTiO <sub>4</sub> / TiO <sub>2</sub>	1111	57
Magnetic Metal	M1	CoNbZr	860	21
	M2	FeNbSiN	1275	73
	M3	FeTaN	1240	74

**Table 4.5 Materials Used in Dummy Heads and their Measured Knoop Microhardness ( $H_k$ )**



#### 4.2.2 Running In

All the ceramic heads were run in for at least 10 hours against MP1 tape, the same or similar to those used in the cycling tests, at 20°C and 80% r.h. in Hi-8 recorders. This was sufficient for heads to be cycled against MP tape at high humidity. Prior to wear measurements against ME tape at high humidity, the heads were further run-in for 100 hours against ME tape at 20°C/80%r.h. Prior to wear tests at low humidities, the heads were run in for at least a further 50hours in the case of ME tape, and 24 in the case of MP tape at low humidity, primarily to remove any residual moisture the head surfaces.

In the case of the metal coated heads, the 3µm metal coating was applied after the initial 10hours against MP tape at 40°C/80%r.h. No further running-in of these heads was possible due to the limited amount of material contained within these films, and hence all the metal wear rates are influenced by changes in head profile to some extent. Although the quoted wear rates for these materials are not therefore the equilibrium values, they are still broadly comparable within themselves, when obtained under similar conditions and times.

#### 4.2.3 Wear Rate Data Tables

Wear Rate Data for S1, S2, and the magnetic materials are summarised in Tables 4.6-8 respectively. These tables, for each dummy head run, specify: environment, tape used, time run, mean wear rate with standard deviation, maximum wear rate, head protrusion and the average wear rate for the heads run under each condition (usually two). In addition, for the two ceramic materials, head width is given, which is either 80 or 120µm. All of the metal coated heads are 100µm wide.

The choice of indentations used to calculate the mean wear rate for an individual head depends on the longitudinal wear profile generated from the wear of individual indents along the heads. Typical examples are shown in Figures 4.18-21 for S1 and S2, and in Figure 4.22 for the metals, and are discussed in Section 4.2.4.

The mean wear rates of individual heads are quoted to the nearest 0.1 nm/hour for wear rates less than 10nm/hour, and to the nearest nm/hour for wear rates greater than this. The standard deviation values justify the quotation of wear rates to two significant figures. The

wear rates quoted for each head are calculated by subtracting the final indent depth from the initial and dividing by the total running time. The cycling tests were halted when the highest worn indentations were almost worn through, thus giving the lowest possible percentage error in the quoted wear rate. Where the wear rate was low, and the heads cycled for extended periods of time (especially ceramic dummies with ME tape), it was possible to observe the wear rate at different time during the cycling.

For the ceramic heads both increases and decreases were observed in wear rate with time. However such variations were small, and of the order of the standard deviation in the mean wear rates being compared and thus no clear trends in changes in wear rate with time could be discerned. For example MP tape, 25°C/20% r.h., mean wear rate (standard deviation): S1C @50hours = 4.0 (3.3) nm/hour and @75hour = 9.6 (2.6)nm/hour; S2D @50hours = 10.2 (3.3) nm/hour and @75hour = 12.1 (2.2)nm/hour; S2 @50hours = 9.2 (0.8) nm/hour and @75hour = 8.4 (0.3)nm/hour. For the ceramic heads, no, or very little change in the extent of the wear zone was observed, as to be expected with fully run-in heads.

For the metal coated heads, where sufficient wear-time data exists, the extent of the wear zone is seen to increase with time, consistent with a “running-in” process occurring due to a non-equilibrium head profile being created by the deposition layer. This effect is demonstrated in the case of M2 cycled against ME tape at 25°C/90%r.h. The wear zone and the wear rate are seen to increase to 50 hours, after which they remain constant. M3 against ME tape at 25°C /90%r.h., which shows an unusually high wear rate (22nm/hour) shows an increase in the wear rate with time to this value at 50 hours.

The average wear rate is calculated from both heads run concurrently, on the same drum, under the same conditions. The trend in average wear rates follows that for individual heads, despite the heads being averaged often showing differences in mean wear rates beyond the deviations quoted for each head. This may in part be expected as these heads may have different widths and protrusions (which are quoted) which may effect head contact pressure and thus abrasive wear rates, as may uncertainty in the positioning of a head on it's mounting plate from the manufacturing process. Also the interaction of additional non-continuous wear mechanisms may result in differences between wear rate snap shots of heads run under the same conditions. The greatest differences in wear rate at

the same condition are for those run under the severest conditions: 40°C and 80%r.h. and MP tape - in particularly see S2, Table 4.7, where S2K shows a wear rate of 450nm/hour and S2L 102 nm/hour. In such cases the quoted average wear rate, though imprecise, is included to indicate the much greater wear rates observed at this condition.

The mean protrusion quoted is the mean of all the protrusion values calculated each time the drum was removed from the recorder in order to measure the wear during the cycling. The method was described in Chapter 3. The error in each protrusion measurement is about  $\pm 2\mu\text{m}$ . The standard deviation in the mean protrusion lay between 1 and  $2\mu\text{m}$ , where sufficient protrusion data was collected.

T (C)	% r.h.	tape	time (hours)	sample identity	mean wear rate (nm/hour)	s.d. (nm/hour)	max wear rate (nm/hour)	mean protrusion ( $\mu\text{m}$ )	head width ( $\mu\text{m}$ )	average wear rate (nm/hour)
25	20	ME3	160.25	S1A	1.2	0.4	1.9	27	120	1.3
				S1B	1.3	0.7	2.2	24	80	
		MP3	75.33	S1C	10	2.6	13	31	80	11
				S1D	12	2.8	16	31	120	
25	90	ME1	100	S1E	0.3	0.2	0.5	25	120	0.3
				S1F	0.3	0.3	0.5	24	120	
		MP1	5.33	S1G	59	30	116	24	80	52
				S1H	46	21	86	21	120	
40	80	ME1	55.33	S1I	10	4.6	18	26	80	7.9
				S1J	5.7	1.0	7.2	23	80	
		MP2	1	S1K						373
				S1L	373	12	380	22	120	

**Table 4.6 Wear Rate Data for S1 (CaTiO<sub>3</sub>) Dummy Heads. Note: S1K Destroyed During Cycling**

T (C)	% r.h.	tape	time (hours)	sample identity	mean wear rate (nm/hour)	s.d. (nm/hour)	max wear rate (nm/hour)	mean protrusion ( $\mu\text{m}$ )	head width ( $\mu\text{m}$ )	average wear rate (nm/hour)
25	20	ME3	160.25	S2A	0.6	0.3	1.0	20	120	0.91
				S2B	1.2	0.4	27	27	120	
		MP3	75.33	S2C	8.4	0.3	8.9	33	120	7.05
				S2D	5.7	1.4	1.0	21	80	
22	90	ME1	101.2	S2E	0.1	0.2	0.7	24	200	0.25
				S2F	0.4	0.2	0.8	25	80	
		MP1	30	S2G	139	48	201	32	80	109.7
				S2H	81	39	135	26	120	
40	80	ME1	55.33	S2I	3.2	1.0	4.5	23	80	3.7
				S2J	4.3	1.2	6.5	32	80	
		MP2	1	S2K	450	57	490	22	120	277
				S2L	102	30	136	25	120	

**Table 4.7 Wear Rate Data for S2 (Zr-CaTiO<sub>3</sub>) Dummy Heads**

metal	T (C)	% r.h.	tape	time (hours)	sample identity	mean wear rate (nm/hour)	s.d. (nm/hour)	max wear rate (nm/hour)	mean protrusion ( $\mu\text{m}$ )	average wear rate (nm/hour)
CoNbZr	25	90	ME1	60.8	M1A	7.8	0.3	7.9	45	7.8
					M1B					
			MP1	5	M1C	194		194	37	128
					M1D	48	10	62	20	
CoNbZr	60	80	ME1	5.33	M1E	12	5.3	21	30	12
					M1F					
			MP2	1.17	M1G	439	39	479	23	595
					M1H	752	76	829	19	
FeNbSiN	20	90	ME1	92	M2A	2.2	0.6	3	32	1.8
					M2B	1.3	1	2.8	35	
			MP2	5.33	M2C	2.3	3.8	9.4	21	47 (M2D)
				14.67	M2D	48	4.4	52	30	
FeNbSiN	40	80	ME1	100.6	M2E	5.4	0.7	6.2	27	5.2
					M2F	5.1	1.1	7.2	26	
			MP2	50.33	M2G	33	28	360	30	394
					M2H	460	52	510	26	
FeTaN	25	90	ME1	49.67	M3A	22	0.7	23	25	22
					M3B	22	0.4	23	31	
			MP1	13.17	M3C	54	14	84	34	48
					M3D	32	4	35	22	

**Table 4.8 Wear Rate Data for Metal Dummy Heads. Note: M1B, M1F and M2C were Destroyed During Cycling**

#### 4.2.4 Longitudinal Wear Rate Profiles

Typical longitudinal wear rate profiles generated from indentation depth changes are shown in Figures 4.18-22. The x-axis represents the entire length of the head, with the indent position given relative to the centre of the head. The left-hand side of the profile represents the leading edge and the right hand-side the trailing edge. Wear rate is shown to change along the length of the head. According to the Archard Wear Law for abrasion, a variation in wear rate will occur along the head with a variation in the head-tape contact pressure, with a maximum at the highest contact pressure. Wear profiles over time show that the contact area grows very slowly, and can thus be treated as constant, and head-tape speed is constant. Added to this is the error associated with individual measurements. Therefore the mean of the wear rates (with corresponding standard deviation) within the contact zone is calculated and presented, alongside the maximum observed wear rate in Tables 4.6-8. Thus enabling the comparison of the wear rate of each material in authentic head-tape conditions.

It is to be noted here that the error bars displayed on the profiles are those due to the instrumental uncertainty in measuring the indent diagonal, as this is the major contribution to the uncertainty in the wear rate. The uncertainty due to the time is a fraction of this. However they maybe addition, significant, but unquantified uncertainty in some of the wear rates of individual indents, not displayed on the profiles due to distortion of the actual indentations or partial obscuration of the indent diagonal by debris.

There is no clear trend in the wear profiles of the ceramic heads. The most common, though not associated with any particular material, tape or condition, is that shown in Figure 4.18 with wear rate rising from near zero at the leading edge, to a maximum near, or at the trailing edge. For this profile all the non-zero indents are used to calculate the mean wear rate. In a few cases the wear rate varied about a level value along the head length, with zero wear observed at either or both ends, for example see Figure 4.19. Again the mean is of all indents within the wear zone. In other cases a maximum in the wear rate is seen within the wear zone, with wear zero at both edges (Figure 4.20) or with wear rising from the leading to the trailing edge (Figure 4.21). Again all the indents within the wear zone were counted towards the mean wear rate.

All the longitudinal wear rate profiles for the metal heads follow the pattern shown in Figure 4.22. There is a well-defined wear scar with a central maximum in the wear rate, which falls to zero at the leading and the trailing edges. The maximum occasionally occurs nearer the leading or trailing edge. The indentations used to calculate the mean wear rate are those which lie on the wear scar. Those indentations lying on the sides of the wear scars, which showed less than half the maximum wear rate were not included in the sample used to calculate the mean wear rate. This is a somewhat arbitrary delineation of the maximum contact pressure zone, but in practise, the wear profiles were as square as Figure 4.22, in which only one indent is close to the cut off point, and no more than two indents in any one head were so involved.

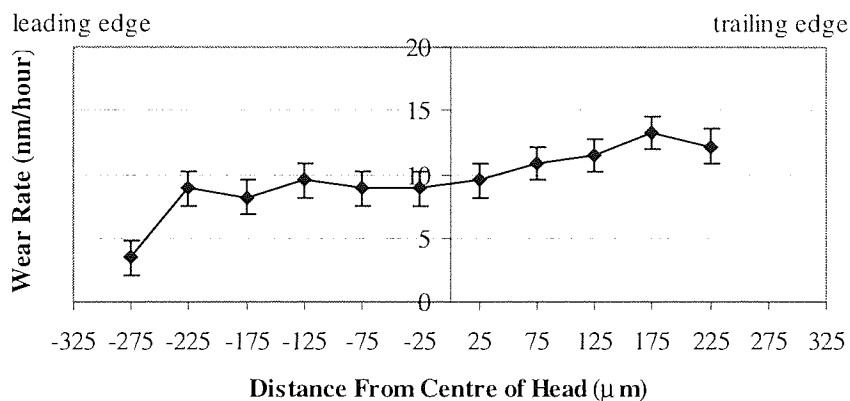


Figure 4.16 S1C Longitudinal Wear Profile. S1, 25°C/20%r.h., MP3, 75hours

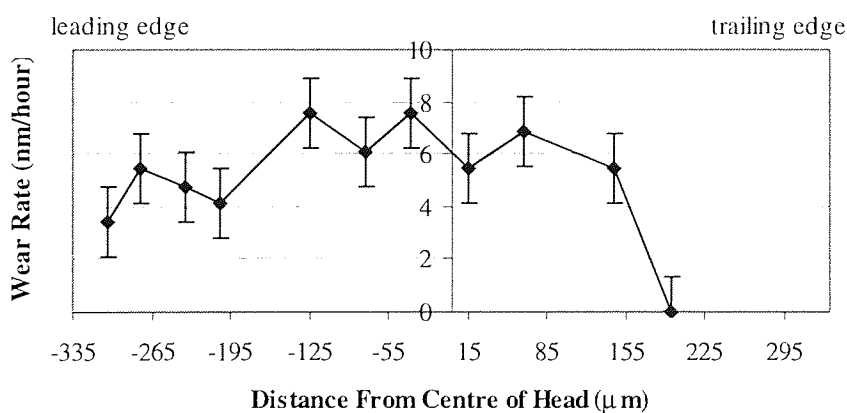


Figure 4.17 S2D Longitudinal Wear Profile. S2, 25/20%r.h., MP3, 75hours

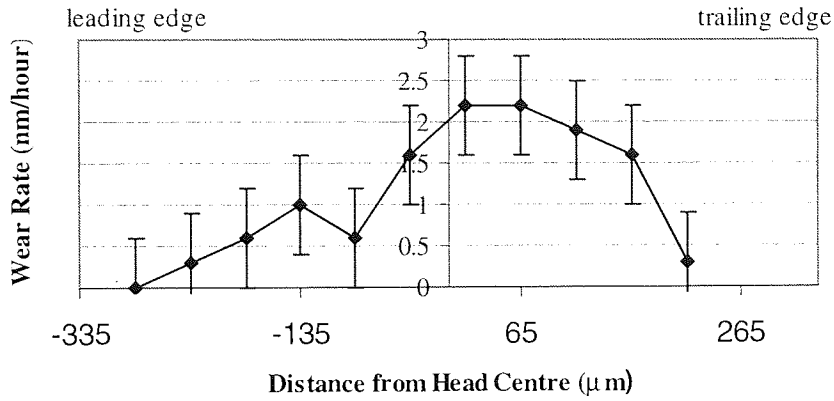


Figure 4.18 S1F Longitudinal Wear Profile. S1, 25°C/90%r.h., ME1, 100hours

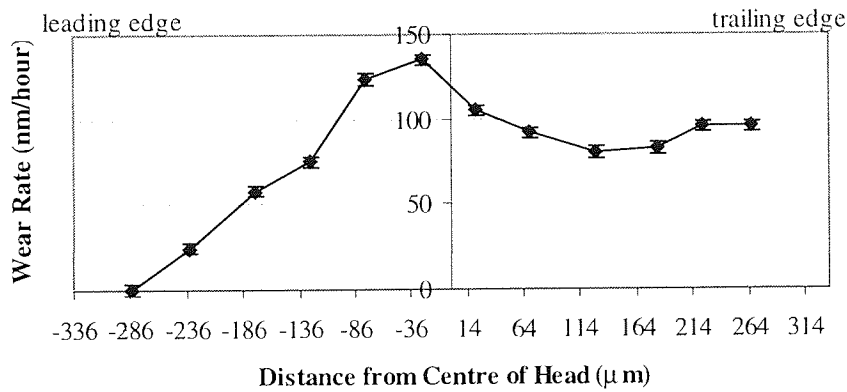


Figure 4.19 S2H Longitudinal Wear Profile. S2, 22°C/90%r.h., MP1, 30hours

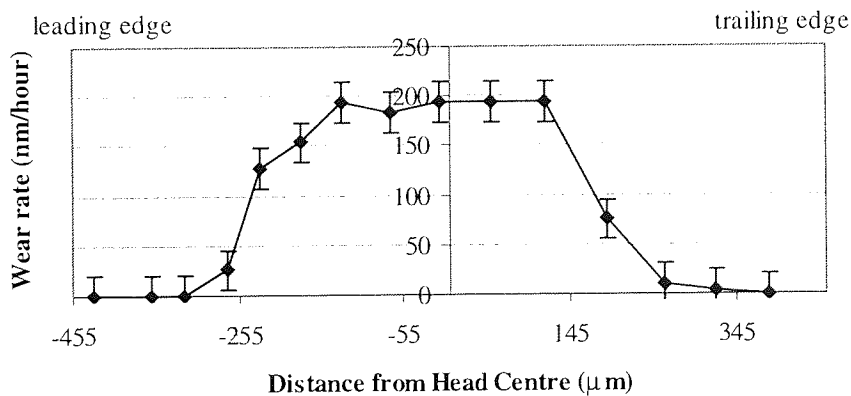


Figure 4.20 M1D Longitudinal Wear Profile. M1, 25°C/90%r.h., MP1, 5hours.  
Typical of All Metal Wear Profiles

#### 4.2.5 Effects of Head Size and Protrusion on Wear Rate

For the ceramic materials heads of both 80 and 120 $\mu\text{m}$  width (all 650-670 $\mu\text{m}$  in length) were employed. Viewing Tables 4.6 and 4.7 it can be seen that there was no correlation between width and wear rate was found. For most conditions, the wear rate of the 120 $\mu\text{m}$  head is very close to the 80 $\mu\text{m}$  head, with example of each being the greater: S2C(120 $\mu\text{m}$ )>S2D(80 $\mu\text{m}$ ) and S1G (80 $\mu\text{m}$ )>S1H(120 $\mu\text{m}$ ). All the metal-coated heads were of the same length and width (900x100 $\mu\text{m}$ ). Similarly, the small differences in head protrusion showed no strong correlation to the wear rate. Thus the noise in the experiment was larger than the effect on change in wear rate by either varying the width of these heads between 80 and 120nm or by varying the protrusion by a few microns.

#### 4.2.6 Trends in Average Wear Rate

The values for average wear rate for all the materials are given in Tables 4.6-8 (together with the precise tape type and environmental condition), and are summarised for ME Tapes in Figure 4.21, and for MP tapes in Figure 4.22. In this discussion the effect of tape type upon wear rate is based upon the ME and MP categories in order to highlight the major trends in wear rate. The extent to which the various types of ME and MP tapes respectively may be influencing the observed trends is noted. However it maybe noted that wear rates against MP tape are roughly an order of magnitude greater than those against ME tape for all conditions, and that the variation in the wear rates within the ME and MP tape types is much less.

For all materials and both tape types, at high humidity there was a very large increase in wear rates going from 20/25 $^{\circ}\text{C}$  to 40 $^{\circ}\text{C}$ , which is at least a doubling (M1, ME) and in most cases a factor of four.

For MP tape the wear rate of the ceramic materials increased from 25 $^{\circ}\text{C}$ /20%r.h. to 25 $^{\circ}\text{C}$ /90%r.h.to 40 $^{\circ}\text{C}$ /80%r.h. However this was not the case for ME tape where there was greater wear in dry than in wet conditions at room temperature. In general the wear rates of S1 and S2 were similar, with S2 exhibiting slightly smaller values, except against MP at



25°C/90%r.h., where S2 exhibited double the wear rate of S1 (both MP1 tape). For MP tape, supply dictated a different type was used for each different environment. For ME tape a different type of tape was used at low humidity to the two high humidity conditions.

In general the wear rates of the nanocrystalline iron materials, M2 and M3 were less than those of the amorphous Co material, M1. At room temperature and high humidity the wear rate of M2 was one quarter that of M1 against ME1 tape, and half against MP tape (Tapes: M1-MP1, M2-MP2). Against MP M3 showed a similar wear rate to M2 (Tapes: M2-MP2, M3-MP1). However against ME (ME1 for each metal) tape at 25°C/90%r.h., M3 showed the highest wear rate of all three metals, almost ten times that of M2 and more than double that of M1.

For ME tape at room temperature and high humidity the wear rates of the metals were higher than those of the ceramics. In higher wear rate regimes the relative wear rates of the metals and the ceramics were more mixed. Against MP tape in the same environment, M1 showed the highest wear rate, S2 the next highest and lowest: M2, M3 and S1 showed similar wear rates. Against ME at the high temperature and humidity M1 had the greatest wear rate, then S1, and M2 and S2 the lowest, showing similar wear rates. Against MP at the high temperature and humidity M1 showed the highest wear rate, then M2 and S1 with similar wear rates, and S2 with the lowest.

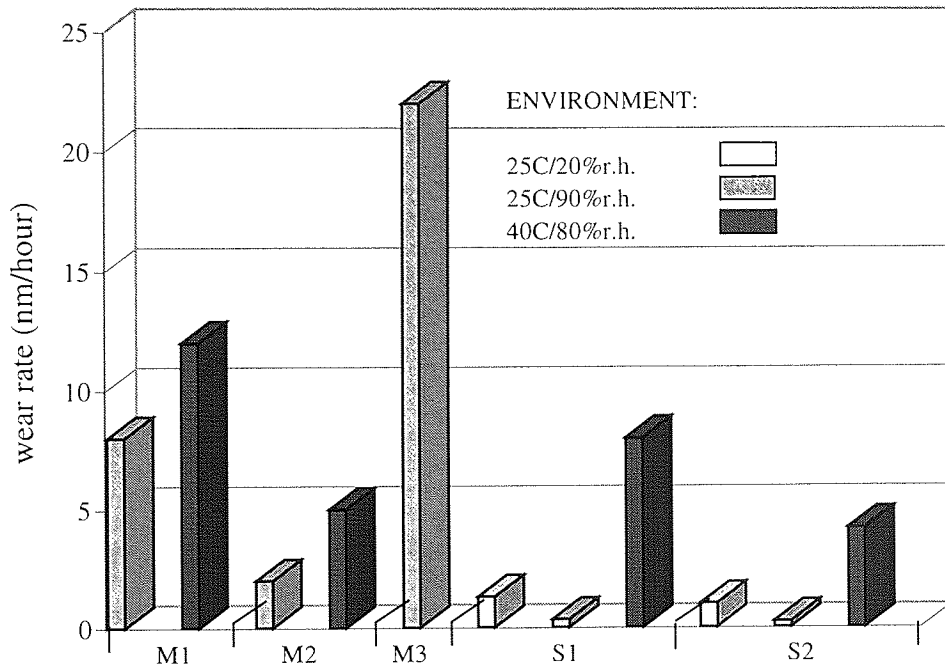


Figure 21 Wear Rates of Dummy Heads Vs. ME Tape. Note M1 60C/80%r.h. not 40C/80%r.h.

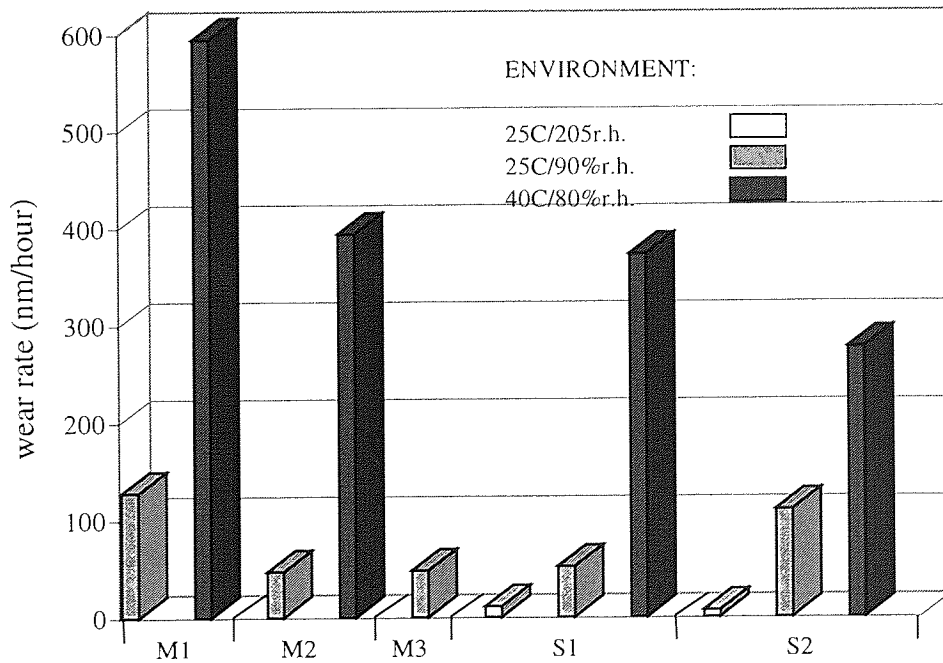


Figure 22 Wear Rates of Dummy Heads Vs. MP Tape. Note M1 60C/80%r.h. not 40C/80%r.h.

## 4.3 Topographical Analysis of Cycled Dummy Heads by Optical and Atomic Force Microscopy.

### 4.3.1 Introduction

Optical Microscopy and AFM were used to examine the head surfaces of the single material dummy heads periodically during and at the end of the cycling experiments. Data and images collected by these techniques are presented in Section 4.3.2. In section 4.3.3, a summary and analysis of this data is given, including some further AFM images, pertaining to the analysis.

The wear rate data, collected by the Microhardness Indentation Technique, for these experiments are presented in section 4.2, and XPS surface chemical analysis in Section 4.4. Reference is made to these experiments and results where necessary in the analysis of the AFM and optical data in 4.3.3. But on the whole the results obtained by different techniques are brought together in the Discussion Chapter.

### 4.3.2 The Data

#### 4.3.2.1 AFM Data

The AFM and optical data collected are summarised alongside the respective cycling experiment from which they were obtained in Tables 4.9-12. Tables 4.9 and 4.10 are for the substrates S1, CaTiO<sub>3</sub>, and S2, CaTiO<sub>3</sub>/ZrTiO<sub>4</sub>/TiO<sub>2</sub> respectively. Table 4.11 is for metals M1, CoNbZr, and M3, FeTaN. Table 4.12 is for the metal M2, FeNbSiN. The precise details of the cycling tests are described in Section 3.2. The tables contain summaries of the features that may be observed on the head surfaces that may be seen in representative sample AFM images of cycled head surfaces for each condition shown in Figures 4.22-46 and 4.60. Given in each table is the sample number and area from which the subsequent data is obtained. This includes an area roughness analysis -  $r_a$ , RMS, mean height (above the lowest point) of the data and the maximum peak-valley height. Also given is a Peak-Valley (p-v) analysis of the microgrooving that is observed parallel to the direction of tape travel. Quoted in the tables are the mean lateral peak-peak separation, and

the mean peak-valley slope angle. Typical histograms showing the distributions of p-v separations and angles from which these mean values are derived are shown in Figures 4.59 and 4.60 included in the analysis section. These analyses (areal roughness and p-v) are described, together with the algorithms used, in the chapter dealing with AFM. In the final row of Tables 4.11 and 4.12, for the metal-coated heads, it is recorded if a brown stain was observed optically on the wear zone. This was never the case for the ceramic dummy heads.

All the AFM images shown, and data presented therefrom have first had the curvature of the head removed, using the levelling/background subtraction routines described in Section 3.3.2. This is valid as all the areas studied are from the contact region between the head and tape (as shown by the wear of surrounding microhardness indentations and abrasive scratching by the tape observed on the head surfaces). The tape is flexible, bending about the contours of the head in the contact zone. Thus with the head contours removed, all height (z) data in the resultant AFM image is perpendicular to the contact plane formed between the head and tape.

For the metal-coated heads, AFM data is available for the uncycled, as deposited state. However the ceramic heads were received after being lapped and run in. The running-in conditions were identical to those being studied in the cycling tests: 10 hours 40°C/80%r.h. MP tape for all heads, followed by a further 100hours 25°C/80%r.h. ME tape for those heads to be cycled against ME tape at high humidity. Those heads to be run at low humidity were run in for at least 50 hours in the case of ME tape and 24 hours in the case of MP tapes at 25°C/80%r.h. After these running in periods the head surfaces resemble those reported for the cycling experiments conducted under the same conditions. The AFM data from which the images presented in Figures 4.23-46, and the values presented in Tables 4.9-12 were derived was collected from head surfaces from which material removal of up to one 1µm in depth had been observed, as measured by the indentation method. Average height and, in the absence of particulate debris, maximum height values were observed to be less than 15nm. Thus the head surface topography observed by AFM was due to the cycling test stated and not a product of the running in, or other prior processing.

conditions	25C/20%r.h.		25C/90%r.h.		40C/80%r.h.	
tape type	ME3	MP3	ME1	MP1	ME1'	MP2
sample number	S1A	S1D	S1E	S1G	S1J	S1L
scan area ( $\mu\text{m}$ )	10	20	20	10	20	20
area ra	3.6	1.1	1.1	0.5	2.3	3.0
roughness RMS	4.4	2.8	1.7	1.0	3.9	14.7
ness mean height (nm)	7.0	42.1	5.8	5.1	30.1	156
(nm) max p-v	37.8	205	77.1	52.2	121	310
grooving sep. ( $\mu\text{m}$ )	0.16	0.17	0.27	0.12	0.24	0.40
$\theta$ (deg)	3.7	1.1	0.9	1.2	1.5	18.2
surface features	pullouts, grooving, scratches, fracture, debris	pullouts, grooving, fracture-scars, debris	grooving, scratches, fracture-scars	grooving, scratches	debris, grooving, scratches	grooving, scratches, fracture scars, protruding grains, cracking

**Table 4.9 S1 Dummy Heads –Summary of AFM Data**

conditions	25C/20%r.h.		22C/90%r.h.		40C/80%r.h.	
tape type	ME3	MP3	ME1	MP1	ME1	MP2
sample number	S2B	S2C	S2F	S2H	S2I	S2K
scan area ( $\mu\text{m}$ )	20	15	20	20	10	10
area ra	4.4	1.5	1.7	1.0	2.4	0.6
roughness RMS	5.7	4.8	2.9	1.7	3.0	0.8
ness mean height (nm)	12.6	10.9	2.4	14.5	6.2	5.6
(nm) max p-v	102	173	71	51	72	25
grooving sep. ( $\mu\text{m}$ )	0.33	0.31	0.27	0.12		0.74
$\theta$ (deg)	2.3	1.7	0.9	1.2		2.0
surface features	deep scratches + grooving dominate	grains visible, fracture scars, grooving, debris	grains visible, fracture scars, grooving, scratches	grains visible, fracture scars, grooving, scratches	roughness isotropic, some scratches, grains not resolved	grains visible, pullout, grooving

**Table 4.10 S2 Dummy Heads – Summary of AFM Data**

conditions	M1			M3		
	uncycled	25C/90%r.h.		uncycled	25C/90%r.h.	
tape type	none	ME1	MP2	none	ME1	MP1
sample number		M1B	M1C		M3A	M3C
scan area (µm)	20	2.6	30	20	20	20
area ra	1.7	1.5	2.2	0.5	3.6	3.8
rough-ness RMS	2.5	1.9	3.6	0.7	5.0	4.8
ness mean height (nm)	3.3	2.65	17.7	1.3	4.6	13.9
max p-v	46	12	150	10	103.8	35
grooving sep. (µm)		0.11	0.49		0.26	
θ (deg)		2.4	0.7		2.6	
surface features	spherical asperities isotropic distribution	plastic grooving	triangular deposits	rough-ness random	deposits smeared direction tape travel, scratching	ribbon deposit, scratching under deposit
staining observed by optical microscopy		NO	brown stain		NO	ribbon deposit
stain length(µm)			1.9			2 to 10
size by width(µm)			1.9			2
AFM height(nm)			35			40

**Table 4.11 M1 and M3 Dummy Heads – Summary of AFM and Optical Data**

conditions	uncycled	22C/90%r.h.		40C/80%r.h.	
		ME1	MP2	ME1	MP2
sample number		M2A	M2C	M2E	M2H
scan area (µm)	2.6	50	30	10	10
area ra	1.1	8.6	2.2	6.7	1.1
rough-ness RMS	1.6	15.3	3.6	8.1	1.1
ness mean height (nm)	1.7	23.2	17.7	15.0	12.2
max p-v	15	506	150	69	54
grooving sep. (µm)			0.49	0.19	0.31
θ (deg)			0.7	10.9	0.6
surface features	two spherical "grain" sizes diameter-44nm 500nm	smeared stain, ribbon deposit, scratching under deposit	delamination, pullout of 500nm grain, scratches	grooving	grooving, scratches, ribbon deposit
staining observed by optical microscopy		wavy brown	brown stain	NO	ribbon - sparse
stain length(µm)		2	10		2 to 8
size by width(µm)		1	10		2
AFM height(nm)		12	30		5

**Table 4.12 M2 Dummy Heads – Summary of AFM and Optical Data**

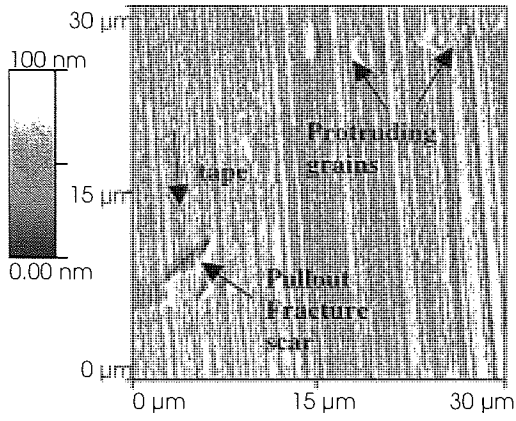


Figure 4.23 S1A AFM: ME Tape, 25C/20% r.h. Images 1-6 on this Page Shaded, Light from Left.

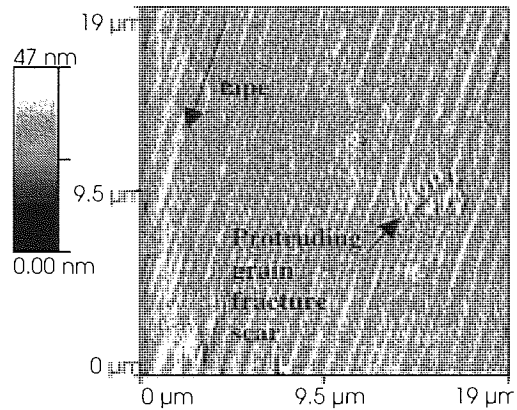


Figure 4.26 S1D AFM: MP Tape, 25C/20% r.h.

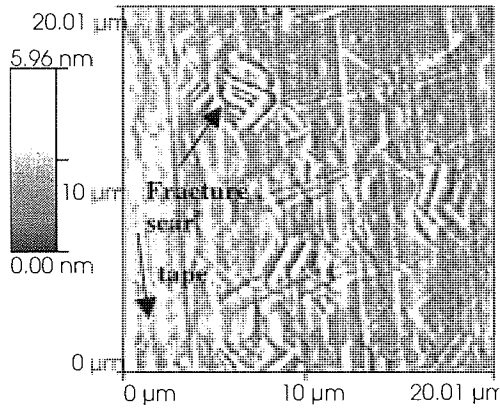


Figure 4.24 S1E AFM: ME Tape, 25C/90% r.h.

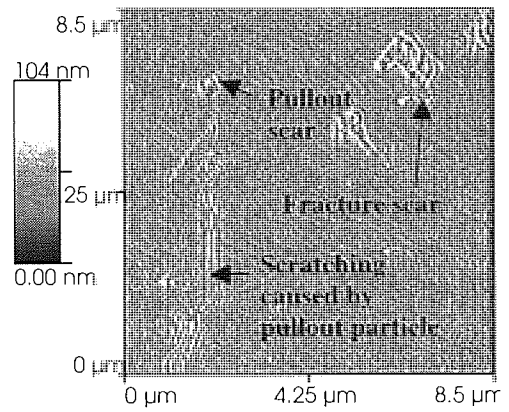


Figure 4.27 S1G AFM: MP Tape, 25C/90% r.h.

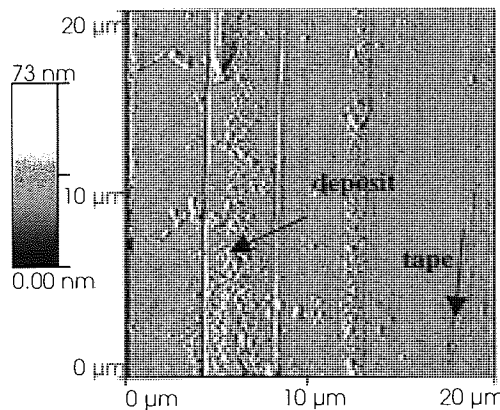


Figure 4.25 S1J AFM: ME Tape, 40C/80%

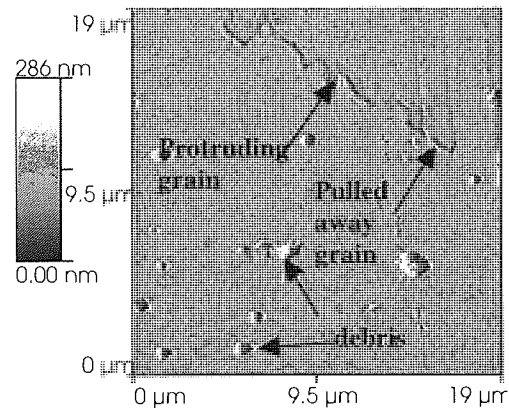


Figure 4.28 S1L AFM: MP Tape, 40C/80% r.h.

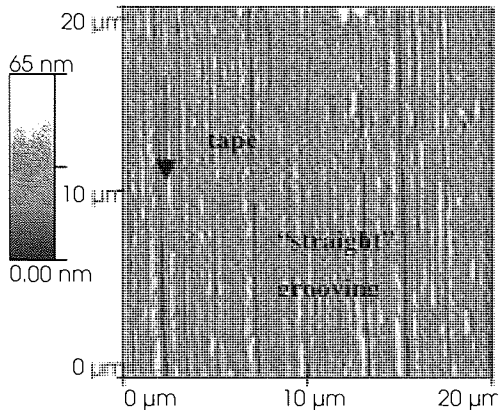


Figure 4.29 S2B AFM: ME Tape, 20C/20% r.h.  
 Figures 7-12 Shaded, Light from Left

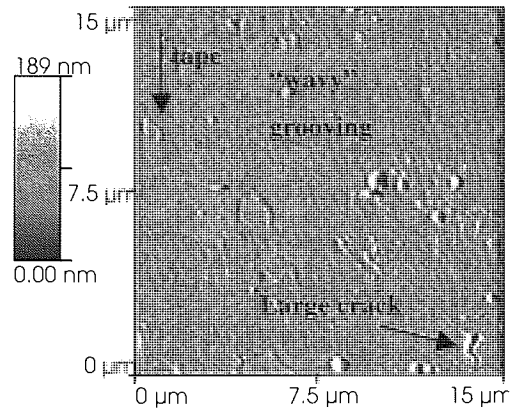


Figure 4.32 S2C AFM: MP Tape, 25C/20% r.h.

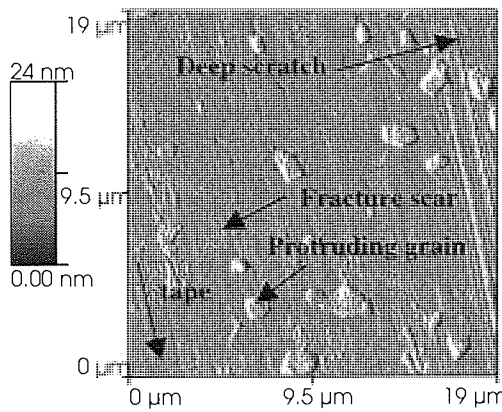


Figure 4.30 S2F: ME Tape, 22C/90% r.h.

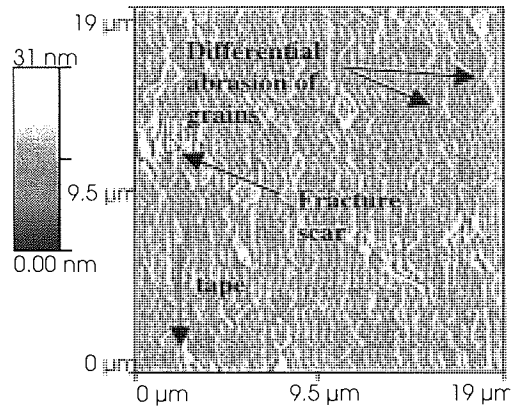


Figure 4.33 S2K AFM: MP Tape, 22C/90% r.h.

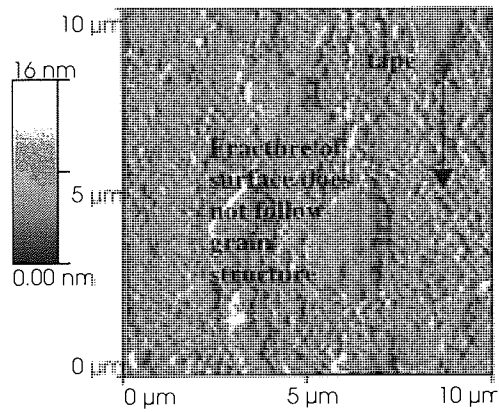


Figure 4.31 S2I AFM: ME Tape, 40C/80% r.h.

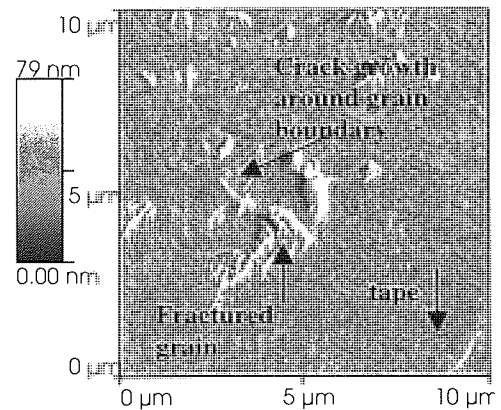


Figure 4.34 S2L AFM: MP Tape, 40C/80% r.h.



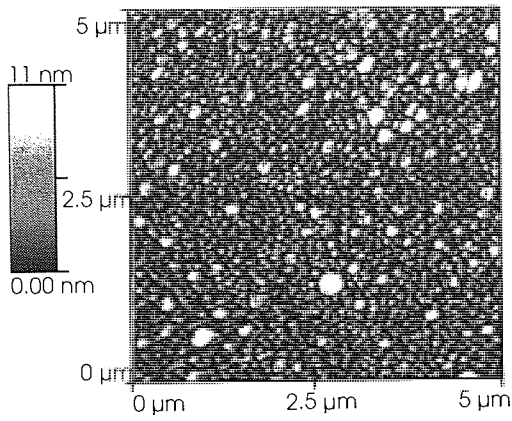


Figure 4.35 M1 AFM: UNCYCLED

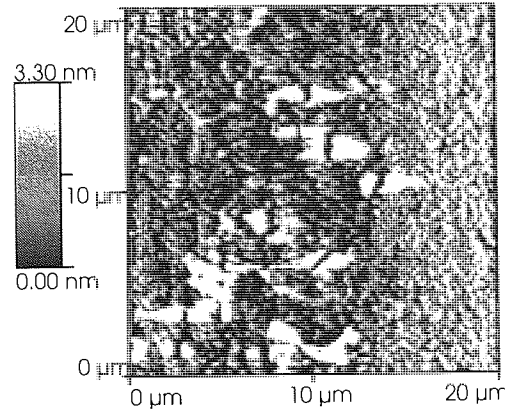


Figure 4.38 M3 AFM: UNCYCLED

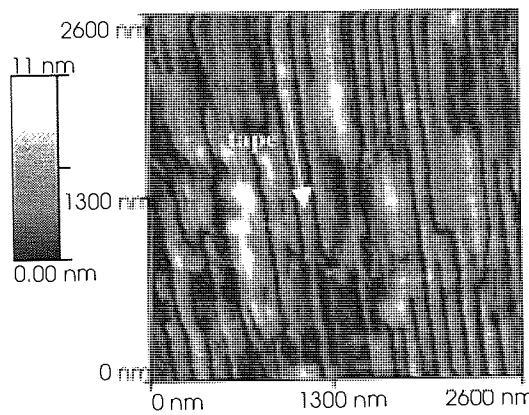


Figure 4.36 M1B AFM: ME Tape, 25C/90%r.h.

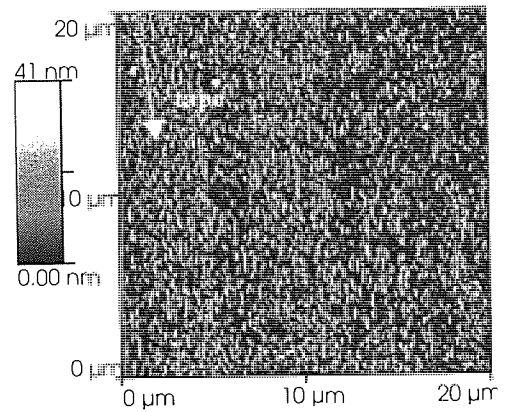


Figure 4.39 M3A AFM: ME Tape, 25C/90%r.h.

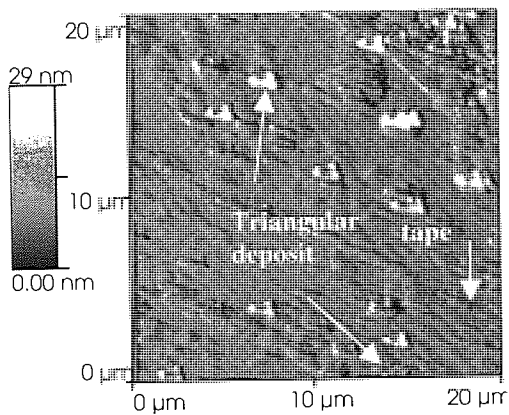


Figure 4.37 M1C AFM: MP Tape, 25C/90%r.h.

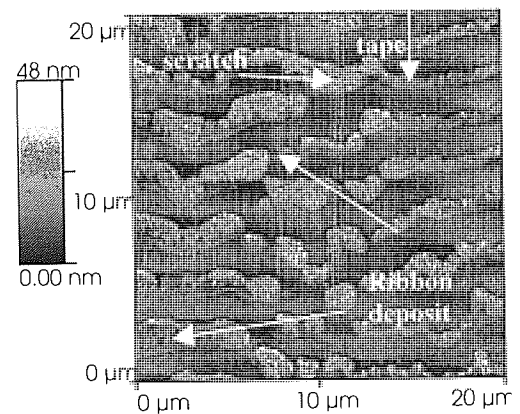


Figure 4.40 M3C AFM: MP Tape, 25C/90%r.h.

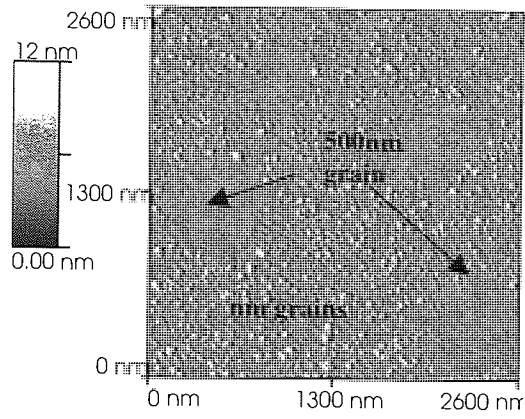


Figure 4.41 M2 AFM: UNCYCLED (Shaded, light from left)

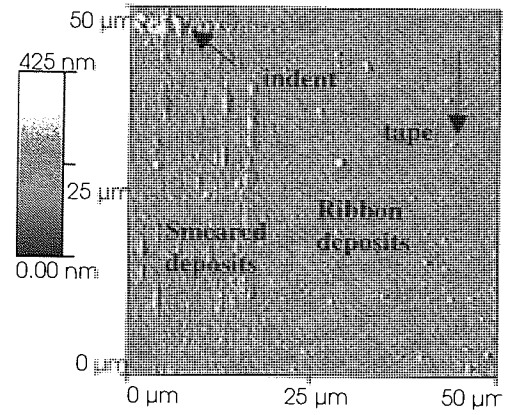


Figure 4.44 M2A AFM: ME Tape, 20C/90%r.h.

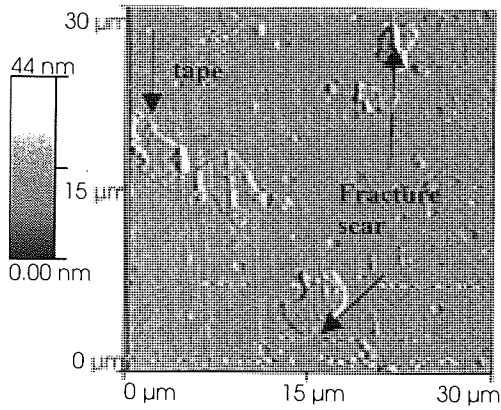


Figure 4.42 M2C AFM: MP Tape, 20C/90%r.h.

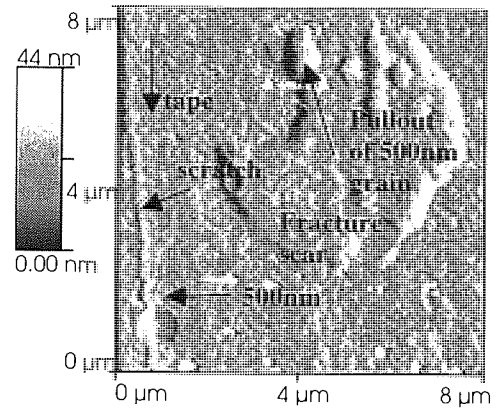


Figure 4.45 M2C AFM: Zoom on Figure 20 Showing Fracture Scar

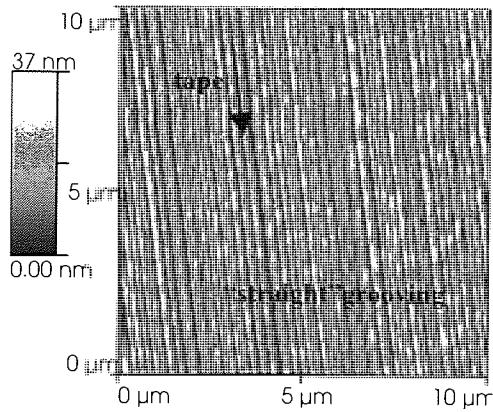


Figure 4.43 M2E AFM: ME Tape, 40C/80%

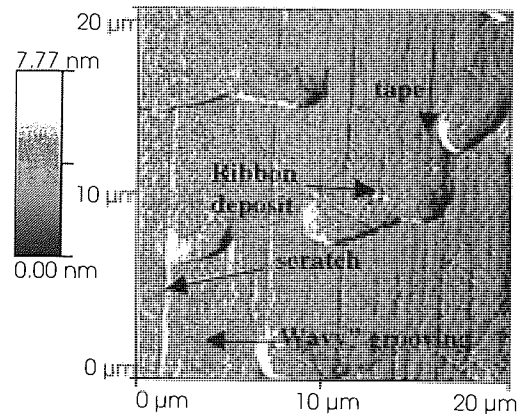
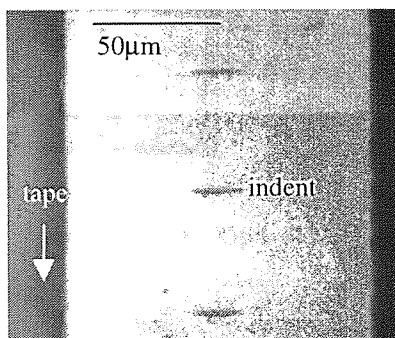


Figure 4.46 M2H AFM: MP Tape, 40C/80%

#### 4.3.2.2 Optical Images

Unlike the AFM images, far fewer differences were observed between the head surfaces by optical microscopy. Its main use was in measuring head protrusion and indentation length, and in checking for gross head damage. However it was also useful in imaging some phenomena associated with the head-tape interface - the extent of the wear zone, deposits on the head, and staining on the wear zone. Therefore optical photomicrographs were made only when novel phenomena were observed, and rather than systematically for each head/tape/environment combination. Representative images of these are presented in Figures 4.47-55. They are described and discussed alongside the corresponding AFM data in the Analysis Section. Figure 4.49 is discussed in 4.3.3.2, the section relating to the wear zone and the rest in Section 4.3.3.3 relating to debris/deposit/stain.



**Figure 4.47 S1L Optical Micrograph -MP Tape, 40C/80% r.h. Note Absence of Staining and Debris, except in Indents**

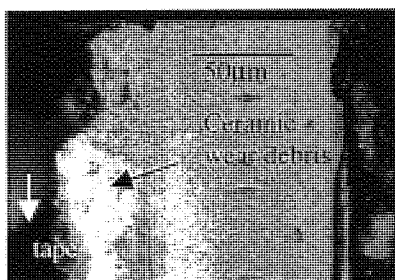


**Figure 4.48 S1G Optical Micrograph -MP Tape, 22C/90% r.h. Note Smearing of Head (Ceramic) Debris**

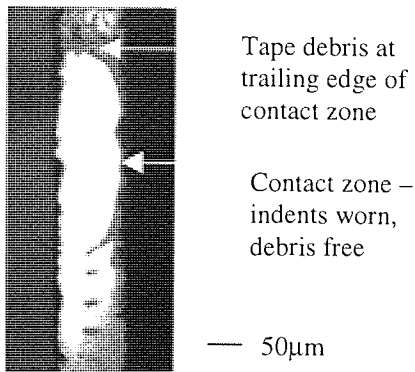


**Figure 4.49 M3A Optical Micrograph -ME Tape, 25C/90%r.h. Note Debris Surrounding Contact Zone (Indents Worn Through)**

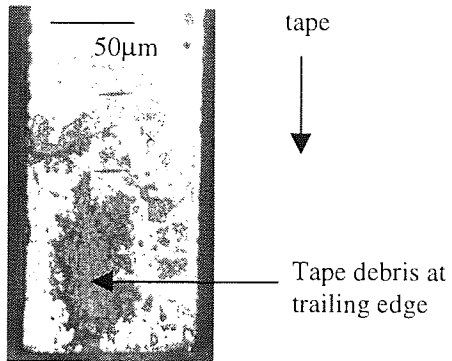


**Figure 4.50 MIC Optical Micrograph-MP Tape, 25C/90%r.h. Tape Debris at Trailing Edge.**

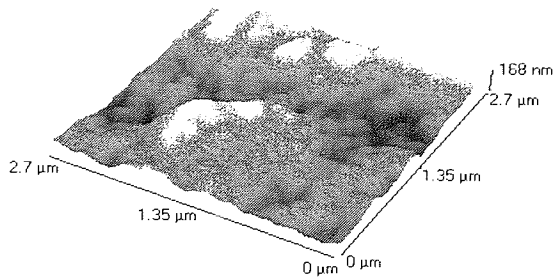


**Figure 4.51 AFM of ME Tape Debris on the Trailing Edge of S2F (22C/90%r.h.)**

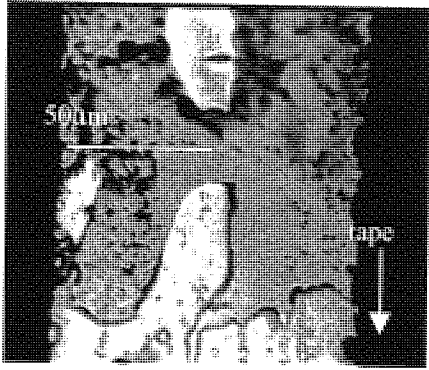


Figure 4.52 M1E Optical Micrograph. ME Tape, 60C/80%r.h. Lubricant Melted on to Head Surface. Centre Section of Head.

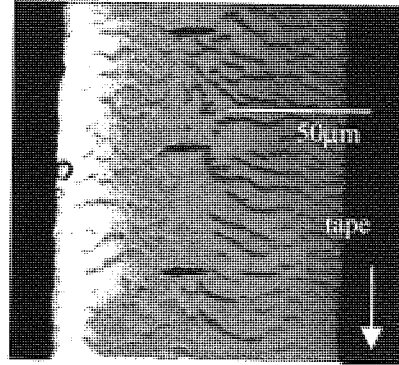


Figure 4.54 M2H Optical Micrograph. MP Tape, 40C/80%r.h. Shows Ribbon-Like Staining. Centre Section of Head.

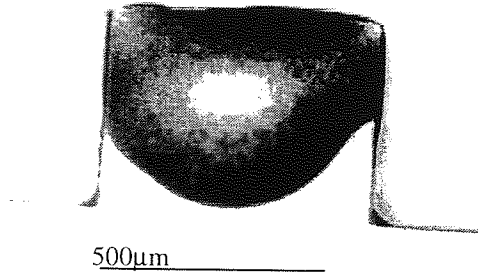


Figure 4.53 M1E Optical Micrograph-Side on View. ME Tape, 60C/80%r.h. Lubricant Melted on to Head Surface.

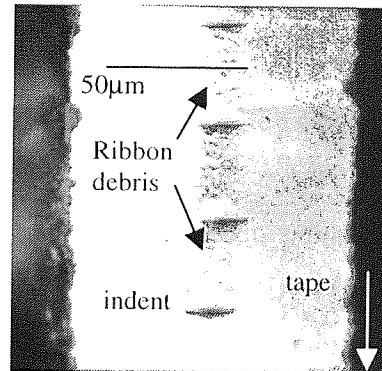


Figure 4.55 M3D Optical Micrograph. MP Tape, 25C/90%r.h. Shows Ribbon-Like Staining. Centre Section of Head.

### 4.3.3 Analysis of Topographical Data of the Cycled Dummy Heads

#### 4.3.3.1 Grain Fracture/Pullout in S1 and S2

Fracture is a wear mechanism by which material loss occurs as a result of subsurface crack growth. Where this occurs at the grain boundaries of a granular material, such as S1 and S2, an entire grain may be pulled out. Evidence for grain pullout may be seen in most of the images presented for S1 and S2. In Figure 4.34 (S2, MP tape, 40°C/80%r.h.) direct evidence is shown for grain pullout. On this image the grain structure may be observed, with some grain sized (~1µm diameter) holes. Also to be observed are a crack developing about a grain boundary and an incompletely pulled out grain exhibiting damage that does not correspond to the direction of tape travel. Such clear examples of pullout are rare – the observed microabrasion, a competitive wear mechanism will constantly act to “polish” out such holes, and indeed, where abrasive wear rate is large, prevent grain pullout. However, it was shown above that fracture leading to pullout occurs with cracking that does not necessarily follow the direction of tape passage, leaving a “scar” on the surface. Thus such grain sized scars, particularly visible where recessed or protruding relative to the underlying grain structure are taken as evidence of grain pullout having occurred.

It is not possible to compare quantitatively the frequency of grain pullout between the various conditions, and the fraction of the contact area they typically effect, due to the rarity of the phenomenon compared to the small number of samples analysed. However it is possible to make some broad, qualitative comparisons regarding pullout and surface topography:

#### *Room Temperature Cycling –*

*S1 Vs. S2* – The grain structure was more noticeable in S2. However this was to be expected as the multiple phase nature of this ceramic should give greater topographical contrast between neighbouring grains due to slightly different abrasive wear rates between phases. No difference between the amount of pullout was observed, between S1 and S2.

*Dry Vs. Wet* – For S1 for both ME and MP tape types, there appeared to be more evidence of grain pullout at 80%r.h. than at 20 %r.h. The microabrasive scratching appeared deeper

at 20%r.h. than that at 80%r.h. For S2 and ME tape there was evidence for a higher degree of fracture at high humidity, but against MP tape the surfaces of S2 looked similar after cycling at low or high humidity.

*Cycling at 40 °C/80%r.h. –*

In general much more damage was observed to the head surfaces, in keeping with the higher degree of wear observed at the higher temperature.

*S1, ME Tape – Deep scratching and surface deposits, but no evidence of pullouts*

*S1, MP Tape – Spherical debris on surface, also a protruding grain structure may be observed at the top of the image. To the right of this is either a break away of a protruding grain or a pullout, behind which lay two scratches along the direction of tape travel suggesting that this had been dragged across the head surface by the tape. A close up of this particle in Figure 4.56 shows cracking in the head surface beneath this particle.*

*S2, ME Tape – No microgrooving observed. Some grains smooth, others with isotropic roughness, suggesting intragranular surface fracture.*

*S2, MP Tape – Large number of grain pullouts, remaining grains show usual microgrooving, otherwise very smooth.*

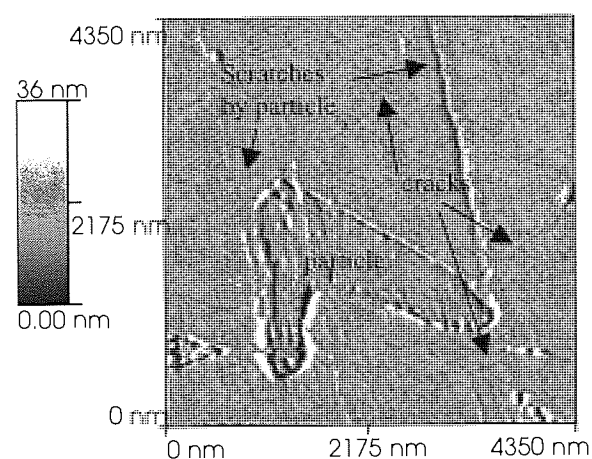


**Figure 4.56 S1L, MP2 Tape, 40°C/80%r.h. Zoom on Cracks under Particle**

*Integrity of Pullouts, and Damage Caused by Them – Figure 4.56 above shows evidence that a pulled out/broken away grain can keep its structure, after being dragged across the*

head surface by the action of the tape. It also shows that damage that may be done by this grain to the head surface includes a deep scratching of the head surface and cracks propagating within the head surface from the points of contact of the particle to the head, possibly following the grain boundary. Figure 4.27 shows for S1, the scar left behind by a grain pullout and the subsequent scratching of the head surface as the particle was dragged across the head surface by the action of the tape. It is worth noting the lateral deviation of the scratching caused by the particle was 3  $\mu\text{m}$  from its starting path, showing that it is possible that such a particle may be dragged across into the metal layer of a sandwich head.

#### 4.3.3.2 AFM of Uncycled Metal Heads

AFM images of the metal head surfaces maybe seen for M1, M2 and M3 in Figures 4.35, 4.38, and 4.41 respectively.

*M1* – Rounded asperities (sub-micron diameters), isotropic in the distribution of diameter and distribution.

*M2* – 500nm diameter “grains”, with smooth surfaces and of isotropic distribution. In between these larger “grains” lies a rougher region, with nm scale “grains” or rounded asperities.

*M3* – Irregular lateral roughness, but maximum peak-valley height of 3.3 $\mu\text{m}$  in sample 20 $\mu\text{m}$  area in Figure 4.38.

With cycling, these metal surfaces undergo wear, showing changes in surface roughness, become grooved in the direction of tape transfer, and in some cases show “pullout” or the adhesion of surface deposits. These phenomena are described in the subsequent sections.

#### 4.3.3.3 The Contact Zone

The wear rate data shows that wear was not uniform along the length of the head. This is shown in Figure 4.49, an optical image of an M3 dummy head having cycled against ME tape. Here the indents in the central part of the head are shown to be worn through and this region itself appears polished as compared to the extremities of the head. The wear zone is itself surrounded by black debris, with a greater accumulation at the trailing edge. This was consistent with the removal of material at the head tape interface due to wear. Inside the



wear zone AFM images, e.g. Figure 4.36, show microabrasive grooving. Outside the wear zone, the metal surfaces resemble those of the uncycled head surfaces, showing the absence of intimate head-tape contact that is necessary to cause ploughing of the head surface. The wear rate plots for the ceramic dummy heads show wear to usually extend the full length of the head, with a corresponding lack of black debris on the head surface.

#### 4.3.3.4 Roughness Values

In Tables 4.9 and 4.10 area roughness values are quoted for the sample areas of S1 and S2 respectively under each condition.  $R_a$ /RMS values for all heads lie in the range 0.5-5nm, except for S1, MP, 40°C/80%r.h. with an RMS roughness of 14.7nm. The much higher value of this head may be attributed to the large amount of debris observed on this head (Figure 4.28). In Table 4.11 area roughness values are quoted for the sample areas of M1 and M3, and for M2 in Table 4.12.  $R_a$  and RMS roughness values for these materials are complicated by the presence of surface deposits/staining in certain cases. However, in most cases, and for all stained heads, roughness values for the cycled metal heads also lie in the range of 0.5-5nm. The exceptions are M2 against MP tape, 20°C/90%r.h. ( $r_a = 8.6$ nm, RMS = 15.3nm), for which fracture/pullout scars maybe observed, adding to the roughness, and M2 against ME tape, 40°C/80%R.H. ( $r_a = 6.7$ nm, RMS = 8.1nm), in which the observed microgrooving is particularly deep.

Certain trends maybe observed in the quoted roughness values ( $r_a$  and RMS), and are discussed below. The trends are discussed for the substrate and metal heads separately, due to the greater range of conditions studied for the substrate heads and the possibility for observing the differences between the uncycled and cycled metal heads. The trends in RMS follow those in  $r_a$  roughness. The maximum and average peak-valley roughnesses, however, show a large variation between heads, due to the presence of pullout scars and particulate debris on the various surfaces.

##### 4.3.3.4.1 Trends in Roughness Observed in the Ceramic Heads, S1 and S2.

*S1 Vs. S2* - where cycled against the same tape and environmental conditions, S2 was at least half as rough again as S1, with the exception of the 40°C/80%r.h. condition with the

high observed RMS roughness for S1. At this condition however the  $r_a$  values were very similar (2.3 and 2.4nm for S1 and S2 respectively).

*ME Vs. MP* - for both S1 and S2, under the same environmental conditions, ME tape produced a rougher surface than MP tape. This is exhibited in the AFM images as deeper grooving in the direction of tape travel. With the exception of S1 in 40°C/80%r.h. condition,  $r_a$ /RMS roughness values produced by ME tape were at least twice those for MP tape.

*Between environmental conditions* – The roughness values produced at 40°C were generally much greater, being dominated by the higher degree of surface damage. Both S1 and S2 were rougher after being cycled at low humidity as compared to high humidity at 25°C whilst keeping tape type constant.

#### 4.3.3.4.2 Trends in Roughness Observed in the Metal Heads, M1-3

*Uncycled Vs Cycled* – For M1, ME tape, where microabrasion only observed,  $r_a$ /RMS roughness values were almost identical to the uncycled samples despite the obvious difference in qualitative topography. This showed no change within the contact zone of the head asperity contribution to head-tape separation, with wear of the as-deposited metal surface. In all the other cases, the presence of other features such as surface deposits/staining and deeper scratching, lead to the cycled surface exhibiting greater roughness values than the uncycled.

*ME Vs. MP, Between environmental conditions* – differences in roughness data was dominated by surface deposits, described in a later section.

#### 4.3.3.5 Microgrooving

In all the cycled heads grooving was observed running parallel to the direction of tape travel. Comparing uncycled and cycled metal heads, it can be seen that this was clearly due to the passage of the tape and shows that the highest asperities of the tape are in contact with the head. From the AFM images of the cycled heads it can be seen that this grooving

includes isolated scratches and in most cases a periodic grooving. The deeper scratches showed peak-valley heights in excess of 30nm, whilst typical peak-valley heights for the periodic grooving were in the order of 5nm. Taking a linescan through an image, perpendicularly to the direction of the grooving highlights this periodic grooving. Examples are given below for both ceramic (S2, MP tape, 22°C/90%r.h.), and metal (M1, ME tape, 25°C/90%r.h.) dummy heads in Figures 4.57 and 4.58 respectively.

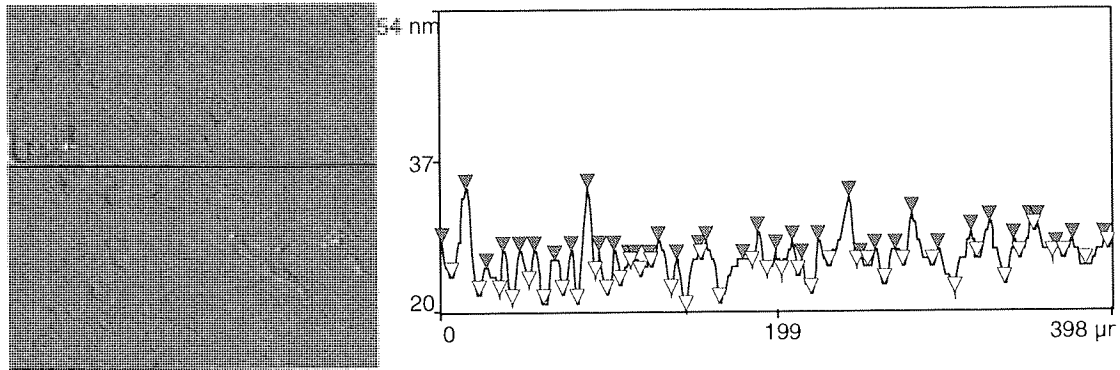


**Figure 4.57 S2C (MP1 Tape, 25/90%r.h.) Left: Line Scanned Perpendicular to Microgrooving. Right: Linescan; Peaks - Dark Triangles, Valleys - Pale Triangles**

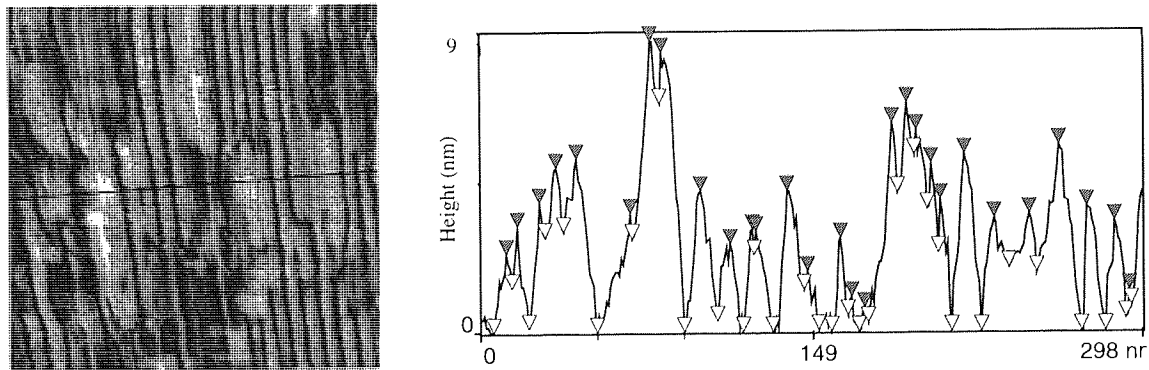


**Figure 4.58 M1, ME Tape, 20C/90%r.h. Left: Line Scanned Perpendicular to Grooving. Right: Line Scan; Peaks - Dark Triangles, Valleys - Pale Triangles**

#### 4.3.3.5.1 Peak-Valley Analysis of Microgrooving

The peaks and the valleys of the grooving can be identified by the TopoMetrix SPMlab software, and are shown in the linescans in Figures 4.57 and 4.59 as dark and pale triangles respectively. The angle between successive peaks and valleys and the lateral separation between successive peaks were calculated, and mean values of these are quoted in Tables

4.9-12. In all cases every tenth line was taken from images of 400 or 500 lines in resolution. These lines were taken perpendicular to the direction of grooving, and threshold values for peak-valley height and separation were set where necessary to exclude noise.

There were no observable trends, within the available sample, in mean peak separation and angle. Neither between metals and ceramics and metals, nor within the metals or ceramics, nor between ME and MP tape types, nor between different environmental conditions. Mean peak separation values for cycled heads were typically between 100 and 500nm, and mean angles between 1° and 3°. M2E (ME tape, 40°C/80%r.h. showed a high mean peak-valley angle of 10.9°. This corresponds with the deeper than usual microgrooving (35nm peak-valley height) exhibited for this head.

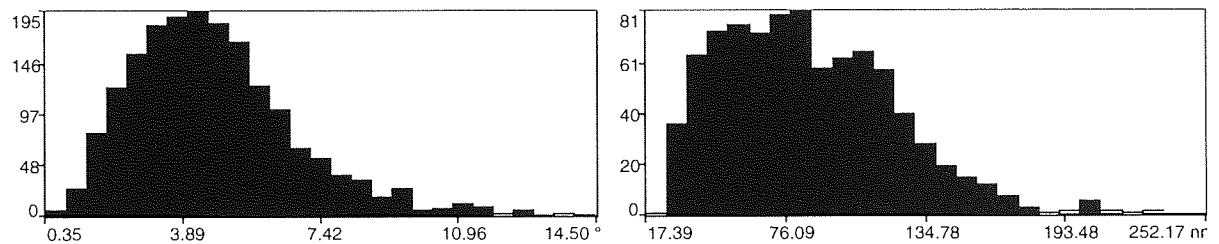


**Figure 4.59 Peak Angle (°) and Spacing (nm) Distribution Histograms. M1B, ME1 Tape, 25°C/90%r.h.**

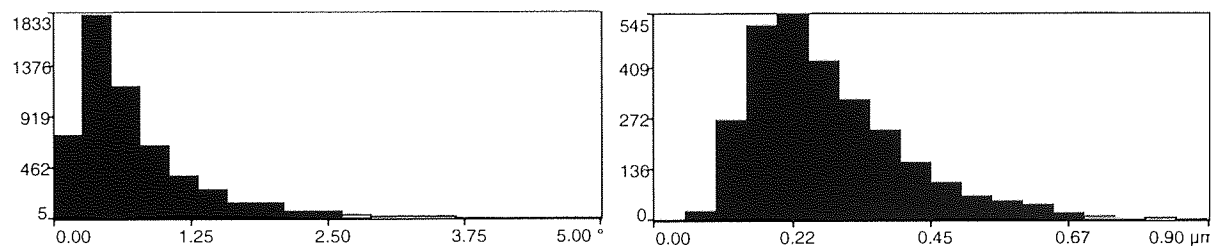


**Figure 4.60 Peak Angle (°) and Spacing (µm) Distribution Histograms. S2F, ME1 Tape, 22°C/90%r.h.**

As well as showing similar mean values, the heads also exhibit similar distributions in peak angle and separation values. Typical peak angle and spacing histograms are shown in Figures 4.59 and 4.60. These show respectively histograms for M1B (ME tape, 25°C/90%r.h.) and S2F (ME tape, 22°C/90%r.h.). These histograms show a distribution skewed to the low value (separation or angle) side of the distribution, with most of the distribution close in value to the mean.

#### 4.3.3.5.2 Differences in Microabrasion of Ceramic Substrates between ME and MP Tapes

The presence of surface deposits on the metal-coated dummy heads hinders a comparison between microabrasion caused by ME and MP tape for these heads. For S1 and S2, quantitatively: roughness values ( $r_a$  and RMS) show that for the same environmental conditions, ME tape produced a rougher surface, whilst peak valley analysis of the microgrooving showed no differences between the two tape types. Qualitatively one may observe (ME and MP images are placed side by side for S1 and S2) a large difference in the microgrooving: Longitudinally (parallel with the grooving) ME produced a straight grooving and MP a wavy grooving. This may also be observed with the metal-coated heads, for example M2 cycled at 40°C/80%r.h.: ME Tape, Figure 4.43, causes very straight grooving, whilst MP Tape, Figure 4.46, causes, in-between the straight scratches, a wavy grooving.

#### 4.3.3.6 Fracture Damage in Metals

This was not seen for the metal dummy heads, except for M2, when cycled against MP tape at 20°C/90%r.h. Fig 4.42 shows a fracture scar produced in such conditions. It can be seen to consist of a shallow delamination approximately 5 $\mu$ m in diameter. It includes, within the delaminated area, a pullout of one of the larger, 500nm diameter “grains “ observed in the uncycled material. Delaminations are also observed to occur in M3 layers in cycled sandwich heads.

#### 4.3.3.7 Debris, Deposits and Staining Observed on the Head Surface

A number of features on the head surfaces were observed by optical microscopy and AFM that show contrast from the head surface in terms of shape, depth and/or colour. These are classified below by appearance and origin as debris, a deposit or a stain. This is accompanied by a brief description of their nature and occurrence in each case. Examples of the various features maybe observed from the referenced AFM and optical images in this chapter. In Tables 4.9-12 the staining observed optically, and the deposits (together with dimensions) observed by AFM on the wear zone are listed systematically for each condition.

*Head and Tape Debris, Visible by Optical Microscopy*— discrete particles or conglomerations of particles sitting on the head surface. These were usually black in colour and may be observed on both ceramic and metal surfaces and for both ME and MP tape. Such debris usually lies around the edges of the wear zone, and within the microhardness indentations as shown in Figure 4.49, an M3 head cycled against ME Tape. Debris accumulation tends to be heavier at the trailing edge of the wear zone, as is shown in this image. Heavy debris accumulation at the trailing edge of a M1 head, this time, cycled against MP tape is shown in Figure 4.50. An AFM image of such debris is shown in Figure 4.51 from the trailing edge of a ceramic run against ME tape. The debris from MP tapes is very similar.

Not all heads show black debris on the head surface itself, but only around the head periphery, this was probably due to the contact, and therefore material removal zone covering the entire head. This is typical of the ceramic dummy heads, as shown in Figure 5.47 (S1 head, MP Tape, 40°C/80%r.h.). Here the accumulation of black debris occurs mainly in the microhardness indentations on the head surface.

This black debris could easily be removed by wiping lightly with a cotton bud or optical tissue soaked in acetone, showing only light adhesion to the head surface.

Figure 4.48, an S1 head run against MP tape at 25°C/90%r.h., shows a smearing of material off the side of the head. This material shows no contrast in colour to the head material, and is thus probably head material wear debris. This was seen for both S1 and S2, but very rarely, probably because such thin layers of ceramic would be expected to be very brittle, and thus easily dislodged.

In summary two optically distinct types of wear debris were observed: An occasional smearing of debris from the ceramic heads, with no colour contrast to the head surface, suspected therefore to be wear debris from the head material itself. The loosely held debris that is common to both metal and ceramic heads under all environmental conditions, is conversely to the first type, black in contrast to the white ceramic, and shiny metal-coated head surfaces and is thus likely to be tape debris.

*Spherical debris, Visible by AFM*- An example of this is shown in Figure 4.28, of an S1 head surface cycled against MP Tape at 40°C /80%r.h. This debris is differentiated from grain pullout, and staining deposits (discussed below), by its spherical shape, and by its height, which is of an order of magnitude (at ~100nm) greater than the peak-valley roughness of the underlying head surface (at ~10nm). Pulled out grains, and staining deposits were typically 10-20nm deep.

*Melting of Lubricant* - When M1 dummy heads were cycled at 60°C/80%r.h. against ME Tape a colourless film was observed to have formed over the head surface, as shown in Figure 4.52. This is shown to extend down the side of the head in Figure 4.53. Subsequent XPS analysis (see Section 4.4.4), shows this film to contain a PFPE, the lubricant class used on ME tapes. Therefore it may be assumed that an ambient temperature of 60°C, either alone or with the additional frictional heating of the head is sufficient to melt the lubricant of ME tapes. Subsequent higher temperature cycling tests were thus carried out at 40°C, at which temperature this effect was not observed.

*Stain* – On the ceramic head surfaces loose tape debris was observed, apart from which the head surfaces showed no marking, see Figure 4.47. However on the metal-coated heads, together with the tape debris, which tended to lie outside the wear zone, a brown stain was observed by optical microscopy on the wear zone itself. Examples of this are shown in Figures 4.54 and 4.55. Figure 4.54 is of an M2 head cycled against MP2 tape at 40°C/80%r.h., and Figure 4.55, an M3 head cycled against MP1 tape at 25°C/90%r.h. Both stains have in common a wavy, ribbon-like structure. However it may be seen that the former is on a much larger scale. The staining can be observed as similarly shaped features, or deposits, on the head surface by AFM, and thus can be measured. They are annotated as “deposits” on the presented AFM images of the head surfaces. AFM images of the ceramic head surfaces confirmed that no such deposits occurred on the ceramic head surfaces. The brown staining could not be removed by wiping the head surface with an optical tissue or cotton bud soaked in acetone. Indeed AFM images of stain, e.g. Figure 4.40, show the surfaces of the stain deposits as being abraded in a similar fashion to the underlying substrate. Thus the stain can be thought of as being strongly adhered to the head surface, persisting long enough on the head surface to be abraded through by the action of the tape, rather than be pulled away from the head surface directly.

For all cases typical dimensions of these staining deposits are included in Tables 4.11 and 4.12. The dimensions of the stain varied from head to head. There was no trend with environmental condition or for tape type within the MP family. The stain was normally ribbon like, however there were two exceptions. M1 run against MP2 tape at 25°C/90%r.h. in which the stain is shown as consisting of triangular particles by AFM and M2 run against MP2 Tape at 20°C/90%r.h.in which the stain consisted of platelets.

There was a marked difference in the frequency of occurrence of stain between MP and ME tape. In all cases passage of MP tape has caused brown staining. The only observed occurrence of brown stain with ME tape was for M2 at 20°C/90%r.h., which showed a brown stain optically, and ribbon like deposits by AFM. It also showed a fairly deep (400nm) deposit, smeared along the direction of tape travel. For M3 cycled under the same conditions against ME tape, there was a similar occurrence of a deposit smeared over the wear surface of the head, albeit with a much lower depth of 40nm, but no brown stain was observed optically on this head.



## 4.4 XPS Results

### 4.4.1 Introduction

In this section the results of the XPS analysis of the dummy heads are presented. For the magnetic materials in Section 4.4.2 these consist of Ar ion sputter depth profiles through the native oxides for each material, deposited on either Si(100) or a CaTiO<sub>3</sub> dummy head surface. For each component of each material, spectra are compared between as deposited, corroded, and cycled heads. Where appropriate, figures showing the synthetic fitting of peaks have been included. Also presented are tabular summaries of the identity, binding energy and quantification of the peaks for each material. For the Ceramic dummy heads in Section 4.4.3 typical spectra are shown from cycled heads together with a quantification of the various components observed, together with an example of each peak synthesis used in the quantification. Finally in Section 4.4.4 XPS spectra are shown of the PFPE lubricant transfer layer observed on the surface of ceramic dummy heads after cycling against ME Tape, and observed to be melted on M1 heads after cycling against ME tape at 60°C.

The cycled dummy heads were produced by the cycling tests described in Section 4.2 and are referred to by the sample numbers given therein. Microscopy (optical and AFM) of these head surfaces is shown in Section 4.3.

The Tapes, Metal Evaporated (ME1, ME2 and ME3) and Metal Particulate (MP1, MP2 and MP3) are as described in Section 4.1

### 4.4.2 Metals

#### 4.4.2.1 Sample Preparation

The three different metals were each studied by XPS: M1 – CoNbZr, M2 – FeNbSiN and M3 – FeTaN. Metal samples were prepared by sputter deposition on to Si(100) wafers or CaTiO<sub>3</sub> dummy heads at Philips Research Laboratories, to recipes, including thermal and magnetic treatments after deposition, devised by Philips, to produce films of the desired magnetic properties<sup>312</sup>. These were produced to a high level of consistency with respect to

composition (by AES), microstructure (by TEM) and magnetic properties<sup>313</sup>. These were then transported, in air, to Aston University for cycling tests and surface analysis, allowing for the formation of a native oxide, and thus changes in surface composition from the as-deposited film. As sandwich heads are stored and used in air this is a desired situation.

Dummy head tape-bearing surfaces were typically 120µm by 600µm and were analysed using the smallest available slit in front of the analyser of the spectrometer giving an analysed area 150µm in diameter. To provide a higher count rate, and hence better signal to noise ratio, analysis of heads prior to cycling was conducted on the side of the head, where this was coated with the magnetic material to an area greater than the tape-bearing surface. It was found that to fully characterise some of the minor components, especially Si in FeNbSiN, a larger area of magnetic material was required, and thus samples were prepared on Si(100). It is for this reason that the depth profile shown for FeNbSiN is for that on Si(100), where as for CoNbZr and FeTaN that on the head is shown. The samples deposited on Si(100) were also used for static corrosion tests, described below.

#### 4.4.2.2 Corrosion Tests

Samples deposited on Si(100) were heated up in water until corrosion products (the development of a rust colouring) were visible on the sample surfaces, and then analysed by XPS. CoNbZr required heating in water to 100°C for 3hours, FeNbSiN to 100°C for 10minutes and FeTaN to 100°C for 2 hours.

#### 4.4.2.3 Quantification and Identification of XPS Spectra

Quantifications are given relative to Fe in FeTaN and FeNbSiN, and relative to Nb in CoNbZr, as these peaks are present in each sample. In many cases, especially the cycled heads, C 1s is the largest peak. This may be attributable to a hydrocarbon contaminant overlayer, and is thus not included in the surface quantification. Similarly, though in some cases an O1s metal oxide peak maybe distinguished, the majority of the oxygen found by XPS on the metal surfaces was found to be associated with the hydrocarbon contamination layer, and that due to metal – oxygen bonds to be subsumed by this. Thus O1s is excluded from the quantification, and O1s peaks not shown in the comparison.

Peak binding energies quoted were charge corrected relative to C1s (CH<sub>2</sub>) at 184.6eV and chemical states identified by comparison with the NIST X-Ray Photoelectron Spectroscopy Database<sup>295,296</sup>.

#### 4.4.2.4 CoNbZr XPS Results

The XPS results for CoNbZr, in terms of peak binding energies, identity, and relative concentration are summarised in Table 4.13. Figure 4.61 shows the result of an Ar ion sputter depth profile of CoNbZr deposited on a CaTiO<sub>3</sub> head. The etch rate of 0.017nm/s was calculated by SUSPRE V 1.4<sup>309</sup>. On this the C 1s signal played a dominant part, reducing to 26%, due to persistence of thick contamination islands on the surface. The binding energy data of the C1s peak remained at 284.6 eV, indicative of CH<sub>2</sub>, and there is no C 1s peak at a lower binding energy where one might expect to see a carbide peak. Hence it may be concluded that there was no C within the film. Spectra C and D on Figures 4.62-64 correspond to 0nm and 30nm of removed depth respectively. The Co 2p signal is very weak at the surface, though A, the surface on the deposited on Si(100) sample shows the presence of CoO (781.5eV) at the surface. At 30nm depth D clearly shows Co as the metal, at 777.9eV. Nb was present as an oxide at the surface. At 206.7eV, this falls in between the expected values of 208.0eV for Nb<sub>2</sub>O<sub>5</sub> and 206.0eV for NbO<sub>2</sub>, and therefore may be due to either or a combination of the two. Zr was present as ZrO<sub>2</sub>, 181.9eV at the surface, and Zr metal, 178.7eV, at 30nm depth. The changes in chemical state from oxide to metal occur within the first 10nm of the depth profile, and thus the native oxide is approximately 10nm in thickness. Apart from the greater definition of the Co 2p peak, there was no other difference between the CoNbZr film deposited on CaTiO<sub>3</sub>, and that on Si(100).

Spectra A and B, in Figures 4.62-63, compare the native oxide with the corroded surface. There is no difference in the chemical states of the Co, Nb or Zr oxides. The major difference being the depletion of the CoO signal in the corroded sample. In the corroded sample the ratio of Co:Nb oxides is 0.29: 1.00, compared to 1.13:1.00 in the uncorroded sample. In both cases the ratio of Nb:Zr oxides is about the same (1:0.5).

Spectra E and F, in Figures 4.62-63, compare CoNbZr heads cycled against ME and MP tapes respectively, at room temperature (25°C) and high humidity (90%r.h.). E shows a small amount of the Nb metal, but the main constituent at the head surface is Co metal. F is very similar to the native oxide, as deposited on the head (C), consisting mainly of Nb oxides.

			Co 2p3		Nb 3d5		Zr 3d5	
			Metal	CoO	metal	NbO2 / Nb2O5	Metal	ZrO2
			777.9eV	781.5eV	202.7eV	206.7eV	178.7eV	181.9eV
A	Surface	Deposited on Si(100)		1.13		1.00		
B	Corroded Surface	Deposited on Si(100)		0.29		1.00		0.41
C	Surface	On CaTiO3 Head				1.00		
D	Sub-Surface	On CaTiO3 Head	3.26		1.00		0.21	
E	M1A-ME1Tape	25C/90%r.h.	32.20		1.00			
F	M1D-MP1Tape	25C/90%r.h.				1.00		

**Table 4.13 CoNbZr Identification and Quantification of XPS Spectra, and Key to Spectra used in Figures 4.62-64**

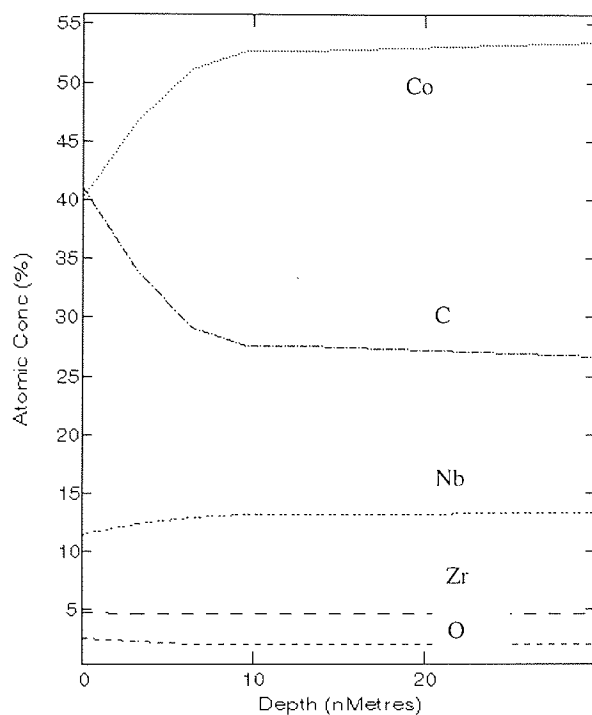


Figure 4.61 CoNbZr on CaTiO<sub>3</sub> Head. Ar Ion Sputter Depth Profile. Etch Rate 0.017nm/s

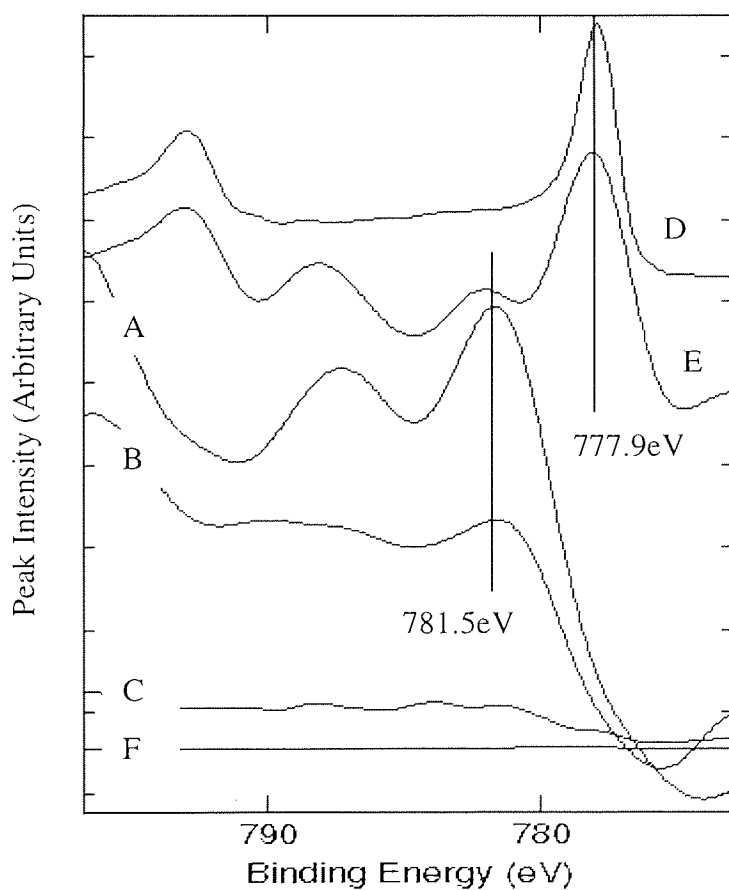


Figure 4.62 CoNbZr Comparison of Co 2p Spectra. Key in Table 4.13.

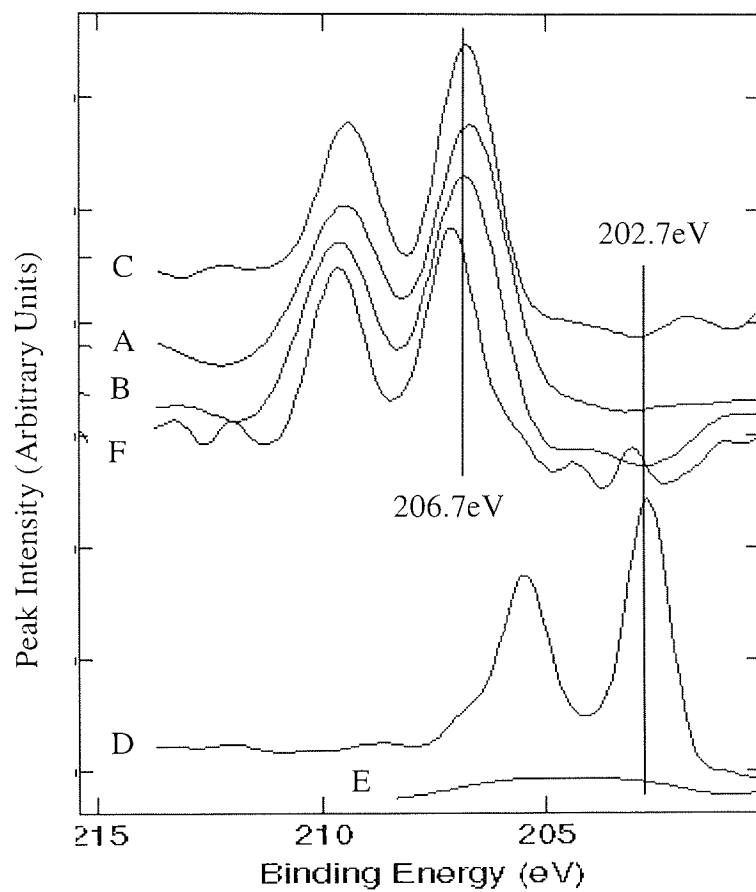


Figure 4.63 CoNbZr Comparison of Nb 3d Spectra. Key in Table 4.13.

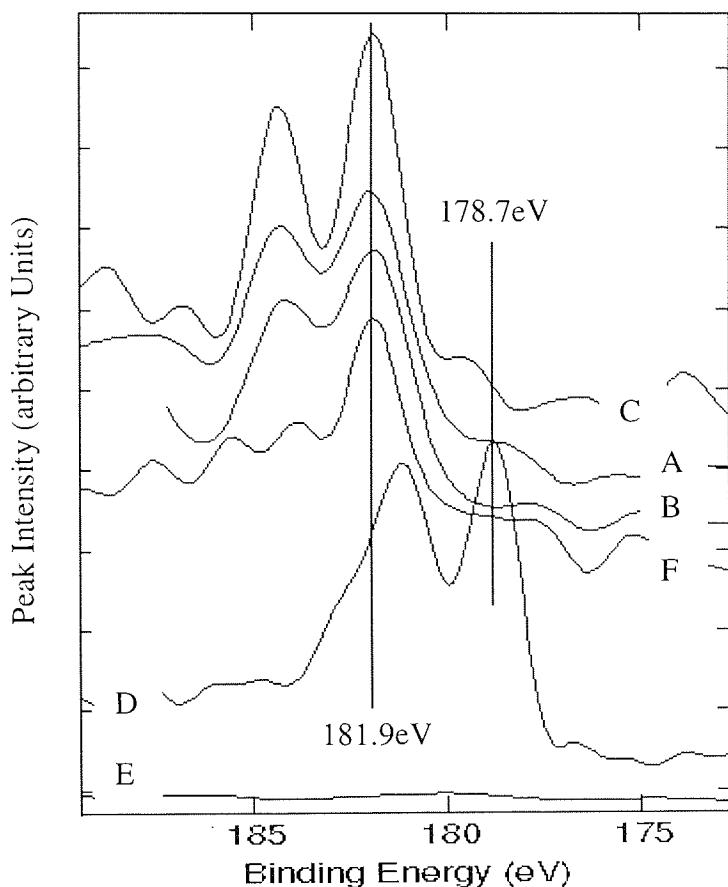


Figure 4.64 CoNbZr Comparison of Zr 3d Spectra. Key in Table 4.13.

#### 4.4.2.5 FeNbSiN XPS Results

The XPS results for FeNbSiN are summarised in Table 4.14, which gives the identities, binding energies and relative amounts for the observed peaks of XPS spectra of standard and cycled FeNbSiN samples.

Figure 4.65 shows an Ar ion sputter depth profile through the native oxide layer for FeNbSiN deposited on Si(100). Depth profiles of FeNbSiN deposited on CaTiO<sub>3</sub> heads are very similar. The etch rate of 0.007nm/s was calculated using SUSPRE V1.4<sup>309</sup>. The depth profile shows a surface oxide layer that was 10-15nm in thickness. The spectra of the components at the surface and at 20nm depth are shown as A and B respectively in Figure 4.66 for Fe 2p, 4.72 for Nb 3d, 4.74 for Si 2p and 4.75 for N 1s. Iron exists as the metal (707.0eV) on the surface as well as the bulk, showing that the native oxide of FeNbSiN contains no iron oxide. Nb exists as a mixture of oxides and nitride at the surface, and as nitride only in the bulk. Figure 4.71 shows the fitting of oxide and nitride peaks to the Nb 3d surface peak (with details given in Table 4.16). This shows Nb exhibiting it's full range

of oxides<sup>314</sup>: NbO(204.5eV), NbO<sub>2</sub>(206.0eV), Nb<sub>2</sub>O<sub>5</sub>(208.0eV), as well as the nitride NbN(203.5eV). Si at the surface is mainly in the form of SiO<sub>2</sub>, with some metal silicide (99.2eV). The Si content increases to a maximum at about 5nm depth as silicide increases and SiO<sub>2</sub> persists, after which with increased depth SiO<sub>2</sub> begins to deplete. This is responsible for the “blimp” seen in the relative concentrations of all the components at 5nm in the depth profile. It is not possible to determine which metal the silicide is associated with. Fe<sub>3</sub>Si occurs at 707.5eV and is not observed, however this does not rule out the possibility of the presence of another iron silicide, close ( $\pm 0.2$ eV) in binding energy to Fe metal. No binding energy values have been found in the literature for niobium silicides, but a niobium silicide may be present with the same ( $\pm 0.2$ eV) binding energy as NbN. N is present mainly as NbN, both at the surface and at 20nm. There is also a very small fraction of nitrate (nitrate “B” at 407.9eV), both at the surface and within the bulk.

The corroded sample, C, shows Fe<sub>2</sub>O<sub>3</sub> at the surface, as compared with Fe metal on the uncorroded sample, A. Like CoNbZr, where this exhibits a niobium oxide, the corroded sample shows niobium oxide at 206.7eV, intermediate between NbO<sub>2</sub> and Nb<sub>2</sub>O<sub>5</sub>. C shows Si 2p and N 1s peaks with unique binding energies (102.2eV and 399.6eV). In both cases these values are intermediate between the oxide and nitride/silicide observed in the uncorroded samples. These values may correspond to the hydroxylation of N and Si of the respective nitrides and silicides.

XPS analysis was carried out on FeNbSiN heads that were cycled under two different atmospheric conditions: High humidity at room temperature (25°C/90% r.h.); ME tape-D, MP tape -E. And high humidity above room temperature (40°C/80%r.h.); ME tape -F, MP tape-G. No N 1s or Si 2p signals were detected for any of these samples, and all show a strong C 1s contamination signal. F shows Fe metal only. E shows Fe<sub>2</sub>O<sub>3</sub> at 710.6eV and niobium oxide at 206.7eV. D and G also show Fe<sub>2</sub>O<sub>3</sub>, but in addition to this show FeOOH components. D shows Nb<sub>2</sub>O<sub>5</sub> at 208.0eV and G niobium oxide at 206.7eV.

The Fe 2p<sub>3/2</sub> peak is asymmetric, showing a tail to higher binding energy, due to spin-orbit coupling of the 3d orbitals in Fe. This complicates the fitting of synthetic peaks to resolve multiple oxidation states of Fe. It was decided to fit a tail experimentally to Fe metal in bulk FeNbSiN, B, where only one oxidation state was present. This is shown in Figure



4.67. The same tail parameters were used to fit the Fe 2p3 peak of the other spectra, confirming the existence of only one oxidation state (Fe<sub>2</sub>O<sub>3</sub>) in C and E, and the presence of two (Fe<sub>2</sub>O<sub>3</sub> and FeOOH) in D and G.

			Fe 2p3			Nb3d5			
			Metal	Fe2O3	FeOOH	Nitride	NbO	NbO2	Nb2O5
			707.0eV	710.6eV	712.8eV	203.5eV	204.5eV	206.0eV	208.0eV
A	Surface	Deposited on Si(100)	1.00			0.19	0.16	0.13	0.24
B	Sub-Surface	Deposited on Si(100)	1.00			0.14			
C	Corroded Surface	On CaTiO3 Head		1.00				0.22(206.7eV)	
D	M2B-ME1Tape	25C/90%r.h.		1.00	0.44	0.10			0.4
E	M2D-MP2Tape	25C/90%r.h.		1.00		0.28		0.19(206.7eV)	
F	M2E-ME1Tape	40C/80%r.h.	1.00						
G	M2G-MP2Tape	40C/80%r.h.		1.00	0.41	0.25		0.22(206.7eV)	
			Si 2p			N1s			
			Metal Silicide	Si-OH?	SiO2	Nitride	Corroded Nitride	Nitrate 'A'	Nitrate 'B'
			99.2eV	102.2eV	103.2eV	396.9eV	399.6eV	407.0eV	407.9eV
A	Surface	Deposited on Si(100)	0.02		0.95	0.21			0.04
B	Sub-Surface	Deposited on Si(100)	0.01			0.3			0.02
C	Corroded Surface	On CaTiO3 Head		0.42			0.1	0.11	
D	M2B-ME1Tape	25C/90%r.h.				0.21			
E	M2D-MP2Tape	25C/90%r.h.							
F	M2E-ME1Tape	40C/80%r.h.						0.83	
G	M2G-MP2Tape	40C/80%r.h.							

Table 4.15 FeNbSiN Identification and Quantification of XPS Spectra, and Key to Spectra in Figures 66,70,72, and 73.

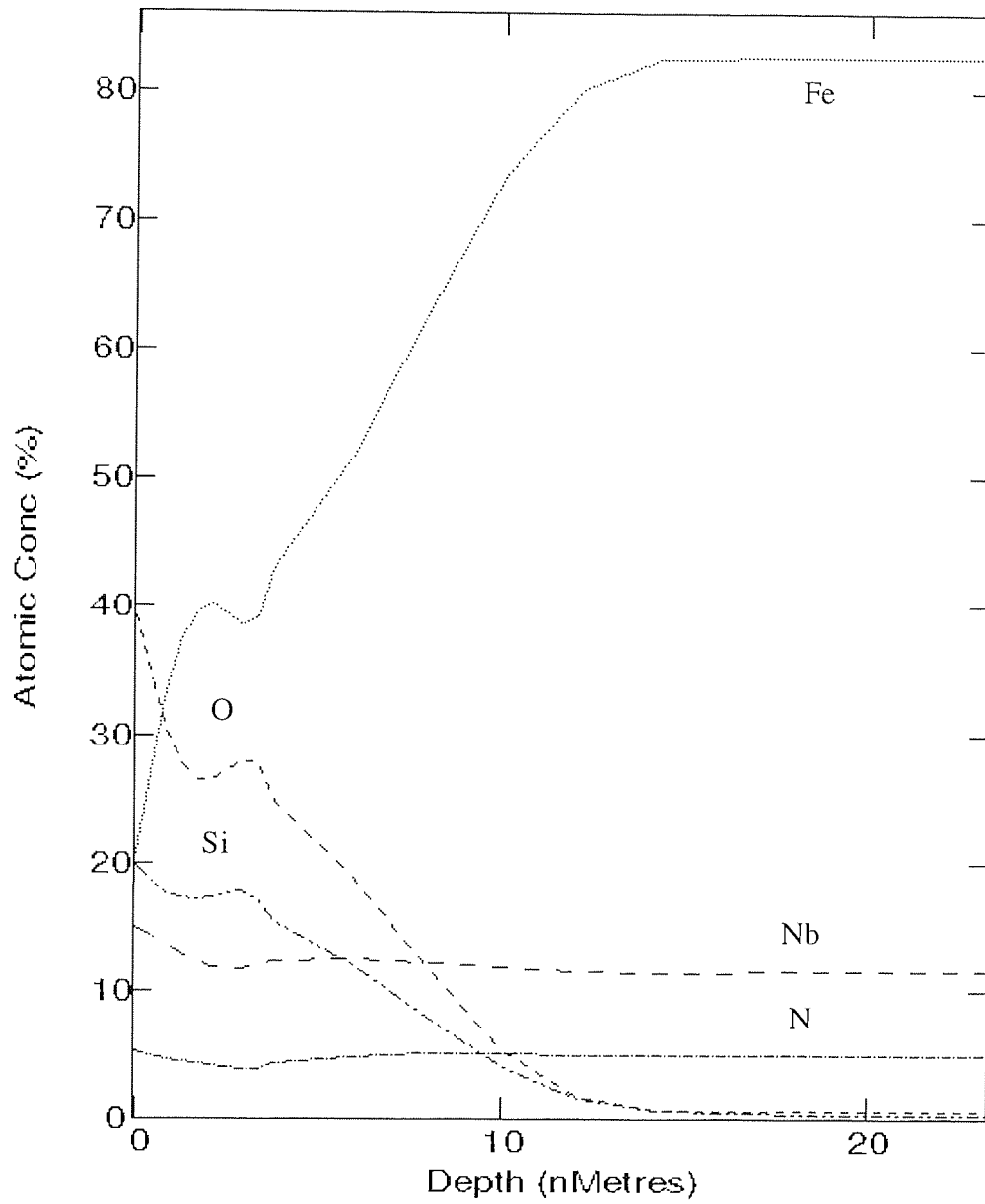


Figure 4.65 FeNbSiN Deposited on Si(100)Ar Ion Sputter Depth Profile. Etch Rate 0.007nm/s

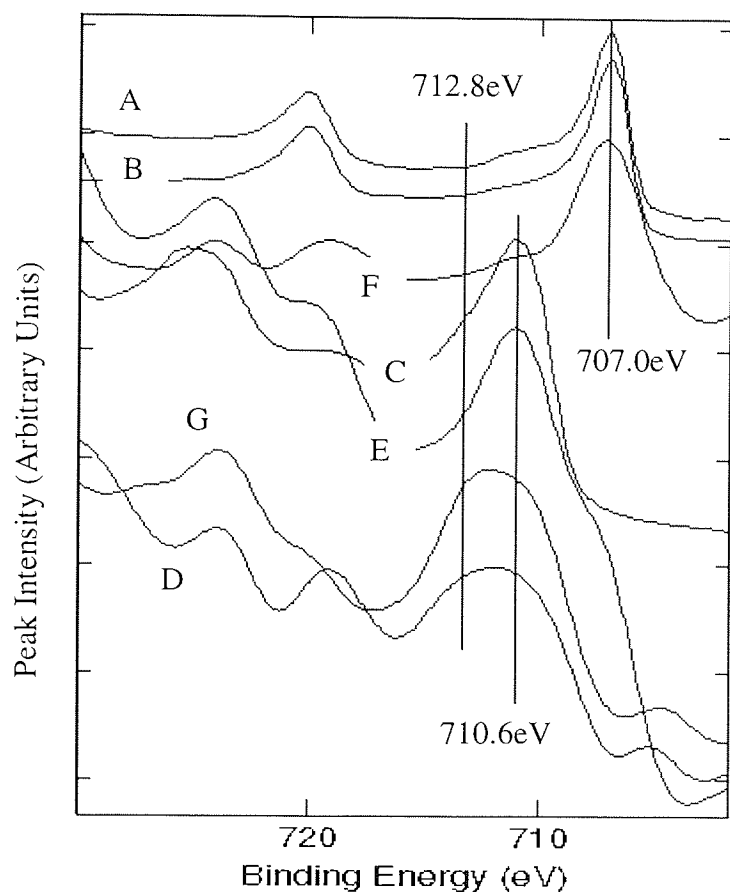


Figure 4.66 FeNbSiN Comparison of Fe 2p Spectra. Key in Table 4.14.

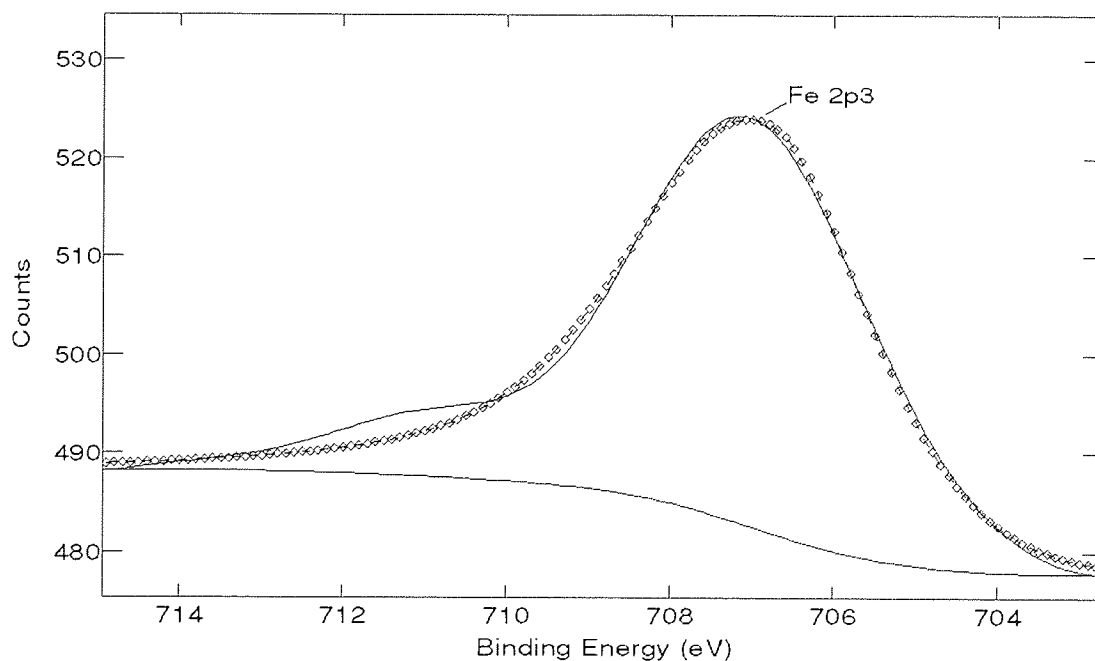


Figure 4.67 FeNbSiN Fitting of Fe 2p<sub>3</sub> Metal Peak at 707.0eV (A, B and F). Diamonds Mark Synthetic peak, Solid Line the Actual Peak. Synthetic Peak: FWHM = 3.06eV. Asymmetric Tail: Height = 0.40, Mixing Ratio = 31.13, Exponential Factor = 0.048

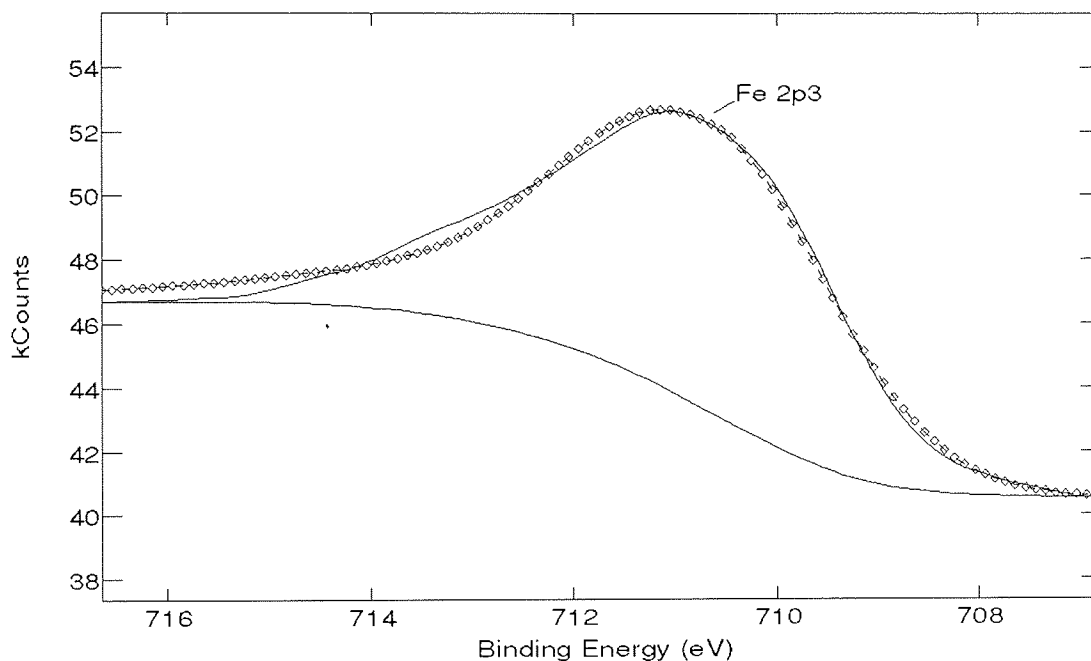


Figure 4.68 FeNbSiN Fitting of Fe2p3 Oxide ( $\text{Fe}_2\text{O}_3$ ) at 710.6eV, FWHM = 2.75eV (C, E). Diamonds Mark Synthetic peak, Solid Line the Actual Peak. Asymmetric Tail Factors as Figure 4.69

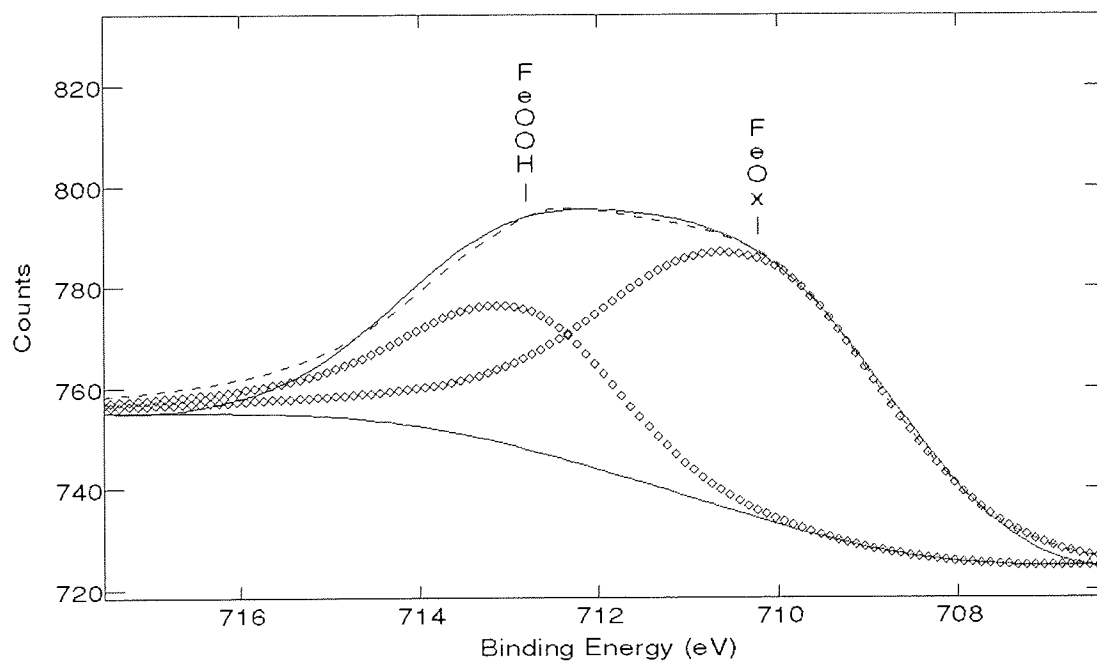


Figure 4.69 FeNbSiN Fitting of Fe2p3 Hydroxide (712.8eV, FWHM = 2.48eV) and Oxide (710.2eV, FWHM 3.40eV) to D and G Cycled against ME and MP at 20°C/90% r.h. and 40°C/80% r.h. respectively. Diamonds Mark Synthetic Peaks, Solid Line the Actual Peak, and the Dotted Line the Envelope of the Synthetic Peaks. Asymmetric Tail Factors as Figure 4.69.

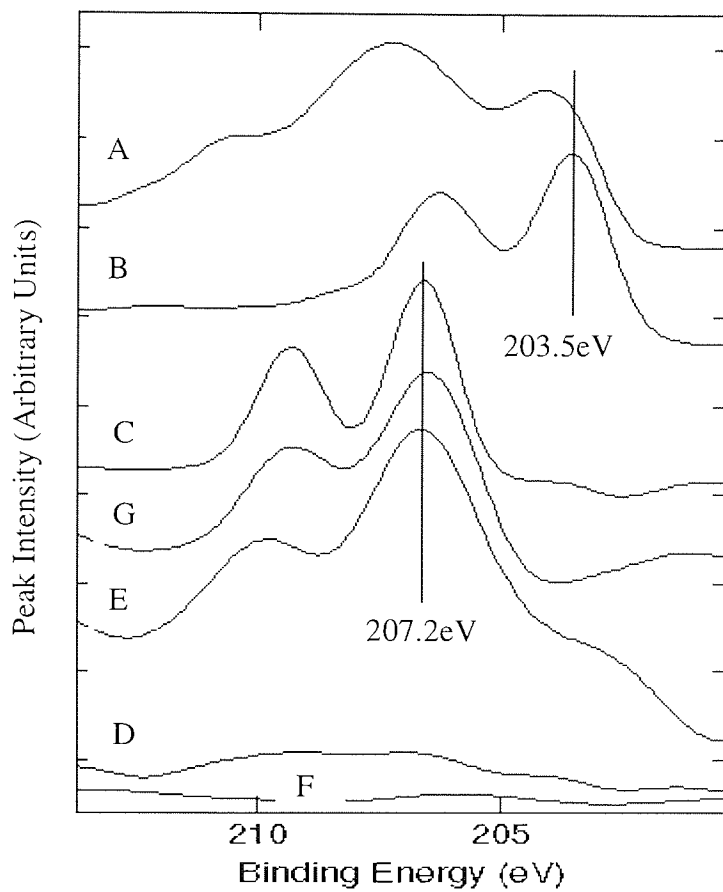


Figure 4.70 FeNbSiN Comparison of Nb 3d Spectra. Key in Table 4.14.

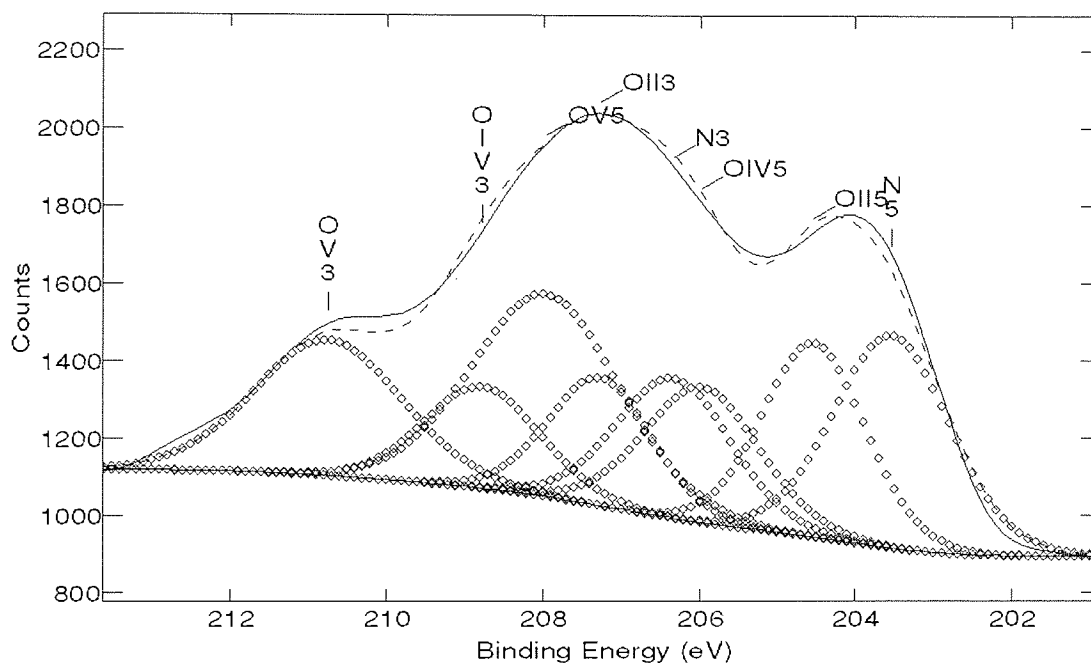


Figure 4.71 FeNbSiN Fitting of Nb 3d Peak on Surface Deposited on Si(100). Solid Line = Peak and Background. Diamonds = Synthetic Peaks. Dotted Line = Envelope of Synthetic Peaks. Key given in Table 4.15.

Chemical State	Component	Label Fig.4.73	B.E. (eV)	Area	Height	FWHM	% (using 3d5)
Nb <sub>2</sub> O <sub>5</sub>	3d5	OV5	208.0	100	100	2.31	33
	3d3	OV3	210.7	65	67	2.31	
NbO <sub>2</sub>	3d5	OIV5	206.0	33	67	1.81	18
	3d3	OIV3	208.8	39	50	1.81	
NbO <sub>2</sub>	3d5	OII5	204.5	67	96	1.61	22
	3d3	OII3	207.3	44	63	1.61	
NbN	3d5	N5	203.5	81	105	1.82	27
	3d3	N3	206.3	54	69	1.80	

Table 4.15 Peak Fit Table for Nb 3d in Figure 4.71, FeNbSiN on Si(100). Peak Area and Height Relative to Nb<sub>2</sub>O<sub>5</sub> 3d5. Doublet Separation 2.8eV, Height Ratio 3:2.

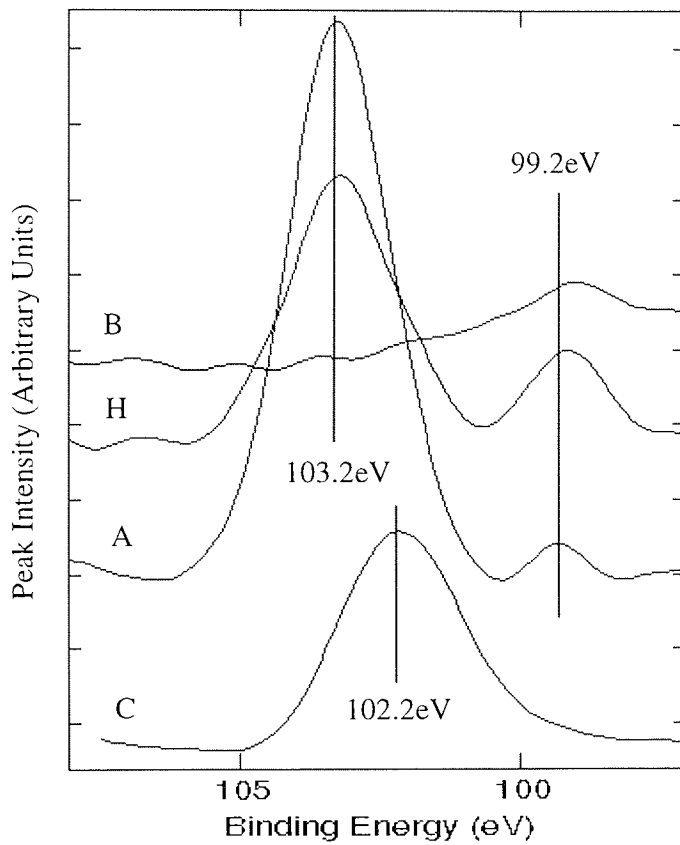


Figure 4.72 FeNbSiN Comparison of Si 2p Spectra. A- As Deposited on Si(100). H- Etched 5-10nm into Sub-surface. B- 20nm into Sub-surface. C- Corroded Surface. Key in Table 4.14.

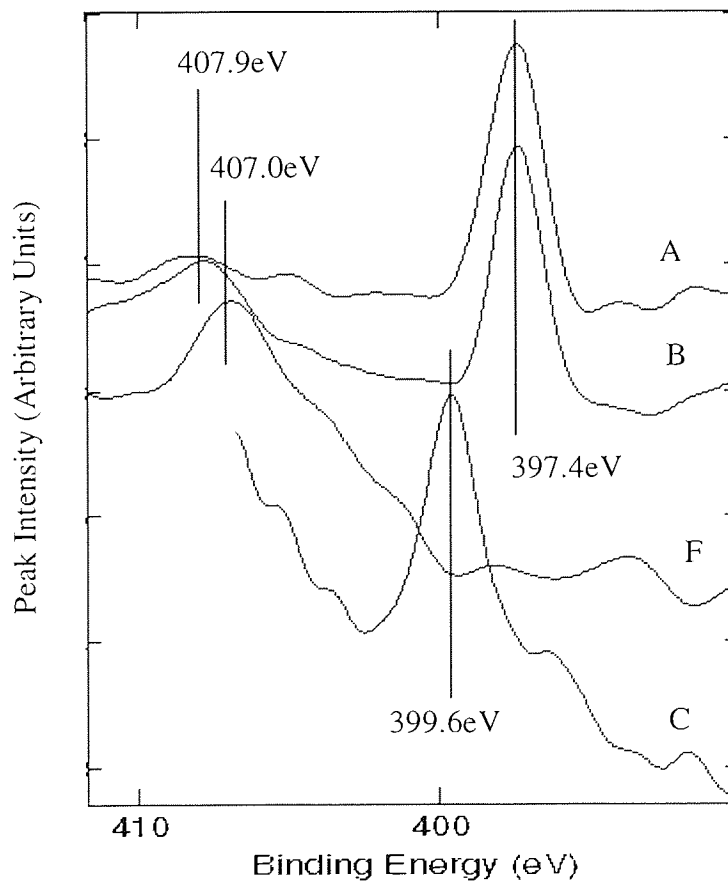


Figure 4.73 FeNbSiN Comparison of N 1s Spectra. Key in Table 4.14.

#### 4.4.2.6 FeTaN XPS Results

Table 4.16 summarises the XPS results for FeTaN, the identity, binding energy and quantification relative to Fe 2p of the XPS spectra of standard, corroded and cycled dummy heads.

Figure 4.74 shows an Ar ion sputter depth profile through the native oxide of FeTaN deposited on a CaTiO<sub>3</sub> head. It shows the surface oxide layer to be approximately 20nm in thickness. Spectra C and D are of the surface and 40nm in depth respectively for Fe, Ta and N in Figures 4.75, 4.76, and 4.77. These show that iron exists as Fe<sub>2</sub>O<sub>3</sub> at the surface, and Fe metal in the bulk. The Fe 2p<sub>3/2</sub> peaks were fitted with asymmetric peaks, with the same tail factors as FeNbSiN, to confirm that only one oxidation state was present in either case. Tantalum exists as Ta<sub>2</sub>O<sub>5</sub> (25.3eV) at the surface, and at 40nm depth, mainly as TaN/Ta metal (22.8eV), but with a significant fraction (1/3) of oxide remaining. Unfortunately it was not possible to confirm whether Ta at 22.8eV was the metal or the nitride, as a binding energy could not be found in the literature for a nitride of tantalum. Implantation of N into Ta at this laboratory<sup>315</sup> showed Ta 4f<sub>7/2</sub> in the nitride to occur at the same binding energy as the metal (22.8eV), within the resolution of the spectrometer. The fitting of the Ta 4f peak at 40nm depth is shown in Figure 4.78, with peak fit details in Table 4.17. At the surface nitrogen exists as both a metal nitride (396.9eV) and the nitrate "C" (404.0eV), and does so at 40nm depth, but with the nitrate peak broader, perhaps encompassing a number of different forms.

The only difference between FeTaN deposited on Si(100) (spectra A) and CaTiO<sub>3</sub> head (C), is in the N1s peak (Figure 4.77). Both show nitrate at 404.0eV, but only the CaTiO<sub>3</sub> deposited sample shows the metal nitride (396.6eV) peak as well. Upon corrosion of the sample deposited on Si(100) (B), iron and tantalum remain in the same oxidation states, albeit with the amount of Ta<sub>2</sub>O<sub>5</sub> reduced relative to Fe<sub>2</sub>O<sub>3</sub>. Like the corroded FeNbSiN sample, N 1s shows only one peak, and at the same energy (399.5eV), which is again likely to be the corrosion product of the metal nitride (N-OH).

The FeTaN dummy heads cycled against ME and MP tapes (spectra E and F) show similar surfaces – iron in the metallic form only and tantalum in the nitride/metallic form only.



			Fe 2p3		Ta 4f7		N1s			
			Metal	Fe2O3	Metal / Nitride	Ta2O5	Nitride	Corroded Nitride	Nitrate 'C'	Nitrate 'D'
			707.0eV	710.6eV	22.8eV	25.3eV	396.9eV	399.5eV	404.0eV	406.7eV
A	Surface	Deposited on Si(100)		1.00		0.68			0.86	
B	Corroded Surface	Deposited on Si(100)		1.00		0.36		0.41		
C	Surface	On CaTiO3 Head		1.00		0.17	0.04		0.11	
D	Sub-Surface	On CaTiO3 Head	1.00		0.15	0.08	0.08		0.07	
E	M3B-ME1Tape	25C/80%r.h.	1.00		0.28					
F	M3C-MP1Tape	25C/80%r.h.	1.00		0.25					

**Table 4.16 FeTaN Identification and Quantification of XPS Spectra, and Key to Spectra in Figures 4.75-77**

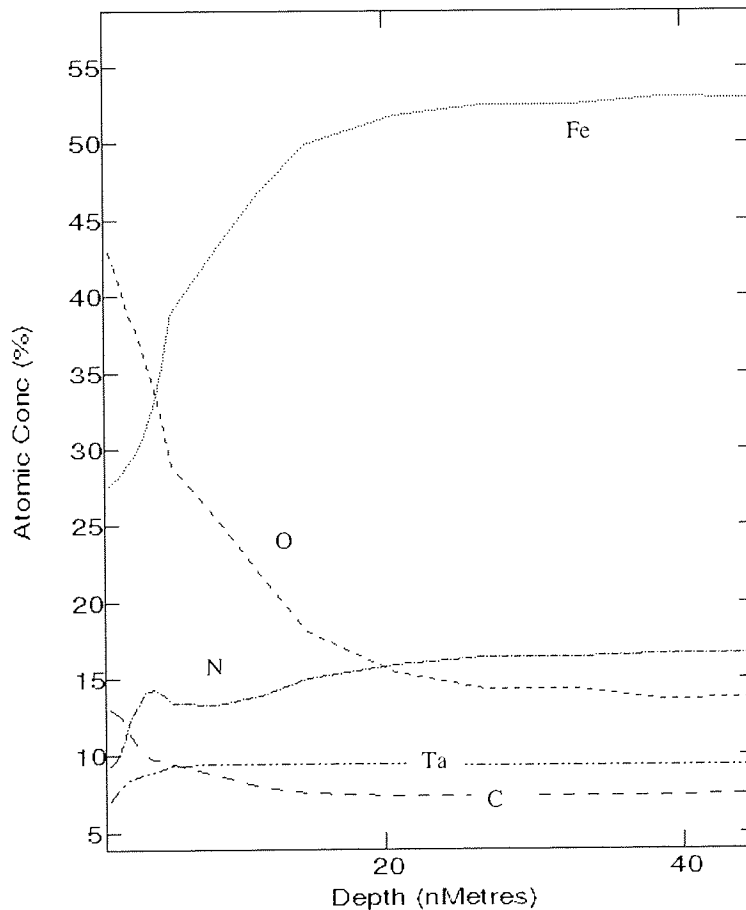


**Figure 4.74 FeTaN Deposited on CaTiO3 Head Ar Ion Sputter Depth Profile. Etch Rate 0.01nm/s**

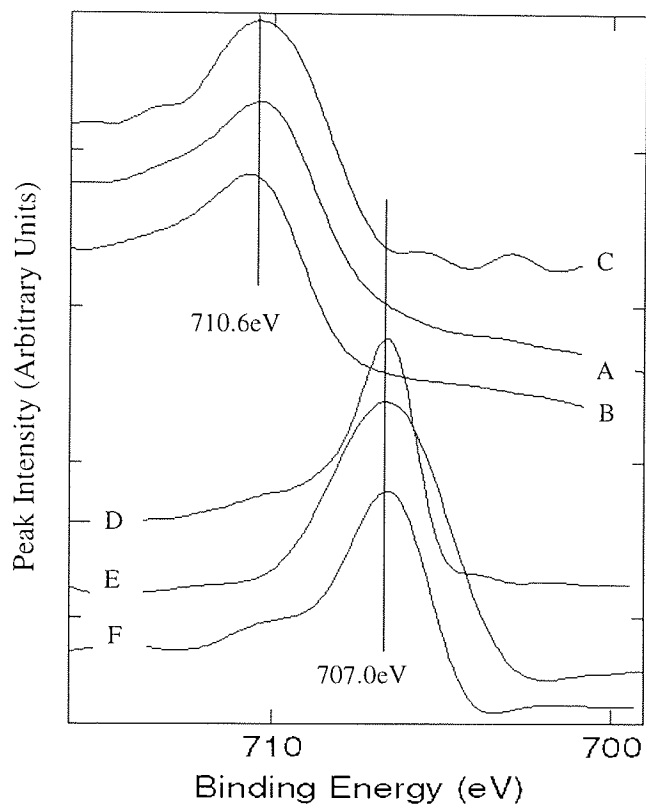


Figure 4.75 FeTaN Comparison of Fe 2p<sub>3</sub> Spectra. Key in Table 4.16

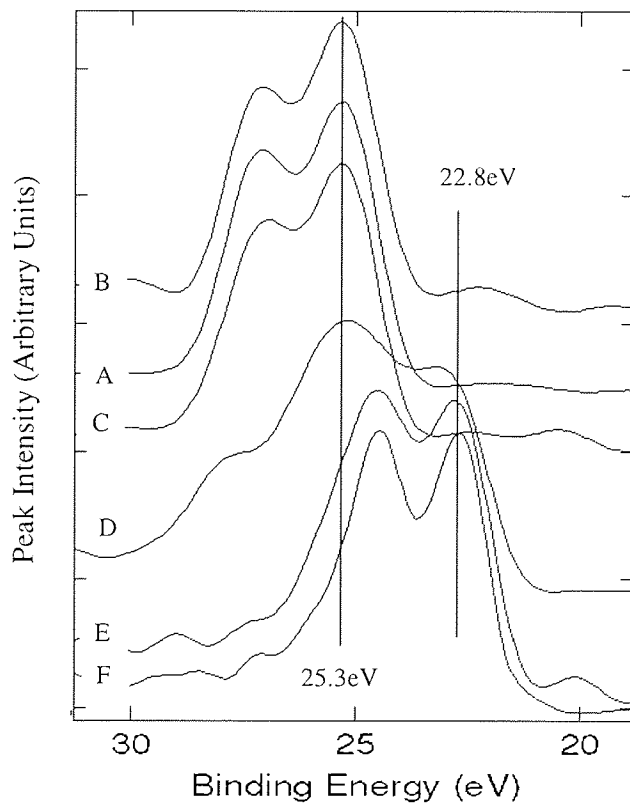


Figure 4.76 FeTaN Comparison of Ta 4f Spectra. Key in Table 4.16.

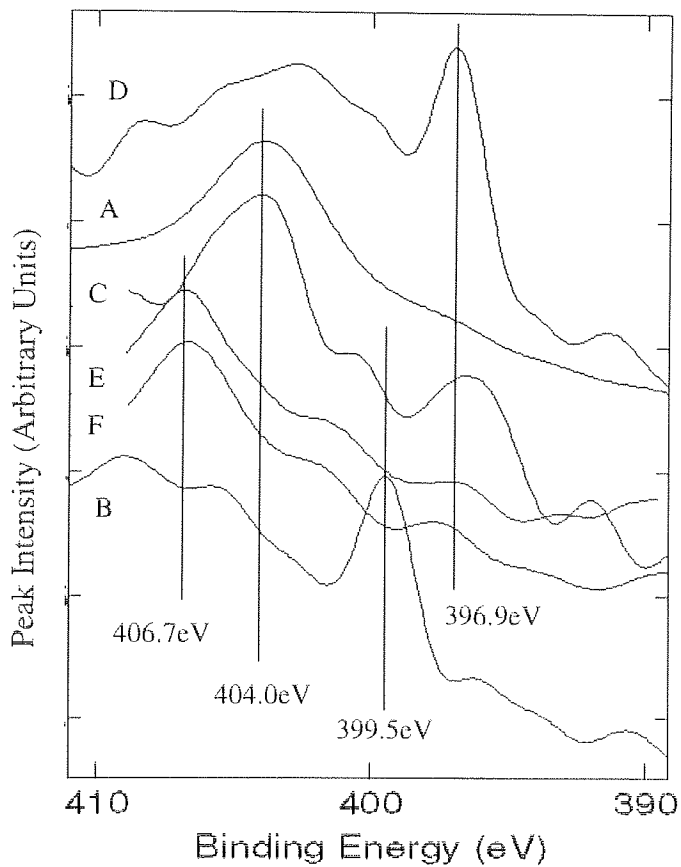


Figure 4.77 FeTaN Comparison of N 1s Spectra. Key in Table 4.16.

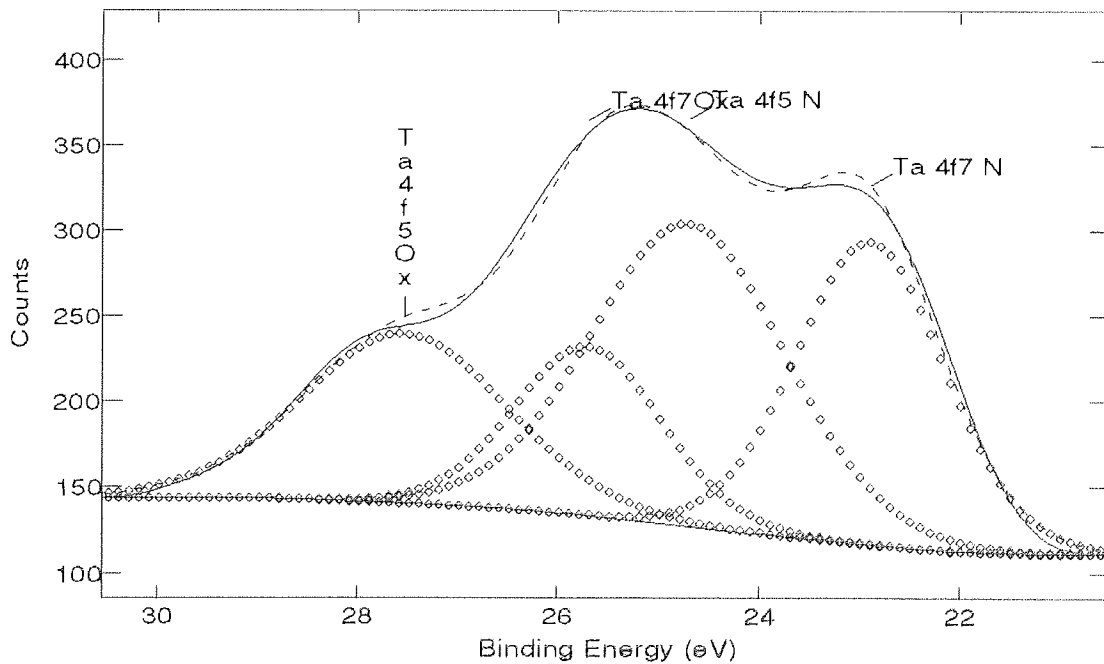


Figure 4.78 FeTaN Fitting of Ta 4f peak, 40nm into Bulk, Deposited on CaTiO<sub>3</sub> Head. Doublet Separation = 1.8eV, 4f7 and 4f5 Equal Height. Peak Fit Table in Table 4.17

Chemical State	Component	B.E. (eV)	Area	Height	FWHM	% (using 4f7)
Ta2O5	4f7	25.7	43	56	1.79	63
	4f5	27.5	57	56	2.51	
TaN	4f7	22.9	74	100	2.36	37
	4f5	24.7	100	100	1.82	

**Table 4.17 Peak Fit Table for Ta 4f in Figure 4.78, FeTaN on CaTiO<sub>3</sub> Head. Peak Area and Height Relative to Ta 3d5 4f5. Doublet Separation 1.8eV, Height Ratio 1:1.**

#### 4.4.2.7 Comparison of the XPS Data Collected for CoNbZr, FeNbSiN and FeTaN

The composition and the depth of the native oxides formed on the metals are shown in Table 4.18. The depth of the native oxide layer was for all three metals between 10 and 20nm. That of the iron materials was thicker than CoNbZr and FeTaN showed the thickest native oxide. The highest oxidation state oxide, together in some instances with lower oxidation state oxides were discovered for each metal except for Fe in FeNbSiN which existed as the metal rather than the oxide near the surface with this material.

Metal	Depth (nm)	Composition of Native oxide
CoNbZr	10	CoO, Nb <sub>2</sub> O <sub>5</sub> , NbO <sub>2</sub> , ZrO <sub>2</sub>
FeNbSiN	10-15	Fe, Nb <sub>2</sub> O <sub>5</sub> , NbO <sub>2</sub> , NbO, NbN, MSi, SiO <sub>2</sub> , N (Nitrate)
FeTaN	20	Fe <sub>2</sub> O <sub>3</sub> , Ta <sub>2</sub> O <sub>5</sub> , MN, N(Nitrate)

**Table 4.18 Depth and Chemical Composition of the Native Oxides of the Metals by XPS. MN, and MSi refer to Nitride N 1s and Silicide Si 2p Peaks that may be Associated with Either or Both of the Metals Present**

In general the oxides of the secondary metals i.e. Nb and Zr in CoNbZr, Nb in FeNbSiN and Ta in FeTaN showed a much greater concentration at the surface relative to the primary metal i.e. Co or Fe than they did in the sub-surface region. This may be due to surface segregation of these metals in the deposition process and or to more rapid oxidation of these metals on exposure to air. After corrosion of these metals by heating in water it was observed however the proportion of the primary metal oxide at the immediate surface

was seen to increase for the iron materials, but decrease for CoNbZr. But no hydroxide of any of the metals: Co, Nb, Zr, Fe or Ta was observed.

The native oxide of FeTaN included nitrogen as a metal nitride (Fe and/or Ta) and as a nitrate, as did the native oxide of FeNbSiN (as NbN), which also showed Si in the form of a metal silicide and SiO<sub>2</sub>. Corrosion of FeTaN in water caused a shift of the N 1s metal nitride peak from 396.9eV to 399.5eV, and from 396.9eV to 399.6eV in FeNbSiN. The metal silicide peak in this material similarly shifted from 99.2eV to 102.2eV. This may be due to the hydroxylation of the metal nitrides and silicides, which form the grain boundaries in these nanocrystalline materials, during the corrosion process.

From the XPS analyses of the cycled heads the sample ME cycled CoNbZr head showed Co metal where as the sample MP cycled CoNbZr head Co oxide at the surface. Both the sample ME and the MP cycled FeTaN heads showed Fe metal (along with TaN) at the surface rather than the oxides. In the case of FeNbSiN, of the sample heads only the one cycled against ME tape at 40°C/80%r.h. showed Fe metal rather than oxide at the surface, the others showed Fe<sub>2</sub>O<sub>3</sub>. In addition to Fe<sub>2</sub>O<sub>3</sub>, those sample FeNbSiN heads cycled against ME Tape at 25°C/90%r.h. and against MP tape at 40°C/80%r.h. showed FeOOH at the surface. This iron hydroxide was not observed for the FeNbSiN sample corroded in water, thus showing an additional corrosion mechanism could occur due to cycling against tape. As only one sample head was analysed successfully by XPS for each condition it cannot be said that such surfaces will always be seen after cycling at each condition. However it can be said that both oxidised and metallic surfaces, in which re-oxidation back to the native oxide has not occurred in the sometimes substantial time period between cycling and XPS can occur for CoNbZr and FeNbSiN heads. In addition hydroxylation of Fe in FeNbSiN can occur against both ME and MP tapes at both 25°C and 40°C at high humidity (80-90%r.h). For FeTaN only the metallic wear surface has been observed. The significance of observed surface chemistry in terms of the wear mechanisms of these metals and their magnetic properties are discussed later.

#### 4.4.3 XPS Analysis of the Ceramics S1 and S2

XPS analyses of sample S1 ( $\text{CaTiO}_3$ ) and S2 (multigranular  $\text{CaTiO}_3/\text{ZrTiO}_4/\text{TiO}_2$ ) ceramic dummy heads were made after cycling against ME and MP tapes at  $20^\circ\text{C}/80\%\text{r.h.}$  and  $40^\circ\text{C}/80\%\text{r.h.}$  The analyses for  $20^\circ\text{C}$  were made after running in at these conditions – 100 hours for ME tape and 10 hours for MP tape, but before cycling to measure wear rates. The wear rates measured and presented in 4.2 suggest that sufficient wear would have occurred for the surfaces measured by XPS after running in to be created under the running in period. The analyses for  $40^\circ\text{C}$  were made after cycling to measure wear rates (which showed much wear).

Peak binding energies quoted were charge corrected relative to  $\text{C1s}$  ( $\text{CH}_2$ ) at  $284.6\text{eV}$  and chemical states identified by comparison with the NIST X-Ray Photoelectron Spectroscopy Database<sup>295,296</sup>.

For all heads the largest peak was the  $\text{C1s}$  at  $284.6\text{eV}$  - associated with hydrocarbon contamination. This varied from head to head in quantity and was thus not included in the relative quantification of the chemical composition of the head surfaces. Fluorine was identified on both S1 and S2 heads cycled against ME tape at  $20^\circ\text{C}/80\%\text{r.h.}$  The  $\text{F 1s}$  peak declined in intensity on exposure to the x-ray beam in the spectrometer and therefore presumed to be part of a volatile adlayer and was thus also not included in the chemical quantification. XPS data showing evidence of fluorine containing lubricant transfer to ceramic and metal head surfaces from ME tape is shown later in 4.4.2.7.

In addition to C and occasionally F, the S1 heads showed a surface composition of Ca, Ti and O. S2 showed these elements and Zr. The binding energies of the XPS peaks of these elements together with their chemical state (oxidation state and element chemically bonded to) are given in Table 4.19. The same binding energies for each peak were observed for each ceramic head material. There was no difference between ME and MP tapes or between  $20^\circ\text{C}$  and  $40^\circ\text{C}$ . However there was a slight difference between S1 and S2, reflecting the difference in chemical composition between the two. The O 1s oxide peak was obtained by the synthetic fitting of such a peak and a peak associated with C to the observed O 1s peak, as shown in Figure 4.79. The binding energies observed were

consistent with Ca, Ti and Zr in the declared components of S1 and S2 – CaTiO<sub>3</sub> and CaTiO<sub>3</sub>/ZrTiO<sub>4</sub>/TiO<sub>2</sub>. A chemical shift in the various components of S2 was not observed for either Ti 2p or O 1s. No hydroxides of Ca, Zr or Ti were observed. Example XPS peaks are shown of Ca 2p, Ti 2p and Zr 3d in Figures 4.80, 4.81 and 4.82 respectively. These are from S2I (ME Tape 40°C/80%r.h.), but are typical of these peaks observed in S1 and S2.

Peak	Chemical State	S1 Binding Energy (eV)	S2 Binding Energy (eV)
Ca 2p	Ca(II)-O	345.8	346.5
Zr 3d	Zr(IV)-O	No Zr in S1	182.0
Ti 2p	Ti(IV)-O	457.8	458.4
O 1s	O(II)-Metal	529.1	530.0

**Table 4.19 The Binding Energies and Chemical States (Oxidation State and Element Bonded to) of the components of S2I and S2 Dummy Head Surfaces Identified by XPS**

The quantification relative to Ca of the surface components of the cycled heads from the XPS spectra are presented in Tables 4.20 and 4.21 for S1 and S2 respectively. The composition of S1 was found not to differ significantly between the different cycling conditions. The composition was found to be CaTi<sub>0.7-0.8</sub>O<sub>2.3-2.5</sub>, deficient in Ti and O from stoichiometric calcium titanate (CaTiO<sub>3</sub>). For S2 the ratio of Ca:Zr was observed to remain constant at 1:0.5. However the ratio of Ca:Ti and Ca:O was observed to vary between cycling conditions for S2 – between 1:0.5 and 1:1.1 for Ti and 1:2.7 and 1:4.3 for O. The variation in Ti and O content are not related.

Head	S1A	S1K	S1J	S1K
Tape	ME1	MP1	ME1	MP2
T(°C)	20	20	40	40
r.h.(%)	80	80	80	80
Ca 2p	1	1	1	1
Ti 2p	0.7	0.7		0.8
O 1s	2.4	2.3		2.5

**Table 4.20 Quantification of the Surface Components of Cycled S1 Dummy Heads From XPS Analysis. Quantification is Relative to The Ca 2p Peak. Quantification with Grey Background, Conditions with White Background**

Head	S2K	S2L	S2I	S2K
Tape	ME1	MP1	ME1	MP2
T(°C)	20	20	40	40
r.h.(%)	80	80	80	80
Ca 2p	1	1	1	1
Zr 3d	0.7	0.5	0.5	0.5
Ti 2p	0.5	0.8	1.0	1.2
O 1s	3.6	3.5	4.3	2.7

**Table 4.21 Quantification of the Surface Components of Cycled S2 Dummy Heads From XPS Analysis. Quantification is Relative to the Ca 2p Peak. Quantification with Grey Background, Conditions with White Background**

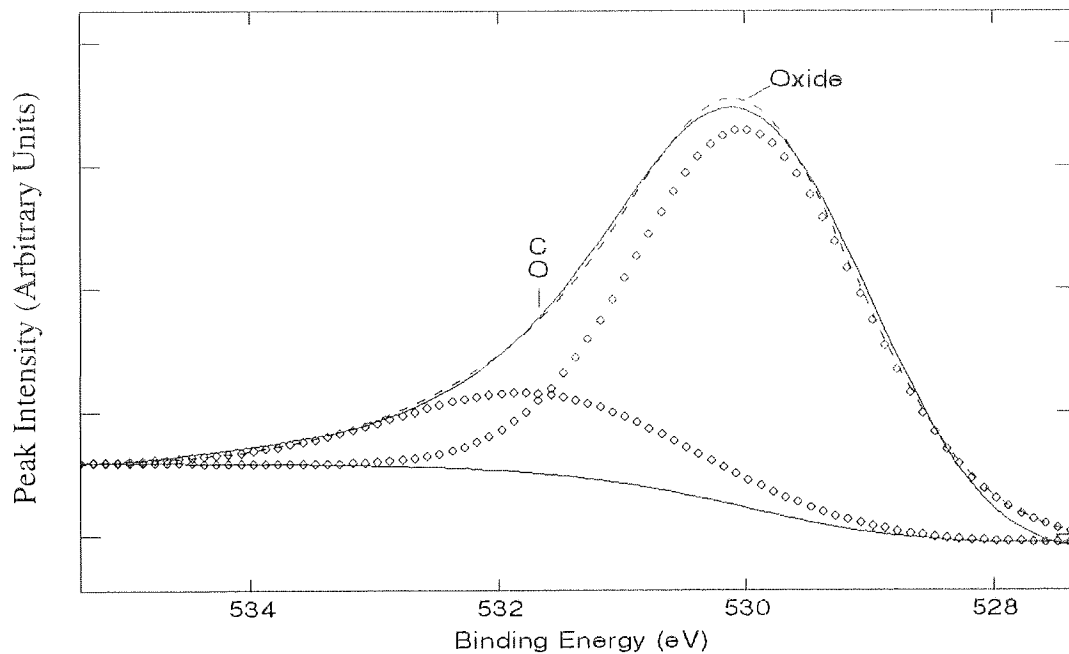


**Figure 4.79 O 1s XPS Peak from S2I after Cycling against ME Tape at 40C/80% r.h. Figure shows the Fitting of Synthetic O-C and O-Metal Peaks. The Solid Lines Represent the Actual Peak and Background, the Diamonds the Synthetic Peaks. Binding Energies (eV): CO-531.7, Oxide-530.0**



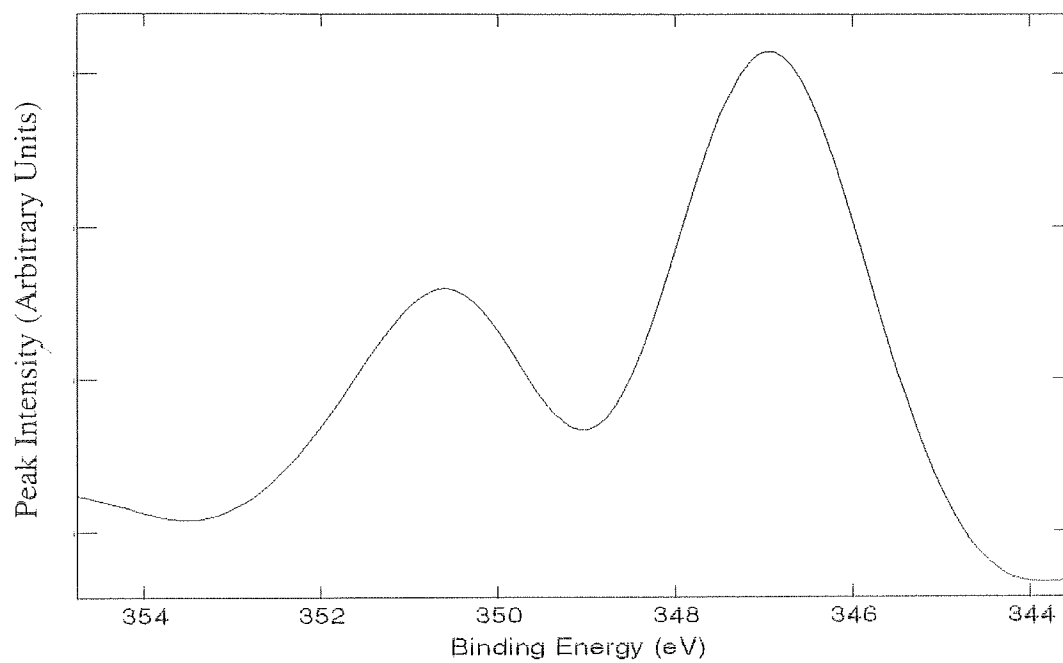


**Figure 4.80** Ca 2p XPS Peak from S2I after Cycling against ME Tape at 40C/80 %r.h.

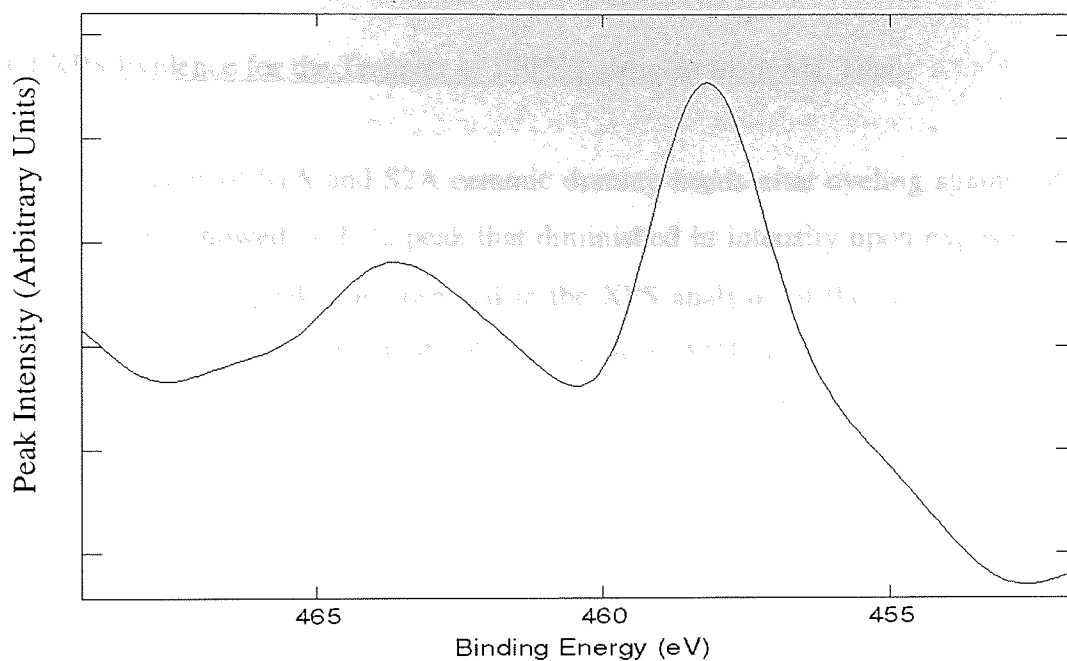


Figure 4.81 Ti 2p XPS Peak from S2I after Cycling against ME Tape at 40C/80% r.h.

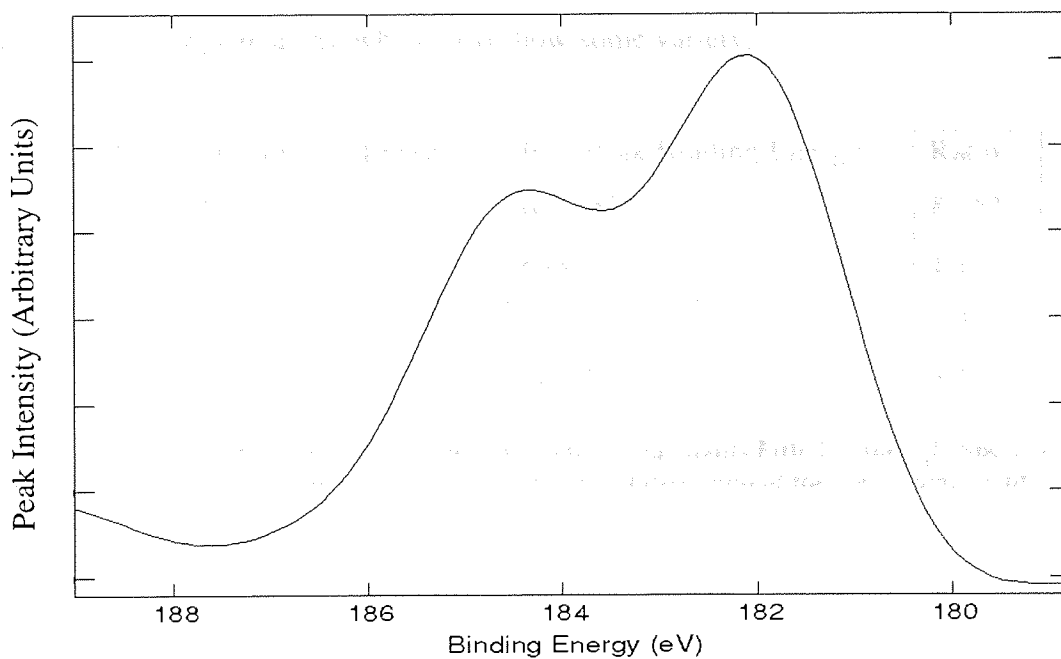


Figure 4.82 Zr 3d XPS Peak from S2I after Cycling against ME Tape at 40C/80% r.h.

#### 4.4.4 XPS Evidence for the Transfer of PFPE Lubricant from ME Tape

The XPS analysis of S1A and S2A ceramic dummy heads after cycling against ME1 tape at 20°C/80%r.h. showed an F 1s peak that diminished in intensity upon exposure to the x-ray beam. A similar peak was observed in the XPS analysis of the clear deposit that was observed on the surface of the CoNbZr dummy head M1E after cycling against ME3 tape at 60°C/80%r.h. (see Section 4.3 for optical photomicrograph) which did not diminish in intensity upon x-ray exposure. Fluorine is present in the PFPE lubricant of ME tapes, but not in MP Tape or in the dummy head surfaces. Thus lubricant is transferred to the ceramic head surfaces by cycling at 20°C/80%r.h. The rapid diminution of the F1s marker peak by heating from the x-ray beam shows the volatility of the lubricant and thus the weak bonding between it and the ceramic surface. The rapid diminution was not observed on the metal head due to the large amount of lubricant that had been transferred to the head surface.

Qualitatively each F 1s peak could be fitted with two components, however with slightly different binding energies in each case. These are shown in Table 4.22, together with their relative ratios (by peak area), which also show some variety.

Head	F 1s Peak Binding Energy (eV) #1	F 1s Peak Binding Energy (eV) #2	Ratio #1:#2
S1A	689.8	688.1	1:1
S2A	688.6	687.1	1:4
M1E	689.0	687.7	3:1

**Table 4.22 Binding Energies (eV) of the Two Synthetic Components Fitted to the F 1s Spectra Observed on Dummy Head Surfaces, together with the relative ratio of the Two Components**

A binding energy in the range 687.7-689.8eV is typical of covalent C-F bonding and not a metal fluoride, further evidence of the lack of chemical bonding between the transfer layer and the head surface. The slight variation in peak heights and positions between the two components in each case may be due to the action of the x-ray radiation observed to have had some effect some effect due to the diminution in intensity of the F1s peak. An example of the peak fitting of two components to the F 1s signal is shown of M1E in Figure 4.83.

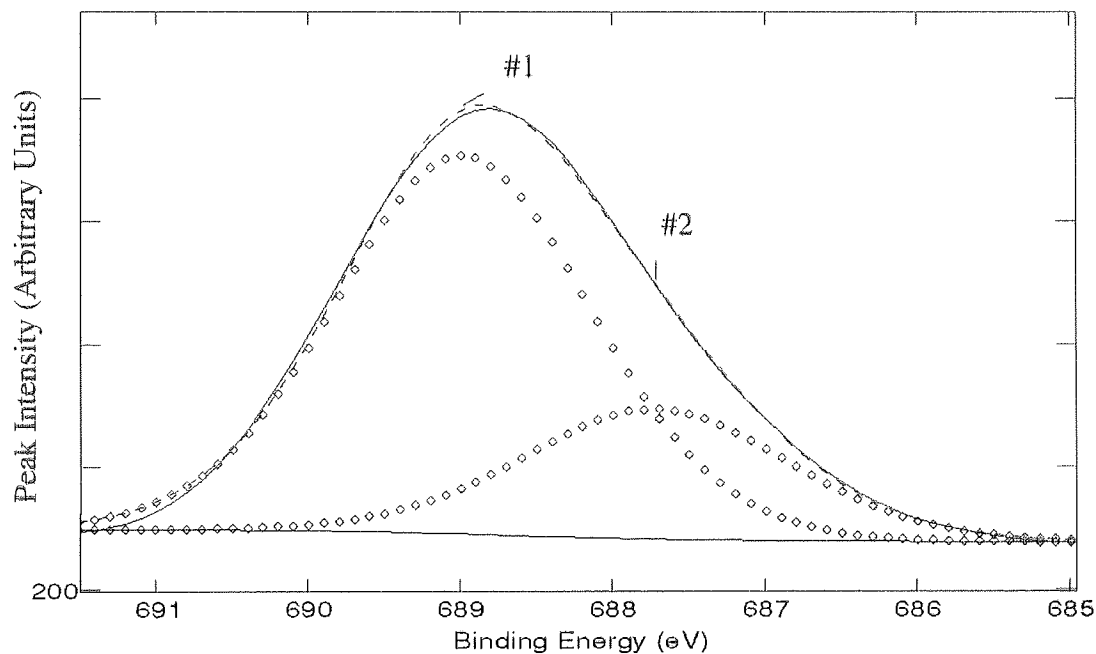


**Figure 4.83 Peak Fitting of Two Synthetic Peaks to the F 1s XPS Spectra of M1E after Cycling against ME1 Tape at 60C/80%r.h. Solid Line Real Peak and Background, Diamonds Mark Synthetic Peaks. Peak Centre: #1 at 689.0eV, #2 at 687.7eV. Relative Ratio (by Peak Area) 3:1**

## 4.5 Sandwich Heads Results Section

### 4.5.1 Introduction

In this section results are presented for the cycling of sandwich heads. These include PTR measurements made by AFM and topographical imaging by AFM showing detail of the head surfaces including the relative wear of the components of the sandwich, and the presence of deposits, debris and delamination on the head surface. Three environmental conditions were studied: 30°C/90%r.h., 22°C/80%r.h. and 25°C/20%r.h. For each of the first two conditions one drum of two sandwich heads was cycled against ME tape (of the type ME2), and another drum of two heads against MP tape (of the type MP3). For the final condition sufficient heads existed only for cycling one drum of two heads against ME tape (of the type ME2). These experiments are summarised in Table 4.23.

Heads	Track Width (µm)	Tape	Climate	Total Cycling Time (hours)
H1, H2	32	ME2	30°C/90%r.h.	200
H3, H4	14	MP3	30°C/90%r.h.	150
H5, H6	32	ME2	22°C/80%r.h.	300
H7, H8	32	MP3	22°C/80%r.h.	300
H9, H10	32	ME2	25°C/20%r.h.	200

**Table 4.23 Sandwich Head Cycling Experiments**

### 4.5.2 The Heads

The sandwich heads were all of the same material combination: The substrate was CaTiO<sub>3</sub>/ZrTiO<sub>4</sub>/TiO<sub>2</sub> (S2), the magnetic metal was FeTaN (M3), the bonding layer was Mo/Au and the insulating layers Si<sub>3</sub>N<sub>4</sub>. All the heads were of identical dimensions, with the exception of H3 and H4, which differed primarily in having half the track width of the other heads, but in all other dimensions were very similar. The head dimensions are given in Table 4.24.

	14 $\mu$ m Track Width	32 $\mu$ m Track Width
Head Length ( $\mu$ m)	1200	1200
Head Width ( $\mu$ m)	150	180
Number of Metal Layers	8	16
Metal Layer Width ( $\mu$ m)	1.5	1.75
Insulation Layer Width ( $\mu$ m)	0.25	0.25
Bonding Layer Width ( $\mu$ m)	0.5	0.25

**Table 4.24 Sandwich Head Dimensions**

The heads were received after being run in against MP tape for 10 hours at 40°C /80% r.h. in Hi-8 recorders to contour the heads.

#### 4.5.3 Cycling Experiments

The cycling experiments were conducted in the same manner and using the same equipment as used for the dummy heads. However, instead of measuring wear rate by the indentation method, PTR and surface topography were measured using AFM. The heads were mounted, as received, onto Hi-8 drums with a protrusion of  $25\pm 5\mu\text{m}$ , which in turn were mounted into the Hi-8 recorders. As received the head surfaces were covered with debris from the running in process. This was removed by running the heads against Sony V8-25CLH Head Cleaning Tape (HCT) for 10 seconds. Debris removal was sometimes incomplete, however no more than a 10 seconds passage of HCT was used, to avoid further head profiling by this highly abrasive tape. After HCT, a  $50\times 50\mu\text{m}$  AFM image of the head was taken in the region of the gap. All heads showed a similar surface after HCT. A typical example is shown in Figure 4.84. All AFM micrographs in this section have been levelled as described in the 3.3.2 to show all heights with respect to a plane representing the head surface. Where shading has been applied to emphasise shallow features, this is stated within the caption to the figure along with the position of the light source. Figure 4.84 shows the track to be recessed with respect to the substrate, more so at the interface between the track and the substrate than at the centre of the track. Within the track the thinner insulation layers can be seen to be protruding above the level of the metal layers and the central bonding layer to be recessed below the metal layers.

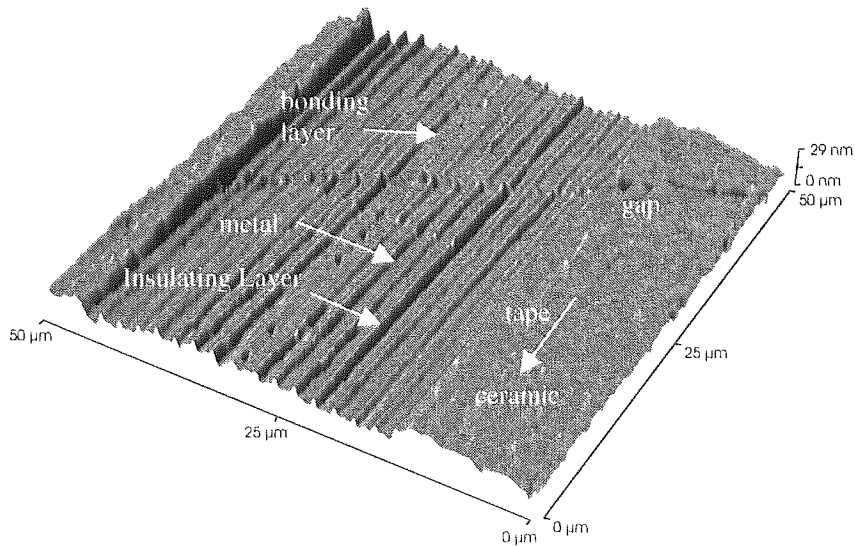


**Figure 4.84 H6 after 10s HCT. Typical Head Surface Prior to Cycling. Shaded with Light from Left.**

At 30°C/90%r.h. head protrusion and PTR were measured before cycling and at the end of the cycling only. For all other cases these were measured periodically during the cycling. The timing of these measurements and the value of the head protrusion measured are given in Table 4.25.

Time (hours):	0	10	50	100	150	200	300
H1	28					31	
H2	32					28	
H3	28				20		
H4	26				15		
H5	29	33	31	23	62	63	57
H6	26	27	32	24	22	22	22
H7	28	27	27	28	24	22	24
H8	30	34	31	28	28	26	24
H9	26	20	20	18		16	
H10	26	30	24	23		24	

**Table 4.25 Protrusion Measurements ( $\pm 2\mu\text{m}$ ) Taken During Cycling of Sandwich Heads. PTR also Measured at these Times. Shaded Rows : ME Tape.**

#### 4.5.4 Measurement of PTR

The metal layers either side of the gap form the magnetic pole tips of the head. It may be seen from the AFM images presented later of the pole tips of various cycled sandwich heads that the recession of these from the tape bearing ceramic surface was not uniform. Various types of debris and deposits on the metal surfaces and delaminations within the metal tracks contribute locally to head-tape spacing, as will protruding insulating layers, where these occur. These, together with other factors identified as possible contributors to spacing loss are discussed later. However in the following paragraphs it is shown how the average recession of the metal layers from the tape-bearing surface at the pole tips was estimated from AFM measurements. Thus giving an idea of the PTR contribution to spacing loss.

For each PTR measurement a 50x50 $\mu\text{m}$  AFM image was taken of the head surface in the region of the gap. After levelling the image to the plane of the tape-bearing surface, three lines were scanned using the Topometrix SPMlab software through the head perpendicularly to the track just adjacent to the track, with at least one line either side of the gap. For each line 6 measurements were taken of the recession of the metal from the ceramic, three from each side of the sandwich. An example of the linescans and the points chosen to calculate PTR for H8 (22°C/80%r.h.) at 50hours is shown below in Figure 4.85. On the ceramic, the points were chosen at the middle height where there was a large variation in grain height and at the most common height where the variation in grain height was low. On the metal the points were chosen on separate metal layers distributed evenly across the head surface. Debris, insulation layers and the bonding layers were avoided, as were delaminations in the metal surface.

The error in the individual measurements made by AFM that were used to calculate PTR was less than 1nm in each case. However 18 such points were used to calculate an average value of PTR. As can be seen in Figure 4.85 the difference in height between the ceramic and the track was not uniform. The standard variation of the values used to calculate the mean PTR for each point in the PTR-time plots showed a minimum value of 2nm and a maximum value of 12nm. The range of standard deviations for the points in each PTR-time plot is given in the legend to that plot.



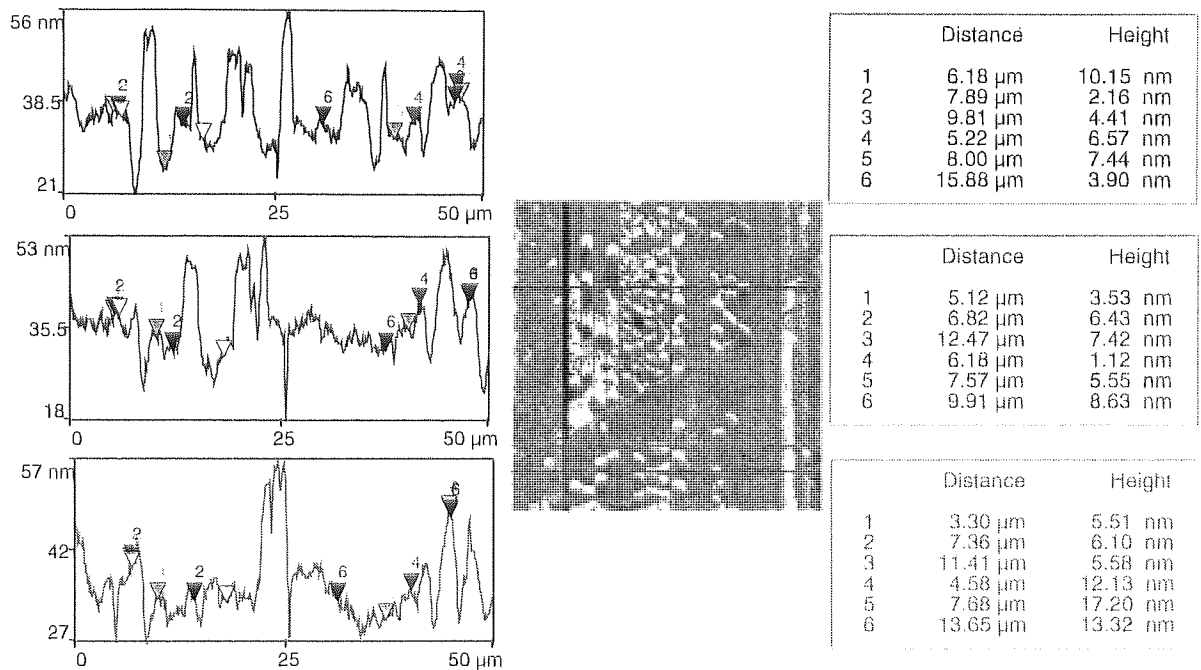


Figure 4.85 An Example of the Linescans and Points Used to Calculate Average PTR. H8, 22/80%r.h., 50hours.

#### 4.5.5 Wear History of Sandwich Heads

##### 4.5.5.1 H1 and H2: Cycled Against ME Tape at 30°C/90%r.h. for 200 Hours

Head	Tape	Average PTR before cycling (nm)	Average PTR after cycling (nm)
H1	ME	4	0
H2	ME	12	17
H3	MP	10	11
H4	MP	15	14

Table 4.26 Average PTR Values for Cycling at 30C/90%r.h. Standard Deviations in the Points Used to calculate the mean 4-8nm.

The average PTR values for these heads prior to cycling (after 10 seconds Head Cleaning Tape) and after 150 hours cycling are presented in Table 4.26. H1 showed very little PTR prior to cycling (4nm) which reduced to zero after cycling. H2 showed a slight increase – from 12 to 17nm. Both heads showed little change in protrusion above the drum (see Table 4.25) therefore showing little total wear. After HCT, prior to cycling both heads were similar in topography to H6 in Figure 4.84. Figure 4.86 shows H1 after 200 hours, H2 was

very similar. Both heads had much scratching parallel to the direction of tape passage on both the ceramic and on the magnetic track. This, together with the zero PTR in the case of H1, makes it hard to differentiate the boundary between the ceramic and the track, and within the track, the metal from the insulation layers.

#### 4.5.5.2 H3 and H4: Cycled against MP Tape for 150 Hours at 30°C/90%r.h.

From Table 4.26 it can be seen that average PTR for both heads was unchanged between 0 and 150 hours. However it can be seen from Table 4.25 that the protrusion of both heads from the drum fell by about one third in 150 hours. H3 fell from 28 to 20 $\mu\text{m}$ , and H4 from 26 to 15 $\mu\text{m}$  – indicating a high degree of wear (8-10 $\mu\text{m}$ ) or a mechanical relaxation of the head into its mount or of the mount into the drum. In any case causing a decrease in head-tape contact pressure. Figure 4.87 shows an AFM of H3 after 150 hours cycling. The ceramic can be seen to have been debris free. Within the track the insulation layers are protruding, and on the metal layers there were MP generated particles. Similar particles were seen on all the sandwich heads that were cycled against MP tapes. They are listed in Table 4.27, together with their dimensions and the separation between the particles in the direction parallel to the tape where this is regular. On H3 at 150 hours they were confined between the insulation layers on the trailing edge side of the gap, whereas on the leading edge side of the gap the particles extend over the insulation layers. The distribution of the particles parallel to direction of tape travel was regular on both sides of the gap, but the packing was denser on the leading side. Figure 4.88 is of H4 and shows its surface to have been very similar to H3 with protruding grains and regularly spaced particles on the track.

Figure 4.89(a)-(c) shows two perspectives and a linescan of a 5x5 $\mu\text{m}$  AFM image of the MP generated particles on H4 at 150 hours. Figure 4.89(a), a two dimensional representation of the image, shows the particles to lie roughly equispaced on the metal layers in-between the recessed insulation layers. It also illustrates the microgrooving parallel to the direction of tape travel both on the underlying metal and on the particles themselves. Figure 4.89(b), a three dimensional representation and 4.89(c), a linescan through the particles show them to have flat tops (apart from the microgrooving) and steep sides and for there to be discrete intervals in-between the particles.

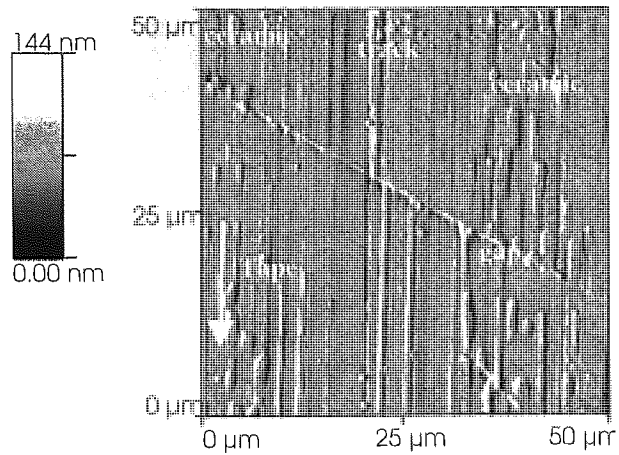


Figure 4.86 H1 AFM: 200 hours ME Tape 30C/90% r.h. Deep Scratching in Both Ceramic and Track (32µm wide) Obscures Boundary between the Two, PTR = 0. Note - Shaded with Light from Left

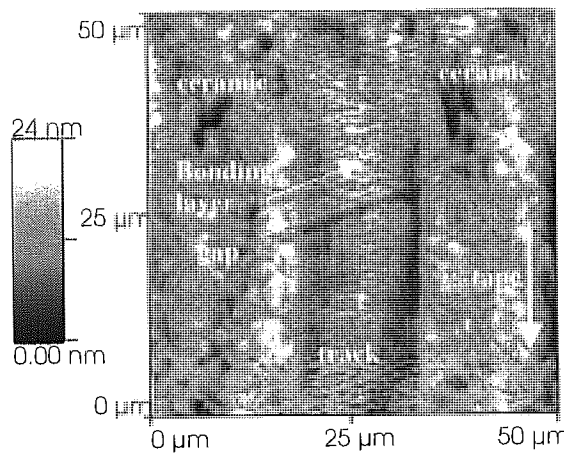


Figure 4.87 H3 AFM: 150 hours MP Tape 30C/90% r.h.

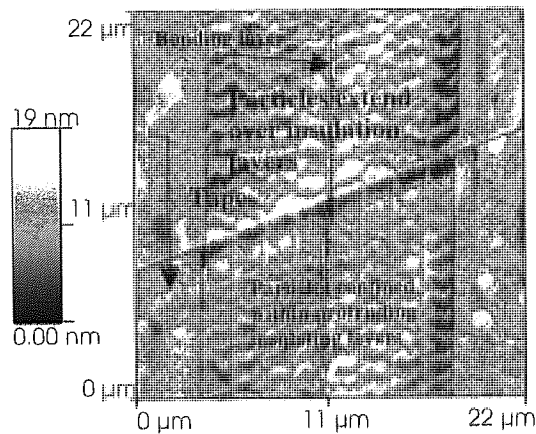
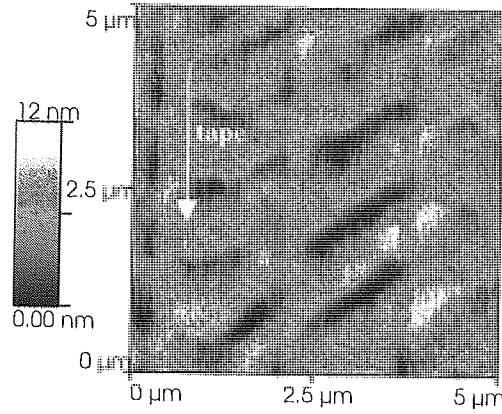
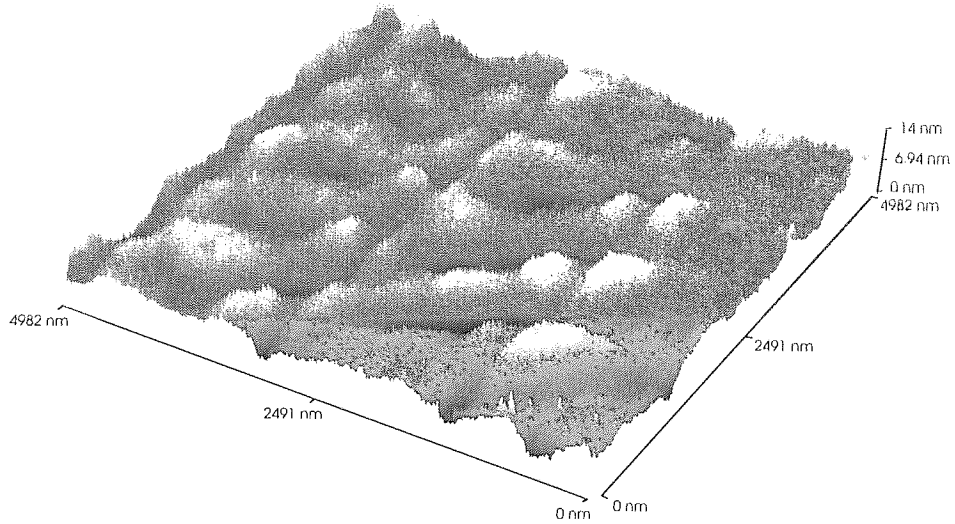


Figure 4.88 H4 AFM: 150 hours MP Tape 30C/90% r.h. 22µm Zoom on Figure 4.87. Shows MP Generated Particles Lying on the Metal Layers within the Magnetic Track



**Figure 4.89(a): AFM of MP Generated Particles. H4 150 Hours MP Tape 30/90%r.h. Particles lies on Metal Layers Inbetween (Recessed) Insulation Layers. Note the Microgrooving Parallel to the Direction of Tape Passage Through both Particles and Metal Layers.**



**Figure 4.89(b): Three-Dimensional AFM Representation of the MP Generated Particles. Illustrates the Discrete Nature of these Particles and the Microabrasion through them. Same Area as Figure 4.91(a) above.**

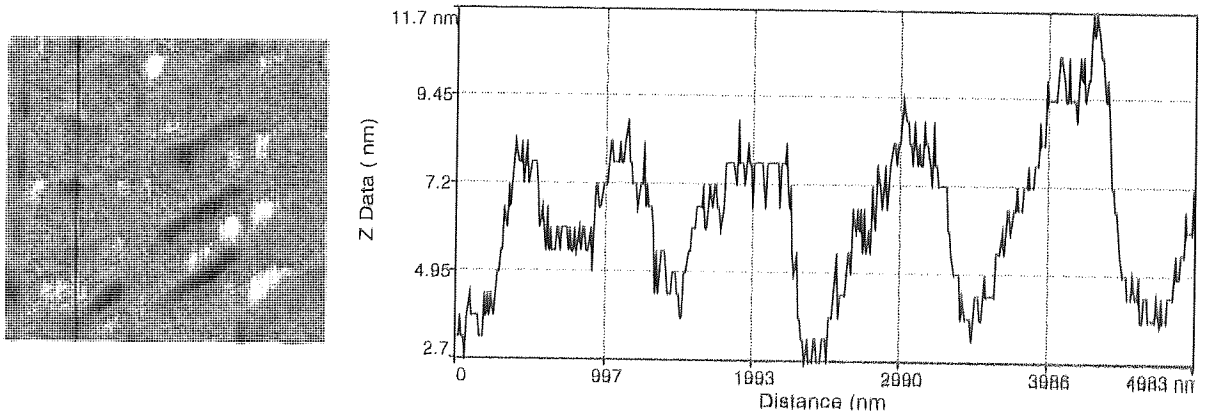


**Figure 4.89(c): Linescan Through AFM of MP Generated Particles. Same Area as Figure 4.91(a) above. Shows Intervals between Adjacent Particles.**

Head	Time (hours)	Length $\perp$ to tape direction ( $\mu\text{m}$ )	Length $\parallel$ to tape direction ( $\mu\text{m}$ )	Height (nm)	Separation $\parallel$ to tape	Comments
H3	150	4	1.4	10	3	Before gap
		1.8	1	10	1.5	After gap
H4	150	1.8	1-1.2	6	1.4	Before gap
		1.8	0.8	6	1.25	After gap
H7	10	1.8	1.3	8-10	2.2	
	50	1.8	1.5	14	Uneven	
	200	1.8	0.85	20	Uneven	Sparse
H8	10	1.8-3.6	1.6	8-12	3.75	Before gap
		1.8	1.5	8-12	2.5	After gap
	50	1.8	1.5	10	Uneven	denser before gap

**Table 4.27 MP Generated Particles - Size and Distribution. "Before Gap" - Leading side of gap, "After Gap" - Trailing Side of Gap.**

#### 4.5.5.3 H5 and H6: Cycled against ME Tape for 300 Hours at 22°C/80% r.h.

In Figure 4.90 PTR with time is plotted for H5 and H6. For H6, PTR oscillates about 10nm for the first 100 hours, before rising slowly to 15nm by 300 hours. Initially PTR for H5 was much greater at 25nm, staying above 20nm for the first 50 hours before declining to 8nm by 100 hours, staying within a few nm of this value until a final value of PTR of 12nm was reached at 300 hours. Despite a large difference in starting PTR, after 100 hours cycling they had reached similar values for PTR and behaved very similarly thereafter. Head protrusion was recorded for both heads in Table 4.25. The protrusion of H6 fell marginally from 26 to 22 $\mu\text{m}$  in 300 hours, however the protrusion of H5 is shown to have increased drastically from 23 to 62 $\mu\text{m}$  at 150 hours, being more or less constant either side of this jump. This is probably due to a mechanical defect in the head drum assembly. However this change in protrusion occurs after PTR had reached its equilibrium value, and did not cause a big oscillation about this value, nor is the equilibrium line for this head much different to H6, which had less than half the protrusion of H5.

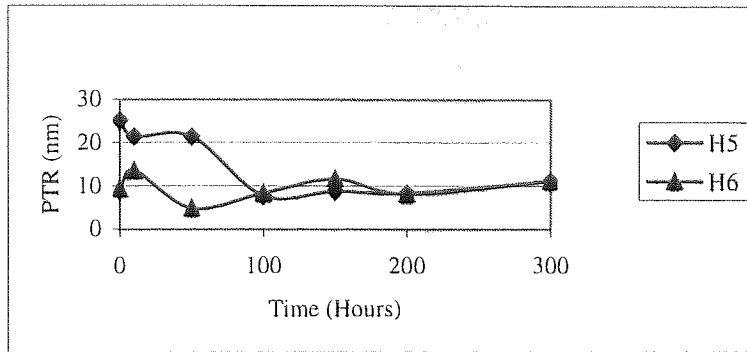
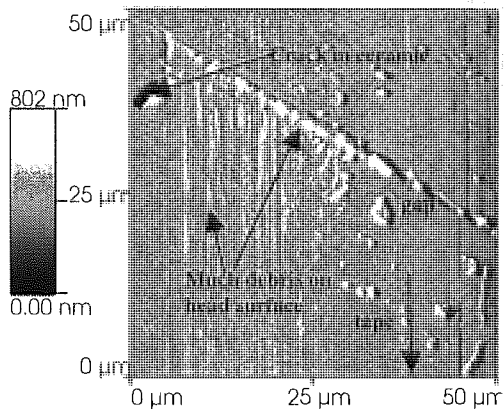


**Figure 4.90 Average PTR vs. Time for H5 and H6 Cycled Against ME Tape 22C/80%r.h. Error in Individual AFM Measurements < 1nm. Each Data Point Average of 18 Measurements - Standard Deviations in the Range 5-8nm.**

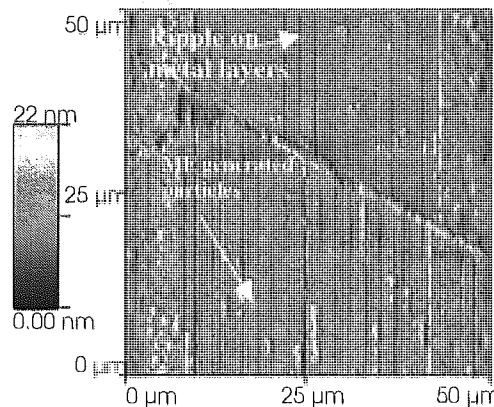
Figure 4.84 shows H6 after HCT and before cycling. H5 was very similar to this. Figure 4.91 (a)-(f) shows 50x50µm AFM images of H5 at 10, 50, 100, 150, 200 and 300 hours respectively. This is repeated for H6 in Figure 4.92. These heads differed initially at 10 hours in that H5 showed much more loose debris on and about the gap, probably generated by the HCT, and transferred to the gap by the action of the first 10 hours of cycling. H5 subsequently showed more scratching of the track region trailing the gap at 50 hours, probably caused by this debris as it was dragged across the head surface by the tape. This would also account for the lower density of the ME generated particles observed on H5 than on the metal layers of H6. The dimensions of these particles for H5 and H6 are given in Table 4.28.

Head	Time measurement taken (hours)	Time particles observed (hours)	Length ⊥ to tape direction (µm)	Length    to tape direction (µm)	Height (nm)
H5	50	50-300	0.5	3.5	14
H6	50	10-150	1.8	1.5	10

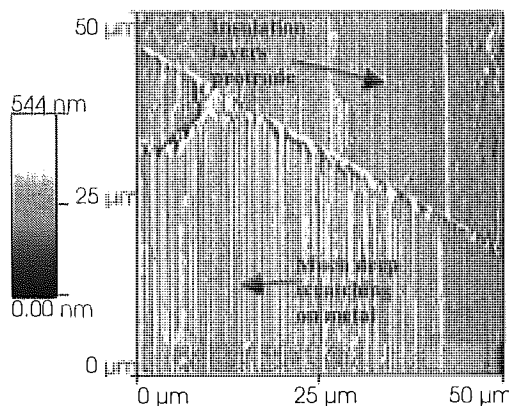
**Table 4.28 Dimensions of the ME Generated Particles**



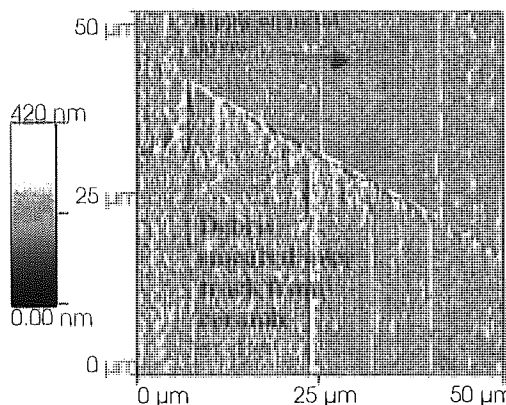
**Figure 4.91(a) H5 AFM: 10 Hours ME Tape 22C/80%r.h. Note - Shaded with Light from Left (All Images on this Page)**



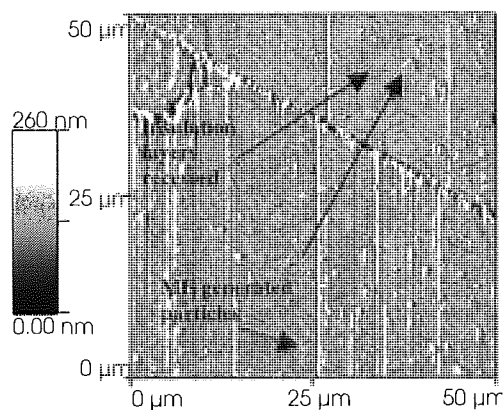
**Figure 4.91(d): 150 Hours**



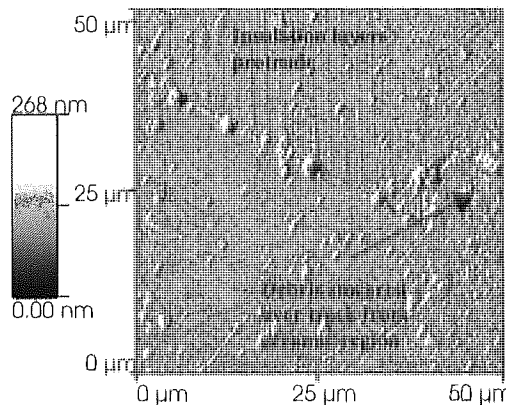
**Figure 4.91(b): 50 Hours**



**Figure 4.91(e): 200 Hours**

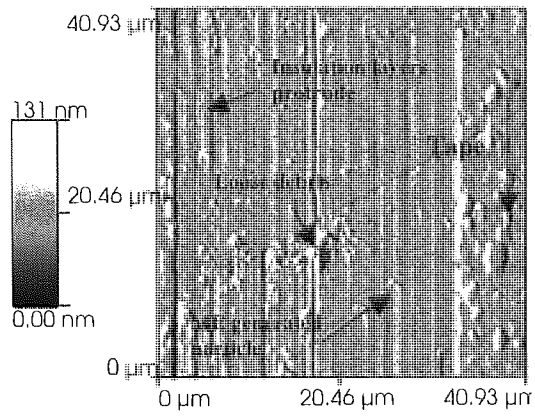


**Figure 4.91(c): 100 Hours**

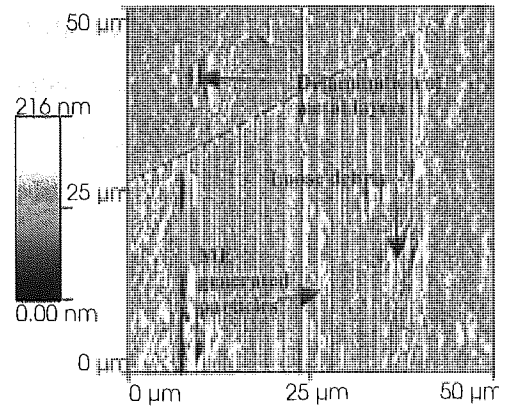


**Figure 4.91(f): 300 Hours**

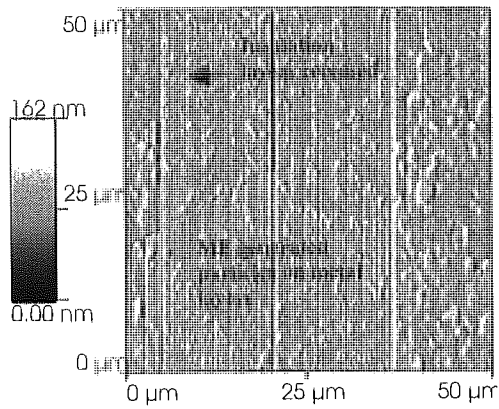




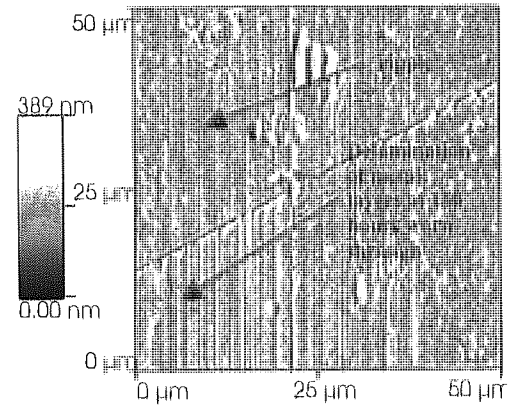
**Figure 4.92(a) H6 AFM: 10 Hours ME Tape 22C/80%r.h. Note - Shaded with Light from Left (All images this Page)**



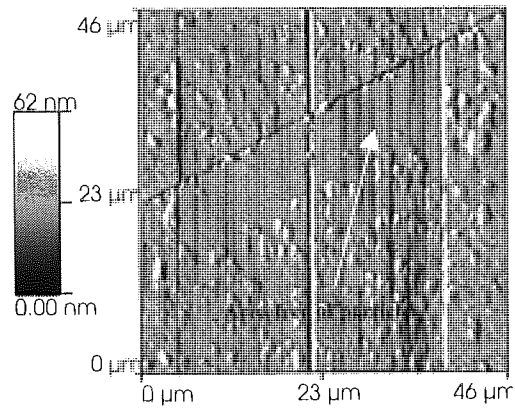
**Figure 4.92(d): 150 Hours**



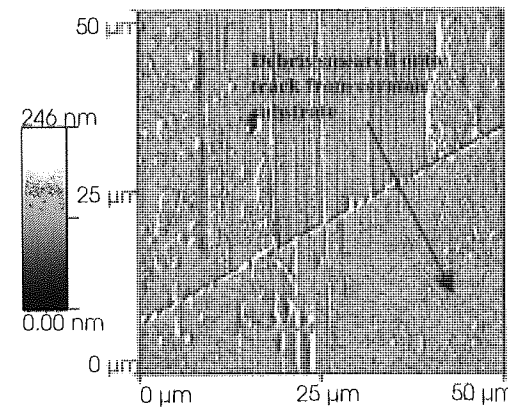
**Figure 4.92(b): 50 Hours**



**Figure 4.92(e): 200 Hours**



**Figure 4.92(c): 100 Hours**



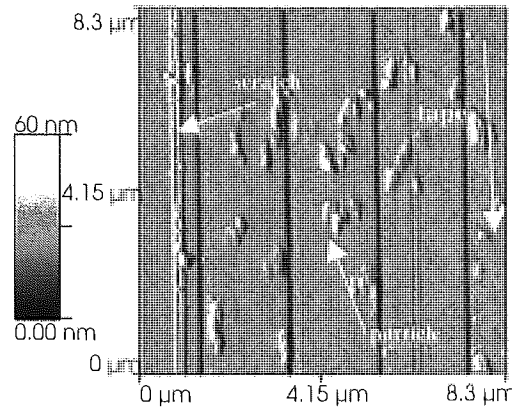
**Figure 4.92(f): 300 Hours**



Figure 4.93 shows some close up AFM images of the ME generated particles on H6 at 50 hours that show how they differ from MP generated particles. Figure 4.93(a) shows that they were more randomly distributed and that they were less regular in both shape and size. Though, like the MP generated particles they were found exclusively on the metal layers, unlike the MP generated particles they did not always fill the entire width of the metal layer on which they sit. Figures 4.93(b) and (c) show respectively two and three-dimensional AFM images of the same ME generated particles. These show that the particles either to have been severely abraded by the action of the passing tape, or that they consist of several smaller particles.

ME generated particles existed from 50 to 200 hours on H5, and to 150 hours on H6. The position of these particles can be seen to have changed after each successive cycling period, thus these particles individually did not persist at the same position on the surface longer than the 50 hours sampling time, suggesting a dynamic equilibrium of particle generation and removal during the period in which they were observed.

At 150 hours on H6, but not on H5, wear scars were seen on the metal layers. These tended to extend the full width of a metal layer ( $1.75\mu\text{m}$ ), and be up to  $5\mu\text{m}$  in length. Their depth was however much less at 80-90nm, thus the scars maybe classed as delaminations. These scars appeared in different locations, though with similar dimensions at 150, 200 and 300 hours. This means that in the intervening time periods the rest of the metal surface must have been worn down at least until the level of the wear scar – at least 90nm in 50 hours – showing a wear rate of nearly 2nm/hour. It also shows that the cracks that which form the sides of the delamination wear scars propagate deep into the metal.



**Figure 4.93 (a) AFM of ME Generated Particles: H6 50 Hours ME Tape 22/80% r.h. Particles lie on Metal Layers, Insulation Layers are Recessed. Deeper Scratches and Microabrasion can be seen on Metal Surface Running Parallel to the Direction of Tape Passage. Image is Shaded with Light from Left**

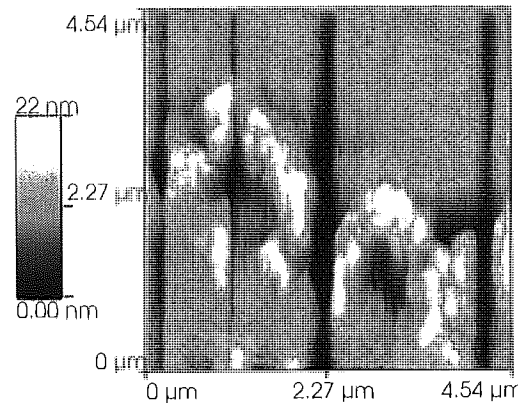


**Figure 4.93(b) AFM of ME Generated Particles: H6 50 Hours ME Tape 22c/80% r.h. It can be seen that Particle is either Agglomeration of Smaller Particles or has been Quite Severely Damaged by the Action of the Passing Tape**

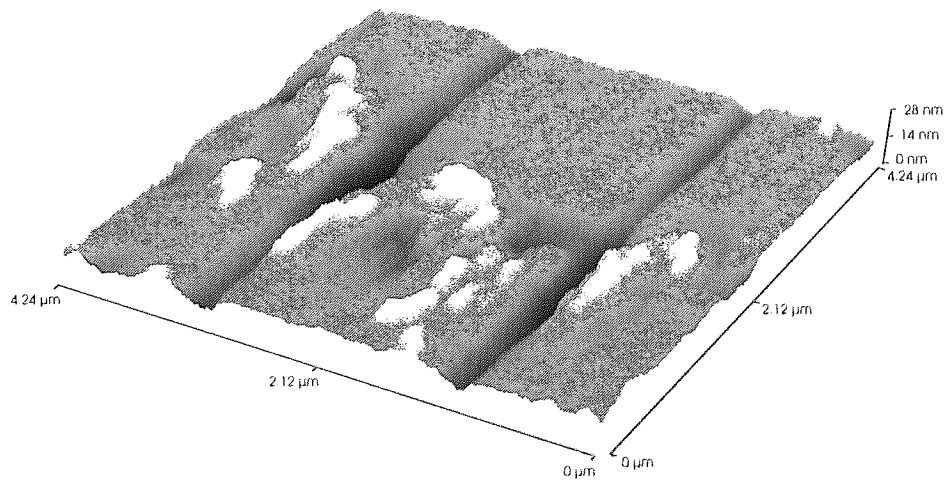


**Figure 4.93(c) Three-Dimensional AFM Representation of the ME Generated Particles shown in Figure 4.95(b) Above.**

At 200 and 300 hours for H5 and at 300 hours for H6 debris can be seen smeared over the track from the ceramic region. This debris covers quite a large area – greater than  $20 \times 20 \mu\text{m}$  on the track and larger on the ceramic region. In neither case however was this debris seen to show colour contrast to the ceramic by optical microscopy. This debris was generally continuous, though contained some particulates that were different in dimension and appearance to either the spherical debris often observed on head surfaces by AFM, and to the ME generated particles. An example is given in Figure 4.94, of such particles on H5 at 300 hours.

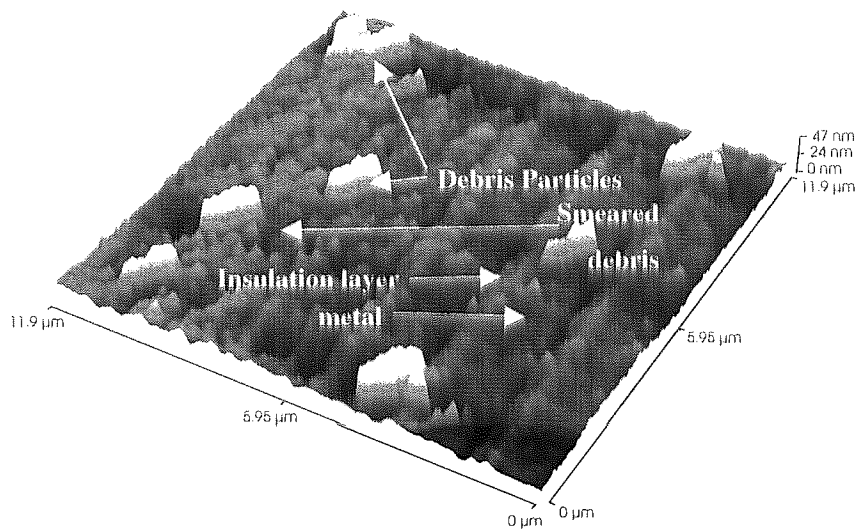
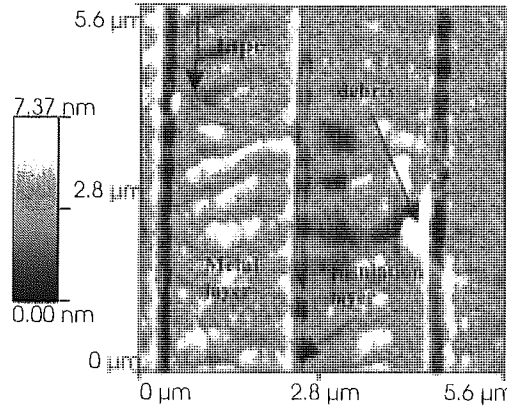


**Figure 4.94 H5 AFM: 300 Hours ME 22C/80%r.h. Particles in the Debris Smeared over the Track from the Ceramic**

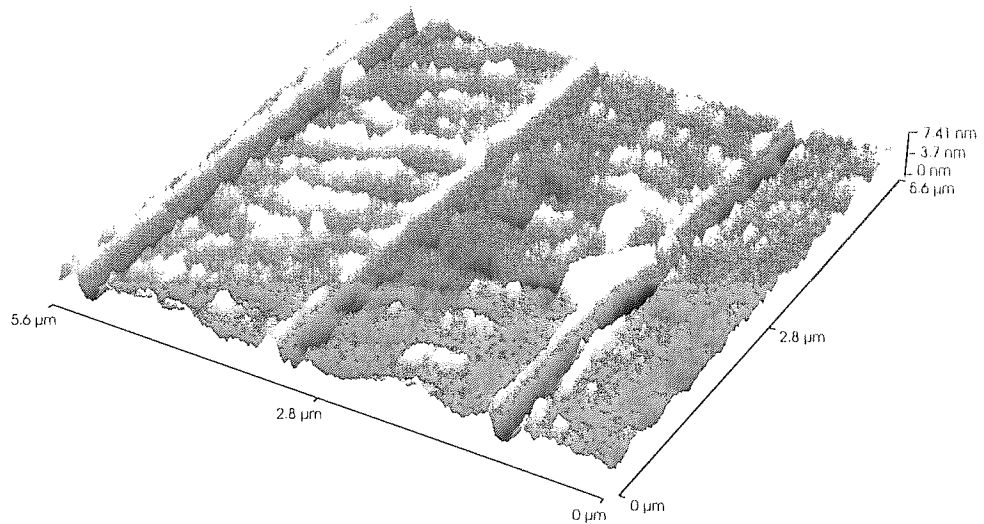
These particles were not distributed regularly. They were not lined up in the direction of the tape travel, but lay at a slight angle to it. The short side, roughly perpendicular to the direction of the tape travel, is about  $1\mu\text{m}$  and the longer side  $2\text{-}3\mu\text{m}$  in length, roughly parallel to the tape. They were about  $50\text{nm}$  in depth. The top surfaces of these particles were flat and the sides almost vertical.

On Figure 4.94, it can be seen that some of the insulation layers were once again protruding above the metal layers, indicating that metal had been worn down beyond the level at which the insulation layers fractured.

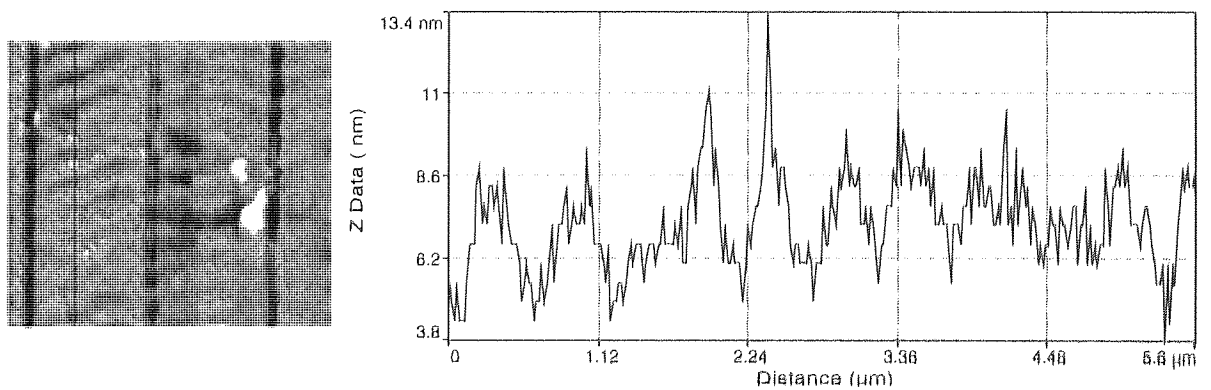
On H6 at 200 and 300 hours, and H5 at 150 and 200 hours can be seen a ripple pattern on the metal layer that ran perpendicularly to the direction of tape travel. H5 at 300 hours was obscured by debris in the gap region, thus this pattern maybe present at this time. This pattern is hard to make out on the  $50\times 50\mu\text{m}$  images, but a zoom is provided in Figure 4.95- a  $5.6\times 5.6\mu\text{m}$  area of the track in H5 at 150 hours. This pattern appears similar to the pattern created by the MP generated particles lying on the metal layers. The peak valley height of these ripples was similarly around  $10\text{nm}$  and the lateral peak to peak separation is  $0.7\mu\text{m}$  – half that of the MP generated particles. However the ripple can be seen to differ in a number of ways to the MP generated particles (compare with the equivalent AFM images of the MP generated particles in Figure 4.89). In Figure 4.95(a), the two dimensional plan perspective shows that the ripple continued through the insulation layer, this is not seen for the MP generated particles. Figure 4.95(b), the three dimensional perspective, and Figure 4.95(c), the linescan, show the ripples to have had a structure that is more wave-like, rather than like the discrete particles observed for MP generated particles. In this case the linescan shows definite minima and maxima connected by sloping sides, rather than plateaux with steep sides interspersed by flat regions. In addition to this patterning observed perpendicular to the direction of tape travel, microgrooving parallel to the direction of tape travel can be observed on Figure 4.95.



**Figure 4.95(a) AFM of Ripple Pattern Observed Running Perpendicularly to the Direction of Tape Passage on Some Metal Layer Surfaces. H5: 150 Hours ME Tape at 22C/80% r.h.**



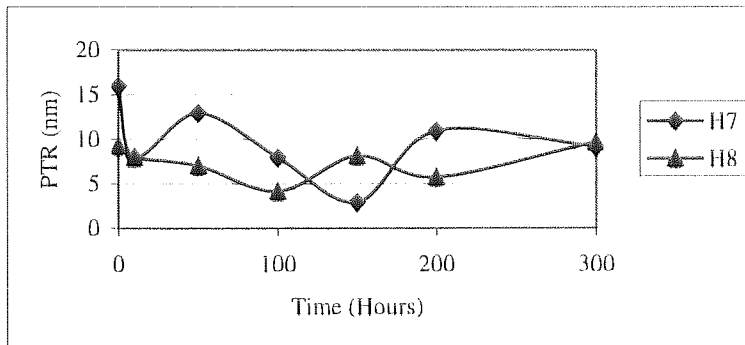
**Figure 4.95(b) Three-Dimensional AFM Representation of the Ripple-Like Pattern Observed on Some Metal Layers. This is the Same Area as Figure 4.97(a) above. It shows the Rippling to Continue through the Recessed Insulation Layers.**



**Figure 4.95 (c) AFM Linescan through Ripple Pattern Shown in Figures 4.97(a) and (b) above. Linescan shows the Ripple to Form a Continuous Wave through the Metal**

#### 4.5.5.4 H7 and H8: cycled against MP Tape for 300 Hours at 22°C/80%r.h.

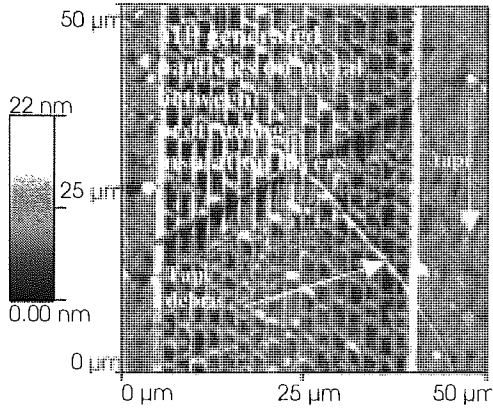
Figure 4.96 shows average PTR of H7 and H8 plotted against time. The PTR of both heads oscillated within a range of a few nm – H7 within 5nm either side of 9-10nm, and H8 within 3nm either side of 7nm. Table 4.25 shows that the protrusion of both heads behaved similarly, starting at 28 and 30 $\mu\text{m}$  ( $\pm 2\mu\text{m}$ ) for H7 and H8 respectively, both fell slightly to 24 $\mu\text{m}$  after 300 hours.



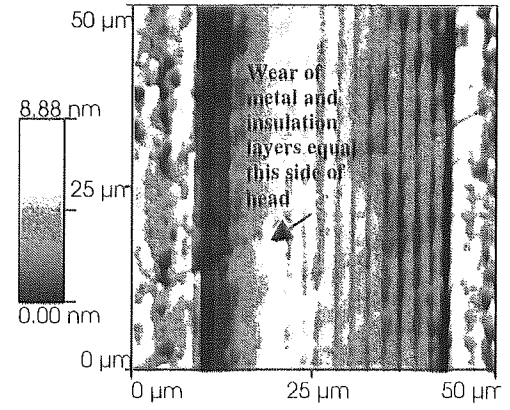
**Figure 4.96 Average PTR vs. Time for H7 and H8 Cycled against MP Tape 22C/80%r.h. Error in Individual AFM Measurements < 1nm. Each Data Point Average of 18 Measurements - Standard Deviations in the Range 3-8nm.**

Figure 4.97 shows a series of 50x50 $\mu\text{m}$  AFM images for H8 at 10, 50, 100, 150, 200 and 300 hours. Both H7 and H8 resembled Figure 4.84 after 10 seconds HCT. H7 resembled H8 during the course of the cycling, except that the MP generated particles could be observed, albeit sparsely distributed for 200 hours. These particles observed on both H7 and H8 at 10 hours trapped between the protruding insulation layers were very similar to those observed on H3 and H4 cycled against MP tape at 30°C/90%r.h. as can be seen by comparing Figure 4.97(a) with Figure 4.88. The dimensions and the distribution of these particles are given in Table 4.27, further illustrating the similarities between the particles generated by MP tape at the two different climates.

The insulation layers of H7 and H8 were recessed at 50 hours and the distribution of the particles was changed. They became more densely, but less regularly packed on the leading side of the gap and very sparse on the trailing side of the gap. From 100 hours to 300 hours the magnetic track of H8 was free of the MP generated particles and virtually



**Figure 4.97(a) H8 AFM: 10 Hours MP Tape  
22C/80%r.h.**



**Figure 4.97(d): 150 Hours**

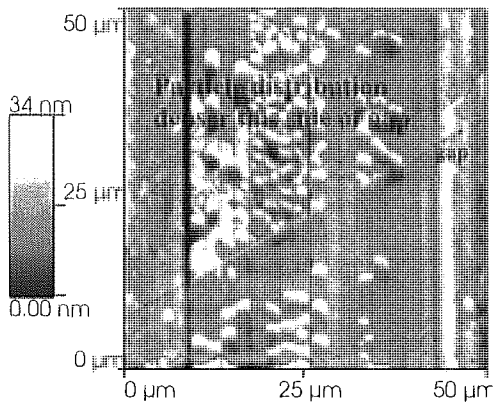


**Figure 4.97(b): 50 Hours**

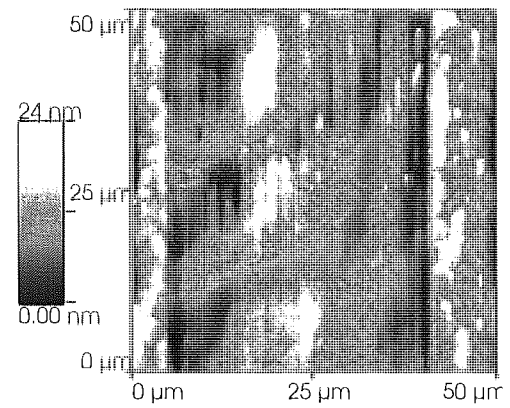


**Figure 4.97(e): 200 Hours**

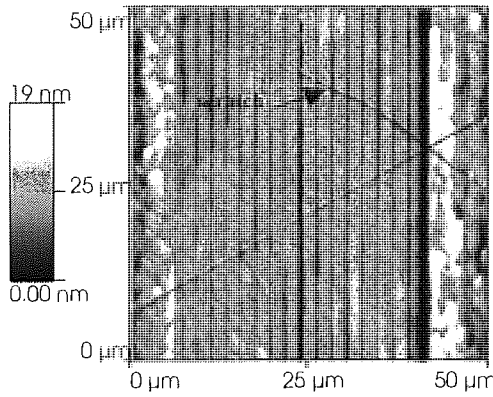


**Figure 4.97(c): 100 Hours**

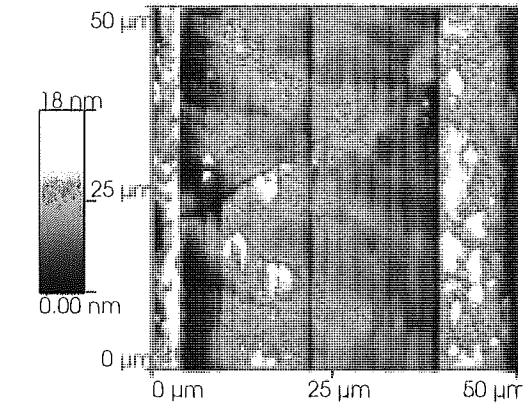


**Figure 4.97(f): 300 Hours**

free of debris. The insulation layers remained recessed relative to the metal layers within the gap. The surface remained similarly clean, with the exception that some of the MP generated particles were observed on the metal until 200 hours.

#### 4.5.5.5 H9 and H10: Cycled against ME Tape for 200 Hours at 25°C/20%r.h.

Average PTR for H9 and H10 are plotted against time in Figure 4.98. H9 started with a very high value of PTR of 55nm which fell to 21nm within the first 10 hours before rising again to 30nm at 50 hours, after which it remained constant, finishing at 31nm at 200 hours. H10 started with almost half the PTR of H9, at 30nm, but which fell to a similar value, 20nm, at 10 hours. H10 then showed a similar PTR to H9 up to and including 100 hours, after which it declined to 12nm whilst H9 remained constant.

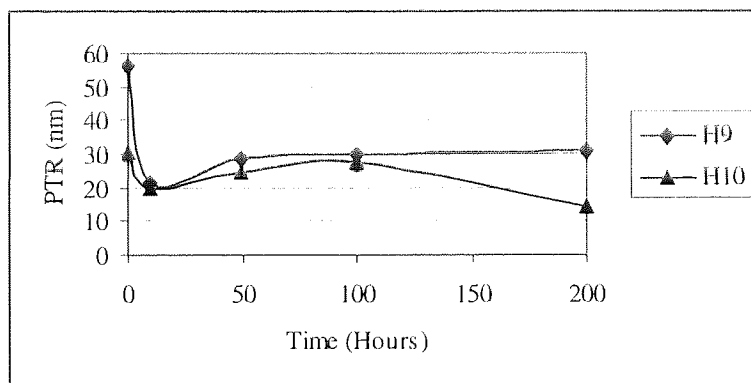


**Figure 4.98 Average PTR vs. Time for H9 and H10 Cycled against ME Tape 25C/20%r.h. Error in Individual AFM Measurements < 1nm. Each Data Point Average of 18 Measurements - Standard Deviations in the Range 8-10nm.**

From Table 4.25 it can be seen that H9 and H10 started with the same protrusion, but where as H10 ended with only a 2µm decrease in protrusion, the protrusion of H9 declined by 10µm from 26 to 16µm. However this decline occurred steadily with cycling, not within the last 100 hours where the PTR plot for H9 deviated from that of H10, suggesting that the deviation in PTR of the two heads was probably not connected to the deviation in protrusion.



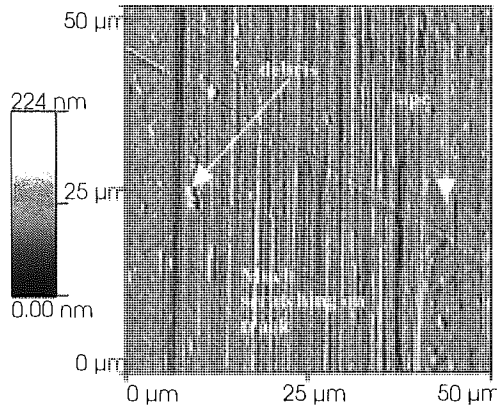


**Figure 4.99(a) H9 AFM: 10 Hours ME Tape 25C/20%r.h. Note - Shaded with Light from Left (All Images on this Page)**

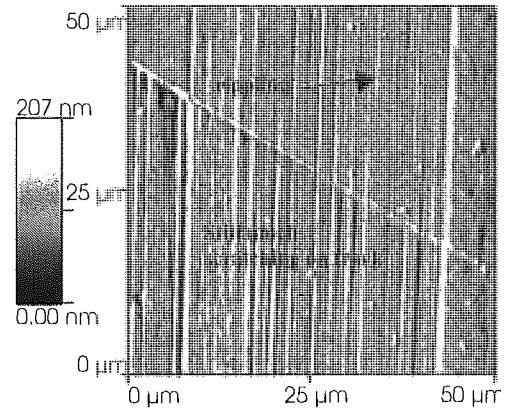


**Figure 4.99(d): 200 Hours**

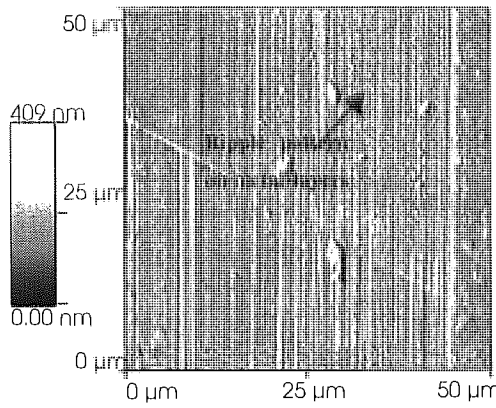


**Figure 4.99(b): 50 Hours**

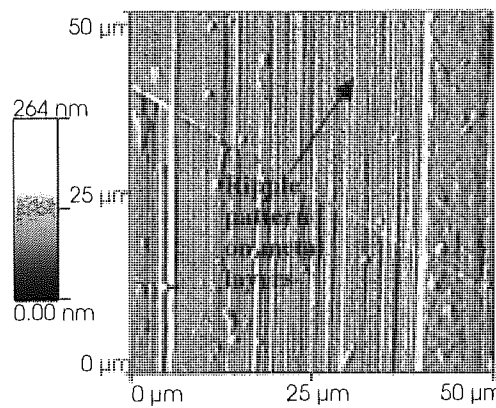


**Figure 4.99(c): 100 Hours**

Figure 4.99 shows 50x50 $\mu\text{m}$  AFM images of H9 at 10, 50, 100 and 200 hours. Both H9 and H10 resembled Figure 4.84 after 10 seconds HCT. Thereafter H10 resembled H9. With both heads the head surface did not change qualitatively with time. The ceramic region was free of debris. The track had a sparse covering of spherical debris – usually about 1 $\mu\text{m}$  in diameter, though sometimes larger. The track itself appeared at all times to be scratched parallel to the direction of tape travel such that the insulation layers were indistinguishable from the scratches, and their accompanying ridges. In some cases the scratching is associated with the debris particles observed on the surface. The continually higher PTR in H9 is probably due to the persistence of deep scratching (and the causal debris) with time with this head.

Like H5 and H6, cycled against ME at 22°C/80%r.h., on the metal layers a rippling was observed that ran perpendicularly to the direction of tape travel. In the case of H9 and H10 this occurred at all times. A similar peak-valley height and peak-peak separation was observed of 10nm and 0.7 $\mu\text{m}$  respectively.

#### 4.5.6 Comparison between Sandwich Heads Cycled against ME Tape under 30°C/90%r.h., 22°C/80%r.h. and 25°C/20%r.h.

There were a number of common features between the heads cycled against ME tape at the various different climates:

*Debris and Scratching:* At 30°C/90%r.h. and 25°C/20%r.h. there was much scratching parallel to the direction of tape travel on the track region. This made it difficult to distinguish between the various components of the head, and in some cases the boundary between the track and ceramic. Also on the surface of these heads loose, “spherical debris” was observed, which was often associated with individual scratches. There was less of this loose debris on the heads cycled at 22°C/80%r.h., though where there was a build up and subsequent release of debris on H5 between 10 and 50 hours, scratching was seen along the path that debris must follow to be removed from the head.

*ME Generated Particles:* At 22°C/80%r.h. a particulate deposit was observed on the metal layers. These particles were not seen at the other two conditions. MP tape generated a different type of particle that was observed at both 22°C/80%r.h. and 30°C/90%r.h.

*Ripple Patterning:* This was not seen at 30°C/22°C, however it was observed to be common on both the metal and insulation layers in both of the other conditions.

*Metal Delamination:* This was seen on one head only: H6 at 25°C/80%r.h.

*Debris Smearred from Ceramic from the Track:* H5 and H6 only at 200 and 300 hours.

#### 4.5.7 Comparison of Features between Sandwich Heads Cycled against MP Tape under 30°C/90%r.h. and 22°C/80%r.h.

*MP Generated Particles:* These were seen on heads run against MP at both conditions

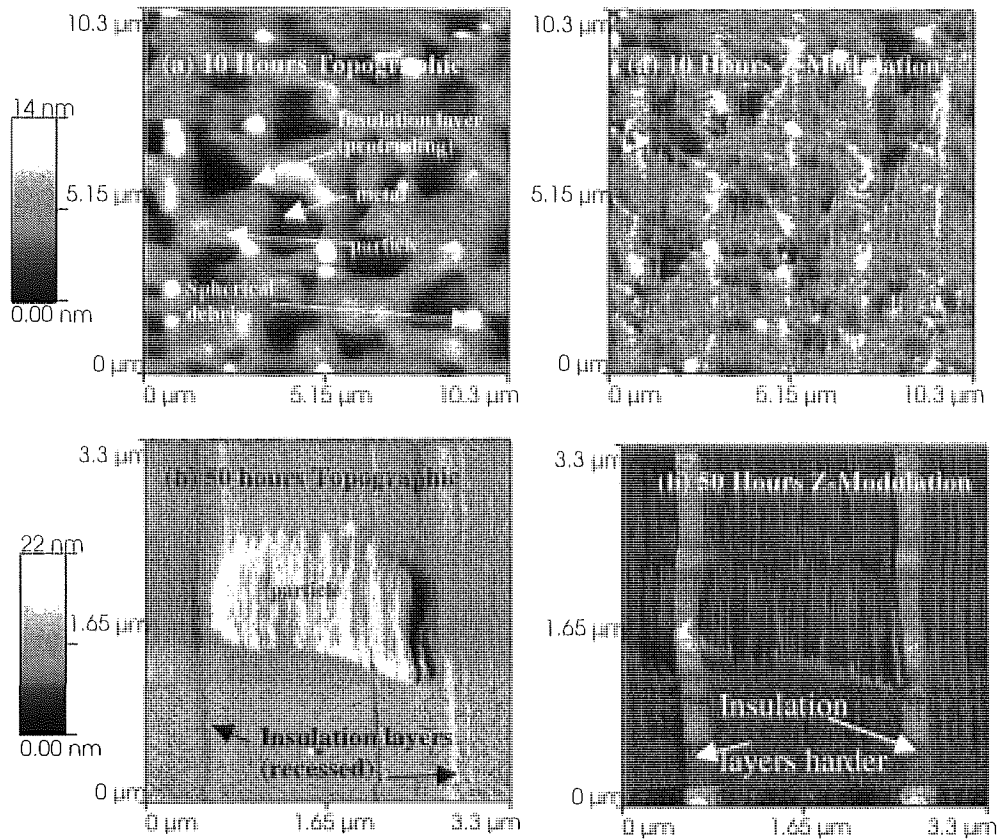
#### 4.5.8 Comparison of PTR with Time Between 30°C/90%r.h., 22°C/80%r.h. and 25°C/20%r.h.

At 22°C/80%r.h. for both ME and MP tapes PTR was shown to reach an equilibrium value or oscillate within a few nm of a value around about 10nm. For MP tape at 30°C/90%r.h. PTR did differ at 150 hours from 0 hours, again close to the 10nm level. However for ME tape at 30°C/90%r.h. and 25°C/20%r.h., PTR behaved more idiosyncratically for each head. This is consistent with the dominance of discrete scratches of varying depths and widths in the topography of the track and as the cause of PTR in these heads.

#### 4.5.9 AFM Hardness Measurements of Insulation Layers and MP Generated Particles

In all heads, after cleaning with HCT these were seen to be protruding. After 50 hours cycling with either ME or MP tape they were observed to be recessed relative to the metal layers by a few nm. They usually remained recessed for the remainder of the cycling period. However after an extended period of cycling, such as H5 after 300 hours ME, some of the insulation layers were again seen to be protruding above the metal – see Figure 4.98.

And both H3 and H4 had protruding insulation layers after 150 hours MP – see Figures 2.87 and 4.88.



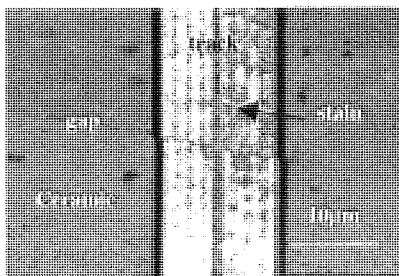
**Figure 4.100 H7: Comparison of the Topographic and Z-Modulation (Hardness/Compliance) Maps of the track region at (a) 10 Hours and (b) 50 Hours. Note - (b) is a different scale to (a). The Z-Modulation Plots – Black = the Softest Area, White = the Hardest, Greyscale = Intermediate. Hardness Measurement Relative, no Units.**

Figure 4.100 shows a z-modulation (hardness/compliance map) image (right) next to the equivalent topographical image (left) of the track of H7 showing the metal and insulation layers and the MP generated particles. Figure 4.100(a) is at 10 hours, at which time the insulation layers were still protruding. Figure 4.100(b) is at 50 hours (smaller area than (a)) with the insulation layers recessed. However in both cases on the z-modulation plot, the insulation layers are shown to have been harder than the neighbouring metal. Therefore the wear mechanism responsible for the recession of the insulation layers is not abrasion.

The z-modulation plots show there to be little contrast in the hardness/ compliance between the MP generated particles and the metal layers underneath, suggesting that they are of similar material

#### 4.5.10 Staining Observed by Optical Microscopy

The heads cycled against MP tape that showed the MP generated particles on the metal layers were observed by optical microscopy to have a brown stain on the metal layers. An example of this is shown in Figure 4.101, an optical photomicrograph of H3, after 150 hours cycling at 30 °C/90%r.h.



**Figure 4.101 H3 Optical Photomicrograph: "Brown Stain" on Metal Layers after 150 Hours Cycling at 30C/90%r.h. Against MP Tape**

## Chapter 5 Discussion

### 5.1 Introduction

In the previous chapter results were presented, discussed comparatively and summarised section by section for: the topographical analysis of MP and ME tapes before and after cycling (4.1), the wear rate data for dummy ceramic and metallic heads (4.2), topographical analysis of these heads (4.3), chemical analysis (XPS) of these heads (4.4), and a PTR study and topographical analysis of sandwich heads (4.5). The purpose of this chapter is to bring together these results and discuss the observed wear mechanisms occurring in the sandwich head materials against MP and ME tapes at the various climates studied. The PTR observed in the sandwich heads is discussed in light of the observed wear mechanisms. Two other phenomena were observed on the metal pole pieces of the sandwich heads that may influence spacing loss: patterning of the metal surface and stain are also discussed. Finally a short conclusion is given in Chapter 6.

### 5.2 Media Wear

Media wear per se is not the primary focus of this work. A study of the topography of the media before and after cycling was conducted to understand the nature of the counter, and wearing surface to the head.

The first stage in analysing the AFM topographical maps of the tapes consisted of removing the experimental tilt from the data. This revealed structure at a number of levels. For both MP and ME tape, cycled and uncycled, examples existed of ridging in the tape surface. This probably related to structure in the underlying tape substrates. It may have been due to the mounting of the tape sample in the microscope, however the period of these ripples, of a few microns makes this unlikely, and also makes it a potential source of noise in the magnetic recording process. At the tape surface both MP and ME tapes contained voids before and after cycling. For MP tape these voids could be seen to lie between asperity clusters (e.g. Figure 4.9(b)) corresponding to clusters of magnetic and head cleaning particles (too small to be seen on the scale of the images presented in

Chapter 4, but observed at higher magnification. In the case of MP tape the voids are probably due to a combination of tape material loss during calendaring in tape manufacture and subsequent cycling. Some of these voids may also be artefacts of the drying process – created by the convection of solvents to the surface during drying. The voids in the ME tape could only be due to delamination of portions of the magnetic layer of the tape. For both tape types it was not possible to detect an increase in the density of voids with cycling. The structure of the ME tape surface consisted of evenly distributed asperities in contrast to the particulate nature of MP tape.

Assuming a compliance of the tape substrate to the head, the structure of the tape surface (ridging, creases, scratches etc) was subtracted to leave the tape asperity distributions. For the MP tape, in agreement with the literature, the RMS roughness, average asperity height, and maximum peak-valley height decreased on cycling. This is consistent with the wear of highest asperities first, however the observed tape height asperity distributions for MP tape (Figure 4.17) show no consistent changes between uncycled and cycled tape. On the other hand the ME tape showed an unexpected increase in average asperity height and maximum p-v height on cycling. The RMS roughness was unchanged, but with the asperity height distribution plot (Figure 4.16) showing an increase in mid height asperities (5-15nm), rather than higher asperities up to 30nm seen on both cycled and uncycled samples. This could be due to a fine build up of wear particles on the tape, with the topical lubricant acting as a binder for the particles.

The RMS roughness values for all three types of ME tape used were identical before and after cycling –  $4.5 \pm 0.1$ nm. There was some variation in the uncycled RMS roughnesses of the MP tape, but after cycling MP1 and MP3 exhibited RMS roughnesses of 4.7 and 4.6nm respectively. On cycled MP2 differed significantly in terms of RMS roughnesses at 6.3nm. From Table 4.4 giving the mean asperity lateral spacing and p-v angle asperity it can be seen that these values overlap between the ME and MP tape type distributions – mean peak-peak separations in the range 0.3-0.6 $\mu$ m, and mean p-v angle 1-3°. The distributions from which these means were calculated were also similar. Thus an important result is that all the ME and MP tapes, despite a qualitative distinction between evenly distributed and agglomerated asperities respectively, after they were cycled showed a very similar asperity height distribution about the mean (RMS roughness) and very similar lateral asperity peak

distributions. A key difference, however is that the similar RMS values mask the greater prevalence of higher asperities in MP tape above 15nm – compare Figures 4.16 and 4.17. The particulate head cleaning tape appeared very similar to the metal particulate tapes, but it had a much greater roughness.

### 5.3 Microabrasion Texture on the Wear Surfaces of the Dummy Heads

The texture of the wear surfaces of both the metal and ceramic surfaces consisted of plastic deformation on the nano-microscale. This was in the form of grooving along the direction of tape passage. For example Figures 4.57 and 4.59 showing linescans through the microgrooving of a ceramic (S2 vs. MP tape) and a metal (M1 vs ME tape). The distributions of peak-peak separation and peak-valley angles thus produced from the metals and the ceramics were similar (e.g. Figures 4.59 and 4.60 – M1/ME and S2/ME). They were also similar in shape to the tape asperity peak-peak separation and peak-valley angle distributions. The mean peak-peak separations and peak-valley angles are given in Tables 4.9, 4.10, 4.11 and 4.12 for S1, S2, M1 and M3, and M2 respectively. The values for peak-peak separation (0.1-0.5 $\mu$ m) and peak-valley angle (1-3 $^{\circ}$ ) are very similar to those found for ME and MP tapes (0.3-0.6 $\mu$ m and 1-3 $^{\circ}$ ). These values confirm that the ploughing of the head wear surfaces is caused by the tape asperities that were abstracted by the background substitution routine used in the image processing of the measured AFM data – validating this technique. And that the ME and MP tapes abrade with similar shaped asperity peak-peak separation and peak-valley angle distributions despite their qualitative differences in surface topography.

ME and MP produced similar mean peak-peak separations in the microgrooving when taking section perpendicular to the direction of tape travel. But when viewed parallel to the direction of tape travel the microgrooving appeared to be universally wavy when caused by MP tape and much straighter when caused by ME tape. Thus showing the ME abrading asperities to be much more constrained, i.e. have a much stronger spring constant, than the MP asperities.

AFM imaging has allowed the direct observation of plastic deformation at the head surfaces and the scale on which it occurs. This begs the question of where the materials



stand on a plasticity index. These were discussed in Section 2.1.3.2. However although the topography of the plastically deformed surfaces were found to a high degree of precision, the mechanical properties (e.g. Poisson's ratio and elastic modulus) are not known. Similarly the tape asperity compliance of the media is also not known, which, as discussed in Section 2.1.3.3 is vital in calculating the head-tape contact pressure. An expansion of this project to utilise respectively nanoindentation to determine the mechanical properties of the material at the correct scale, and tape asperity compliance measurements would undoubtedly lead to a greater understanding of the elastic-plastic stressing of the head surfaces. And subsequently a greater knowledge of the wear processes.

#### 5.4 Relation of Measured Knoop Microhardness on the Observed Wear Rates

Knoop microhardness ( $H_k$ ) measurements were made from the wear rate measurement indentations and are listed in table 4.5. Comparing these to the wear rate measurements for 25°C/90%r.h., common to all materials it can be seen that wear rates do not follow closely trends in Knoop microhardness. This can be seen particularly in comparing the metals M2 and M3 that have a higher Knoop microhardness than the ceramics S1 and S2 (1275 and 1240 vs. 1082 and 1111Kg/mm<sup>2</sup> respectively), but higher wear rates against ME tape, though wear rate follows  $H_k$  with MP tape. This may be due to the low abrasive wear rates seen against ME allowing for the influence of other wear mechanisms. Also, these microhardness values come from static measurements of the indentations after the indenter was withdrawn, thus ignoring the effect of any hysteresis in the loading and unloading of the indenter. At a more fundamental level, as stated above the observed wear mechanisms, nanoscale mechanical properties are probably a better guide to the wear behaviour of these materials.

#### 5.5 Wear Mechanisms Observed in the Ceramic Materials

It was shown that by using XPS no detectable chemical differences were observed in the surface of the two ceramics S1 (CaTiO<sub>3</sub>) and S2 (CaTiO<sub>3</sub>/ZrTiO<sub>4</sub>/TiO<sub>2</sub> composite) to their nominal chemical state. Thus a general chemical wear mechanism was not operating across the surface of the ceramic. However this does not rule out the possibility of stress corrosion

at the grain boundaries as the fractional surface area of the grain boundaries was minuscule (<1%) and the low surface area sampled by the spectrometer was small producing only a small secondary electron count rate at the detector. Hence the signal to noise ratio of the experiment was unfortunately too great to pick up chemistry at the grain boundaries.

The wear rates produced by the MP tape class were generally an order of magnitude greater than those produced by the ME tape class. This is in line with the literature as discussed in Section 2.4.2.1. Mechanically three mechanisms of surface damage and of material removal were observed by AFM: microabrasion by the tape, scratching by third bodies, and by grain pullout. These three mechanisms have all been shown in the literature<sup>184,185</sup> to operate in ferrite multigranular ceramic recording heads. All three were generally observed in most S1 and S2 heads cycled against both tape classes and all conditions. In addition, very infrequently (but for both MP and ME tape) a thin sheet of the ceramic material was observed sheared from the head, either to one side of the head (Figure 4.48), or over into the metal region of a sandwich head (Figure 4.94). In the latter case the smeared debris also contain particles consistent in size with grain pullouts. Thus in this example at least the layer is not homogeneous. This suggests that these layers are wear debris bound together by lubricant from the tape (which is observed to be transferred the head in the case of ME media), rather than originating from homogeneous delaminations from the head surface. And thus does not represent an additional wear mechanism to the three outlined above.

Under all three environmental conditions studied (25°C/205r.h., 25°C/90%r.h., 40°C/80%r.h.), evidence for all three mechanisms were generally observed. Yet for both tape types different wear rates were observed, resulting from a different balance of these three mechanisms. Much the greatest wear rate (by about a factor of four over the next highest) was observed when the temperature was increased to 40°C keeping the relative humidity high at 80% - thus a temperature effect. At this temperature the greatest difference between the wear rates of the individual heads was also seen, and between the AFM images of the head surfaces. These showed much damage including deep scratching (Figure 4.25), a high density of debris including pullouts (Figure 4.28), and large-scale intra-granular fracture (Figure 4.31). The tapes, both MP and ME are causing much greater damage at this temperature. A rise in ambient temperature of 15°C is unlikely to affect

grossly the mechanical properties of the refractory ceramic, and the damage is likely to be due to a change in the tape. Definite evidence for a melting and removal of lubricant from both tape types was observed when cycling at an ambient of 60°C. The massive increase in “abrasivity” of the tape on an increase in temperature may be due to a change in the elastic-plastic properties of the binder system, or indeed of the tape substrate as discussed in Section 2.4.3.1.

At room temperature (22-25°C) in going from 20%r.h. – dry, to 80-90%r.h. – almost saturated, for the MP tape class an increase in wear rate was observed, consistent with the literature discussed in Section 2.4.3.2. Comparing the surface of the ceramics (S1 or S2) between dry and wet conditions (e.g. for S2: Figures 4.32 and 4.34) the density of fracture scars associated with inter-granular fracture and grain pullout does not seem to differ greatly. This suggests that the dominating mechanism is an increased rate of microabrasion with relative humidity. A subsidiary increase in inter-granular fracture may have been occurring, but evidence of if this occurred has been masked by the large material removal rate due to microabrasion.

The heads cycled against the ME class showed a contrary trend, with a higher wear rate at 20%r.h. than at 90%r.h. ME3 tape was used at 20%r.h., which as it was a 90minute tape would be thinner and hence less stiff than the 60minute ME1 tape used at 90%r.h., would be expected to produce a lower rather than a higher wear rate. Their surface roughness distributions were found to be equal and their surface finishes (DLC layer and lubricant) of the tapes were the same. Hence it is likely that the higher wear rate observed at 20%r.h. compared with 90% is a humidity-related phenomenon. Comparison of the head (S1 or S2) topography between 20%r.h. and 90%r.h. shows there to be a greater density of pullout fracture scars at the higher humidity (e.g. compare S2, Figures 4.29 and 4.30). Again, it is not possible to detect an increase of the rate of this wear mechanism relative to abrasion, and as the wear rate at the higher humidity was lower, this is not the dominating wear mechanism. This was likely to be tape microabrasion, with maybe a large contribution of the third body scratching, as there appears to be a fair density of deeper scratching on the head surfaces.

The factors that may be responsible for the variation in the room temperature tape microabrasion wear rates with humidity were discussed in Sections 2.4.3.2 and 2.4.4.2. XPS showed that this was not a chemical phenomenon with either S1 or S2. Any of the proposed mechanisms may contribute to the increase in wear rate with increase in humidity observed with the MP tape. These included: mechanical damage by ingress of water molecules, increased surface porosity caused by the ingress of water molecules, and a change in boundary lubrication regime to one which results in a greater surface normal force thus accelerating the Archard wear rate. The surprise result of the higher wear rate for ME tape at the lower humidity suggests that the boundary lubrication condition changes that occur with changes in relative humidity are of key importance in understanding the humidity dependence of the wear rate of these materials. In detailing their theory of how the spontaneous formation of water menisci formation about wear particles and asperities changes the boundary lubrication at the head tape interface, Patton and Bhushan<sup>119</sup> did not specifically measure wear rate. However they observed differences between MP and ME tape. The major difference being that even at low humidity the topical lubricant present on the ME tape was capable of forming menisci bridges between the head and the tape which increase the normal force at the head surface thus increasing the abrasive wear rate. Thus there exists a mechanism which may be responsible for the low humidity wear rate anomaly. Clearly the interaction of water and lubricant and their meniscus formation at the head tape interface. Another possible area of study on the humidity dependence on wear rate is the temperature/humidity dependence of the mechanical properties of magnetic tape.

Evidence for crack formation at the grain boundaries leading to grain fracture and removal –“pullout” is very clearly shown in Figure 4.34. But the mechanism of crack growth at the grain boundary is not clear. XPS was not sensitive enough to confirm or deny stress corrosion. Pullouts indeed were observed even at low humidity (e.g. Figure 4.23) suggesting that moisture is not essential to their formation. As discussed above this is a secondary wear mechanism at 25°C. Figure 4.56 shows surface cracks, probably along grain boundaries appearing under a particle on the head (S1) surface. The higher stress transmitted through a third body trapped at the head-tape interface in this case causing cracking at the ceramic surface. This is obviously a mechanism that must be considered for surface crack formation, though the relative contribution of this mechanism has not been

ascertained. However, as discussed in Section 5.7, pullout particles are an important source of third bodies that cause PTR. Thus environments that produce more pullout particles, i.e. where the microabrasion wear rate is low, might be expected to suffer from third-body PTR e.g. ME tape at 25°C/90%r.h., and any tape at 40°C.

### 5.6 Surface Chemistry of the Three Metallic Materials, Topographic Features and Wear Mechanisms.

Unlike the ceramic materials, the wear surfaces of the three metallic materials: CoNbZr, FeNbSiN, and FeTaN (M1-M3) generally exhibit a change in surface chemistry (as measured by XPS) at the wear surface from the unworn state (the native oxide). The XPS measurements were made after wear of much greater depth (0.5-1µm) than the depth of the native oxide (10-20nm) The wear tests were carried out at high humidity, but the surfaces formed were different to those produced by the forced corrosion of these metals in boiling water.

By eye corrosion products were observed during the course of the forced corrosion experiments on FeNbSiN after 10 minutes, FeTaN after 2 hours, and CoNbZr after 3 hours. Thus giving a rough indicator on the speed of corrosion of these three metals. FeNbSiN corrodes much more easily than the other two.

CoNbZr shows a relative increase of the ratio of ZrO<sub>2</sub> and niobium oxides to CoO at the surface of the forced corroded sample relative to the native oxide. Cycled against ME tape at 25°C/90%r.h. the surface consists mainly of Co metal with a small amount of Nb metal. A thick hydrocarbon coating is the only explanation for the lack of a native oxide reformation on this wear surface given the standing time in air between the cycling test and the XPS analysis. Against MP tape Nb oxides dominate the wear surface (similar to the native oxide for this head).

The non-metals in the two Fe alloys show a similar behaviour on forced corrosion. The nitride peaks in both and the silicide shift to higher binding energy perhaps indicating their partial (they have not shifted enough to become pure oxide peaks) oxidation or hydroxylation in the corrosion mechanism. In the native oxide of FeTaN the iron exists as

Fe<sub>2</sub>O<sub>3</sub>, and Ta as the highest oxide (Fe<sub>2</sub>O<sub>5</sub>), with some nitrate. However FeNbSiN shows nitrates, SiO<sub>2</sub>, mixed Nb oxides and Fe as the metal. Thus the greater susceptibility of this material to corrosion may be due to the existence of lower oxides of Nb and Fe metal, all of which will be thermodynamically unstable with respect to (further) oxidation. Given the difference in susceptibility to corrosion between the two metals, but the commonality of nitrates in the native oxides, the presence of nitride reaction products in the native oxide is a less significant factor in the susceptibility to corrosion.

For FeNbSiN heads studied at both 25° and 40°C the main constituent in the wear surface was Fe<sub>2</sub>O<sub>3</sub>. In two cases (ME at 25°C/90%r.h. and MP at 40°C/80%r.h.) FeOOH was definitely seen. At the surface some Nb existed as both the nitride and the oxide and nitrogen in the form of nitrates were also observed, indicating some corrosion of the grain boundaries. The odd sample out was that cycled against ME at 40°C/80%r.h. which showed iron metal at the wear surface. For FeTaN the wear surfaces both consisted of Fe metal with a smaller amount of TaN probably acting as a passivating layer preventing the oxidation of the iron.

For all three metals it is clear that the surfaces undergo tribochemical changes that are different from their corrosion in the absence of mechanical action. No systematic changes due to the tape type used could be determined due to the low number of samples. It was only possible to catalogue some of the possible changes in tribochemistry. For CoNbZr the presence of a fresh layer preserved by a hydrocarbon layer on one head and the native oxide observed on another head compliments Auger mapping of CoNbZr wear surfaces by this author<sup>316</sup> which show the wear scar to have a thinner oxide layer than the unworn surface. Thus suggesting that wear occurs through the native oxide, creating a “fresh” metal surface which re-oxidises to the native oxide to some extent if exposed to air. For FeNbSiN one head shows evidence of a fresh Fe/NbN surface, with all the others showing some re-oxidation. However this differs from the native oxide or corrosion formation due to the presence of iron hydroxides and the lack of nitrogen and silicon hydroxylation products. Both the FeTaN heads examined showed a fresh Fe/TaN surface.

In terms of magnetic performance at high frequency an oxide, or magnetic dead layer build up at the surface of the metal is disadvantageous as it is a source of spacing loss. On the

limited evidence presented here CoNbZr and FeTaN perform better in this respect than FeNbSiN. The Native oxides were measured at between 10 and 20nm thick contributing up to a 2dB spacing loss at a recording wavelength of 1 $\mu$ m. Material selection to minimise oxidation dead-layer thickness may be necessary to minimise spacing losses as the desired recording wavelength decreases.

The measured surface chemistry showing as it does an absence of corrosion at the worn head surfaces does not explain the observed differences in wear rate. All three metal surfaces show microabrasion. And against MP tape the wear rates follow the trend in Knoop microhardness with FeTaN and FeNbSiN showing similar wear rates and the softer CoNbZr showing a larger wear rate. Against ME tape FeTaN shows a surprisingly higher wear rate than either CoNbZr or FeNbSiN. This is hard to explain in terms of the metal surface after wear either chemically or topographically. Figure 4.38 does show however that the as deposited surface shows a much less regular surface compared to either M1 (Figure 4.35) or M2 (figure 4.41). Deng et al<sup>253</sup> also found the as deposited FeTaN surface was prone to pitting. Thus it may be that the poorer surface quality of FeTaN is causing a higher relative wear rate in the low rate regime with ME tape, but not influencing to the same extent the wear rate against MP where wear occurs more deeply.

FeNbSiN is alone amongst the metals in showing grain pullout like the ceramics showing perhaps a grain structure beyond the nanocrystalline.

## 5.7 Observed Pole Tip Recession

For the material combination studied, S2 ceramic and M3 metal with Si<sub>3</sub>N<sub>4</sub> spacers and a Mo/Au bonding layer PTR was low. After over 100 hours of cycling the PTR value did not reflect the starting value and was less than 15nm. The main difference was in the case of cycling against ME tape at low humidity - 25°C/205r.h. in which one head showed a PTR of 30nm and increasing. Like the wear of the ceramic materials the surface condition of the heads and the amount of PTR depended upon the environmental conditions. PTR was very rarely constant across or along the pole pieces - it was sometimes both biased towards one ceramic piece or the other, and often contained individual trenches. In addition to PTR much staining was observed on metallic pole pieces of many of the heads, and in a few

cases a patterning of the pole pieces was observed. The harder ceramic spacers between the individual metallic laminations usually started off protruding relative to the metallic layers, but were observed to become fractured after some number of hours cycling, lying below the level of the metal until the metal had once again worn past the spacers.

At 40°C the wear of the ceramic heads was shown to be large and with a large amount of damage to the head surfaces that varied from head to head. A temperature of 30°C was used as the elevated temperature for the sandwich heads. At 150 hours Figures 4.86 (ME) and 4.87 and 4.88 (MP) show much pullout from the ceramic. In the case of ME worn surface there is evidence of these grains being dragged across the surface of the ceramic and the track causing damage to both the ceramic and the track. The pole tip recession was zero within the track except for the deep scratches, which were observed more on one head than the other illustrating the random nature of the gross wear at elevated temperatures. The baseline zero measure of PTR shows that the pole pieces and the substrate were wearing equally, except for the individual scratching events. Against MP tape the average PTR was similar (11-14nm). The main difference as compared to the ME worn heads is the protection of the metal layer by stain particles standing proud from the recessed metal layers.

At 22°C/80% against ME tape PTR was shown to reach an equilibrium value of around 9-10nm after 100hours of wear. Up until 100 hours PTR was dominated by the starting values and its growth influenced by 3<sup>rd</sup> body abrasion by debris particles (Figures 4.91 and 4.92). The Si<sub>3</sub>N<sub>4</sub> spacing layers had fractured by 50 hrs cycling. Between 50 and 150 hours particles were seen adhered to the metal lamination. In H6 fracture was occurring at some of the Si<sub>3</sub>N<sub>4</sub>/FeTaN interfaces leading to delamination of FeTaN. The continued occurrence of thin FeTaN delaminations through a greater wear of the head indicates a deep running interface fault. This is a phenomenon that if it affects a large area of the magnetic pole pieces that will be a large contribution to spacing loss. It is probably an artefact of the head manufacture, indicating a key quality control factor to be monitored to ensure head reliability. From 200 hours onward a large amount of ceramic debris is shown smearing onto the pole pieces, containing small and pullout wear debris, as discussed in Section 5.5 above. It act a source of spacing loss in itself, and upon break up may contribute a source of third body abrasives which cause additional PTR.



Against MP tape at 22°C/80% PTR was seen (Figure 4.96) to oscillate ( $\pm 5\text{nm}$ ) about 7nm – a similar value to the equilibrium value achieved against ME tape. However in the case of MP tape this was achieved from 10hours rather than 100hours cycling, perhaps due to higher material removal rate of the MP tape allowing for the equilibrium to be reached more quickly. Stain particles were observed on the metal layers between the protruding spacing layers at 10 hours. At 50 hours the spacing layers were observed to have fractures and the density of stain particles to have decreased. From 100 hours no more stain was observed on the head.

Against ME tape at dry conditions - 25°C/20%r.h. PTR became larger at 30nm after the starting surface had been removed by wear at 100 hours, than any of the other environments. It was shown not to maintain an equilibrium value (Figure 4.98). From 10-200 hours the texture of the pole pieces was dominated by deep scratching (Figure 4.99) – as indeed was the ceramic surface, as discussed in Section 5.5. There is also evidence of for the presence of the responsible debris, but not its origin. Like 30°C, PTR is not at equilibrium where the passage of third bodies along the pole piece is not at equilibrium. Unlike at 30°C the base PTR is not zero probably due to a low and therefore differential tape abrasive wear rate for the metal and the ceramic.

For the sandwich heads employed PTR has been shown to be an equilibrium process at 22°C/80%r.h. The value of PTR observed at this equilibrium ( $\sim 10\text{nm}$ ) is such that the highest measured tape asperities of both MP and ME tape can impinge on the metal pole pieces even when recessed. The principal wear mechanism in this climate for both materials has been shown to be microabrasion by the tape. Thus it is highly likely that the model for differential wear due to Abe, Tsuchiya and Noro<sup>285,217</sup> which was discussed in Section 2.7.5 holds for this climate. That is to say that the faster wearing metal pole piece becomes recessed causing the pressure on the metal to fall reducing the wear rate of the metal reaching an equilibrium recession at the point at which the wear rate of the ceramic and the metal have become equalised. With the higher base wear rates exhibited against MP tape this equilibrium will be reached more quickly as was shown by the experimental behaviour. As the chemical changes occurring at the metal surface are not thought to be influencing wear of FeTaN they are unlikely to be influencing pole tip recession.

In addition to differential tape microabrasion, PTR was also shown to be caused by third body scratching, with the main source of third bodies thought to be from grain pullout from the ceramic. It has been shown (Figure 4.28) that these pullout particles could keep their integrity as they were transported across the head surface ploughing the surface. This was shown to be the case particularly for the dry (25°C/20%r.h.) and warm (30°C/80%r.h.) climates. The third body PTR was more irregular across the poles with a depth that was often greater than that caused by differential abrasion. It generally did not reach an equilibrium level showing that the passage of third bodies across the track did not reach equilibrium. When the author<sup>316</sup> examined a S1/M1 sandwich head with no laminations in the metal layer, a very large PTR (>100nm) which could not possibly be caused by tape asperity ingress third bodies were identified in the track that were shown to originate from the ceramic by Auger chemical analysis. Thus adding further evidence for confirming this mechanism.

## 5.8 Staining

Stain was not studied extensively in this work, but was recorded and measured by AFM when and where it was observed. Stain build up was seen uniquely on the metal surfaces only and not on either of the ceramic materials. Stain is observed on ferrite heads – see the discussion of the literature in Section 2.6, and thus marks a major difference between the use of these CaTiO<sub>3</sub> based tape bearing surfaces compared to ferrite. It was seen more frequently on heads cycled against MP than those cycled against ME tape. It was observed on all the heads cycled against MP tape (22°C/80%r.h. and 30°C/90%r.h.) e.g. Figure 4.88. These were shown to consist of discrete particles sitting on the metal laminations (in between whilst these still protrude), but not on the Si<sub>3</sub>N<sub>4</sub> spacers. The dimensions of the MP generated stain particles are given in Table 4.27. Their distribution on the pole pieces varies from head to head, but the separation of the particles down the length of the heads was often quite regular with separation values typically 1.5-5µm. The length is constrained by the width of the metal laminations – generally 1.8µm. The width -parallel to the direction of tape travel was generally slightly less at 1-1.5µm. The height of these particles was usually around 10nm, and they sat within the recessed metal layers generally not protruding above the level of the ceramic tape-bearing surface. Together with the lack of

stain formation on the ceramic tape bearing surface, this suggests that stain will not provide an additional contribution to spacing loss with a sandwich head of this material combination.

Stain build occurred less frequently in the sandwich heads cycled against ME tape. The stain generated by the ME tape consisted of particles that sat on the metallic laminations only. They were of similar dimensions to the MP generated particles, but showed a qualitative difference in appearance (compare Figure 4.90 (MP) with 4.93(ME)), suggesting a different origin, which suggests pullout from the tape rather than pullout debris from the ceramic.

Figures 4.90 and 4.93 show that both the ME and MP generated particles persist long enough on the metal surfaces to be abraded by the tape rather than be removed by the next pass of tape. With cycling time the position of these particles changes e.g. compare Figure 4.92(c) – vs. ME at 100 hours to 4.94(b) at 50 hours. Thus a dynamic equilibrium of particle adhesion and particle removal (either by abrasion or pull away) of this staining exists. In all cases this staining did not generally persist beyond 150 hours and in the case of ME tape at 25°C/20%r.h. not beyond 50 hours. In terms of the dynamic equilibrium of stain formation, the rate of removal has become much greater than that of generation. There was no evidence for a rapid increase in wear rate for all heads beyond 150 hours. Therefore the rate of particle adhesion has been slowed. This may be due to the repeated cycling of the media during the course of the wear test with the wear of the virgin or nearly virgin tape creating more wear debris.

Stain formation on the dummy metal heads followed the same pattern of stain formation on the metal laminations of the sandwich heads in that it was more common for MP rather than ME tape. One major difference was that the stain particles that were observed on the dummy head surfaces that were not bounded by other materials show larger, though generally not thicker particles. The stain on the metal dummy heads surfaces adopted a ribbon-like or a triangular shape and in common with the stain on the sandwich head laminations there was a regular separation between waves of stain along the length of the head.

## 5.9 Ripple Texturing of the Metal laminations of the Sandwich Heads

This distinct phenomenon illustrated in Figure 4.95 was observed infrequently on sandwich heads cycled against ME tape. It is perhaps caused by some stick-slip action of the head tape contact. This is would perhaps be a cause of noise in the magnetic recording or playback signal. Similar patterns have been observed<sup>317</sup> on the ferrite component of metal in gap (MIG) heads, either specifically on the leading or the trailing edge, or both. Steep wave fronts developing in the boundary lubrication layer in the solid-polymer interface have been reported<sup>318</sup> as the cause of such wear patterns is seen in the extrusion of polymers<sup>319</sup>, the abrasion of rubber<sup>320</sup> and in Schallamach's waves of detachment<sup>321</sup>. These are of course wear patterns occurring on the polymeric surface (i.e. tape), but these waves must also be acting on the opposite surface (i.e. head). The initiation of these waves at specific times is not understood and could be the subject for further research.

## Chapter 6 Conclusion and Suggestions for Further work

This work has identified the mechanisms that lead to Pole Tip Recession in laminated magnetic recording heads composed of soft magnetic laminations sandwiched in a multi-granular non-magnetic ceramic tape-bearing substrate. The wear rates, wear mechanisms and surface chemistry with cycling against MP and ME tapes of individual materials that together compose these heads were studied separately. The conclusions of this work are stated below, followed by a discussion on the implications for the industry and suggestions for further work.

The wear rates produced by MP tapes were generally an order of magnitude greater than those produced by ME tape. This ordering of wear rate is to be expected due to the presence of hard head cleaning agents included in the binder system of MP tapes. No simple Knoop microhardness dependence of wear rate was found and it was concluded that this was due to the influence of secondary wear mechanisms (those that are independent of microhardness) and because the Knoop microhardness indentations were made on too large a scale (depth of  $1\mu\text{m}$ ). It was considered that nanohardness measurements are more likely to represent the material properties given the estimated depth of the wear process (a few nm).

Wear rates were found to be highly dependent on climate. A very strong temperature effect on wear rate was found for all materials measured with a large increase from  $25^{\circ}\text{C}$ - $40^{\circ}\text{C}$ . This was attributed to a change in mechanical properties of the tape, though more direct experimental evidence for the changes in tape properties with running temperature is required to understand this phenomenon. For MP tapes the wear rate of the ceramic materials was ranked in descending order:  $40^{\circ}\text{C}/80\%\text{r.h.} > 25^{\circ}\text{C}/90\%\text{r.h.} > 25^{\circ}\text{C}/20\%\text{r.h.}$ . For ME tapes:  $40^{\circ}\text{C}/80\%\text{r.h.} > 25^{\circ}\text{C}/20\%\text{r.h.} > 25^{\circ}\text{C}/90\%\text{r.h.}$ . The unexpectedly low wear rate against ME tape of the ceramic materials at  $25^{\circ}\text{C}/90\%\text{r.h.}$  compared to  $25^{\circ}\text{C}/20\%\text{r.h.}$  could not be explained satisfactorily. Neither could the high wear rate of FeTaN against ME tape at  $25^{\circ}\text{C}/20\%\text{r.h.}$

XPS data showed that the ceramic heads underwent no chemical changes over the area of the grains, but was not sensitive to detect stress corrosion, if any, at the grain boundaries. In contrast to the chemical stability of the ceramic surface XPS showed changes to the chemical structure of the native oxide surfaces of the metals with cycling at high humidity (25°C/90%r.h). The surface chemical states of the cycled heads were different to those in which the metals were corroded in the absence of mechanical action..

Wear rates, topographical changes and XPS data were used together to determine the wear mechanisms for the 5 materials. At 40°C/80%r.h. for the ceramic materials against both ME and MP tape gross damage to the heads was observed due to a number of mechanisms – intra-granular and inter-granular fracture and third body scratching. Together these produced a much larger wear rate than observed at the lower temperatures. For all materials, at 25°C/90%r.h and 25°C/20%, against both ME and MP tapes the principal wear mechanism was found to be microabrasion by the action of tape asperities. The difference in wear rates between utilising different tape types or climates was in the main due to a change in the microabrasive wear rate rather than the influence of additional wear mechanisms. At low humidity for the ceramic materials third body scratching probably contributed to the wear rate. This wear mechanism, along with grain pullout was seen occur in both ceramic materials under most conditions, but were not contributing significantly to the wear rate. However grain pullout was found to be an important source of third bodies responsible for PTR.

PTR was shown to be caused by two mechanisms, the relative contribution of both depending upon the climate at which the heads are run:

- (1) Differential rates of microabrasion, by the tape asperities, of the substrate and pole materials. This reaches equilibrium as the pressure declines on the pole piece as it becomes recessed. This was similar in value for both MP and ME tapes, although under low wear rate regimes i.e. ME tape, a long tape cycling time (100 hours) was required to achieve equilibrium. This was the main mode of PTR at 22°C/80%r.h.
- (2) Third body scratching. The main source of third bodies is probably grain pullout from the ceramic. This mode is particularly active at elevated temperatures (>30°C) and high

humidity (80-90%r.h.), and at low humidity at room temperature (25°C/20%r.h.). It is irregular in appearance (a non-uniform level of PTR within the recessed area), and can cause greater values of PTR than can be generated by the first mechanism as it is not limited in depth by the limit tape contact with the well of the recession. It does not necessarily produce an equilibrium value of PTR.

In addition to PTR, two other distinct phenomena were observed at the surface of the laminated heads. The first, brown staining, occurred exclusively on the metallic laminations. MP tape showed a greater propensity than ME tape to staining. This staining was seen to consist of discrete particles that were different for MP and ME tape types. This staining did not sit proud of the tape bearing surface thus not adding to the spacing loss of the pole tip recession. The second phenomenon is a ripple texturing of areas of the metallic laminations observed after cycling against ME tape. This may be due to a stick-slip of the head-tape interface and thus a source of noise within the magnetic recording or playback signal.

The above stated conclusions lead to a number of implications for the magnetic recording industry, and for the users of magnetic tape recording devices. The wear rate of the ceramic materials and hence a fully functional head was shown to be an order of magnitude greater against MP than against ME tape. Thus a preference for use of MP over ME tape by the consumer will tend to increase the AFR (average failure rate) of the tape recorders due to head wear out. The exaggerated wear of the heads due to MP tape becomes particularly apparent at higher humidities and especially higher temperature. Thus the manufacturer may wish to investigate more closely the environmental envelope in which heads consisting mainly of the  $\text{CaTiO}_3$  ceramic may operate against particulate tapes without the risk of accelerated wear and the coincidental damage to the magnetic pole pieces caused by removal of large amounts wear debris. If the operating envelope of these heads is found to be too narrow as compared with expected customer usage then an alternative substrate material may be advisable to avoid a large warranty bill. It is advisable for the user of a video camcorder utilising  $\text{CaTiO}_3$  based heads to use ME tapes to avoid shortening the head life when operating in tropical environments (>30°C and near saturation humidity).

This work has shown that an underlying level of PTR is reached in laminated heads due to differential wear of the metal by abrasion of the metal by the tape and third body wear debris. CoNbZr has been shown to be significantly softer than the two ceramic materials and thus might be expected to show higher values of equilibrium PTR. The two iron materials, with a higher Knoop microhardness seem to be better suited on this front. Of these two metals, FeTaN showed no surface oxide formation with cycling at high humidities whereas FeNbSiN exhibited iron oxide and hydroxide. Thus FeTaN is less likely to suffer spacing loss as a result of magnetic dead layer formation. After confirming this on a larger number of samples FeTaN would seem more suitable than FeNbSiN for high bandwidth magnetic recording heads where spacing loss must be minimised. Indeed a 30nm of spacing due to oxide layer formation is equivalent to a playback loss of 5.4dB at a recording wavelength of 0.3 $\mu$ m.

This work has identified pole tip damage by pulled-out grains as major risk in using multigranular ceramics in high bandwidth tape heads. In addition to the use of calcium titanate based ceramics in laminated heads, multigranular ceramics (in the form of AlTiC – with aluminium oxide and titanium carbide phases) are commonly used as the substrate and tape bearing surface in thin film magnetic heads in linear tape systems such as the Travan, DLT and LTO data tape formats. Following the identification of the significance of this damage mechanism in this work, thin film tape head manufacturers have supported this laboratory in the exploration of the genesis of grain pullout in AlTiC tape bearing surfaces and the subsequent pole tip damage<sup>322</sup>. There would therefore be a benefit in using single crystal substrates for tape heads, however this must be weighed against the increased costs of producing single crystals.

The multigranular CaTiO<sub>3</sub> based ceramics used did not become stained under any of the varied environmental conditions used. Thus, in this respect, are superior as a tape-bearing surface to traditional ferrite head materials that do stain under certain environmental conditions leading to spacing loss.

It is an implication of the above-described model for PTR that one must always expect some degree of PTR. Thus one must consider the extent to which this hampers the operation at higher frequencies of laminated tape heads? Equilibrium values of PTR in this



work were found to be in the low tens of nanometres – and 30nm is equivalent to 5.4dB signal loss on playback at a recorded wavelength of 0.3 $\mu$ m. With low PTR (<30nm) evidence for tape-pole contact was observed suggesting that such PTR values will not yield a spacing loss. However examples were observed where PTR extended to levels beyond head tape contact and where much damage was caused to the pole structure by third bodies although even though overall PTR was low. Both of these cases are likely to introduce signal loss, and may lead to catastrophic loss. Hence a hard but thin (~10nm) coating on the head surface should be considered, that will result in a non zero, but constant spacing loss, and will prevent head wear. Such coatings are used on some linear tape heads and hard disk heads. The implication of zero head wear removes the option of running in a tape head to the tape used, and thus the ideal conformation must be machined to the head before the hard coating is applied. It also limits the use of tape to those that may be conformed to the standardised head profile instantaneously by tape tension control alone, without raising the tape tension to levels that may wear the head or damage the tape. In practise this acts to rule out backward compatibility with older thick, but cheaper tapes. The condition for zero wear of the coated head surface also tends to rule out particulate media reliant on hard HCA particles. This limits the use of coated helical scan tape heads to ME media. Thus the hard-coated laminated tape head is not a possibility for tape formats that use or need backward compatibility with particulate and thicker ME media, but is an option that should be considered for new formats.

In this work wear rates were successfully calculated from the rate of change of depth of Knoop microhardness indentations made into the surface of the dummy heads. However relatively long experiments (>100hours) were required to obtain sufficient measurable wear in the indentations. The use of nano-indentations measured by AFM would rapidly reduce the experimental time scale. In addition the lower relative surface area of nano-indentations would allow their use on real head structures as opposed to dummy heads. The benefit of obtaining material mechanical properties on the nano-scale have already been discussed. Thus the author would advise workers embarking on similar work to use nanohardness techniques.

AFM has proven to be a powerful tool for non-destructive, in-situ examination of the head surfaces allowing for quantitative measurement of phenomena such as PTR recession and

stain thickness on the nanoscale within structures whose lateral dimensions may be expressed in microns. AFM was also useful for observing the qualitative changes in the microstructure of the tape-bearing surface which have enabled the elucidation of the wear mechanisms. However AFM cannot make chemical analysis and further understanding of the third body pole tip recession mechanisms could be made by having the means to identify the chemical composition of individual third bodies on the pole pieces. Unfortunately the surface analytical technique Scanning Auger Microscopy which was available to perform this task could not be used due to the residual magnetisation of the magnetostatically coupled laminations.

To continue the work began here it would be of interest from a tribological point of view to evaluate in more detail the mechanical interactions at the head-tape interface in order to understand more the observed variations in the abrasive wear rate, especially the effect of humidity. Further techniques, not available to the author during this research include “tape-asperity compliance” techniques to examine the dynamic load of the tape and of the examination of the mechanical properties of both the heads and tapes using nanoindentation techniques. Humidity is not only important at the head-tape interface because of its influence on head wear. Water adsorbed at the head-tape also has an effect on the head-tape contact force and the playback signal strength with resultant modulated head-tape spacing. Further work on the effects of humidity on signal in the recording or play back process are thus of importance in their own right, and may give insight into the processes by which wear may be influenced by the presence and absence of airborne moisture.

The wear mechanisms for the materials involved and a model for PTR have been identified in this work. In order for this to become a predictive quantitative model for PTR growth with much more PTR Vs. time data would be required. However it has been identified in this work that for the case where the material combination (ceramic and magnetic material) results in low or zero equilibrium PTR, then non equilibrium events such as third body scratching dominate the pole – tape contact, and that these events are influenced by climate and/or tape type rather than just showing a dependence on distance of tape pulled.

## References

- <sup>1</sup> A. Broese van Groenou, H.J.J.C. Meulenbroeks and M. de Jongh, "Level differences in Hybrid Heads after Contact with Various Tapes", *IEEE Trans. Magn.*, 26(1), 1990, 153-155
- <sup>2</sup> C. Dennis Mee & Eric D. Daniel, "Magnetic Recording Handbook", McGraw-Hill, 1990, p284
- <sup>3</sup> R.L. Wallace, "The Reproduction of Magnetically Recorded signal", *Bell Syst. Tech. J.*, 30, 1145-1173
- <sup>4</sup> H.Neal Bertram, "Fundamentals of the Magnetic Recording Process", *Proceedings of the IEEE*, Vol 74, No.11, 1986, 1494-1512
- <sup>5</sup> J.C. Mallinson, "Maximum Signal-to-Noise Ratio of a Tape Recorder", *IEEE Trans. Magn.*, MAG-5, 1969, 182-186
- <sup>6</sup> J.C. Mallinson, "The Foundations of Magnetic Recording", Academic Press, San Diego, California, 1987
- <sup>7</sup> K. Tsuneki, T. Ezaki, J. Hirai and Y. Kubota, "Development of the High-Band 8mm Video System
- <sup>8</sup> K. Okamoto, Y. Okazaki, N Nagai and S. Uedaira, "Advanced Metal Particle Technologies for Magnetic Tapes", *J. Magn. Magn. Mater.*, 155, 1996, 60-66
- <sup>9</sup> Finn Jorgensen, "The complete Handbook of Magnetic Recording", 3<sup>rd</sup> Edition, Tab Books Inc., Blue Ridge Summit, PA, 1988
- <sup>10</sup> E.P. Wohlfarth, "Magnetism", Academic Press, New York, 1963, Vol. 3, 351
- <sup>11</sup> K. Tsuneki, T. Ezaki, J. Hirai and Y. Kubota, "Development of the High Band 8mm Video System", *IEEE Transactions on Consumer Electronics*, 35(3), 1989, 436-440
- <sup>12</sup> H. Inaba, K. Eejiri, K. Masaki and T. Kitahara, "Development of an advanced Metal Particulate Tape", *IEEE Trans. Magn.*, 34(4), 1998, 1666-1668
- <sup>13</sup> L.R. Bickford, J.M. Brownlow and R.F. Penoyer, "Magnetocrystalline Anisotropy in Cobalt Substituted Magnetic Single Crystals", *Proc. Inst. Elec. Eng. (London)*, 104B, 1956, 208
- <sup>14</sup> D.E. Spekiotis, "Performance of MP<sup>++</sup> and BaFe<sup>++</sup> Tapes in High Density Recording Applications", *IEEE Trans. Magn.* 31(6), 1995, 2877-2882
- <sup>15</sup> D.E. Spekiotis, "Advanced MP<sup>++</sup> and BaFe<sup>++</sup> Tapes", *J. Magn. Magn. Mater.*, 155, 1996, 83-85
- <sup>16</sup> F Weingart, G. Brodt and A. Lehner, "AB-Block Copolymers as Dispersants in Magnetic Coating Formulations", *J. Magn. Magn. Mater.*, 155, 1995, 77-79
- <sup>17</sup> D. Perretie, H. Wang, P. Pierini, D. Speliotis, J. Judy and Q. Chen, "A High-Performance Flexible Substrate for Thin-Film Media", *J. Magn. Magn. Mater.*, 120, 1993, 334-337
- <sup>18</sup> D. Perretie and D. Speliotis, "The Effect of Substrate and Environmental Conditions on the Stability of Advanced Magnetic Media", *J. Mag. Soc. Jpn.*, 18, 1994, 279-282
- <sup>19</sup> B.L. Weick and B. Bhushan, "The Tribological and Dynamic Behaviour of Alternative Magnetic Tape Substrates", *Wear*, 190, 1995, 28-43
- <sup>20</sup> D.E. Spekiotis, "Performance of MP<sup>++</sup> and BaFe<sup>++</sup> Tapes in High Density Recording Applications", *IEEE Trans. Magn.* 31(6), 1995, 2877-2882
- <sup>21</sup> H. Inaba, K. Ejiri, N. Abe, K. Masaki and H. Araki, "The Advantages of the Thin Magnetic Layer on a Metal Particulate Tape", *IEEE Trans. Magn.* 29(6), 1993, 3607-3612
- <sup>22</sup> S.B. Luitjens, *IEEE Trans. Magn.* 24, 1990, 6
- <sup>23</sup> J. Hokkyo, T. Suzuki, K. Chiba, K. Sato, Y. Arisaka, T. Sasaki, and Y. Ebine, *J. Magn. Magn. Mater.*, 120, 1993, 281
- <sup>24</sup> T. Hinemo and T. Katahu, *J. Magn. Magn. Mater.*, 134, 1994, 255
- <sup>25</sup> C. Yamamitsu, A. Iketani, J. Ohta and N. Echima, *IEEE Trans. Magn.* 31, 1995, 1037
- <sup>26</sup> S.B. Luitjens, S.E. Stupp and J.C. Lodder, "Metal Evaporated Tape: State of the Art and Prospects", *J. Magn. Magn. Mater.*, 155, 1996, 261-265
- <sup>27</sup> G. Fisher, H. Richter, H.P. Schildberg, and H. Hibst, *IEEE Trans. Magn.*, 26, 1990, 3757
- <sup>28</sup> K. Shinohara, H Yoshida, T. Kuneida, *J. Magn. Soc. Jpn.*, 18, S1, 1994, 291
- <sup>29</sup> H. Seki, H. Ueda, K. Kuwahara, M. Odagiri and T. Kuneida, *J. Magn. Soc. Jpn.*, 18, S1, 1994, 291
- <sup>30</sup> M.S. Hempstock and J.L. Sullivan, "A Study of the Mechanical and Magnetic Performance of Metal Evaporated Tape", *J. Magn. Magn. Mater.*, 155, 1996, 323-328
- <sup>31</sup> C. Dennis Mee and Eric D. Daniel, "Magnetic Recording Handbook", McGraw-Hill, 1990, p284
- <sup>32</sup> K Ozawa, H. Wakasugi, and K. Tanakawa, "Friction and Wear of Magnetic Heads and Amorphous Metal Sliding Against Magnetic Tapes", *IEEE Trans. Magn.*, MAG-20, 1984, 425

- <sup>33</sup> Bharat Bhushan, "Tribology and Mechanics of Magnetic Storage Devices", Springer-Verlag, New York, 1990
- <sup>34</sup> G.Y. Chin and J.H. Wernick, "Soft Magnetic Metallic Materials", Ferromagnetic Materials, North Holland, Amsterdam, 1980, Vol. 2
- <sup>35</sup> P.I Slick, "Ferrites for Non-Microwave Applications", Ferromagnetic Materials, North holland, Amsterdam, 1980, Vol. 2
- <sup>36</sup> M. Mitzushima, "Mn-Zn Single Crystal Ferrite as a Video-Head Material", IEEE Trans. Magn. MAG-7, 1971, 345-350
- <sup>37</sup> E. Hirota, T. Mihara, A. Ikeda and H. Chiba, "Hot-Pressed Mn-Zn Ferrite for Magnetic Recording Heads" IEEE Trans. Magn. MAG-7, 1971, 337-341
- <sup>38</sup> K. Mukasa, "Recent Magnetic Recording Technology II – Magnetic Heads", J. Inst. Telev. Eng-Japan, 39, 1985, p295
- <sup>39</sup> F. Jeffers, R.J. McClure, W.W. French, and N.J. Griffith, "Metal in Gap Record Head", IEEE Trans. Magn., MAG 18(6), 1982, 1146-1148
- <sup>40</sup> H. Fujimori, M. Kikuchi, Y. Obi and T. Masumoto, "High Permeability Properties of Amorphous Co-Fe Base Alloy", J. Jpn. Inst. Metal, 41, 1977, 111
- <sup>41</sup> K Matsuura, K. Oyamada and T. Yazaki, "Amorphous Video Heads for High Coercive Tape", IEEE Trans. Magn., MAG-19, 1983, p1623
- <sup>42</sup> Y Shimada, "Cobalt Amorphous Materials Produced by Sputtering", J. Jpn. Inst. Metals, 22, 1983, 11
- <sup>43</sup> K. Takahashi, K. Ihara, I. Sato, S. Muraoka, E. Sawai and M. Kaminaka, "A High Performance Video Head with Co Based Alloy Laminated Films", Dig. Intermag. Conf. 1987, EB-08
- <sup>44</sup> Jun Zhu and Pradeep Thayamballi, "Frequency Losses of Readback efficiency for Thin-Film Inductive Heads", IEEE Trans. Magn., 32, 1996, 84-89
- <sup>45</sup> Jun Zhu and Garry Petty, "Modelling of lamination Effects for Thin Film Inductive Heads", IEEE Trans. Magn., 32, 1996, 3533-3535
- <sup>46</sup> I. Himeshima, I. Enomoto, A. Hara, T. Fujine, T. Satou, Y. Kitaya and T. Kimura, Sharp Technical Journal, 64, 1996, 35-41
- <sup>47</sup> J. P. Lazzari and I. Melnick, "Integrated Magnetic Recording Heads", IEEE Trans. Magn., MAG-7, 1971, 146
- <sup>48</sup> K. Ohashi., "Mechanisms of 90° Wall Motion in Thin Film Heads", IEEE Trans. Magn., MAG 21, 1985, 1581
- <sup>49</sup> W. Rave, L. Belliard, M. Labrune, A. Thiaville and J. Miltat, "A Magnetic Force Analysis of Soft Thin Film Elements", IEEE Trans. Magn., 30, 1994, 4437-4478
- <sup>50</sup> K. Nago, A. Natsui, H. Yohda, H. Sakakima, Y. Nakatini and I. Aokura, "Double-Structured Laminated Heads with Substrate Bias-Sputtered FeTaN Films", IEEE Translation Journal on Magnetism in Japan, Vol. 9, No. 4, 1994, 28-33
- <sup>51</sup> K. Mukassa, "Recent Magnetic recording Technology II – Magnetic Heads", J. Inst. Telev. Eng-Japan, 39, 1985, 295
- <sup>52</sup> Y. Shimada, T. Hasegawa and H. Kojima, "Sputtering of FeCo-B Amorphous Films with Soft Magnetic Properties", IEEE Trans. Magn., MAG-17, 1981, 1199
- <sup>53</sup> M. Nose, K. Esashi, J. Kanehira, S. Ohnuma, K. Shirakawa and T. Masumoto, "Low Field Magnetic Properties of Co-Zr Base Amorphous Alloys", in Proc. 4<sup>th</sup> Int. Conf. On Rapidly Quenched Metals, Sendai, 1981, p941
- <sup>54</sup> J. A. Oboaf and E. Klokholm, "Amorphous Magnetic Alloys of Cobalt-Titanium", J. Appl. Phys., Vol. 52, No. 3, 1981, 1844
- <sup>55</sup> H. Sakakima, "Properties of Amorphous Alloy Films Mainly Composed of Co-Nb", IEEE Trans. Magn., MAG-19, No. 2, 1983, 131-135
- <sup>56</sup> H. Fujimori, N.S. Kazama, K. Hirose, J. Zhang, H. Morita, I. Sato and H. Sugawara, J. Appl. Phys., 55, 1984, 1769
- <sup>57</sup> C. Nishimura, K. Yangisawa, A. Tago and J. Kishiyami, IEEE Trans. Magn., 25, 1989, 3683
- <sup>58</sup> F.W.A. Dirne and J.J.M Ruigrok, IEEE Trans. Magn., 26, 1990, 1683
- <sup>59</sup> K. Takahashi, K. Ihara, S. Muraoka, H Yohda, E. Sawai, and N. Kaminaka, IEEE Trans. Magn., 23, 1987, 2928
- <sup>60</sup> H.J. de Witt, J. Magn. Mater., 79, 1989, 167
- <sup>61</sup> G. Herzer, IEEE Trans. Magn., 26, 1990, p1397
- <sup>62</sup> H. Hofmann, IEEE Trans. Magn., MAG-4, 1968, p32
- <sup>63</sup> H. Hofmann, IEEE Trans. Magn., MAG-9, 1973, p17
- <sup>64</sup> G. Herzer, IEEE Trans. Magn., 25, 1989, p3327
- <sup>65</sup> G. Herzer, IEEE Trans. Magn., 26, 1990, p1397

- <sup>66</sup> F.W.A. Dirne, J.A.M. Tolboom, H.J. de Witt, and C.H.M. Witmer, *J. Appl. Phys.*, 66, 1989, 167
- <sup>67</sup> F. Roozeboom and F.W.A. Dirne, "Rapid Thermal Annealing of Amorphous and Nanocrystalline Soft Magnetic Metal Alloys in a Static Magnetic Field", *J. Appl. Phys.*, 77(10), 1995, 5293-7
- <sup>68</sup> K. Hayashi, M. Hayakawa, W. Ishikawa, Y. Ochiai, Y. Iwasaka, and K. Aso, "Soft Magnetic Properties of FeRuGaSi Alloy Films: SOFTMAX®", *J. Appl. Phys.*, 64(2), 1988, 772-779
- <sup>69</sup> K. Hayashi, M. Hayakawa and K. Aso, "Effects of Ru and Ti Additions on Soft Magnetic Properties in FeGaSi and FeAlSi Sputtered Films", *Journal of Magnetism and Magnetic Materials*, 92, 1990, 284-288
- <sup>70</sup> K. Nakanishi, O. Shimizu and S. Yoshida, *J. Magn. Soc. Jpn.*, 15, 1991, 371
- <sup>71</sup> K. Nago, H. Sakakima and K. Ihara, *J. Magn. Soc. Jpn.*, 15, 1991, 365
- <sup>72</sup> N. Ishiwata, C. Wakabayashi and H. Urai, "Soft Magnetism of High Nitrogen Concentration FeTaN Films", *J. Appl. Phys.*, 69, 1991, 5616
- <sup>73</sup> T. Okumura, A Osaka, N. Ishiwata, M Kitamura and Haruo Urai, "Read/Write Characteristics for Laminated High Moment Fe-Ta-N Film Heads for HDTV VTR", *IEEE Trans. Magn.*, 28(5), 1992, 2121-2123
- <sup>74</sup> T. Okumura, N. Ishiwata and H. Urai, "Laminated Fe-Ta-N Heads for HD-digital VTR", *IEEE Translation Journal on Magnetism in Japan*, 8(8), 1993, 551-561
- <sup>75</sup> K. Nago, I. Aokura, H. Yamanishi, H. Sakakima and K. Osano, "Substrate Bias Effects on the Magnetic Properties of Fe-Ta-N Films", *IEEE Translation Journal on Magnetism in Japan*, 8(12), 1993, 934-940
- <sup>76</sup> K. Nago, "Nano-Crystalline Fe-Based Nitride (Fe-Ta-N) Films for Magnetic Heads", *National Technical Report*, 40(1), 1994, 128-134
- <sup>77</sup> F.W.A. Dirne and J.J.M. Ruigroek, "Sputtered Sandwich Heads for High Density Digital Recording", *IEEE Trans. Magn.*, 26(5), 1990, 1683-1685
- <sup>78</sup> A.E.T. Kuiper and H.J. de Wit, "Topographically Controlled Anisotropy in Sandwich Video Heads", *IEEE Trans. Magn.*, 32(2), 1996, 515-519
- <sup>79</sup> R. Stribeck, "Characteristics of Plain and Roller Bearings", *Zeit. Ver. Deut. Ing.*, 46, 1902, 1341-1348, 1432-1438, 1463-1470
- <sup>80</sup> F.E. Talke, "A Review of 'Contact Recording' Technologies", *Wear*, 207, 1997, 118-121
- <sup>81</sup> F.P. Bowden and D. Tabor, "Friction and Lubrication of Solids, Part 1", Clarendon Press, 1950, 90-121
- <sup>82</sup> F.P. Bowden and D. Tabor, "Friction and Lubrication of Solids, Part 2", Clarendon Press, 1964, 52-86
- <sup>83</sup> E. Rabinowicz, "Friction and Wear of Materials", Wiley, 1965, 51-108
- <sup>84</sup> B.V. Deryagin and I.I. Abrikosova, *J. Exp. Theor. Phys.*, 3, 1956, 819
- <sup>85</sup> N.P. Suh and H.C. Lin, "The Genesis of Friction", *Wear*, 25, 1973, 111-124
- <sup>86</sup> J.L. Sullivan, "The Tribology of Flexible Magnetic Recording Media", *J. Magn. Magn. Mater.*, 155, 1996, 312-317
- <sup>87</sup> B.J. Briscoe and D. Tabor in *Polymer Surfaces*, eds. D.T. Clarke and W.J. Feast, Wiley, New York, 1988
- <sup>88</sup> P.J. Sharma, "Factors Affecting the Durability of Floppy Diskette Media and Mechanisms of Wear", PhD Thesis Aston University, Birmingham, 1989
- <sup>89</sup> B. Bhushan, "Contact Mechanics of Rough Surfaces in Tribology: Multiple Asperity Contact", *Tribology Letters*, 4, 1998, 1-35
- <sup>90</sup> B. Bhushan and G.S. Blackman, "Atomic Force Microscopy of Magnetic Rigid Disks and Sliders and its Applications to Tribology", *ASME Journal of Tribology*, 113, 1991, 452-457
- <sup>91</sup> J.A. Greenwood and J.B.P. Williamson, "Contact of Nominally Flat Surfaces", *Proc. Roy. Soc. Lon. A*, 295, 1966, 300-319
- <sup>92</sup> D.J. Whitehouse and J.F. Archard, "The Properties of Random Surfaces of Significance in Their Contact", *Proc. Roy. Soc. Lon. A*, 316, 1970, 97-121
- <sup>93</sup> R.A. Onions and J.F. Archard, "The Contact of Surfaces having a Random Structure", *J. Phys. D: Appl. Phys.* 6, 1973, 289-304
- <sup>94</sup> P.R. Nayak, "Random Process Model of Rough Surfaces in Plastic Contact", *Wear*, 26, 1973, 305-333
- <sup>95</sup> A.W. Bush, R.D. Gibson, and T.R. Thomas, "The Elastic Contact of a Rough Surface", *Wear*, 35, 1975, 87-111
- <sup>96</sup> A.W. Bush, R.D. Gibson, and G.P. Keogh, "Strongly Anisotropic Rough Surfaces", *ASME Journal of Lubrication Technology*, 101, 1979, 15-20
- <sup>97</sup> R.D. Gibson, "The Surface as a Random Process", in: *Rough Surfaces*, ed. T.R. Thomas, Longman, London, 1982
- <sup>98</sup> D.J. Whitehouse and J.F. Archard, "The Properties of Random Surfaces of Significance in Their Contact", *Proc. Roy. Soc. Lon. A*, 316, 1970, 97-121
- <sup>99</sup> C.A. Kotwall and B. Bhushan, "Contact Analysis of Non-Gaussian Surfaces for Minimum Static and Kinetic Friction and Wear", *Tribol. Trans.*, 39, 1996, 890-898

- <sup>100</sup> B. Bhushan, "Contact Mechanics of Contact Mechanics of Rough Surfaces in Tribology: Single Asperity Contact", *Appl. Mechanics Rev.* 49, 1996, 275-298
- <sup>101</sup> B. Bhushan, "Analysis of the Real Area of Contact Between a Polymeric Magnetic Medium and a Rigid Surface", *J. Trib., Trans. ASME*, 106, 26-34
- <sup>102</sup> P.I. Oden, A. Majumdar, B. Bhushan, A. Padmanbhan, and J.J. Graham, "AFM Imaging, Roughness Analysis and Contact Mechanics of Magnetic Tape and Head Surfaces", *ASME Journal of Tribology*, 114, 1992, 666-674
- <sup>103</sup> C.Y. Poon and B. Bhushan, "Comparison of Surface Roughness Measurements by Stylus Profiler, AFM, and Non-contact Optical Profiler", *Wear*, 190, 1995, 76-88
- <sup>104</sup> B. Bhushan, "The Real Area of Contact of Polymeric Magnetic Media II: Experimental Data and Analysis", *ASLE Transactions*, Vol. 28, 181-197
- <sup>105</sup> A. Majumdar and B. Bhushan, "Role of Fractal Geometry in Roughness Characterisation and Contact Mechanics of Rough Surfaces", *ASME Journal of Tribology*, 112, 1990, 205-216
- <sup>106</sup> S. Ganti and B. Bhushan, "Generalised Fractal Analysis and its Applications to Engineering Surfaces", *Wear*, 180, 1995, 17-34
- <sup>107</sup> A. Majumda and B. Bhushan, "Fractal Model of Elastic-Plastic Contact Between Rough Surfaces", *ASME Journal of Tribology*, 113, 1991, 1-11
- <sup>108</sup> B. Bhushan and A. Majumda, "Elastic-Plastic Contact Model of Bifractal Surfaces", *Wear*, 153, 1992, 53-64
- <sup>109</sup> C. Lacey and F.E. Talke, "Measurement and Simulation of Partial Contact at the Head Tape Interface" *ASME Journal of Tribology*", 114, 1992, 646-652
- <sup>110</sup> R. Swain, E. Baugh and F.E. Talke, "Full-Field Interferometric Measurement Of Head-Tape Contact Spacing"
- <sup>111</sup> M.H. Wahl, S. Casmer, and F.E. Talke, "Multi-Wavelength Intensity Based Interferometry for Flexible Head-Medium Interface", *Tribology and Mechanics in Magnetic Storage Systems*, STLE SP-36, 9, 1994, 17-24
- <sup>112</sup> K.J. Stahl, J.W. White and K.L. Deckert, "Dynamic Response of Self Acting Foil Bearings", *IBM Journal of Research and Development*, 18, 1974, 513-520
- <sup>113</sup> J. Heinrich and S. Wadwha, "Analysis of Self-Acting Foil Bearings: A Finite Element Approach", *Tribology and Mechanics in Magnetic Storage Systems*, STLE SP-21, 3, 1986, 152-159
- <sup>114</sup> C. Lacey and F.E. Talke, "Simulation of Wear of Tape Head Contours", *IEEE Trans. Magn.*, 1992, 2554-2556
- <sup>115</sup> E.L. Wang, Y. Wu, and F.E. Talke, "Tape Asperity Compliance Measurement Using a Pneumatic Method", *IEEE Trans. Magn.*, 32, 1996, 3732-3734
- <sup>116</sup> Y. Wu and F.E. Talke, "The Effect of Surface Roughness on the /Head-Tape Interface", *ASME Journal of Tribology*, 118, 1996, 376-381
- <sup>117</sup> H. Kwon, M.H. Wahl, F.E. Talke, "Finite Element Simulation of a Helical Scanner with Head/Tape Contacts", *IEEE Trans. Magn.*, 32, 1996, 3735-3737
- <sup>118</sup> T. Okuwaki, T. Kawakita, N. Akahane and K. Kusumoto, "Investigation on Head-tape Contact in VTR", *IEEE Trans. Magn.*, 29, 1993, 3954-3956
- <sup>119</sup> S.T. Patton and B. Bhushan, "Environmental Effects on the Streaming Mode Performance of Metal Evaporated Tapes", *IEEE Trans. Magn.*, 33, 1997, 2513-2530
- <sup>120</sup> A.W. Adamson, "Physical Chemistry of Surfaces", Wiley, New York, 1982
- <sup>121</sup> J.N. Israelachvili, "Intermolecular and Surface Forces", 2<sup>nd</sup> Edition, Academic, San Diego, Ca, 1992
- <sup>122</sup> Eds D.R. Lide and H.P.R. Fredrikse, 75<sup>th</sup> Edition, CRC Press, Boca Raton, Fl, 1994
- <sup>123</sup> S.T. Patton and B. Bhushan, "Friction, Wear and Magnetic Performance of Metal Evaporated and Particulate Magnetic Tapes", *Proc. Instn. Mech. Engrs, J – J. Eng. Tribol.*, 211, 1997, 327-347
- <sup>124</sup> B. Bhushan, "Tribology and Mechanics of Magnetic Storage Devices", Springer Verlag, New York, 1990
- <sup>125</sup> B. Bhushan, R.E. Davis and M. Gordon, "Metallurgical Re-Examination of Wear Modes I: Errrosive, Electrical Arcing and Fretting", *Thin Solid Films*, 123, 1985, 93-112
- <sup>126</sup> B. Bhushan, R.E. Davis and H.R. Kolar, "Metallurgical Re-Examination of Wear Modes II: Adhesive and Abrasive", *Thin Solid Films*, 123, 1985, 113-126
- <sup>127</sup> J.T. Burwell, "Survey of Possible Wear Mechanisms", *Wear*, 1, 1957/58, 119-141
- <sup>128</sup> P.A. Engel, "Impact Wear Of Materials", Elsevier, Amsterdam, 1976
- <sup>129</sup> I.V. Kragelskii, "Friction and Wear", Butterworth, London, 1965
- <sup>130</sup> E. Rabinovicz, "Friction and Wear of Materials", Wiley, New York, 1965
- <sup>131</sup> T.S. Eyre, "Wear Characteristics of Metals", *Trib. Int.*, 9, 1976, 203-212
- <sup>132</sup> J.C. Archard, *Wear*, 2, 1958, 438

- <sup>133</sup> E. Rabinowicz and Z. Li, "The Abrasivities of Gamma Ferric Oxide and Chromium Dioxide", Tribology and Mechanics of Magnetic Storage Systems IV, SP-22, 1987, 138-142
- <sup>134</sup> A. Broese van Groenou, H.J.J. Meulenbroeks and R.C.F. Schaake, "Wear By Magnetic Tapes in the Sphere-On-Tape Apparatus", Tribology and Mechanics of Magnetic Storage Systems IV, SP-22, 1987, 143-151
- <sup>135</sup> A. Broese van Groenou, H.J.J. Meulenbroeks and R.C.F. Schaake, "Tests on Materials for Video Heads by CRO2 Tapes in the Sphere-On-Tape Apparatus", Tribology and Mechanics of Magnetic Storage Systems IV, SP-22, 1987, 152-158
- <sup>136</sup> Y. Tsumamoto, H. Yamaguchi and M. Yanagisawa, 1988, "Mechanical Properties and Wear Characteristics of Various Thin Films for Rigid Magnetic disks", IEEE Trans. Magn., MAG-24, 1988, 2644-2646
- <sup>137</sup> A. Broese van Groenou, "Tribology of Magnetic Storage Systems, a Short Review", J. Magn. Magn. Mat., 95, 1991, 289-312
- <sup>138</sup> N.H. Cook and B. Bhushan, "Sliding Surface Interface Temperatures", J. Lub. Tech., Trans ASME, 95, 1973, 31-36
- <sup>139</sup> E. Rabinowicz, "Friction and wear of Materials", Wiley, New York, 1965
- <sup>140</sup> N. P. Suh, "The Delaminative Theory of Wear", Wear, 25, 1973, 11-124
- <sup>141</sup> J.G.A. Bitter, "A Study of Erosion Phenomena", Wear, 6, 1963, Part I: 5-21, Part II: 169-190
- <sup>142</sup> I. Finnie, "Erosion of Surfaces by Solid Particles", Wear 3, 1960, 87-103
- <sup>143</sup> R. Bellman and A. Levy, "Erosion Mechanism in Ductile Materials", Wear, 70, 1981, 1-27
- <sup>144</sup> S. Soderberg, S. Hogmark, and H. Swahn, "Mechanisms of Material Removal During Erosion of A Stainless Steel", ASLE Trans., 26, 1983, 161-172
- <sup>145</sup> I.M. Hutchings, and R.E. Winter, "Particle Erosion of Ductile Metals: A Mechanism of Material Removal", Wear, 27, 1974, 121-128
- <sup>146</sup> I.M. Hutchings, R.E. Winter, and J.E. Field, "Solid Particle Erosion of Ductile Metals: The Removal of Surface Material by Spherical Projectiles", Proc. Roy. Soc. (Lond.), A348, 1976, 379-392
- <sup>147</sup> P.A. Engel, "Impact Wear Of Materials", Elsevier, Amsterdam, 1976
- <sup>148</sup> Quin, 1983
- <sup>149</sup> J.L. Sullivan and S.O. Saied, "A Study of the Development of Tribological Oxide Protective Thin Films Mainly by Auger electron Spectroscopy", Surface and Interface Analysis, 12, 1988, 541-547
- <sup>150</sup> J.L. Sullivan, Private Communication
- <sup>151</sup> B. Bhushan and R.E. Davis, "Surface Analysis Study of Electrical-Arc induced Wear", Thin Solid Films, 108, 1983, 135-156
- <sup>152</sup> Anonymous, "Fretting and Fretting Corrosion", Lubrication, 41, 1955, 85-96
- <sup>153</sup> R.B. Waterhouse, "Fretting Wear", Proc. Int. Conf. On Wear of Materials, ASME, New York, 1981, 17-22
- <sup>154</sup> Y. Mizoh, "Wear of Tribo-Elements of Video Tape Recorders", Wear, 200, 1996, 252-264
- <sup>155</sup> P.J. Flanders, IEEE Trans. Magn., MAG-13, 1977, 1673-??
- <sup>156</sup> T. Shioyama, N. Yokobori, H. Okamoto and M. Koda, "Rotary Head Assembly Having Direct Coupled Electronics Communications Motor For VHS VTRs", National technical Report, 28, 1982, 532-541
- <sup>157</sup> T. Asada, A. Maruyama, M. Kishimoto, N. Hujimori, and M. Khoda, "Hydrodynamic for Portable VTR Head Assemblies", National technical Report, 31, 1988, 854-860
- <sup>158</sup> K. Matsuota, "Tribology in Mechanical Components of VCRs", J. Jap. Soc. Tribol., 40, 1995, 969-974
- <sup>159</sup> K. Lee, K.Y. Eun, K. Kim and K. Choi, "Application of Diamond-Like-Carbon Films for Anti-abrasion and Low Friction Properties of VCR Head Drums", Surface and Coatings Technology, 76-77, 1995, 786-790
- <sup>160</sup> H. Hashi, A. Konishi, and S. Murata, "A Study of Tape Driving Force for Magnetic Recording or Reproducing Apparatus", I. Inst. Telev. Engr. Jap., 46, 1992, 1301-1307
- <sup>161</sup> K. Matsuota, "Tribology in Mechanical Components of VCRs", J. Jap. Soc. Tribol., 40, 1995, 969-974
- <sup>162</sup> K. Masuda, T. Terada, K. Ogiro, and S. Kozama, "Mechanism for Muse-VTR, VTR", TV. Sc. & Techn. Rep., VT-70, 1985, 25-30
- <sup>163</sup> K. Yoneda and T. Sawada, "Simulation of Spacing Between Magnetic Head and Medium on Video Floppy", J. Magn. Soc. Jpn, 10(2), 1986, 117-120
- <sup>164</sup> A.E.E. Rogers and H.F. Hinterzegger, "Measurement of Magnetic Tape Abrasivity by Interchanging Tape Thickness", Trib. Trans., 36(1), 1993, 139-143
- <sup>165</sup> A. Broese van Groenou and H.J.J.C. Meulenbroeks, "On the Laws of Head Wear in Video Tape Recording: The Influence of Pressure and Time", In: Tribology and Mechanics of Magnetic Storage Systems", 5, Ed. B. Bhushan and N.S. Eiss, STLE, Park Ridge, 1988, 108-116
- <sup>166</sup> F.W. Hahn Jr., "An Evaluation of a Wear Resistant Coating", IEEE Trans. Magn., 11, 1975, 1242-1244

- <sup>167</sup> T. Maegawa, Y. Morioka, A. Kuroe, and M. Kobayashi, "Optimum Magnetic-Head Shape Design for High-Density Recording", *IEEE Trans. Magn.*, 28(5), 1992, 2557-2559
- <sup>168</sup> Y. Mizoh and H. Yohda, "Effects of Magnetic Head Wear on Envelope", *IEEE Transl. J. Magn. Jap.*, 5, 1990, 238-243
- <sup>169</sup> Y. Mizoh, H. Yohda, H. Kotera, H. Kita and N. Kaminaka, "Finite Element Analysis of Tape Floating Behaviour on Magnetic Head and Grooved Drum in a Video Cassette Recorder", *ASME Adv. Info. Storage Syst.*, 5, 1992, 481-492
- <sup>170</sup> K. Tanaka, K. Miyoshi, and T. Murayama, "Friction and Wear on the Sliding of VTR Head against Magnetic Tape (3<sup>rd</sup> Report) – Effect of Wear on the Output Signal Level", *J. Jap. Soc. Precision Engng.*, 40, 1974, 785-791
- <sup>171</sup> A. Kuroe, H. Uenaka, H. Hirokoh, and N. Itoh, "A Short-Time Measuring Method of Head Wear in VCR", *Trans. Inst. Electron. Inf. Commun. Engr.*, J-73-C11, 1990, 803-812
- <sup>172</sup> K. Tanaka, "Friction and Wear of Magnetic Particles", *J. Jap. Soc. Lubri. Engr.*, 26, 1981, 296-302
- <sup>173</sup> K. Tanaka and O. Miyazaki, "Wear of Magnetic Materials and Audio Heads Sliding Against Magnetic Tapes", *Wear*, 66, 1981, 289-306
- <sup>174</sup> K. Tanaka, K. Miyoshi, H. Araki, and T. Murayama, "Friction and Wear on the Sliding of VTR Head against Magnetic Tape (2<sup>nd</sup> Report) – Wear of VTR Head made of a Ferrite Single Crystal", *J. Jap. Soc. Precision Engng.*, 40, 1974, 651-657
- <sup>175</sup> K. Miyoshi, "Lapping of Manganese-Zinc Ferrite by Abrasive Tape", *J. Am. Soc. Lubri. Engng.*, 38, 1982, 165-172
- <sup>176</sup> B. Bhushan and D.V. Khatavkar, "Role of Tape Abrasivity on Friction, Wear, Staining and Signal Degradation in Audio Tape", *Wear*, 190, 1995, 16-27
- <sup>177</sup> K. Matsuoka, D. Forrest, M.K. Tse, E. Rabinowicz, "Accelerated Wear Testing of Mn-Zn Ferrite using the Grit Size Effect", *Trans. Jap. Soc. Mech. Engr.*, 60-576, 1994, 2609-2614
- <sup>178</sup> F.W. Hahn, "Wear of Recording Heads by Magnetic Tapes", *Tribology and Mechanics of Storage Systems*, SP-16, 1984, 41-48
- <sup>179</sup> H. Hayashi, H. Yoshimitzu, T. Takayasu and T. Nishiyama, "Magnetic Thin Film Head for VCR", *Tech. Rep. IEICE*, MR94-12, 1994, 1-6
- <sup>180</sup> A. Kuroe, H. Uenaka, H. Hirokoh, and N. Itoh, "A Short-Time Measuring Method of Head Wear in VCR", *Trans. Inst. Electron. Inf. Commun. Engr.*, J-73-C11, 1990, 803-812
- <sup>181</sup> B. Bhushan and D.V. Khatavkar, "Role of Tape Abrasivity on Friction, Wear, Staining and Signal Degradation in Audio Tape", *Wear*, 190, 1995, 16-27
- <sup>182</sup> K. Okada and K. Namura, "Fine Mechanics for Video Tape Recorders", *Trans. Jap. Soc. Mech. Engr.*, 87-791, 1984, 1187-1192
- <sup>183</sup> T. Kojima, Y. Suzuki, and S. Mitani, "Study for the Wear Mechanism of Magnetic Head by Passing of Magnetic Heads", *Trans. Inst. Electron. Inf. Commun. Engr.*, J-65-C, 1982, 285-291
- <sup>184</sup> B. Bhushan and J.A. Lowry, "Friction and Wear Studies of Various Head Materials and Magnetic Tapes in a Linear Mode Accelerated Test Using a New Nano-Scratch Wear Measurement Technique", *Wear*, 190m 1995, 1-15
- <sup>185</sup> B. Bhushan and J.A. Lowry, "Friction and Wear of Particulate and ME Magnetic Tapes Sliding Against Mn-Zn Ferrite in a Linear Mode", *IEEE Trans. Magn.*, 30, 1994, 4182-4184
- <sup>186</sup> W.D. Kehr, C.B. Meldrum, and F.M. Thornley, "The Influence of Grain Size on the Wear of Nickel – Zinc Ferrite by Flexible Media", *Wear*, 31, 1975, 109-117
- <sup>187</sup> B. Bhushan and M.J. Martin, "Accelerated wear Test Using Magnetic Particle Slurries", *Tribol. Trans.*, 31, 1988, 228-231
- <sup>188</sup> D.H. Mayer, "On the Abrasivity of  $\gamma$ -Fe<sub>2</sub>O<sub>3</sub> and CrO<sub>2</sub> Magnetic Tape", *IEEE Trans. Magn.*, 10, 1974, 657-659
- <sup>189</sup> H. Yoshida, Y. Nishizawa, T. Fijita, M. Murai, K. Takahashi, and Y. Odagiri, "Metal Evaporated Tape with DLC protective Layer", *National Technical Report*, 41, 1995, 188-193
- <sup>190</sup> B. Bhushan, "Mechanics and Reliability of Flexible Magnetic Media", Springer, New York, 1992
- <sup>191</sup> K. Tanaka, "Friction and Wear of Magnetic Particles", *J. Jap. Soc. Lubri. Engr.*, 26, 1981, 296-302
- <sup>192</sup> K. Miyoshi, "Lapping of Manganese-Zinc Ferrite by Abrasive Tape", *J. Am. Soc. Lubri. Engng.*, 38, 1982, 165-172
- <sup>193</sup> K. Matsuoka, D. Forrest, M.K. Tse, and E. Rabinowicz, "Accelerated wear Testing of Mn-Zn Ferrite using the Grit Size Effect", *Trans. Jap. Soc. Mech. Engr.*, 60-576, 1994, 2906-2614
- <sup>194</sup> A. Kuroe, H. Uenaka, M. Hirokoh and N. Itoh, "A Short-Time Measuring Method of Head Wear in VCR", *Trans. Inst. Electron. Inf. Commun. Engr.*, J73-C-11, 1990, 903-812
- <sup>195</sup> T. Kojima, Y. Suzuki and S. Mitani, "Study for Wear Mechanism of Magnetic Head by Passing Magnetic Tapes", *Trans. Inst. Electron. Inf. Commun. Engr.*, J65-C, 1982, 285-291



- <sup>196</sup> T. Kawamata, Y. Mizoh, H. Ushigome and H. Hagiwara, "Abrasive Effect of Magnetic Recording Tape on Rubbing Noise", *Trans. Inst. Electron. Inf. Commun. Engr.*, J67-C, 1984, 62-69
- <sup>197</sup> F.W. Hahn Jr, "Head Wear as a Function of Isolated Asperities on the Surface of Magnetic Tapes", *IEEE Trans. Magn.*, 20, 1984, 918-920
- <sup>198</sup> A. Kuroe, F. Shinoda and M. Mikoda, "An Experimental Analysis of the Recorded Signal Decrease Phenomena in the Repeated Tape Running", *Trans. Inst. Electron. Inf. Commun. Engr.*, J74-II, 1991, 194-200
- <sup>199</sup> H. Yohda and N. Echigo, "Anisotropic Wear of Ferrite Sliding on CoCr Tape", *J. Magn. Soc. Jap.*, 13-S1, 1989, 247-252
- <sup>200</sup> F.W. Hahn Jr., "Wear of Recording Heads by Magnetic Tape", *ASLE Tribol. Mech. Magn. Storage syst.*, Sp-16, 1984, 41-48
- <sup>201</sup> B. Bhushan, "Magnetic Head – Media Interface Temperatures Part 2 – Applications to Magnetic Tapes", *J. Trib. Trans. ASME*, 109, 252-256
- <sup>202</sup> F.P. Bowden and D. Tabor, "Friction and Lubrication of Solids", Vol. 1, Clarendon Press, Oxford, 1950
- <sup>203</sup> B. Bhushan, "Magnetic Head – Media Interface Temperatures Part 1 – Analysis", *J. Trib. Trans. ASME*, 109, 243-251
- <sup>204</sup> J.F. Carroll and R.C. Gotham, "The Measurement of Abrasiveness of Magnetic Tape", *IEEE Trans. Magn.*, 2, 1966, 6-13
- <sup>205</sup> R. Gulino, S. Bair, W.O. Winer, and B. Bhushan, "Temperature Measurement of Microscopic Areas Within a Simulated Head/Tape Interface using Infrared Radiometric Technique", *J. Trib., Trans. ASME*, 108, 1986, 29-34
- <sup>206</sup> D. Mekala, Private Communication
- <sup>207</sup> Y. Mizoh, "Wear of the Magnetic Video Head", *J. Jap. Soc. Trib.*, 40, 1995, 981-986
- <sup>208</sup> D.H. Meyer, "On the Abrasivity of  $\gamma$ -Fe<sub>2</sub>O<sub>3</sub> and CrO<sub>2</sub> Magnetic Tape", *IEEE Trans. Magn.*, 10, 1974, 657-659
- <sup>209</sup> A.F.E. Rogers and H.F. Hinteregger, *STLE Tribol. Trans.*, 36, 1993, 139-143
- <sup>210</sup> A. Kuroe and M. Kobayashi, "Recent Study of Analytical Techniques for Head/Tape Interface Problems", *J. Inst. Telev. Engr. Jap.*, 45, 1991, 1515-1520
- <sup>211</sup> F.W. Hahn, "Wear of Recording Heads by Magnetic Tapes", *Tribology and Mechanics of Storage Systems*, SP-16, 1984, 41-48
- <sup>212</sup> E.F. Cuddihy, "Hygroscopic Properties of Magnetic Recording Tape, *IEEE Trans. Magn.*, 12, 1976, 126-135
- <sup>213</sup> M. Chu, B. Bhushan and L. C. DeJonghe, "Wear Behaviour of Ceramic Sliders in Sliding Contact with Rigid Magnetic Thin-Film Disks", 9-16
- <sup>214</sup> A.S. Chekanov, T.S. Low, S. Alli, O. Kolosov, A. Briggs, "Microcracks of the Thin-Film Head Alumina: "L" Cracks and "U" Cracks", *IEEE Trans. Magn.*, 32(5), 1996, 3696-3698
- <sup>215</sup> S. Chandrasekar, and B. Bhushan, "Friction and Wear of Ceramics for Magnetic Recording Applications – Part I: A Review", *ASME Journal of Tribology*, 112, 1990, 1-16
- <sup>216</sup> S. Chandrasekar, and B. Bhushan, "Friction and Wear of Ceramics for Magnetic Recording Applications – Part I: Friction Measurements", *ASME Journal of Tribology*, 113, 1991, 313-317
- <sup>217</sup> T. Tuchia, M. Abe, Y. Noro, and K. Inada, "The Gap Recession Reduced MIG Head", *IEEE Trans. Magn.*, 29, 1993, 3945-3947
- <sup>218</sup> B. Bhushan and J.A. Lowry, "Friction and Wear Studies of Various Head Materials and Magnetic Tapes in a linear Mode Accelerated Test using New Nano-Scratch Wear Measurement Technique", *Wear*, 190, 1995, 1-15
- <sup>219</sup> N. Ishiwata, T. Okumura, A. Osaka, S. Shinkai, N. Itogawa, N. Kitamura, and H. Urai, "High Abrasion Resistance Laminated Sendust VTR Heads", *IEEE Trans. Magn.*, 1992, 2118-2220
- <sup>220</sup> A. Broese van Groenou and H.J.J.C. Meulenbroeks, in *Tribology and Mechanics of Magnetic Storage Systems*, 4, Ed. B. Bhushan and N.S. Eiss, ASLE, Park Ridge, 1987, 152
- <sup>221</sup> Y. Wang and S.M. Hsu, "Wear and Wear Transition Mechanisms of Ceramics", *Wear*, 195, 1996, 112-122
- <sup>222</sup> K. Ozawa, H. Wakasugi, and K. Tanaka, "Friction and Wear of Magnetic Heads and Amorphous Metal Sliding Against Magnetic Tapes", *IEEE Trans. Magn.*, MAG-20, 425-430
- <sup>223</sup> B. Bhushan, "Assessment of Accelerated Head Wear Test Methods and Wear Mechanisms", In: *Tribology and Mechanics of Magnetic Storage Systems*, 2, Ed. B. Bhushan and N.S. Eiss, ASLE, Park Ridge, 1988, 101-111
- <sup>224</sup> A.G. Evans and D.B. Marshall, "Wear Mechanisms in Ceramics", In: "Fundamentals of Friction and Wear of Materials", Ed. D.A. Rigney, ASM, Metals Park, Ohio, 1980, 439-453

- <sup>225</sup> R.W. Polleys, "Work Hardening of Ferrite Head Surfaces by Wear with Flexible Recording Media", IBM J. Res. Dev., 22, 1978, 675-680
- <sup>226</sup> J.L. Sullivan and M.R. Middleton, "The Pitting and Cracking of SAE 52100 Sliding Rolling Contact in the Presence of an Aqueous Lubricant", ASLE Trans., 1985, 28(4), 431-438
- <sup>227</sup> S.M. Hsu and M.C. Shen, "Ceramic Wear Maps", Wear, 200, 1996, 154-175
- <sup>228</sup> K. Mitzuhara and S.M. Hsu, Tribochemical Reaction of Oxygen and Water on Silicon Surfaces", Wear Particles, Ed. D. Dowson et al, Elsevier, Amsterdam, 1992, 323
- <sup>229</sup> H. Tomizawa and T.E. Fischer, "Friction and Wear of Silicon Nitride and Silicon Carbide in Water", ASLE Trans., 30(1), 1987, 41
- <sup>230</sup> R.E. Gates, E.E. Klaus, and S.M. Hsu, "Tribochemical Reaction of Alumina with Water", Tribol. Trans., 32(3), 1989, 357-363
- <sup>231</sup> T.E. Fischer, M.P. Anderson, S. Jahanmir and R. Salher, "Friction and Wear of Tough and Brittle Zirconia in Nitrogen, Air, Water, Hexadecane, and Hexadecane Containing Stearic Acid", Wear, 124, 1988, 133
- <sup>232</sup> T.E. Fischer and W.M. Mullins, "Chemical Aspects Of Ceramic Tribology", J. Phys. Chem. 96, 1992, 5690-5701
- <sup>233</sup> W.M. Mullins, "The Effect of Fermi Energy on Reaction of Water with Oxide Surfaces", Surface science, 217, 1989, 459-467
- <sup>234</sup> Yoshimura, M. Ceram. Bull., 67, 1988, 1951
- <sup>235</sup> E. Orawan, Nature, 154, 1044, 341
- <sup>236</sup> S.M. Wiederhorn, "Influence of Water Vapour on Crack Propagation In Soda Lime Glass", J. Amer. Cer. Soc., 50, 1969, 407-414
- <sup>237</sup> T.A. Michalske and S.W. Freiman, J. Amer. Cer. Soc., 66, 1983, 284-290
- <sup>238</sup> T.A. Michalske and S.W. Freiman, J. Amer. Cer. Soc., 66, 1983, 284-2
- <sup>239</sup> T.A. Michalske and B.C. Bunker, "Slow Fracture Model Based on Strained Silicate Structures", J. Appl. Phys., 56(100), 1984, 2686-2693
- <sup>240</sup> B.A. Morrow and L.A. Cody, J. Phys. Chem, 80, 1976, 1995-1998
- <sup>241</sup> B.A. Morrow and L.A. Cody, J. Phys. Chem, 80, 1976, 1998-2001
- <sup>242</sup> B.A. Morrow and L.A. Cody, J. Phys. Chem, 80, 1976, 2761-2764
- <sup>243</sup> T.A. Michalske, S.W. Friedman, and B.C. Bunker, Am. Cer. Soc. Bull., 61, 1982, 414
- <sup>244</sup> J.B. Peri, J. Phys. Chem., 69, 1965, 231
- <sup>245</sup> S.M. Wiederhorn, S.W. Freiman, E.R. Fuller Jr., and C.J. Simmons, "Effects of Water and Other Dielectrics on Crack Growth", J. Mater. Sc., 17, 1982, 3460-3478
- <sup>246</sup> B. Bhushan and D.V. Khatavkar, "Role of Water Vapour on the Wear of Mn-Zn ferrite Heads Sliding Against Magnetic Tapes", Wear, 202, 1996, 30-34
- <sup>247</sup> H. Sakakima, Y. Yanagiuchi, M. Satomi, H. Senno and E. Hirota, "Improvement in Amorphous Magnetic Alloys for Magnetic Head Core", Proc. Conf. Rapidly Quenched Materials, Sendai, Japan, 1981, p941
- <sup>248</sup> K. Katori, H. Ohmori, M. Shoji and K. Hayashi, "Wear and Corrosion Resistance of Fe-N Based Micrograin Soft Magnetic Thin Films", IEEE Trans. Magn., 30(2), 1994, 331-336
- <sup>249</sup> K.I Arai and K. Ishiyama, "Recent Developments of New Soft Magnetic Films", J. Magn. Magn. Mater., 133, 1994, 233-237
- <sup>250</sup> Gerard Theunissen and Matthew Harrison, Private Communication
- <sup>251</sup> H. Deng, V.R. Inturi, and J.A. Barnard, "Nanoindentation and Tribological Study of Magnetically Soft High Moment FeTaN Thin Films", IEEE Trans. Magn., 31(6), 1995, 2697-2699
- <sup>252</sup> H. Deng, V.R. Inturi, and J.A. Barnard, "The Effect of Ta and N content on Mechanical Properties of DC Magnetron Sputtered FeN and FeTaN Thin Films", Proc. Conf. Thin Films: Stresses and Mechanical Properties VI. Symposium April 1996, Mater., Rex. Soc., 1997, 195-200
- <sup>253</sup> H. Deng, M.K. Minor, and J.A. Barnard, "Comparison of Mechanical and tribological Properties of Permalloy and High Moment FeTaN Thin Films for Recording Heads", IEEE Trans. Magn., 32(5), 1996, 3702-3704
- <sup>254</sup> H. Osaki, J. Kurihara and T. Kanou, "Mechanisms of Head-Clogging by Particulate Magnetic Tapes in Helical Scan Video Recorders", IEEE Trans. Magn., 30, 1994, 1491-1498
- <sup>255</sup> H. Osaki, "Tribology of Videotapes", Wear, 200, 1996, 244-251
- <sup>256</sup> B. Bhushan and V.N. Koinkar, "Microtribology of Metal Particle, Barium Ferrite and Metal Evaporated Magnetic Tapes", Wear, 1995, 181-183, 1995, 360-370
- <sup>257</sup> S.T. Patton, and B. Bhushan, "Friction and Wear of Metal Particle, Barium Ferrite and Metal Evaporated Magnetic Tapes in Rotary Head Recorders", J. Tribol., Transactions of the ASME, 118, 1996, 21-32
- <sup>258</sup> B. Bhushan and J.A. Monahan, "Accelerated Friction and Wear Studies of Various Particulate and Thin-Film Magnetic Tapes Against Tape Path Materials in Pure sliding and Rotary/Sliding Modes", Tribol. Trans., 38, 1995, 329-321

- <sup>259</sup> M.S. Hempstock and J.L. Sullivan, "The Durability and Signal Performance of Metal Evaporated and Metal Particulate Tape"
- <sup>260</sup> H. Hibst, "Metal Evaporated Tapes and Co-Cr Media for High Definition Video Recording", in K.H.J. Bushow, G.J. Long and F. Grandjean, (eds.), "High Density Digital Recording", Vol. E229, Kluwer, Dordrecht, 1993, 137-159
- <sup>261</sup> H. Osaki, K. Fukushi and K. Ozawa, "Wear Mechanisms of Metal-Evaporated Magnetic Tapes in Helical Scan Videotape Recorders", IEEE Trans. Magn., 26, 1990, 3180-3185.
- <sup>262</sup> H. Osaki, J. Kurihara and T. Kanou, IEEE Trans. Magn., MAG-29, 1993, 41-43
- <sup>263</sup> K. Shinohara, H. Yoshida, T. Kunieda, J. Magn. Soc. Jpn, 18, S1, 1994, 291
- <sup>264</sup> H. Tosai and D.B. Bogy, "Characterisation of Diamond-Like Carbon Films and Their Application as Overcoats on Thin Film Media for Magnetic Recording", J. Vac. Sci. Technol. A, 1987, 3287-3312
- <sup>265</sup> W.F. Vom and H. Hornbogen, "Wear Properties of Metal Evaporated Video Tape", Wear, 128, 1988, 291-305
- <sup>266</sup> H. Osaki, "The Role of Surface Asperities on Durability of Metal-Evaporated Magnetic Tapes", IEEE Trans. Magn., 29, 1993, 11-20
- <sup>267</sup> P. Berar, K. Kato, H. Osaki, and P. Kapsa, "Wear Mechanisms of Carbon Coated Metal Evaporated Magnetic Tape in VCR", Proc. International Tribology Conference, Yokohama, Japan, Oct. 29-Nov.2, 1995, 1817-1822
- <sup>268</sup> J. Xu, K. Kato, and T. Nishida, "The Effect of Temperature and Humidity on the Friction and Wear of Magnetic Tape", Wear, 203-204, 1997, 642-647
- <sup>269</sup> H. Osaki, E. Oyanagi, H. Aonuma, T. Kanou and J. Kurihara, "Wear Mechanism of Particulate Magnetic Tapes in Helical Scan Video Tape Recorders", IEEE Trans. Magn, 28, 1992, 76-83
- <sup>270</sup> J.U. Lemke, "Ferrite Transducers", in D.E. Spiliotis and C.E. Johnson (eds.), "Advances in Magnetic Recording", Ann. NY. Acad. Sci., 189, 1972, 171-190
- <sup>271</sup> J. Kelly, "Tape and Head Wear", in F. Kelil (Ed.), "Magnetic Tape Recording for the Eighties", NASA Washington DC, Ref. Pub. 1075, 1982, 7-22
- <sup>272</sup> B. Bhushan and F.W. Hahn, Jr., "Stains on Magnetic Tape Heads", Wear, 184, 1995, 193-202
- <sup>273</sup> J.L. Lauer and W.R. Jones, "Friction Polymers", in B. Bhushan and N.S. Eiss (Eds.), "Tribology and Mechanics of Magnetic Storage Systems", ASME, New York, Vol.3, 1986, 14-23
- <sup>274</sup> K. Tanaka and I. Uchiyama, Wear 23, 1977, 153-55
- <sup>275</sup> R.L. Arudi and J.A. McCracken, "Metal-in-Gap Head Staining", Minutes of THIC Meet., October 3, 1989
- <sup>276</sup> S. Reichlmaier, "High Spacial and Mass Resolution TOF-SIMS Analysis of Video Head Contamination", The Phi Interface, Perkin Elmer, Eden Prairie, MN, 14(2), 1992
- <sup>277</sup> C.M. Stahle and T.D. Lee, "Characterisation of the Deposits on Helical Scan Heads", Adv. Inf. Storage Sys., 4, 1992, 79-86
- <sup>278</sup> H. Ota, K. Namura, and N. Ohmae, "Brown Stain on VCR Head Surface through Contact with Magnetic Tape", Adv. Inf. Storage Syst., 2, 1991, 85-96
- <sup>279</sup> Y.F. Liew, J.L. Lauer, F.E. Talke and K. Connell, "Analysis of Deposits from Friction at Head-Tape Interfaces by Raman Spectroscopy", Tribol. Trans., 38, 1995, 728-732
- <sup>280</sup> T. Tsuchiya and B. Bhushan, "Metal Core Recession and Head Stain Studies of MIG Heads Sliding against Cobalt-Doped Gamma Iron Oxide and Metal Particle Tapes", Tribol. Trans., 38, 1995, 941-949
- <sup>281</sup> B.K. Gupta, B. Bhushan, Y. Zhou, N. Winograd and K. Krishnan, "Chemical Analyses of Stains Formed on Co-Nb-Zr Metal-in-Gap Heads Sliding Against oxide and Metal in Particle Magnetic Tapes", J. Mater. Res., 10(7), 1995, 1795-1810
- <sup>282</sup> T. Tsuchiya and B. Bhushan, "Running Characteristics of MIG Heads against MP, Barium Ferrite and ME Tapes", IEEE Trans. Magn., 30, 1994, 4176-7178
- <sup>283</sup> S.T. Patton and B. Bhushan, "Friction, Wear and Magnetic performance of Metal Evaporated and Particulate Magnetic Tapes", Proc. Instn. Mech. Engrs. Part J, J. Eng. Tribol., 211, 1997, 327-348
- <sup>284</sup> L.A. Reeves and J.L. Sullivan, "The Effect of Head Cleaning Agents on the Wear Mechanisms of Video Heads", J. Phys. D: Appl. Phys., "25, 1992, A328-A333
- <sup>285</sup> M. Abe, T. Tsuchiya, and Y. Noro, "A Study of Recess by Tape Running in Metal and Ceramics Hybrid Heads", Dig. ICF-6, 1992, 451-455
- <sup>286</sup> C.H. Bajorek, M.A. Nicolet and C.H. Wilts, "Preferential Oxidation of Fe in Permalloy Films", Appl. Phys. Lett., 19, 1971, 82-84
- <sup>287</sup> W.Y. Lee and J. Eldridge, "Oxidation Studies of Permalloy Films by Quartz Crystal Microbalance, AES and XPS", J. Electrochem. Soc., 124, 1977, 1747-1751
- <sup>288</sup> W.Y. Lee and Guanieri, "Effects of Oxidation on the Atmospheric Corrosion of Permalloy Films", J. Electrochem. Soc., 126, 1979, 1533-1539

- 
- <sup>289</sup> T. Matsuura and M. Uchizawa, "Wear Behaviour of Thin Film heads for VCR in Sliding with Metal Evaporated Tapes", *Tribol. Trans.*, 37, 1994, 661-665
- <sup>290</sup> S.T. Patton and B. Bhushan, "Micromechanical and Tribological Characterisation of Alternative Pole Tip Materials for Magnetic Recording Heads", *Wear*, 202, 1996, 99-109
- <sup>291</sup> Olympus System Microscope Model BHC Instruction Manual, Olympus Optical Company Ltd, Tokyo
- <sup>292</sup> B. Bhushan and R.J. Martin, "Accelerated Wear Testing using Magnetic Particle Slimes", *Tribol. Trans.*, 31, 1980, 228-238
- <sup>293</sup> D. Briggs and M.P. Seah, *Practical surface Analysis*, 2<sup>nd</sup> Edition, Vol.1, John Wiley and Sons, Chichester, 1990
- <sup>294</sup> D.P Woodruff and T.A. Delcher, *Modern Techniques of Surface Science*, Cambridge University Press, 1986
- <sup>295</sup> C.D. Wagner, NIST X-ray photoelectron spectroscopy database, version 1.0, 1989
- <sup>296</sup> C.D. Wagner, NIST X-ray photoelectron spectroscopy database, version 2.0, 1997
- <sup>297</sup> C.D. Wagner et al, *Handbook of photoelectron spectroscopy*, Perkin Elmer Corporation, Minnesota, 1979
- <sup>298</sup> K. Siegbahn et al. ESCA, atomic, molecular and solid state structure studied by means of electron spectroscopy, Almqvist and Wiksells, Uppsala, 1967
- <sup>299</sup> P. Swift, *Surf. Interface Anal.*, 4, 47, 1982
- <sup>300</sup> D.A. Shirley. *Phys Rev, B*, 1972, 5, 4709-4714
- <sup>301</sup> H.E. Bishop. *Surf. Interface Anal.*, 3, 272, 1981
- <sup>302</sup> S. Tougaard. *Surface Science* 216, 343-360, 1989
- <sup>303</sup> A. Savitsky and M.J.E. Golay. *Anal. Chem*, 1964, 36, 1627-1639
- <sup>304</sup> A. Proctor and M.A. Sherwood. *Anal. Chem*, 1980, 52, 2315-2321
- <sup>305</sup> J.H. Schofield, *J. Electron Spectrosc.*, 8, 129, 1972
- <sup>306</sup> J.L. Sullivan and S.O. Saied, Aston University, Escalab Schofield library.
- <sup>307</sup> J.L. Sullivan and S.O. Saied, Aston University, unpublished results
- <sup>308</sup> J.A. Nedler and R. Mead. *Computer Journal*, 7, 1965, 308.
- <sup>309</sup> SUSPRE VI, Surrey University Sputter Profile Resolution from Energy Deposition
- <sup>310</sup> H Sanghera, J.L. Sullivan and S.O. Saied, Aston University.
- <sup>311</sup> *Handbook of Physics and Chemistry*, 70.
- <sup>312</sup> Philips Research Labs internal report
- <sup>313</sup> Philips Research Labs internal report
- <sup>314</sup> N.N Greenwood and A. Earnshaw, *Chemistry of the Elements*, Pergamon Press, Oxford 1984
- <sup>315</sup> M.J.K. Harrison, unpublished work
- <sup>316</sup> M.J.K. Harrison, J.L. Sullivan, and G.S.A.M. Theunissen, "Wear mechanisms of Sandwich-Type Video Heads", *Proc. Instn. Mech. Engrs J*, 211, 1997, 263-277
- <sup>317</sup> 10 P. Clifton and M.J.K. Harrison, Unpublished work
- <sup>318</sup> 11 D.D. Joseph, "Steep Wave Fronts on Extrudates of Polymer Melts and Solutions: Lubrication Layers and Boundary Lubrication", *J. Non-Newtonian Fluid Mech.*, 70, 1997, 187-203
- <sup>319</sup> 12 D.D Joseph, and J.Y. Liu, "Steep wave Fronts on Extrudates of Polymer Melts and Solutions", *J. Rheol*, 36, 1992, 845-884
- <sup>320</sup> A. Schallamach, "Abrasion and Tyre wear", *Wear*, 1, 1958, 406-410
- <sup>321</sup> A. Schallamach, "How Does Rubber Slide?", *Wear*, 17, 1971, 301-312
- <sup>321</sup> E Sourty, J.L. Sullivan and M. Byjker, *Tribology International*, To be published 2000

---

## Appendix Published Papers

1. M.J.K. Harrison, J.L. Sullivan, and G.S.A.M. Theunissen, "Wear mechanisms of Sandwich-Type Video Heads", *Journal of Engineering Tribology, Proceedings of the Institution of Mechanical Engineers J*, 211, 1997, 263-277
2. M.J.K. Harrison, J.L. Sullivan, and G.S.A.M. Theunissen, "A Study of the Wear Mechanisms of Sandwich Type Video Heads using Various Surface Analytical Techniques", *Proc. ECASIA '97, Gothenburg, Sweden, June 1997, Wiley, London, 1998*, 1131-1134
3. M.J.K. Harrison, J.L. Sullivan, and G.S.A.M. Theunissen, "Pole Tip Recession in Sandwich Heads Incorporating a FeTaN Soft Magnetic Track", *Tribology International*, 31(9), 1998, 491-500

ASTON UNIVERSITY  
- 5 OCT 1999  
30 Edon Road  
Bishopston  
Bristol BS7 8DD

23<sup>rd</sup> September 1999

Sharen Lloyd and Katy Barry  
School of Engineering and Applied Science  
Aston University  
Birmingham B4 7ET

**Concerning the submission of the PhD thesis: "The tribology of laminated recording heads" by Matthew Harrison.**

To the School of Engineering and Applied Science

It has been suggested to me by my supervisor, Professor John Sullivan that it would be useful to readers of the above thesis to have access to the scientific papers published by myself relating to the work contained therein:

1. M.J.K. Harrison, J.L. Sullivan, and G.S.A.M. Theunissen, "Wear mechanisms of Sandwich-Type Video Heads", *Journal of Engineering Tribology, Proceedings of the Institution of Mechanical Engineers J*, 211, 1997, 263-277
2. M.J.K. Harrison, J.L. Sullivan, and G.S.A.M. Theunissen, "A Study of the Wear Mechanisms of Sandwich Type Video Heads using Various Surface Analytical Techniques", *Proc. ECASIA '97, Gothenburg, Sweden, June 1997, Wiley, London, 1998, 1131-1134*
3. M.J.K. Harrison, J.L. Sullivan, and G.S.A.M. Theunissen, "Pole Tip Recession in Sandwich Heads Incorporating a FeTan Soft Magnetic Track", *Tribology International*, 31(9), 1998, 491-500

I would therefore like to add to my submission copies of these papers to be included as an appendix. This does not constitute any addition to the work presented for examination. Full references to these papers are indeed given as an appendix on page 249 of the thesis, and I would like to add these three papers after this page. Please find enclosed three appropriately numbered sets of pages for addition to the three submitted copies of my thesis.

Yours Faithfully



Matthew Harrison

---

## Wear mechanisms of sandwich-type video heads

---

M J K Harrison<sup>1</sup>, J L Sullivan<sup>1</sup> and G S A M Theunissen<sup>2</sup>

<sup>1</sup>Department of Electronic Engineering and Applied Physics, Aston University, Birmingham

<sup>2</sup>Philips Research Laboratories, Eindhoven, The Netherlands



Aston University

Content has been removed due to copyright restrictions

Pages 250 - 277

REMOVED